Università degli Studi di Firenze

FACOLTÀ DI SCIENZE MATEMATICHE FISICHE E NATURALI

Dipartimento di Astronomia e Scienza dello Spazio

Tesi di Dottorato di Ricerca in Astronomia
XVII CICLO

Physical and chemical properties of low–mass starless cores from millimetric observations

Antonio Crapsi

Relatori:	Dr. Paola Caselli
	Prof. Malcolm C. Walmsley
Coordinatore:	Prof. Mario Perinotto

FIRENZE, DICEMBRE 2004

alla mia Famiglia

Contents

Chapter 1

Low–mass star formation

Understanding the details of the star formation process has a big impact in advancing our knowledge of galaxy evolution, planet formation, down to the origin of life. In general, astrophysical research is aimed at i) finding the starting conditions of a problem, ii) describing the physical processes and iii) predicting the final product. In the star formation field, the bulk of the research can be summarized with the following questions:

- how can we distinguish the "sterile" and "fertile" components of the interstellar medium?
- which is the physical mechanism that breaks the equilibrium of the cloud and therefore governs the collapse?
- does our theory explain the observed properties of the stellar population?

The process of star formation spans a great range of masses and dimensions and it has been observed in regions with very different physical conditions. A first distinction can be made between "spontaneous" star formation and induced, or "triggered", star formation. In fact, while in the former case we search for a physical process internal to the cloud which causes gravitational collapse (see next section), in the latter, we assume that there is a *distinct, external event* which furnishes the compression which induces the collapse. This "event" could be represented by a variety of astrophysical processes such as winds from young O and B stars, supernovæ explosions, crossing of a spiral arm density wave or galaxy merging (see, e.g., Loren 1976; Elmegreen & Lada 1977). It is evident that this mode of star formation i) is effective over a large region at the same time, ii) is connected to the formation of high-mass stars (due to the presence of O and B stars and supernovæ), iii) is peculiar to particular regions in the galaxy (like spiral arms or shock fronts), iv) is a run-away or "contagious" process, v) is a very efficient way of converting gas into

stars. As a consequence "triggered" star formation is the preferred mode for producing clusters of high mass stars, such as those seen in the young OB associations. Examples of triggered star formation has been recognized in several star forming regions like IC1805 (Heyer et al. 1996), the Rosette Molecular Cloud (White et al. 1997), IC1396 (Patel et al. 1998), and in bright-rim clouds (Sugitani, Fukui, & Ogura 1991), where the location of newly born stars with respect to the dense gas compressed by expanding HII regions supports the "induced" scenario. On the other hand, expansive motions have also been invoked to prevent star formation by disrupting molecular clouds or releasing turbulent support (the so-called negative feedback of star formation). More importantly stellar birth is observed also far from OB stars or spiral arms and in the absence of nearby supernovæ or galaxy merging effects. This implies the need for a mechanism which progressively dissipates the mechanical support of the clouds and spontaneously leads to star formation. The spontaneous mode is often referred to as "isolated" star formation since it relies on the ability to separate a particular region of the cloud, enhancing the density and favouring the collapse. The term "isolated", anyway, does not preclude a further fragmentation that can lead to multiple star formation. For the purpose of this thesis, I will briefly review in the following the current status of the theoretical and observational knowledge of *isolated, low-mass* star formation, but to proceed further it is necessary to introduce first the environment where the action take place and the nomenclature adopted in the literature.

Giant molecular clouds (GMC) represent the largest coherent structure where star formation occurs. GMCs are condensations of gas and dust with temperatures in the range $10 - 100$ K, masses up to $\sim 10^6$ $M_\odot$ and dimensions of tens of parsecs. GMCs are generally identified through ^{12}CO emission. The density in the GMCs is not uniform but the clouds are organized in smaller structures of parsec scale, called *clumps*, that, unlike GMCs, are not found in virial equilibrium. The clumps are typically traced by spectral line maps of molecular emission such as ^{13}CO or CS. On a smaller scale (0.1 pc) we find the *dense cores*, high extinction condensations with densities between 10^3 and 10^7 H_2 molecules cm^{-3} and temperatures around 10 K. Some of these small dark clouds have been found to be associated with infrared sources with spectral energy distributions compatible with Young Stellar Objects (YSO) in some cases followed by the discovery of the presence of bipolar outflows. This can be seen in Figure 1.1 taken from Palla & Stahler (2002), in which the positions of YSO and dense cores belonging to Taurus Molecular Cloud are superimposed on integrated intensity maps of ^{12}CO, ^{13}CO and C^{18}O;

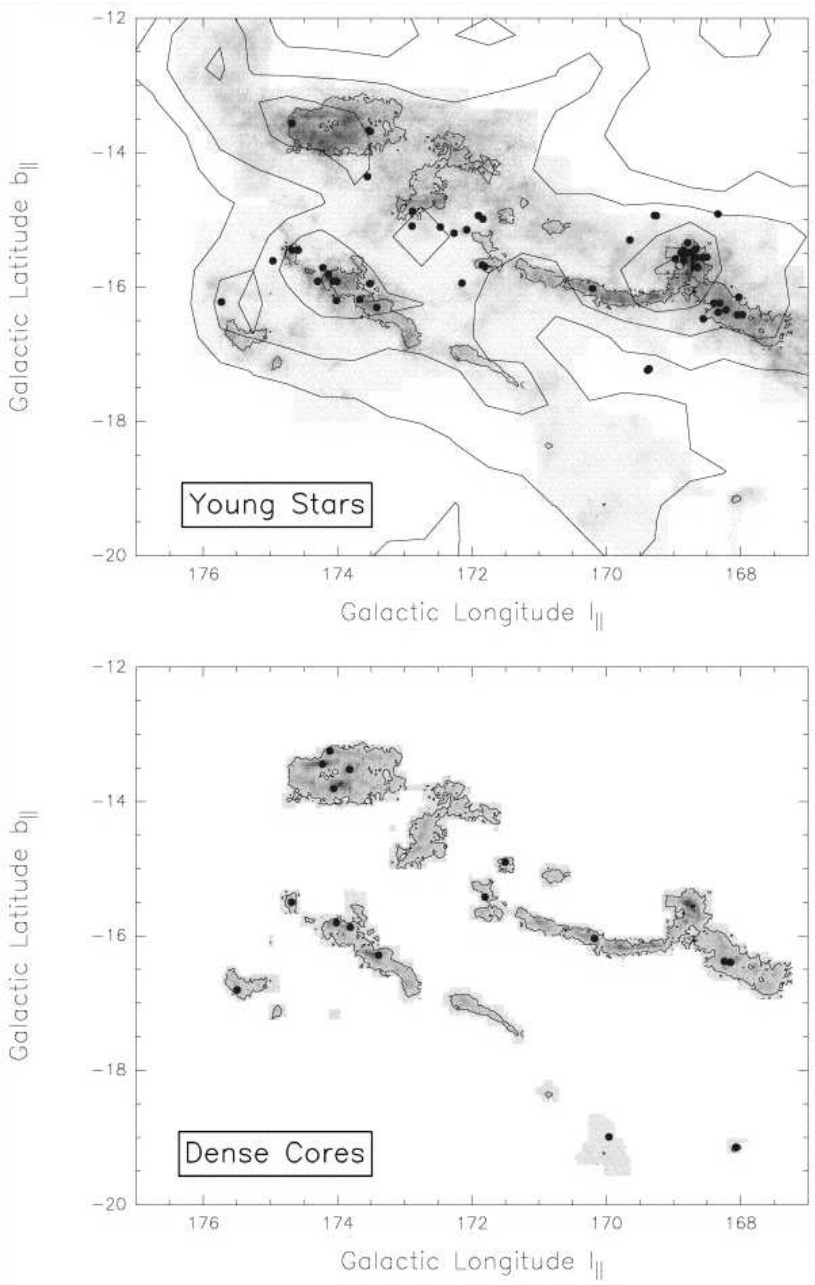

Figure 1.1 Location of T Tauri stars and dense cores within the Taurus Molecular Cloud (TMC) star forming region, taken from Palla & Stahler (2002). Top panel, T Tauri stars positions are shown on top of ^{12}CO integrated intensity emission (outer contours), ^{13}CO (grey scale) and C^{18}O (inner contours). Bottom panel, positions of dense cores identified from NH_3 observations are superimposed to C^{18}O integrated intensity emission (grey scale and contours).

it is evident that the two classes of objects are located in the same regions within the cloud. It seems, thus, natural to believe that dense starless cores are the location where "isolated" stellar birth take place and that they represent the last phase before protostar formation.

After the formation of the protostar, the standard model predicts the ejection of bipolar jets which dissipate angular momentum, favours the accretion of gas onto the protostar and disperses the envelope of gas and dust around the newborn star. Subsequently, the protostar becomes optically visible and shows an optically thick disk and powerful winds (T Tauri phase) until all the material is dispersed or accreted. At this stage the central object has not entered the main sequence yet. In fact, the radiation of a protostar is mainly produced by the release of its gravitational energy and not by nuclear reactions for a time scale $t_{Kelvin-Helmholtz} = \frac{G\,M_\star^2}{R_\star\,L_\star}$, which is roughly proportional to $M_\star^{-3.5}$. In order to establish if accretion lasts shorter or longer than the radiation of gravitational energy, we can compare $t_{Kelvin-Helmholtz}$ with the characteristic time scale for accretion, $t_{accr} = \frac{M_\star}{\dot{M}_\star}$, which increases linearly with the mass of the star. Accurate calculations (Palla & Stahler 1993) showed that, for stars with masses of 8 $M_\odot$, the two time scales are comparable, thus, low-mass stars end the accretion phase before reaching the main sequence.

The three phases (accretion phase, protostar with protoplanetary disk and pre-main-sequence star with debris disk) can be identified through the study of the Spectral Energy Distribution (SED) of the dust continuum emission in dense cores. In fact, dust grains absorb the radiation at visual wavelengths and reprocess it in the infrared. Therefore, the SED of a starless core will appear similar to a black-body[1] with $T \sim 10$ K, peaking around 300 μm. As the central protostar forms, another black-body with temperature > 100 K will emerge at shorter wavelengths altering the SED. Thus, the ratio between fluxes at ~ 100 and ~ 10 μm can be used to distinguish the different phases of the protostar evolution. This was typically done using the fluxes obtained by the InfraRed Astronomical Satellite (*IRAS*) at 12, 25, 60 and 100 μm. In this way, Lada & Wilking (1984) divided the protostars in *Class I*, sources with SED much broader than a single temperature black-body and positive spectral index between 2 and 10-25 μm, *Class II*, sources with SED still larger than a single temperature black-body but with negative spectral index in the range 2–100 μm, and *Class III*, sources with little or no far-infrared excess and whose SEDs are almost comparable to a single temperature, reddened black-body.
Subsequently André, Ward-Thompson & Barsony (1993) extended this classification to

[1] See § 1.2.1 for a brief explanation of deviations from black-body emission.

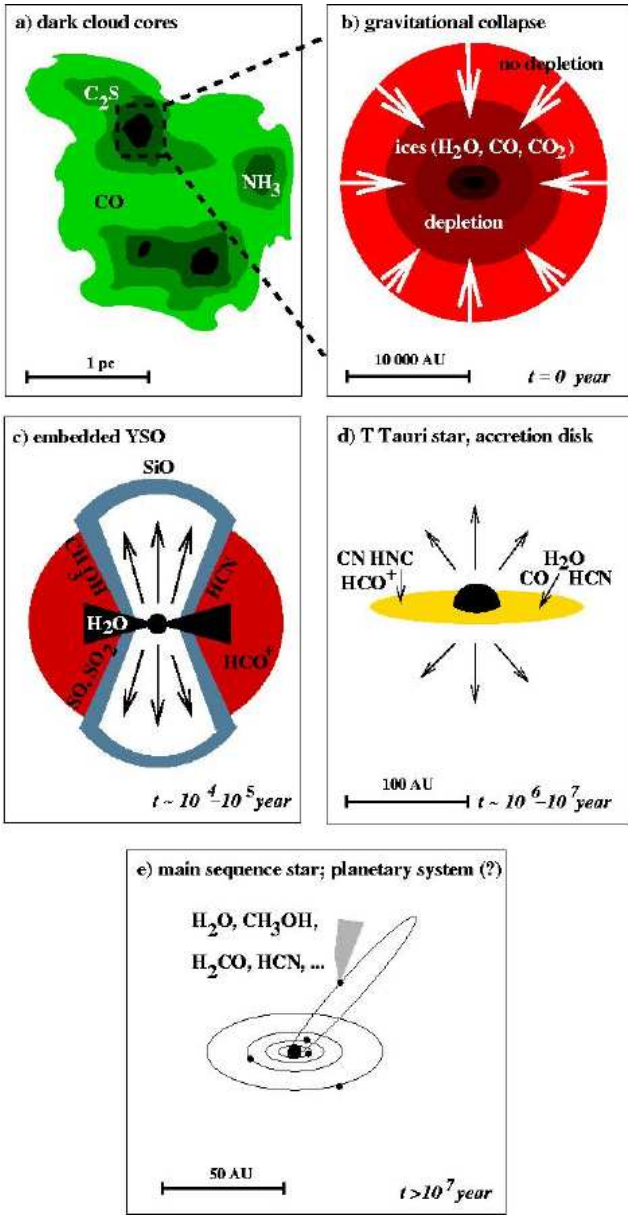

Figure 1.2 A schematic view of the evolutionary sequence from molecular clumps to main sequence stars. In panel a) the dense cores traced by complex molecules are immersed in the molecular clump traced by CO. In panel b), on a 10 times smaller scale, we can observe the last phase of core evolution where both dynamical processes (gravitational collapse) and chemical effects (CO depletion) takes place (see §1.4 and §1.3 for more details). This corresponds to the pre-stellar core phase. Once the protostar is formed, strong outflows are driven and a disk is formed, as depicted in panel c). After the Class 0 and Class I phases, the protostar-disk system becomes optically visible, this corresponds to the T Tauri phase. Finally in panel e), all the surrounding material is dispersed or accreted leaving a pre-main-sequence star.

include objects with dust continuum emission peaking at even longer wavelengths than in Class I, and negligible emission shortward of 10 μm but which show signs of the presence of a protostar (such as bipolar outflows or compact centimeter radio continuum source). These sources have been classified as Class 0 protostars, which intuitively corresponds to a phase in which the mass of the protostar is lower than the mass of the infalling envelope.
As well as the spectral index classification, other alternative measures have been introduced to classify the protostar evolution. Myers & Ladd (1993) defined $T_{\rm bol}$ as the equivalent temperature of a black-body that peaks at the same frequency as the weighted mean frequency observed, and showed that Class 0, I , II and III corresponds to $T_{\rm bol} < 70$ K, 70 K $< T_{\rm bol} <$ 650 K, 650 K $< T_{\rm bol} <$ 2880 K and $T_{\rm bol} > 2880$ K, respectively. Another useful parameter for protostar classification is the ratio between the submillimeter luminosity and the bolometric luminosity $L_{\rm submm}/L_{\rm bol}$, which is a measure of $M_{\rm envelope}/M_{\star}$ and thus is more sensitive to the first phases of evolution. André, Ward-Thompson & Barsony (1993) showed that Class 0 protostars have $L_{\rm submm}/L_{\rm bol} > 0.5\%$, approximately corresponding to $M_{\rm envelope}/M_{\star} > 1$.

A very effective summary of the evolution from dense cores to stars with planets is presented in the sketch in Figure 1.2, reproduced from van Dishoeck & Blake (1998).

1.1 The theoretical issue

Although astrophysicists recognized long ago that stars are born from the gravitational collapse of the interstellar medium, the debate on the details of the star formation mechanism is still open.

Molecular clouds were early identified as potentially unstable sites since their internal conditions of temperature and density cannot provide thermal support (Goldreich & Kwan 1974). This can be easily shown evaluating the Jeans mass - i.e. the minimum collapsing mass - for a spherical isothermal molecular cloud:

$$\mathrm{M_J} = \frac{\pi}{6}\left(\frac{7\pi k}{5mG}\right)^{\frac{3}{2}} T^{\frac{3}{2}}\rho^{-\frac{1}{2}} = 15\,T^{\frac{3}{2}}n^{-\frac{1}{2}}\,(\mathrm{M_\odot}),$$

where k is the Boltzmann constant, T is the kinetic temperature, m is the mass of the mean particle (here we assumed a mean molecular mass equal to 2.33 a.m.u.), G is the Newton constant, ρ is the mass density and n is the number density of H_2 molecules. Using the

typical values of temperature (10 K) and particle density ($10^2 - 10^3$ cm^{-3}) observed in the GMC we derive that the Jeans mass for these objects ($47 - 15$ M$_\odot$) is orders of magnitude smaller than the measured value ($10^3 - 10^4$ M$_\odot$; see Blitz 1993), therefore molecular clouds should find themselves in an unstable state (Evans 1978). In absence of alternative support against the gravitational attraction, collapse would proceed undisturbed in a free-fall timescale (Spitzer 1978),

$$t_{ff} = \left(\frac{3\pi}{32G\rho}\right)^{\frac{1}{2}} = 3.4 \times 10^7 n^{-\frac{1}{2}} \text{ (years)},$$

which in the case of a molecular cloud with $n = 10^2 - 10^3$ H_2molecules cm^{-3}, is of the order of one million years. This number is in strong disagreement with the observed cloud lifetime of about 10^7 years as inferred from the presence of OB stars in GMCs (e.g. Bash & Peters 1976) or measured by chemical clocks (Glassgold 1985). Moreover, converting the $\sim 10^9$ M$_\odot$ contained in the Milky Way molecular clouds into stars at the free-fall rate would yield a star formation rate of few hundreds of solar masses per year, two orders of magnitude higher than the average value in our galaxy (~ 3 M$_\odot$ yr^{-1}, see e.g. Scalo 1986).

These simple considerations evidence the necessity for a support mechanism in the molecular clouds. Two physical processes are currently believed to be relevant to keep the cloud from freely collapsing: the magnetic pressure and the turbulence support.

The former involves the presence of a magnetic field threading the cloud, which provides an opposition to the infall of the charged particles in the direction perpendicular to the magnetic field lines. In fact, the contraction of the charged plasma, which is well coupled with the magnetic field, would result in a compression of the magnetic field lines; thus, while the charged particles are free to move along the field lines, they feel an additional pressure perpendicular to them. Analytical calculations (Mestel & Spitzer 1956; Li & Shu 1996) and numerical simulations (Mouschovias & Spitzer 1976) show that magnetic support is granted only until the ratio between mass and magnetic flux ($\Phi = B\pi R^2$) reaches a critical value beyond which the cloud collapses freely. This can be qualitatively shown by comparing the total magnetic energy ($E_{mag} = B^2/(8\pi)\ 4/3\ \pi R^3 = B^2\ R^3/6$, for a spherical cloud with uniform magnetic field) to the total gravitational energy ($E_{grav} = 3/5\ GM^2/R$, for a spherical cloud with uniform density). The collapse condition is given

by $|E_{grav}| > |E_{mag}|$, which translates in the condition

$$M > M_{crit} = BR^2\sqrt{\frac{5}{18G}} = \frac{\Phi}{3\pi}\sqrt{\frac{5}{2G}}.$$

If magnetic field is perfectly coupled with matter, as it happens for a completely ionized plasma, magnetic flux is conserved, thus, if a cloud is magnetically supported at a given time it would remain supported even after an external compression. Similarly, if $M > M_{crit}$, we should not expect magnetic forces to overcome the gravitational forces at any point during contraction as it may happen for, e.g., rotational effects.

Crutcher, Nutter, Ward-Thompson & Kirk (2004) using maps of polarization of dust emission measured magnetic fields towards three starless cores (see also § 1.2.1). Observed field strengths between 80 and 160 μG indicate that these object are close to the critical value for magnetic support, although uncertainties in the geometry and observational errors prevented to tell if these cores are sub- or super-critical. Magnetic field measurements through Zeeman effect towards clouds with various masses found mass-to-flux values twice than critical. However, this does not necessarily require that magnetic support is insufficient since only the component along the line of sight is probed (see Crutcher 1999 for a review).

Of course molecular clouds are far from being completely ionized. Neutral species are not directly affected by magnetic forces, nevertheless they are not completely free to collapse since they are subject to the frictional drag due to the drift relative to the charged particles. This relative motion, also known as ambipolar diffusion, has as a result the slow decrease of magnetic flux in the inner regions and the progressive contraction of the cloud, resulting in an increase of the ratio between mass and magnetic flux in the cloud centre. Note that the ambipolar diffusion has the additional advantage of easily explaining the observed decrease of the magnetic field flux from the molecular clouds to the stars. In fact, considering the conservation of magnetic flux $BR^2 = const$ and using $B_{\rm core} \sim 20\ \mu$G, $R_{\rm core} \sim 0.1$ pc and $R_\odot = 1 \times 10^6$ km as typical values for molecular cores and stars, we obtain that, in absence of dissipation of magnetic fields, stars should have a magnetic field strength exceeding 10^8 G, a hundred millions times the value observed in the sun ($\sim$1 G).

The characteristic time to reach the critical value of M/Φ individuates the time scale of the ambipolar diffusion mechanism; this is approximately given by $\mathrm{t}_{AD} \simeq 7 \times 10^{13} x_e$ years (McKee, Zweibel, Goodman & Heiles 1993), where $x_e (\equiv \frac{n(e^-)}{n(H_2)})$ is the ionization fraction of the core. The ionization fraction, which is the result of ionization by cosmic rays or high energy photons and recombination, is inferred from other chemical properties such

as the DCO^+/HCO^+ ratio (see Guelin, Langer & Wilson 1982; de Boisanger, Helmich & van Dishoeck 1996; Caselli, Walmsley, Terzieva & Herbst 1998; Williams et al. 1998; Caselli et al. 2002b, for details on results and techniques) . These authors found typical values for x_e between 10^{-8} to few times 10^{-7} towards a number of low-mass cores with central density of few 10^4 molecules cm^{-3}, suggesting that the ambipolar diffusion timescale is at least a factor of ten longer than the free fall time.

Turbulence support was introduced after the realization that CO line widths in molecular clouds could not be explained by thermal broadening effects alone. In fact, the thermal line width of a species with molecular mass m at temperature T_k is given by

$$\Delta v_{th} = \sqrt{\frac{8 \ln 2 \; k \; T_K}{m}} = 0.68 \text{ km s}^{-1} \left(\frac{T_K}{10 \text{ K}} \right)^{0.5} \left(\frac{m}{\text{a.m.u}} \right)^{-0.5} \tag{1.1}$$

which in the case of ^{13}CO at 10 K corresponds to a tenth of km s^{-1}. Thus, the observed velocity dispersions in molecular clumps are found to be highly supersonic with Mach numbers exceeding 10 (see e.g. Blitz 1993 and references therein). In this scenario the pressure associated with turbulent motions would furnish the necessary support to explain the observed cloud lifetimes. The progressive decay of this motions would lead then to star formation. An observational support for this theory comes from the measurement of line width decrease towards the center of molecular clouds (Myers 1983; Myers & Goodman 1988). Although early 1D simulations (Gammie & Ostriker 1996) demonstrated that the turbulence dissipation is slow enough to prevent clouds from collapse for a time longer than the free-fall time, recent more sophisticated, 3D, numerical calculations showed that the decay rates are too high for systems with dimensions comparable to the injections scales (Mac Low, Klessen, Burkert & Smith 1998; Stone, Ostriker & Gammie 1998; Padoan & Nordlund 1999). In fact, the turbulence dissipation time is proportional to l/v, where l is the typical length scale of the injection and v the turbulent velocity, and this cannot exceed the crossing time of the cloud R/v, with R being the size of the structure. As a result l should be much smaller than R in order to provide support for a sufficient time (see Vazquez-Semadeni et al. 2000, for a more comprehensive review). In this framework, turbulence support could work only for the giant molecular cloud, where the turbulence injection is furnished by the internal motion of the clumps, while it seems to fail for the support of clumps and cores. A possible solution for the replenishment of turbulence at small scales could be found in the winds from young stars (Norman & Silk 1980) or in the conversion of magnetic energy in turbulent energy (Zweibel 1998;

Gammie & Ostriker 1996). Magneto-hydrodynamical simulations have also suggested that the presence of magnetic fields would have the additional advantage of slowing the dissipation of turbulence in the low density medium, therefore extending the duration of the turbulence support (Arons & Max 1975; Vazquez-Semadeni et al. 2000). On the other hand, observations of polarized dust emission and extinction in dark clouds (Weintraub, Goodman & Akeson 2000; Crutcher, Nutter, Ward-Thompson & Kirk 2004) suggested that turbulent energy could not totally prevail over magnetic energy.
It has been proposed that turbulence pressure and magnetic support act in different phases of cloud evolution. Given the shorter dissipation time, turbulence should govern the first phase of contraction, while after its decay the course should be determined by the ratio of mass to magnetic flux left after this first phase. If M/Φ is subcritical, the cloud has to dissipate magnetic flux before collapsing, otherwise the contraction proceeds undisturbed. Shu, Adams & Lizano (1987) suggested that the first case could describe the formation of low-mass isolated stars while the latter should be typical of high-mass clustered star formation, although an agreement on this topic is not found yet.

1.2 Observational approach

In order to understand the physics of star formation, we need to observe the properties of the molecular clouds. Molecular clouds are mainly constituted of H_2 molecules and helium, thus, naively, it would seem straightforward to extract the necessary informations from observations of these species. In practice, the extreme conditions of low temperature and low density present in the star formation sites make the collisional excitation of H_2 and He very difficult given the large energy needed to occupy the first levels. In fact, electronic transitions of helium are far in the UV part of the spectrum, like also those of H_2 given its very small moment of inertia. Moreover, the absence of a permanent dipole moment and the weakness of the quadrupole moment makes the opacity of rotational lines very low, requiring very high column densities in order to detect these lines in emission. However, direct observation of H_2 lines in emission is possible although only in the lower density medium where the UV radiation provides the necessary heating via photoelectric effect (fluorescence), but not in the denser molecular clouds where the dust grains absorb the UV photons (Luhman & Jaffe 1996). Alternatively, we can use background sources of ultraviolet radiation to measure the H_2 absorption along the line of sight. H_2 column densities are then derived by fitting the observed spectra with damping profiles of the

lower transitions lines. Two examples are the works of Savage, Drake, Budich & Bohlin (1977) using Copernicus and Rachford et al. (2002) using the Far Ultraviolet Spectroscopic Explorer (FUSE) towards a large sample of low density molecular clouds ($\sim 10^{21}$ H_2 molecules cm^{-2}) in the Lyman and Werner bands between 912 and 1120 Å.
Vibrational and rotational transitions of H_2 are visible in shocked regions where temperatures exceed 1000 K. These conditions are met in molecular outflows where the first vibrational transitions $\lambda = 2.122\ \mu$m and $\lambda = 2.247\ \mu$m, are clearly detected (see Bachiller 1996, and references therein). Only outflows with shock velocities in the range 10-50 km s^{-1} are detected with this technique, in fact at higher shock velocity H_2 is dissociated. A direct probe of "quiet" H_2 in molecular cores is furnished by the absorption of background infrared continuum. This experiment was performed successfully towards a couple of embedded protostars by Lacy, Knacke, Geballe & Tokunaga (1994).

Finally, H_2 content in molecular clouds can be extracted indirectly from observations of γ rays, being the final product of the interaction of H_2 with cosmic rays (Bloemen et al. 1986). The main problems with this technique are due to the difficulties in the detection of γ rays and angular resolution of γ rays maps as well as uncertainties in the cosmic rays properties such as their local flux or their diffusion in the molecular clouds.

As a consequence of the limited conditions of applicability of these techniques or the current technological limits, physical probes of molecular cores have been extracted from alternative tracers such as dust and molecules other than H_2. For this reason, in addition to the basic properties of molecular clouds that we need to extract, like *density*, *temperature*, *magnetic field* and *velocity field*, we need to know also the *abundance* of our tracer with respect to H_2.

Observing the earliest stages of star formation has been possible only with the advent of sub-millimeter telescopes. In fact, stars form in environments deeply embedded under high column densities of dust grains with typical sizes of few microns. Therefore, it would not be possible to use optical observations to probe these regions since grains absorb efficiently wavelengths shorter than their size, on the contrary millimeter wavelenghts can escape from the cloud.
Specific detectors have been developed to collect millimeter photons such as heterodyne receivers and bolometers, and large antennas have been built. A major problem for millimeter astronomy is constituted by atmospheric opacity. In fact, in the same way as molecules in star forming regions emits at millimeter wavelength so molecules in earth atmosphere absorb these photons. It is, thus, fundamental to build telescope at high alti-

Figure 1.3 The advancement of technology in submillimeter, millimeter and infrared detection and imaging furnished fundamental informations to develop our understanding of the star formation process. Above, some of the more important past, current and future facilities. From top to bottom, the IRAM-30m and the IRAM-Plateau de Bure interferometer, the Caltech Submillimeter Observatory and the Five College Radio Astronomy Observatory, the Swedish-ESO Submillimetre Telescope and the SubMillimeter Array, and two concept images of the Atacama Large Millimeter Array and the Spitzer space telescope.

tude or possibly construct space facilities. The angular resolution for a 10 meter telescope at 1 mm is approximately $20''$, corresponding to 20,000 AU in the favourable case of a cloud distant 100 pc only . This lack of resolution is solved by the use of interferometric techniques which combine informations from multiple telescopes and increase the resolving power by a factor proportional to the distance between antennas. Few examples of current and future (sub-)millimeter facilities are shown in Figure 1.3

1.2.1 Probing the cloud structure with dust observations

Dust grains have a fundamental role in the survival of molecular clouds as they shield them from the ultraviolet and visible radiation preventing the dissociation of molecules. Visible extinction is at the base of the early works on molecular clouds properties. The conventional way of deriving the total column density towards a molecular cloud has been through the use of optical star counts (see e.g. Bok 1937). This method is based on the comparison of the number of stars within a region of interest to a nearby reference field assuming that the latter is extinction-free and that the background population of stars is homogeneous in the two fields. Using dust extinction as a measure of total column density, Barnard (1927), Bok & Reilly (1947), Lynds (1962) and, more recently, Clemens & Barvainis (1988) and Lee & Myers (1999) determined the location and measured sizes of molecular cores from the examination of optical plates. The conversion factor from visual extinction to H_2 column density, $\sim 1 \times 10^{21}$ mol. cm^{-2} per magnitude, was evaluated from the comparison of ultraviolet absorption and visual extinction in low column density clouds ($N(H_2) < 10^{21}$ mol. cm^{-2}) (see e.g. Savage, Drake, Budich & Bohlin 1977; Bohlin, Savage & Drake 1978). In analogous fashion, near infrared observations in H and K bands are now used to probe higher column densities, up to 3×10^{22} mol. cm^{-2} (Lada, Lada, Clemens & Bally 1994, Alves et al. 1998, see also Chapter 4 for an application). In Figure 1.4, we show optical and NIR observations of B68 (Alves, Lada, & Lada 2001). While the cloud is totally opaque at visible wavelengths, observations in H and K bands of background protostar are possible up to higher values of extinction and can furnish the total column density with a pencil-beam resolution.

The visible and ultraviolet radiation absorbed by the dust grains is then re-emitted at (sub-)millimeter wavelengths where the cloud is optically thin to its own radiation (dust opacity at 1.2 mm is $\sim 4 \times 10^4$ times less than at visual wavelengths; Kramer et al. 1998). Assuming a constant gas-to-dust mass ratio and the dust opacity, we can convert the dust emission into H_2 column density. Calculations for a wide range of interstellar conditions

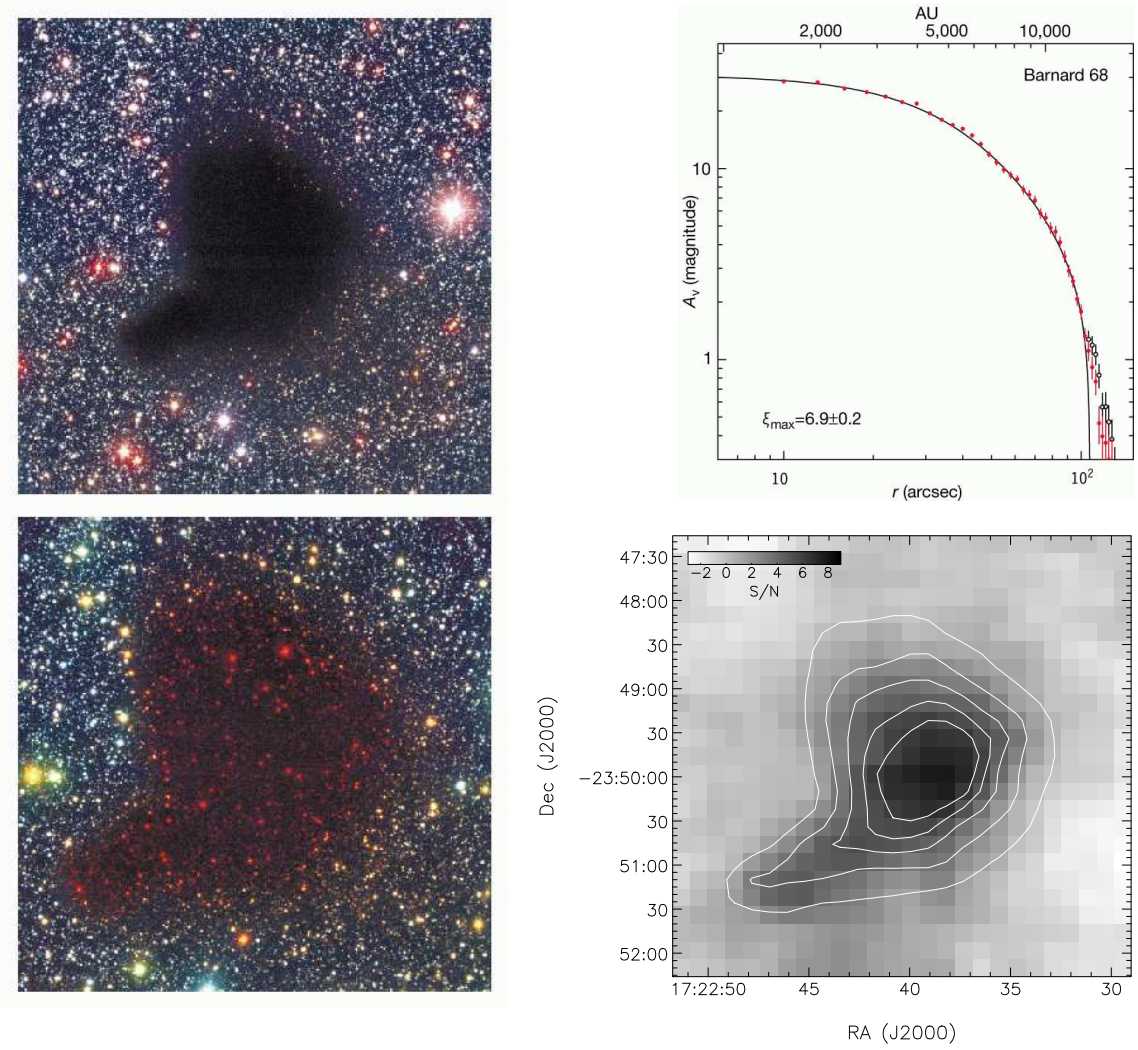

Figure 1.4 An example of dust emission–absorption in a dark cloud: Barnard 68. In the top left panel, the combined B, V and I deep image taken with the ESO-VLT (Alves, Lada, & Lada 2001). At visible wavelengths Barnard 68 is totally opaque to the background light of the stars in the galactic bulge. In the bottom left panel, Alves, Lada, & Lada (2001) combined the B and I images with a deep observation in near-infrared (K-band) from ESO-NTT. Since background stars are visible in NIR only they appear red. Near infrared extinction was then converted in magnitudes of visual extinction and azimuthally averaged in the top right panel (Alves, Lada, & Lada 2001), providing evidence that B68 appears like a self-gravitating, pressure-confined, isothermal sphere. Finally in the bottom right panel, we reported the superimposition of dust emission at 850 μm with dust absorption (Bianchi et al. 2003). Combining these informations Bianchi et al. (2003) measured the dust absorption coefficient in this relatively dense core.

and for several shapes, compositions and size distributions of the dust grains (see Draine 2003 for a review), furnished a value of $\sim$0.005 cm^{2}g^{-1} for the dust absorption coefficient per gram of gas, κ, at $\lambda = 1.2$ mm (Preibisch, Ossenkopf, Yorke & Henning 1993; Ossenkopf & Henning 1994). The uncertainties on this number were estimated to be a factor of 2–3 (Henning, Michel & Stognienko 1995). More recently, comparisons between dust extinction maps from NIR data and emission maps at (sub-)millimeter frequencies determined the absorption coefficient observationally, setting the numerical value of $\kappa_{1.2mm}$ to 0.004 ± 0.001 cm^2 per gram of gas (within a factor of 2) and confirming the predicted increase of κ within the cloud due to formation of ice mantles in the cold interiors of the core (Kramer et al. 1998; Bianchi et al. 2003; Kramer et al. 2003). At present, observations of dust emission are able to probe molecular densities up to 10^{23} mol. cm^{-2} with an angular resolution of about $10''$ (e.g., Ward-Thompson, Motte & André 1999; Pagani et al. 2003; Chapter 3). Dust continuum emission emits as a gray-body, defined as

$$S_\nu = B_\nu(T_{dust})(1 - e^{-\tau_\nu})\Delta\Omega,$$

where B_ν is the Planck function at temperature T_{dust}, τ_ν the dust opacity and $\Delta\Omega$ is the solid angle; thus, multiwavelengths observations can furnish a measure of temperature. Typical values for dust temperatures in regions far from young stellar objects are around $\sim$10–15 K as expected from the balance of interstellar radiation heating and radiative cooling. Recently, Zucconi, Walmsley & Galli (2001) and Evans, Rawlings, Shirley & Mundy (2001) showed that in the cloud interiors the dust temperature drops to 7–8 K due to the attenuation of the external radiation field.

As mentioned in the previous section, dust observations can also furnish estimates of magnetic field strength through dust polarization measurements. This technique relies on the fact that in presence of an ordered magnetic field, magnetic torque should align the shorter axis of dust grains to the field lines (Lazarian, Goodman & Myers 1997; Draine 2003). This anisotropy in grain orientation has as a consequence a preferential direction of absorption for background sources, finally resulting in a polarization of the intrinsically unpolarized background starlight. Moreover, the alignment of dust grains would also cause a polarization in dust emission at far-infrared wavelengths. Chandrasekhar & Fermi (1953) suggested that studying the dispersion of polarization vectors could yield a measure of the magnetic field strength in the plane of the sky, B_{pos}, and related the small scale irregularity of the field lines to the regular field strength according to the equation

$$B_{pos} = \sqrt{\frac{4\pi\rho}{3}}\frac{\delta V}{\delta\phi} \simeq 9.8\sqrt{n(\mathrm{H_2})}\frac{\Delta V}{\delta\phi}\,\mu\mathrm{G},$$

where ρ is the gas density, δV and $\delta\phi$ are the velocity and polarization dispersion, while on the right hand side ΔV is the observed line width in km s^{-1}, $n(H_2)$ is the H_2 number density in molec. cm^{-3} and $\delta\phi$ is expressed in degrees.
Although this overview makes the magnetic field measurements sound easy, interpretation of the observations has to take into account differences in grain size, shape and composition, variations in the direction of magnetic field lines along the line of sight and alternative mechanisms of grains alignment. An example of polarization map in emission towards a dense core is given in Figure 1.5 (taken from Crutcher, Nutter, Ward-Thompson & Kirk 2004). Superimposed to the 850 μm emission map (grey scale and contours), vectors length represents the observed polarization intensity while the direction show the magnetic field in the plane of the sky.

1.2.2 Probing the cloud structure with molecular line observations

Molecules are the other main constituent of the clouds and can be used to probe several properties of the star forming region. The most abundant species after H_2 is carbon monoxide, CO, which is the main tracer of molecular gas on a large scale. Although its large optical depth means that we are looking only at a thin shell at the cloud boundary, CO luminosity has been found to be well correlated with the virial mass in giant molecular clouds (see e.g. Young & Scoville 1991). This can be understood considering the clumpy structure of the giant molecular clouds; the total luminosity of CO is a measure of the number of clumps which is statistically correlated to the total mass. For scales within the giant molecular clouds, CO cannot be used to trace the column density and isotopologues with smaller abundances (hence smaller optical depth but also smaller intensity) have to be used instead. Using ^{13}CO , and then $C^{18}O$ and $C^{17}O$, it has been possible to identify cores with H_2 particle densities up to 10^4 cm^{-3}. This limit is not due to optical depth effects but to selection effects due to chemical processes (see next subsection). Conversion from CO column density to total column density is generally done applying the abundance observed in the objects where $N(H_2)$ was measured both directly (but in low column density clouds only; Lacy, Knacke, Geballe & Tokunaga 1994) and indirectly (up to 10 magnitudes of visual extinctions; Frerking, Langer & Wilson 1982; Alves, Lada & Lada 1999; Kramer et al. 1999). Although the CO abundance seems to be constant from cloud to cloud when measured with a single technique, differences of a factor of 2 were observed between measurements done through dust extinction and observations of H_2 line absorption (Frerking, Langer & Wilson 1982; Lacy, Knacke, Geballe & Toku-

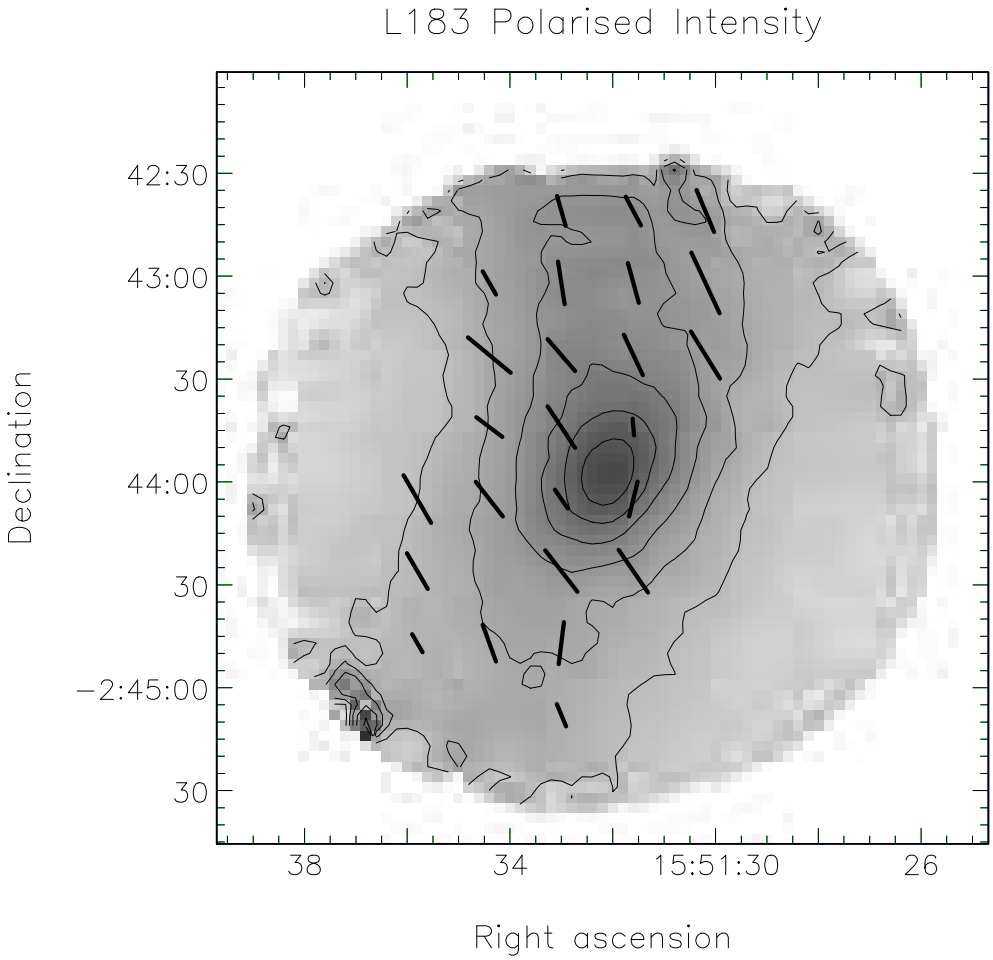

Figure 1.5 Polarization map of the starless core L183, taken from Crutcher, Nutter, Ward-Thompson & Kirk (2004). Vectors show the direction of the magnetic field projected on the plane of the sky, while vectors length display the polarization intensity. Contours and grey scale represent the 850 μm emission.

naga 1994). Further measurements are strongly needed to understand the causes of CO abundance variation between molecular clouds. On the other hand, differences in CO abundance between high density and low density clouds can be explained with freeze-out on dust grain surfaces (Section 1.3).

Molecular observations are used also to derive the volume density, n, and gas temperature, T_K, through observations of multiple energy levels. This can be done comparing the observed populations in the molecular energy levels with modeling of the excitation of the source. The molecular energy levels populations are inferred from the observations of the column density at a given level l that can be expressed by,

$$N_l = \frac{8\pi}{c^3}\frac{g_l}{g_u}\frac{\nu^3}{A_{ul}}\frac{1}{1-e^{-h\nu/kT_{ex}}}\int \tau dV,$$

where g_l and g_u are the degeneracies of the upper and lower levels of a transition, A_{ul} is the Einstein coefficient for spontaneous emission, τ is the line optical depth and T_{ex} the excitation temperature defined as the equivalent temperature which would furnish the observed population in the levels according to the Boltzmann law. If the excitation is determined only from collisions, the population in the levels depends only on the kinetic temperature, while if the radiative rates of the level are high enough, density also influences the population in the levels and can be derived from it. The determination of the levels population from multiple molecular transitions is complicated by geometric effects (such as beam averaging and line of sight integration) and by radiation trapping effects, therefore accurate radiative transfer modeling is needed to interpret the data. Radiative transfer can be treated in several ways starting from the simplistic Local Thermodynamical Equilibrium (LTE) in an isothermal, homogeneous, spherical cloud to the sophisticated Monte Carlo simulations in which the geometry of the cloud, and the spatial distribution of density and temperature can be varied to best fit the data. Of course, more flexibility implies a larger number of observations needed to constrain the models and vice-versa. Modeling the emission from an extended source requires the knowledge of how much radiation is emitted locally and how this is degraded in its travel through the source. It is thus evident that in order to extract the cloud properties from line profile fitting one needs to furnish a model of the cloud itself in the first instance. This leads to an iterative process that must use informations from several data sets including multiple molecular species in several line transitions and dust continuum. A useful approximation that is often used to model molecular cloud emission is the Large Velocity Gradient (LVG), which assumes that, in presence of coherent motions through the line of sight, emission is trapped only locally.

This simplification can be usually applied in dense cores where the local velocity gradient is larger than the ratio of line width to cloud size, for lines with moderate opacity (Goodman, Benson, Fuller & Myers 1993).

Spectroscopic observations, in fact, probe also gas kinematics in the line of sight direction. The first three moments of the line profile – central velocity, width and skewness – can help us to reconstruct the velocity field of the cloud. It was immediately recognized that line widths were too broad to be explained by thermal effects; for instance, in the database of ammonia cores of Jijina, Myers & Adams (1999) the observed line widths range between 0.17 km s^{-1} and 8 km s^{-1} while the thermal line width for NH_3 at 10 K is equal to 0.125 km s^{-1} (see eq. 1.1). This increased line width is currently ascribed to turbulent motions although systematic rotational motions can also contribute significantly. Rotation at large scale is observed also from the study of central velocity maps in many star forming cores (Goodman, Benson, Fuller & Myers 1993; Caselli, Benson, Myers & Tafalla 2002).

Infall or contraction features capable of discriminating between different theoretical scenarios have been searched for for a long time. This search is complicated by the small velocities involved. In fact, if we consider the free fall of a particle under the gravitational attraction of a point mass using the conservation of energy, $\frac{GM}{R} = \frac{1}{2}v^2$, we can see that even at the free fall speed the infall velocity is of the order:

$$v_{inf} = 0.9 \text{ km s}^{-1} \left(\frac{M_{central}}{M_\odot} \right)^{0.5} \left(\frac{r}{0.01 \text{ pc}} \right)^{-0.5} .$$

Therefore, to detect infall motions towards low mass forming stars one needs to probe the very inner nucleus. Moreover, more dramatic dynamical effects, like the ejection of molecular outflows and bullets, easily obscure the effects of infall. In fact, not only outflows were found to begin very soon after a central source is formed but they move matter at velocities ranging from 10 km s^{-1} up to 100 km s^{-1} (see Bachiller 1996). The current state of observations of infall is reviewed in more detail in Section 1.4.

Estimates of magnetic field strength are provided also from observations of molecular species subject to the splitting of energy levels under magnetic fields, also known as the Zeeman effect. Zeeman measurements, unlike dust observations, furnish the component of the magnetic field projected along the line of sight. The Zeeman effect has been observed in OH, CN, CCS both in emission and in absorption (see Crutcher 1999, Bourke et al. 2001, and references therein), but given the high chemical reactivity of these molecules these measurements probe only gas with number density lower than 10^3 cm^{-3}.

Magnetic field strength in dense cores, as estimated from Zeeman effect alone, are found either approximately critical or supercritical by a factor of 2 (Crutcher 1999; Bourke et al. 2001).

1.3 The effect of chemistry in the evolution of dense cores

The choice of the tracer in molecular cloud observations is of fundamental importance since molecular species are not equally abundant throughout the cloud. It is thus possible to study the physical quantity of interest in the targeted region by using the appropriate transition of the appropriate molecule. We already made the example of rarer isotopologues of CO which trace higher column density of gas; here, we analyze in more detail the chemical effects which differentiate the molecular content of the cloud.

The formation of dense cores has a deep impact on the chemical interaction between gas and dust inside the star forming core. In particular, as the density increases, molecules in the gas phase collide with dust grains with higher frequency and, depending on the relative sticking efficiency of the species, there will be a progressive depletion of the molecule from the gas phase. This can be quantified with the rate of deposition of a molecule on a dust grain, $k_{dr}[\mathrm{s}^{-1}] = (\pi a^2 \langle V \rangle S n_{gr})$, where a is the grain radius, $\langle V \rangle$ is the mean thermal velocity, S is the sticking coefficient and n_{gr} is the grain number density. Sticking efficiently to the grain mantle does not ensure the depletion of a species since we have to balance for desorption from grains. Apart from thermal desorption, which is ineffective at the low dust temperatures present in the dense core nuclei, heating by impact of cosmic rays and high energy photons or by chemical reactions has been discussed as mechanisms causing desorption. Since molecules are bound to the grain mantle through Van der Waals forces, molecules with high polarizabilities (like CS) will be less volatile. Moreover, Sadlej, Rowland, Devlin & Buch (1995) suggested that CO has a stronger bond to water ice mantles than N_2, thus we would expect CO to deplete in regions with lower density compared to N_2.

From this simple consideration, it is evident that chemical composition varies with the variation in density of the cloud. Therefore, since core contraction will result in a density gradient, we will end up with a chemical gradient with the outer parts of the core relatively unchanged and a progressive disappearance of the species with higher binding energy going towards the nucleus. This chemical pattern can identify the degree of chemical evolution of a dense core. An example of chemical models of dense cores is presented

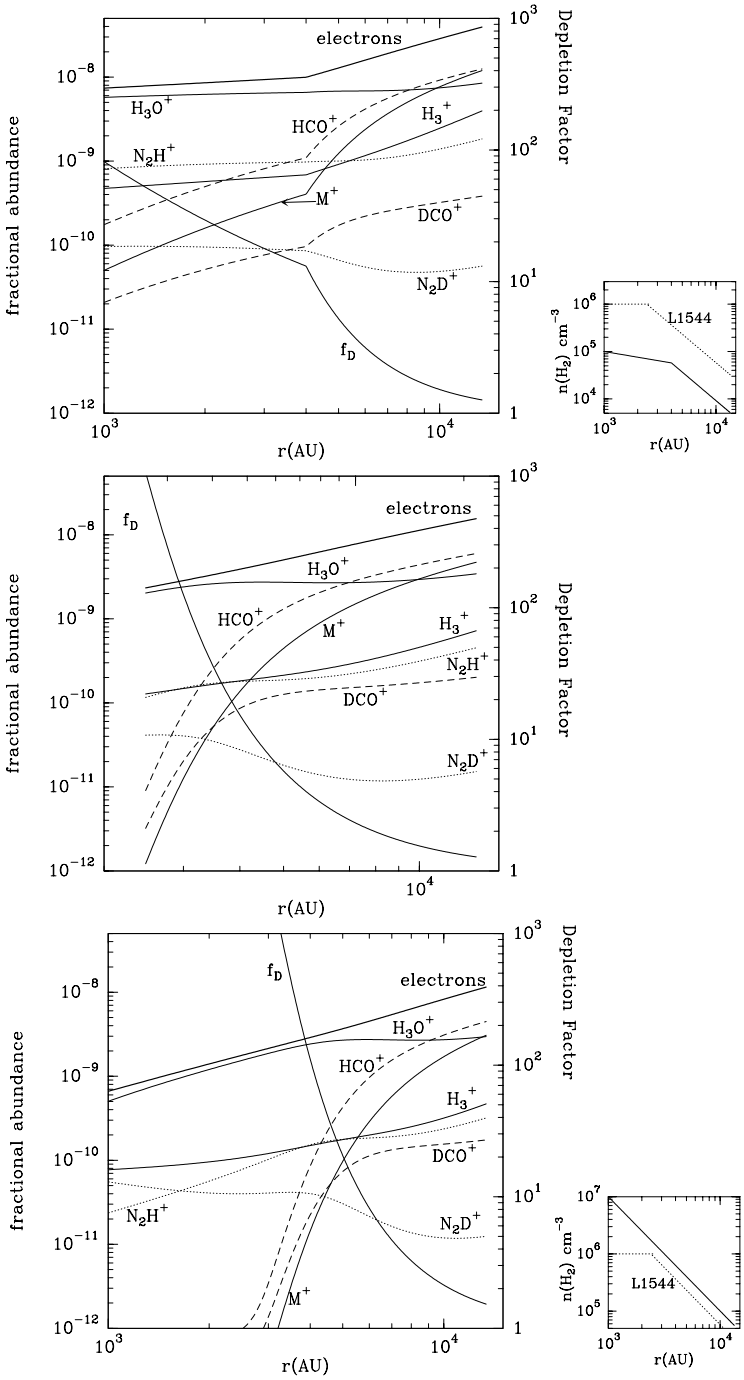

Figure 1.6 Three examples of chemical models of dense cores taken from Caselli (2002). These figures follow the fractional abundances of electrons, metal ions and some important ions in dense cores diagnostics inside three starless cores with different density profiles. In the middle panel the density distribution is taken from the model which best fit the dust emission of L1544, one of the best studied, evolved starless cores (Ward-Thompson, Motte & André 1999; Caselli et al. 2002a,b; Tafalla et al. 2002). In the top panel a less dense and less concentrated density profile is chosen as starting input, while in the bottom panel the density is increased of a factor of 10 with respect to L1544.

in figure 1.6. In these plots, Caselli (2002) showed the variation of the fractional abundance of several molecules and ions together with the CO depletion factor throughout three dense cores with different density profiles. In the top panel, a typical profile of a low-density core is taken as the starting input for the calculations. Central depletion is already seen in all the examined species with the exception of $N_2D^+$and H_3O^+, and more marginally N_2H^+. Increasing the central density to the one observed in L1544 (central panel) or a factor of 10 more (bottom panel) results in a more marked depletion of CO, HCO^+, DCO^+ and metal ions, while N_2H^+, H_3O^+ and H_3^+declines more gradually comparing the different models. N_2D^+ fractional abundance does not show any drop for cores with densities up to $n(H_2)$=10^7 cm^{-3} and is predicted to exceed the N_2H^+ abundance in the central regions of the more evolved starless cores.

Measurements of molecular depletion became possible only recently with the advent of bolometers capable of measuring dust emission, hence total column density, in great detail. Knowledge of the $N(H_2)$ profile is fundamental for comparison with integrated intensity distribution of molecular transitions and as a starting point for radiative transfer calculations which will ultimately furnish the column density of the species of interest. Lack of spatial correlations between dust emission distributions and maps of integrated intensity of carbon-bearing species like $C^{18}O$, $C^{17}O$, CS, H_2CO, were observed towards a large number of centrally concentrated, high density cores ($n(H_2)> 10^4$ cm^{-3}) (Caselli et al. 1999; Carey et al. 1998; Tafalla et al. 2002; Bergin, Alves, Huard & Lada 2002). In contrast, nitrogen-bearing molecules such as N_2H^+, N_2D^+ and NH_3 were proved to be good tracers of the dust emission. This effect is clearly seen in Figure 1.7 taken from Tafalla et al. (2002), where the dust emission map of two starless cores with central density above 10^5 cm^{-3} is compared to their emission in $C^{18}O$, $C^{17}O$, CS, N_2H^+ and NH_3. While N_2H^+ and NH_3 peak at the same position as the dust continuum, the other carbon bearing species do not show a correlation between integrated intensity and column density.

Results of Monte Carlo radiative transfer models indicate that the $C^{18}O$, $C^{17}O$ and CS emission in dense cores is consistent with an abundance drop in the inner part, while N_2H^+ shows a constant abundance and NH_3 an increase of abundance towards the core peak (Tafalla, Myers, Caselli & Walmsley 2004). As a consequence, the use of $C^{18}O$ and CS to probe the high density gas is no longer appropriate in cold starless cores. Better tracers of the gas kinematics in this objects are N_2H^+ and NH_3 and their isotopologues.

Reactions with carbon monoxide are the main channel to destroy H_2D^+ and H_3^+ (Dalgarno & Lepp 1984), thus the disappearance of CO in the gas phase causes the enhance-

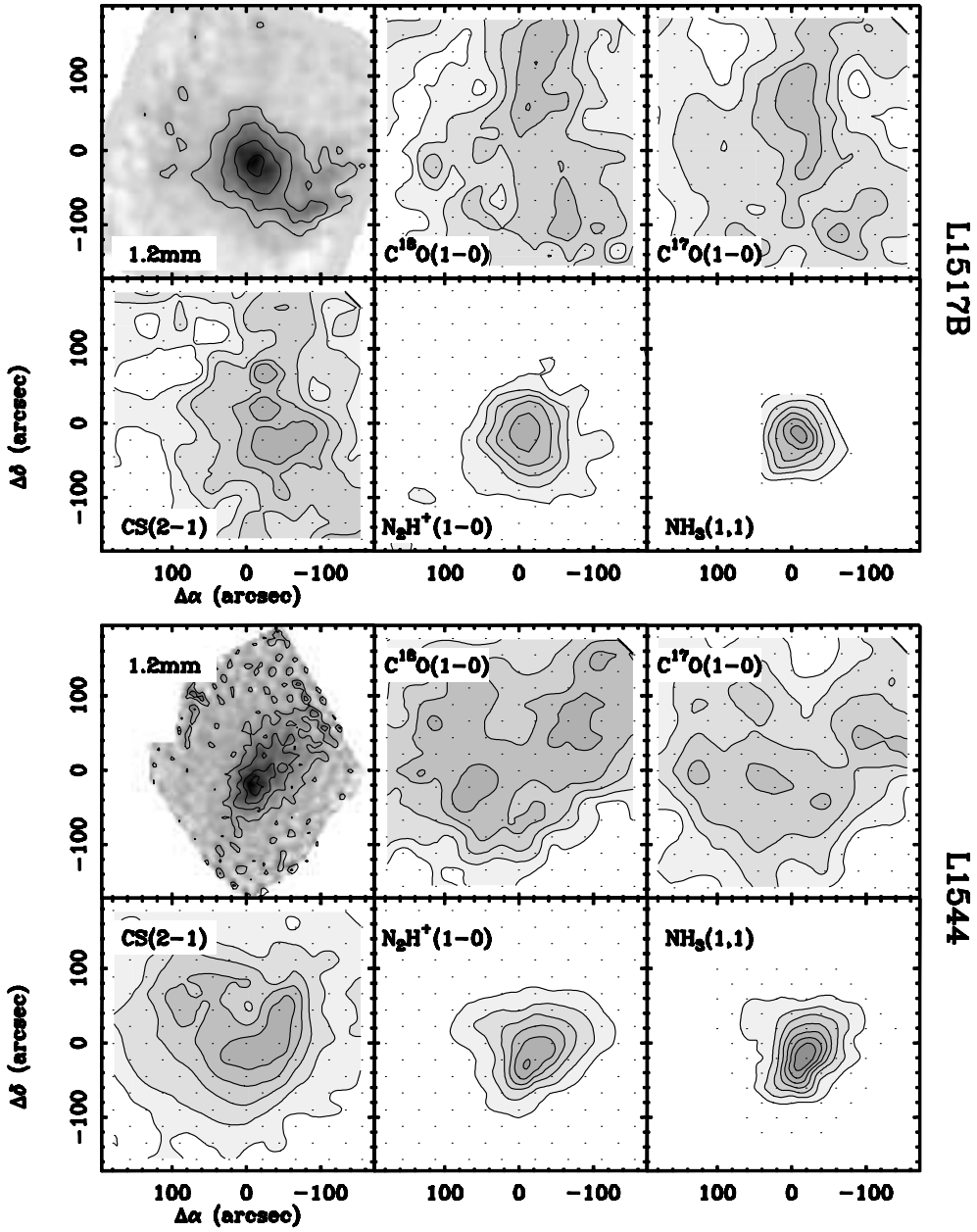

Figure 1.7 Maps of integrated intensity of $C^{18}O(1–0)$, $C^{17}O(1–0)$, CS(2–1), $N_2H^+(1–0)$ and $NH_3(1–1)$ and the dust continuum at 1.2 mm towards two starless cores in the Taurus Molecular Cloud. These maps, taken from Tafalla et al. (2002), confirms the theoretical idea that carbon-bearing species depletes in regions where the H_2 number density exceeds 10^5 molecules cm^{-3}, while species generated from N_2 seem to survive.

ment of these two ions. If we consider, now, that the proton-deuteron exchange reaction that regulates the proportion between them,

$$H_3^+ + HD \rightarrow H_2D^+ + H_2 + \Delta E,$$

is exothermic in the conditions of dense starless cores, we end up with an increase of the ratio $[H_2D^+]/[H_3^+]$ when the CO depletes. To get an idea about the efficiency of this mechanism, consider that the abundance ratio [D]/[H] in the diffuse interstellar medium is $\sim 1.5 \times 10^-5$ (Oliveira et al. 2003), while $[N_2D^+]/[N_2H^+]$ can exceed 20% in a prestellar core (Caselli et al. 2002b; Bacmann et al. 2003). Direct observations of H_2D^+ and H_3^+ are complicated by the very high frequency of their rotational transitions, but recently H_2D^+ has been successfully detected in prestellar cores (Caselli, van der Tak, Ceccarelli & Bacmann 2003). The boost in deuterium fractionation is reflected in the isotopologues that originates from reaction with H_2D^+ and H_3^+ , through the schematic reactions

$$\begin{aligned} H_3^+ + X &\rightarrow XH^+ + H_2, \\ H_2D^+ + X &\rightarrow XD^+ + H_2. \end{aligned}$$

Therefore from the observations of N_2H^+ and N_2D^+ or HCO^+ and DCO^+ we can retrieve the deuterium fractionation in starless cores. From these simple arguments, it is evident that "deuterated" nitrogen-bearing species, abundant in the very inner nucleus where CO is totally depleted, are among the best tracers to search for evidences of infall in starless cores with central densities up to few 10^6 H_2 cm^{-3}. In fact, above this density N_2 is also supposed to freeze-out onto the dust grains and the only species (other than H_2 and He) present in the gas phase are H_2D^+ and H_3^+.

Interestingly, with the formation of the protostar and the consequent internal heating, molecules are desorbed from the dust grains and carbon-bearing species return to trace the gas kinematics. This effect has been observed in Class 0 and Class I protostars (Jørgensen, Schöier & van Dishoeck 2002) and in high-mass hot cores (Lintott et al. 2005).

1.4 Observing infall in dense cores

A conclusive proof of collapse could come from the determination of the spatial distribution of inward motions. This piece of information should also be able to distinguish between the different theoretical models. In fact, line profile modeling of dense gas tracers can provide the velocity field integrated along the line of sight and in the telescope

beam. If the excitation temperature increases towards the center, optically thick lines appear double peaked with a higher intensity peak corresponding to the background blue-shifted emission and a lower intensity peak for the foreground red-shifted emission (see the reviews of Evans 1999 and Myers, Evans & Ohashi 2000). In Figure 1.8, we report two cartoons from Evans (1999) which explain the infall profiles more intuitively. In panel (a), the different regions in a contracting cloud are associated with the spectral feature in the line profile. The central absorption feature is present only if the static envelope outside the core is optically thick. Evans (1999) in these cartoons also shows the velocity wings expected to arise from the central gas infalling with very high velocity. In practice, these wings have never been seen both because of confusion with molecular outflows and because of the large beam width of sub-millimeter telescopes. The velocity field along the line of sight has to be assumed in order to model the line profile. In panel (b) a velocity field of a free falling gas under gravitational attraction, $\mathrm{v}(r) \propto r^{-0.5}$, is assumed and points of "iso-velocity" are shown. From this sketch, it is evident that each line of sight intercept two points with the same velocity, thus, in presence of optically thick lines, we will see only the radiation coming from the one that is closer to us (points labeled B_2 and R_2 in Figure 1.8). Considering now that density, hence excitation temperature, increases towards the center in dense cores, we can see that the blue peak should appear brighter than the red peak, because $T_{ex}(\mathrm{B}_2) > T_{ex}(\mathrm{R}_2)$.

Line profiles consistent with the velocity field predicted in the inside-out collapse model (Shu 1977) were observed towards B335, a globule with an embedded Class 0 protostar, using multiple transitions of CS and $\mathrm{H_2CO}$ (Zhou, Evans, Kömpe & Walmsley 1993; Choi, Evans, Gregersen & Wang 1995).
Having a double peaked line profile with a stronger blue peak does not ensure the presence of infall since the same profile can be produced by e.g. rotation or ejection of an "outflow blob". The latter can be ruled out by observing an optically thin line that is predicted to peak in the central absorption dip in case of infall, or show a consistent double peaked profile otherwise. To reject the possibility of rotation, one needs to map the line asymmetry that is supposed to increase towards the center in case of infall. On the contrary, along the rotation axis line profiles should be symmetric and they should show opposite asymmetries on the two sides (Belloche, André, Despois & Blinder 2002).

Infall asymmetry has been recognized towards a few other sources (Myers et al. 1995; Moriarty-Schieven et al. 1995; Ward-Thompson et al. 1996); then in order to check how representative these object are and possibly to find objects at different evolutionary stage,

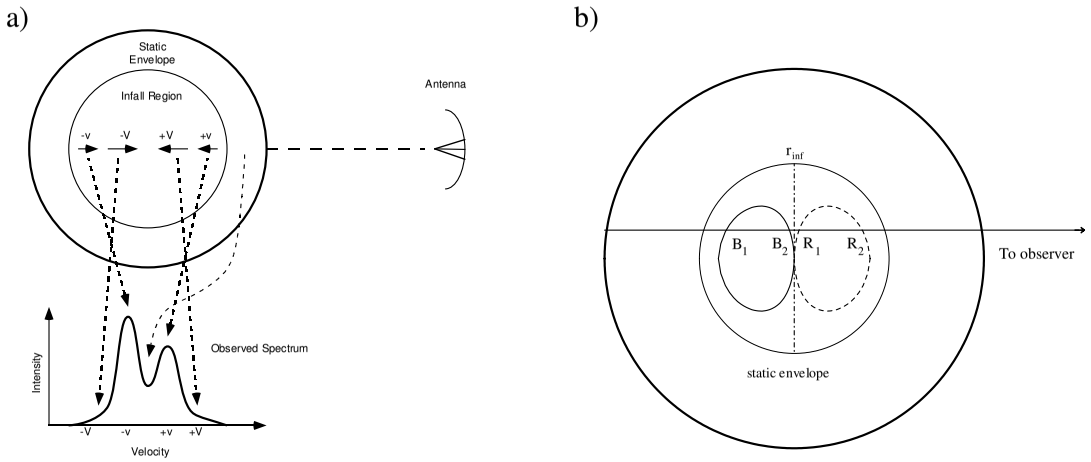

Figure 1.8 These two cartoons, taken from the review of Evans (1999), illustrate how we can obtain a double peaked asymmetric profile for optically thick lines observed in centrally condensed, contracting cores. The optical depth provides the central dip while the velocity field combined with the increase in density produce the asymmetry between the peaks.

many "unbiased" surveys have been carried out to search for an excess of sources with infall asymmetry. The rationale is that if blue-skewed profiles are produced by rotation or ejection of molecular bullets, then a large sample should show a similar number of red-skewed and blue-skewed profiles. On the contrary, Gregersen, Evans, Zhou & Choi (1997), found 9 blue-skewed profiles and 3 red-skewed profiles in a sample of 23 Class 0 sources observed in HCO^+. Mardones et al. (1997) confirmed this result using CS, H_2CO and HCO^+ lines towards 37 Class 0 and Class I sources finding 15 cases of blue-skewed profiles in at least one line (with no evidence of red-skewed asymmetry in other lines) against 4 cases with the opposite trend. Lee, Myers & Tafalla (1999) extended this search to younger objects finding 20 blue-skewed profiles against 3 red-skewed profiles in a sample of 69 starless cores detected in CS and N_2H^+.

1.5 This thesis

The aim of the present thesis is to advance the study of the initial conditions of star formation by first identifying the starless cores closest to forming a star and second determining

the physical and chemical conditions of the best candidates.

In the beginning of this chapter, we saw that dense starless cores are believed to be the precursors of Class 0 and Class I protostar given the similarity in their spectral energy distributions at millimeter and sub-millimeter wavelengths. This statement is not necessarily true since not *all* starless cores might eventually form a protostar. For this reason, recognizing the starless cores closest to protostar formation is of fundamental importance to understand the physical mechanism behind star formation.
The subsample of starless cores which are on the verge of forming a protostar are often referred to as pre-stellar cores or pre-protostellar cores (André, Ward-Thompson & Barsony 2000; Ward-Thompson, Kirk, & André 2003), we will adopt pre-stellar cores hereafter.

The prototype of pre-stellar core is represented by L1544, a dense core located in the outskirt of the star forming complex seen towards the constellations of Taurus-Auriga. Several characteristics associated with an enhanced evolution were observed towards this object. In particular, we would expect that a pre-stellar core should exhibit:

- a high central density, due to contraction
- broad line widths increasing towards the center, due to inward motions
- double peaked line profiles with infall asymmetry, as seen in §1.4
- decreasing CO abundance towards the center and large H_2D^+ and N_2H^+ abundance, as seen in §1.3;
- high degree of deuterium fractionation

All these properties were observed in L1544 through observations of dust and several molecules using many different sub-millimeter antennas (Ward-Thompson, Motte & André 1999; Caselli et al. 1999, 2002a, b, 2003; Lee et al. 1999, 2001, 2004; Tafalla et al. 2002; Bacmann et al. 2000, 2002, 2003).

Of course testing a theory on a single object is not possible. Thus, in Chapter 2, in order to enlarge the number of evolved pre-stellar cores known, we tested the physical and chemical properties of a sample of 30 starless cores through N_2H^+, N_2D^+, $C^{18}O$ and 1.2 mm continuum observations. We found that 7 cores in our sample show the majority of the L1544 properties described above and thus are believed to be closer to forming a protostar than are the other members of our sample.
These data validate the proposed chemical scenario that links the enhancement of deuterated molecules to the disappearance of CO from the gas phase.

Among the pre-stellar cores selected by the N_2H^+ and N_2D^+ observations, in Chapter 3 we concentrated on L1521F, the only core, other than L1544, found to be more evolved than the average core in each test we performed. Moreover, both L1544 and L1521F belong to the same star forming region, the Taurus Molecular Cloud; this provides a more similar external conditions for the two objects suggesting that their differences principally arise from intrinsic evolutionary effects rather than being caused by distinct environmental properties (e.g. degree of turbulence, interstellar radiation field, ionization factor, large scale magnetic field, ...).

Detailed chemical and kinematical analysis suggest that L1521F is less evolved than L1544, although, in analogy with L1544, it is approaching the "critical" state.

Finally in Chapter 4, we present the results of line observations of L1014, the first starless core where the Spitzer Space Telescope found an embedded protostar (Young et al. 2004). After Young et al. (2004) detected of a point-like source with colors compatible with protostar-disk emission close to the L1014 dust peak, we used IRAM-30m, FCRAO and CSO to map L1014 in several species including CO and N_2H^+ isotopologues and CS in order to study its molecular content and to search for the presence of an outflow.

Our data show physical and chemical properties in L1014 typical of moderately evolved starless cores and no classical signatures of molecular outflow from ^{12}CO and ^{13}CO observations, giving important constraints on the models of this puzzling source.

Chapter 2

Probing the evolutionary status of starless cores through N_2H^+ and N_2D^+ observations

Abstract.

We have undertaken a survey of N_2H^+ and N_2D^+ towards 31 low-mass starless cores using the IRAM 30-m telescope. Our main objective has been to determine the abundance ratio of N_2D^+ and N_2H^+ towards the nuclei of these cores and thus to obtain estimates of the degree of deuterium enrichment, a symptom of advanced chemical evolution according to current models. We find that the $N(N_2D^+)/N(N_2H^+)$ ratio is larger in more "centrally concentrated cores" with larger peak H_2 and N_2H^+ column density than the sample mean. The deuterium enrichment in starless cores is presently ascribed to depletion of CO in the high density ($> 3 \times 10^4$ cm^{-3}) core nucleus. To substantiate this picture, we compare our results with observations in dust emission at 1.2 mm and in two transitions of $C^{18}O$. We find a good correlation between deuterium fractionation and $N(C^{18}O)/N(H_2)_{1.2\ mm}$ for the nuclei of 14 starless cores. We thus identified a set of properties that characterize the most evolved, or "pre–stellar", starless cores. These are: higher N_2H^+ and N_2D^+ column densities, higher $N(N_2D^+)/N(N_2H^+)$, more pronounced CO depletion, broader N_2H^+ lines with infall asymmetry, higher central H_2 column densities and a more compact density profile than in the average core. We conclude that this combination of properties gives a reliable indication of the evolutionary state of the core. Seven cores in our sample (L1521F, OphD, L429, L694, L183, L1544 and TMC2) show the majority of these features and thus are believed to be closer to forming a protostar than are the other members of our sample. Finally, we note that the subsample of Taurus cores behaves

more homogeneously than the total sample, an indication that the external environment could play an important role in the core evolution.

A. Crapsi, P. Caselli, C.M. Walmsley, P.C. Myers, M. Tafalla, C.W. Lee and T.L. Bourke, 2005, Astrophysical Journal, 619, in press

2.1 Introduction

Understanding the physical and kinematic conditions in a molecular cloud core just prior to the onset of gravitational collapse is of paramount importance if one wishes to study the subsequent protostellar evolution. Molecular line measurements can provide the kinematical informations to probe infall motions in the highest density nucleus as long as the observed species is reasonably abundant in the region of interest.
An important step forward in starless core studies has been the understanding of the fact that, at temperatures of roughly 10 K and densities above a few times 10^4 cm^{-3}, CO, as well as other carbon-bearing molecules, condenses out onto dust grain surfaces preventing us from observing the high-density structures from where one expects the first signs of collapse (Leger 1983). This is most clearly seen from the comparison of maps made in the millimeter dust continuum with maps of CO isotopologues (Kuiper, Langer & Velusamy 1996; Kramer et al. 1999; Alves, Lada & Lada 1999; Caselli et al. 1999).
For reasons that are thought to have to do with the low binding energy of the N_2 molecule on ice mantle surfaces (Sadlej, Rowland, Devlin & Buch 1995; Bergin & Langer 1997), there are some N-containing molecular species that survive in the gas phase at least for densities in the range 10^5–10^6 cm^{-3}. In particular, maps of N_2H^+ and NH_3 (as well as their deuterated counterparts) show reasonable agreement with the distribution of dust emission. Thus, only from observations of such species one can hope to probe the physical and chemical conditions of the most evolved pre–stellar cores that show a high column density peak in the dust emission.
One can also hope that by studying samples of such high density objects it will be possible to identify the cores where collapse has already been initiated or is at the point of doing so.

The aim of the cthis chapter is to report the results of a survey of 31 cores in various transitions of N_2H^+ and N_2D^+ observed with the IRAM 30-m telescope.

These observations, besides probing the kinematics of the high density nucleus of starless cores, enable us to gauge the deuterium enrichment in our sample. This parameter, evaluated from the N_2D^+ over N_2H^+ column density ratio, can be used as a tool to discriminate the evolutionary status of a starless core. In fact, the disappearance of CO from the gas phase, together with the exothermicity of the production of H_2D^+, leads to abundances of deuterated species in cold molecular clouds more than 3 orders of magnitudes larger than the [D]/[H] elemental abundance ($\simeq 1.5 \times 10^{-5}$ Oliveira et al. 2003). The freeze-out of the CO onto the grain mantles decreases the destruction of H_2D^+ and H_3^+. As a result, the enhanced H_3^+ abundance speeds up the reaction that leads to a higher production of H_2D^+ and this increases the ratio of $[H_2D^+]/[H_3^+]$ (e.g. Dalgarno & Lepp 1984; Roberts & Millar 2000a).

We expect to use the $N(N_2D^+)/N(N_2H^+)$ ratio to discriminate the less evolved starless cores from the more advanced pre–stellar cores. For practical purposes in this study, we define "pre–stellar cores" to be those with an $N(N_2D^+)/N(N_2H^+)$ abundance ratio ≥ 0.1, and we believe that this approximately corresponds to a core with central density greater than 5×10^5 cm^{-3} that is in the last phase of its evolution prior to dynamical collapse. We base this partly on the cross-correlation of our $N(N_2D^+)/N(N_2H^+)$ measurements with other properties expected to probe an enhanced evolution of the starless cores such as broader line widths, larger $n(H_2)$ central density, or larger amount of CO freeze-out. For this reason, supplemental dust continuum and $C^{18}O$ measurements, able to furnish the H_2 density profile and the CO depletion, were carried out in cases in which these were not available in the literature.

In § 2.2 of this chapter, we outline our observational technique both for the N_2H^+ and N_2D^+ observations and for the dust continuum and $C^{18}O$. In § 2.3, we summarize our direct observational results, and in § 2.4 we derive physical and chemical quantities for the cores in our sample. In § 2.5, we discuss statistical correlations between the physical properties derived for our sample and in § 2.6, we summarize our conclusions.

2.2 Observations

2.2.1 The Sample

We have selected 31 cores to be observed in N_2H^+ and N_2D^+. The criteria used in the sample selection were not completely homogeneous, but we think that the sample should be representative of evolved starless cores.

Table 2.1. Core Sample

core (1)	RA (J2000) (2)	DEC (J2000) (3)	dist (4)	ref (5)	env. (6)	N (7)	1.2-mm (8)	$C^{18}O$ (9)
L1498	$04^h10^m51.''5$	$+25°09'58''$	140	a	T	25	y (b)	y (b)
L1495	$04^h14^m08.''2$	$+28°08'16''$	140	b	T	20	y (b)	y (b)
L1495B	$04^h18^m05.''1$	$+28°22'22''$	140	a	T	1	n	n
L1495A-N	$04^h18^m31.''8$	$+28°27'30''$	140	a	T	1	n	n
L1495A-S	$04^h18^m41.''8$	$+28°23'50''$	140	a	T	1	n	n
L1521F	$04^h28^m39.''8$	$+26°51'35''$	140	a	T	89	y (g)	y (g)
L1400K	$04^h30^m52.''1$	$+54°51'55''$	140	b	T	20	n	n
L1400A	$04^h30^m56.''8$	$+54°52'36''$	140	a	T	1	n	n
TMC2	$04^h32^m48.''7$	$+24°25'12''$	140	a	T	1	y (h)	y (h)
TMC1	$04^h41^m32.''9$	$+25°44'44''$	140	a	T	1	n	n
TMC1C	$04^h41^m38.''8$	$+25°59'42''$	140	c	T	3	n	n
L1507A	$04^h42^m38.''6$	$+29°43'45''$	140	a	T	1	n	n
CB23	$04^h43^m27.''7$	$+29°39'11''$	140	a	T	1	n	n
L1517B	$04^h55^m18.''8$	$+30°38'04''$	140	a	T	21	y (b)	y (b)
L1512	$05^h04^m09.''7$	$+32°43'09''$	140	a	T	25	n	n
L1544	$05^h04^m15.''1$	$+25°11'08''$	140	a	T	38	y (i)	y (o)
L134A	$15^h53^m33.''1$	$-04°35'26''$	165	a	B	1	n	n
L183	$15^h54^m06.''4$	$-02°52'23''$	165	a	B	77	y (l)	y (h)
OphD	$16^h28^m30.''4$	$-24°18'29''$	165	d	O	78	y (i)	y (p)
L1689A	$16^h32^m13.''1$	$-25°03'43''$	165	e	O	1	n	n
L1689B	$16^h34^m45.''8$	$-24°37'50''$	165	a	O	1	n	n
L158	$16^h47^m23.''2$	$-13°58'37''$	165	a	O	1	n	n

Table 2.1—Continued

core (1)	RA (J2000) (2)	DEC (J2000) (3)	dist (4)	ref (5)	env. (6)	N (7)	1.2-mm (8)	$C^{18}O$ (9)
L234E-S	$16^h48^m08.''6$	-10°57′25″	165	a	O	1	n	n
B68	$17^h22^m38.''9$	-23°49′46″	125	f	B	1	y (m)	y (f)
L492	$18^h15^m46.''1$	-03°46′13″	200	a	A	9	y (h)	y (h)
L328	$18^h17^m00.''4$	-18°01′52″	200	d	B	4	y (d)	y (p)
L429	$18^h17^m06.''4$	-08°14′00″	200	a	A	68	y (d)	y (p)
GF5	$18^h39^m16.''4$	-06°38′15″	200	d	A	1	n	n
L694-2	$19^h41^m04.''5$	+10°57′02″	250	a	···	96	y (n)	y (h)
L1197	$22^h37^m02.''3$	+58°57′21″	···	a	···	5	n	n
CB246	$23^h56^m49.''2$	+58°34′29″	140	a	B	3	n	n

Note. — Col (1) most common core name; col. (2) and (3) reference position in J2000; col. (4) distance; col. (5) references for the position and distance, see below for coding; col. (6) Star forming environment: T: Taurus molecular cloud; O: Ophiucus molecular cloud; B: Bok globules; A: Aquila rift; col. (7) number of observed positions in both N_2H^+ and N_2D^+; col. (8) availability of a 1.2-mm continuum map and reference to it, coding below; col. (9) availability of a $C^{18}O$ map and reference to it, coding below.

References. — a: Lee, Myers & Tafalla (2001); b: Tafalla et al. (2002); c: Caselli, Benson, Myers & Tafalla (2002); d: Bacmann et al. (2000); e: Shirley, Evans, Rawlings & Gregersen (2000); f: Bergin, Alves, Huard & Lada (2002); g: Chapter 3; h: this work; i: Ward-Thompson, Motte & André (1999); l: Pagani et al. (2003); m: Bianchi et al. (2003); n: Tafalla et al. (in preparation); o: Caselli et al. (1999); p: Bacmann et al. (2002).

"Evolved" in this context means that there is evidence for high density in the form either of strong N_2H^+(1–0) emission ($\gtrsim 3$ K km s^{-1} in T_{MB} scale) or strong 1.2-mm dust continuum ($\gtrsim 30$ mJy/(11″ beam)) emission or both. The rationale here is that both of these criteria suggest a high central H_2 column density and hence high central pressure, given that N_2H^+ appears to trace the dust well (e.g. Tafalla et al. 2002).

Of the 31 objects selected in this manner, 24 belong to an earlier survey of N_2H^+ and CS by Lee, Myers & Tafalla (2001), aimed at detecting "extended" infall in starless cores through the comparison of the line profiles of optically thick (CS) and thin (N_2H^+) tracers. We considered all cores in the Lee, Myers & Tafalla (2001) sample showing strong N_2H^+(1–0) lines and compact morphology. Among these, 13 show infall asymmetry (i.e., CS spectra peaking at lower velocities than N_2H^+), 7 show no asymmetry and 4 show outflow asymmetry.

Of the other 7 cores (L1495, L1400K, TMC1C, L1689A, B68, L328, GF5) in our sample some have been mapped in lines of NH_3 (Benson & Myers 1989) and N_2H^+ (Caselli, Benson, Myers & Tafalla 2002) and all have been mapped in dust continuum emission and show compact morphology and relatively high central number densities ($n(H_2) \gtrsim 10^5$ cm^{-3}; Bacmann et al. 2000; Shirley, Evans, Rawlings & Gregersen 2000; Tafalla et al. 2002).

Finally, the cores in our sample are nearby enough (within 250 pc), to spatially resolve the dense core nucleus. The total sample is listed in Table 2.1; columns (2), (3) and (4) show the J2000.0 coordinates and the distance in parsec, taken from the reference in column (5). In column (6) we specify if the core is isolated or embedded in a particular star forming region. Then in column (7) we give the total number of positions observed in both N_2H^+ and N_2D^+. Finally, in column (8) and (9) we report on the availability of a 1.2-mm map and of a $C^{18}O$ map with the reference to it.

2.2.2 N_2H^+ and N_2D^+

The N_2H^+ and N_2D^+ observations were carried out between April 2002 and January 2003 using the IRAM 30-m telescope. We observed in frequency switch mode and used the autocorrelator as the back end. Details on the telescope setting used are given in Table 2.2. The frequencies of N_2H^+(1–0), N_2D^+(2–1) and N_2D^+(3–2) were updated following the recent results of Dore et al. (2004). A new value for the N_2H^+(3–2) frequency was calculated, first evaluating the N_2H^+ rotational constant ($B = 46586.87546 \pm 0.00025$ MHz) from the new N_2H^+(1–0) frequency determination (Dore et al. 2004), and then using the

Table 2.2. Telescope settings and parameters.

line (1)	frequency (2)	HPBW (3)	F_{throw} (4)	T_{SYS} (5)	Δv_{res} (6)
N_2H^+(1–0)	93.1737725	26	7.5	200	0.063
N_2H^+(3–2)	279.511863	9	14.3	2000	0.042
N_2D^+(2–1)	154.217137	16	7.5	400	0.038
N_2D^+(3–2)	231.321966	10	14.3	900	0.050
$C^{18}O$(1–0)	109.782173	22	···	170	0.026
$C^{18}O$(2–1)	219.560357	11	···	450	0.033

Note. — Col. (2) line rest frequency (GHz); Col. (3) Half Power Beam Width ($''$) Col. (4) Freq. Throw (kHz); Col. (5) System Temperature (K); Col. (6) Channel Spacing (km s^{-1})

centrifugal distortion constant from Verhoeve et al. (1990). In Table 2.2, we report the frequency of the $F_1\,F = 45 \rightarrow 34$ hyperfine component which has a relative intensity of 17.46%. The pointing and focus were checked approximately every two hours observing planets or quasars in continuum. The pointing corrections never exceeded $4''$. The intensity scale was converted to main beam temperature according to the efficiencies reported on the IRAM 30-m Web site.[1]

We first observed the total sample at the peak position given either from previous N_2H^+ observations (Lee, Myers & Tafalla 2001) or from the dust maps (Bacmann et al. 2000). Then, we made a map of the cores that showed the strongest N_2D^+(2–1) lines: L1521F, L1544, TMC2, L183, OphD, L492, L429 and L694-2. TMC2 was mapped only in N_2D^+ and we thus evaluate the ratio of N_2H^+ and N_2D^+ towards the only available position observed in N_2H^+ ($25''$ off the N_2D^+ strongest position). The N_2H^+ and N_2D^+ maps towards L1495, L1517B, L1498, L1400K and L1512 were taken as part of a different project on starless cores aimed at determining the ionization degree (P. Caselli et al., in preparation, T. Gatti et al., in preparation); here we just use the N_2H^+ and N_2D^+ values at the dust peak (determined by Tafalla et al. 2002). The L1544 and L1521F data used in the present chapter are taken from Caselli et al. (2002a) and Chapter 3. respectively.

[1] Available at http://www.iram.fr/IRAMES/index.htm

2.2.3 Dust continuum and $C^{18}O$

Millimeter continuum observations, taken with MAMBO (the IRAM 30-m bolometer), were already available in the literature for 13 cores in our sample (L1544, OphD: Ward-Thompson, Motte & André 1999; L1689B, L328, L429, GF5: Bacmann et al. 2000; L1498, L1495, L1517B, L1400K: Tafalla et al. 2002; L183: Pagani et al. 2003; L1521F: Chapter 3; L694-2: M. Tafalla et al. 2005, in preparation). Moreover, a 1.2-mm map of B68 taken with SIMBA (the facility bolometer at SEST) was published in Bianchi et al. (2003). We obtained a 1.2-mm map of two more cores: TMC2, which presents high N_2D^+emission and L492 which has very strong N_2H^+(1–0) lines. Observations were carried out by the IRAM staff between January 2003 and February 2003 using the new 117-channel bolometer. The IRAM 30-m half-power beamwidth (HPBW) at 1.2 mm is approximately $11''$. The calibration error is estimated to be $\sim$10%.
We mapped TMC2 in a $7'\times7'$ region scanning in the azimuthal direction at $5''\mathrm{s}^{-1}$ with a spacing between the scans of $9''$, reaching a sensitivity of 6 mJy/beam at the map center. The zenith optical depth, measured before and after the map, was 0.2. L492 was mapped in a $3'\times3'$ region scanning in the azimuthal direction at $5''\mathrm{s}^{-1}$ with a spacing between the scans of $8''$; the RMS at map center is 5 mJy beam^{-1}. The zenith optical depth, measured before taking the map, was 0.2. The data reduction (baseline fitting, sky-noise subtraction and regridding) was performed using the NIC program of the GAG software developed at IRAM and the Observatoire de Grenoble (Broguière et al. 2003).
In the same fashion, we observed the $C^{18}O$(1–0) and (2–1) for those cores where data were not already available in literature, i.e., L183, L694-2, L492 and TMC2. We mapped in the on-the-fly mode in a region $150''\times150''$ wide ($200''\times300''$ for L183 and $200''\times200''$ for TMC2) scanning in the azimuthal direction. Both the separation between two scans and the separation between two dumps were $5''$. $C^{18}O$ data were already available for L1544 (Caselli et al. 1999), OphD, L328, L429 (Bacmann et al. 2002), L1495, L1498, L1517B (Tafalla et al. 2002), B68 (Bergin, Alves, Huard & Lada 2002) and L1521F (Chapter 3).

2.3 Results

2.3.1 Spectra at dust peak

In Figure 2.1 and 2.2, we show the observed spectra of N_2H^+(1–0) and N_2D^+(2–1) towards the core dust peaks. The cores where no line was detected were omitted. The data

were reduced using CLASS, the line analysis program of the GAG software (Buisson et al. 2002). Notable in particular is the double-peaked profile with an infall asymmetry observed in L1544, as well as the red shoulder or wing seen in several other sources (OphD, L694-2, L492, L1521F, TMC1-C). In general, these more "complex" profiles are more apparent in the sources where the N_2D^+(2–1) line is strong (see below), although there are exceptions (e.g. TMC1 which has a relatively broad N_2H^+ line with "outflow asymmetry" but weak N_2D^+(2–1))[2]. The integrated intensities of these spectra plus the N_2H^+(3–2) and N_2D^+(3–2) are reported in Table 2.3. We also give there the offset of the N_2D^+(2–1) peak from the reference position given in Table 2.1. In our sample of 31 cores, we detected N_2H^+(1–0) emission with S/N>10 in 29 cores. L1689A and GF5, which have a weak detection, will not be considered further in this work. We detected N_2D^+(2–1) lines with signal-to-noise-ratio (S/N) higher than 10 in 10 cores (L1521F, TMC2, L1517B, L1544, L183, OphD, L492, L328, L429, L694); another 13 were detected with S/N higher than 4. In our calculations, as well as the error due to the RMS noise (shown in Table 2.3), we adopt a calibration uncertainty of 10% for N_2H^+(1–0) and 15% for N_2D^+(2–1).

From hyperfine structure fitting of the spectra in Figure 2.1 and 2.2, we derived the line parameters shown in Table 2.4. We report the observed LSR velocities and line widths in the two species and find in first approximation good agreement, suggesting that we are sampling the same regions along the line of sight.

Total optical depth estimates are derived from a simultaneous fit to the hyperfine satellites assuming that hyperfine levels are populated proportional to their statistical weights. These results show that the total optical depth (i.e., the sum of the optical depths of the seven satellites) in N_2H^+(1–0) can reach values as high as 20; considering the hyperfine structure of N_2H^+(1–0), a total optical depth of 20 means that the main component ($F_1\,F = 2\,3 \rightarrow 1\,2$), which has a fraction of 7/27 ($\equiv 25.9\%$) of the total line strength, is often optically thick while the weakest satellite ($F_1\,F = 1\,0 \rightarrow 1\,1$), with an intrinsic line strength of 1/27 (or 3.7%) of the total transition strength, is in almost all cases optically thin (its maximum opacity in our sample is 0.7, towards L183, L1521F and B68). We note, however, that the combination of excitation anomalies (non-LTE effects in the hyperfine level populations, see Caselli, Myers & Thaddeus 1995) and highly non-Gaussian line profiles (e.g., L1544, B68, L492, L1521F, L694-2) increases the uncertainty in the opacity estimate from the simultaneous fitting of the hyperfine components. In fact, the fitting model adopted assumes constant abundance and excitation temperature along

[2]The TMC1 position observed is close to the "CS peak", see Pratap et al. (1997).

Table 2.3. Observed line integrated intensities at N_2D^+peak.

core	RA off ″	DEC off ″	I(N_2H^+(1–0)) K km s^{-1}	I(N_2H^+(3–2)) K km s^{-1}	I(N_2D^+(2–1)) K km s^{-1}	I(N_2D^+(3–2)) K km s^{-1}
L1498	0	0	2.27±0.01	0.11±0.02	0.12±0.02	<0.01
L1495	40	40	3.18±0.03	0.24±0.04	0.23±0.05	0.08±0.02
L1495B	0	0	1.35±0.05	<0.09	0.14±0.04	0.30±0.09
L1495A-N	0	0	3.46±0.05	<0.09	0.18±0.02	<0.09
L1495A-S	0	0	1.08±0.06	<0.12	0.15±0.04	<0.11
L1521F	-10	0	5.86±0.02	0.74±0.04	0.97±0.02	0.29±0.01
L1400K	-20	-40	1.39±0.02	0.10±0.04	<0.04	<0.02
L1400A	0	0	1.48±0.04	0.25±0.12	0.08±0.02	0.13±0.07
TMC2	0	40	3.48±0.03	0.32±0.11	0.66±0.04	0.17±0.05
TMC1	0	0	3.51±0.06	0.35±0.11	0.20±0.03	<0.10
TMC1C	0	40	1.87±0.03	<0.19	0.24±0.04	0.08±0.06
L1507A	0	0	1.78±0.05	0.21±0.12	0.15±0.03	0.15±0.07
CB23	0	0	2.22±0.06	0.20±0.14	0.21±0.04	0.37±0.10
L1517B	-15	-15	2.57±0.01	0.11±0.02	0.26±0.02	<0.01
L1512	0	0	2.11±0.02	<0.05	0.17±0.03	<0.02
L1544	20	-20	5.46±0.04	0.56±0.09	2.23±0.05	0.55±0.03
L134A	0	0	1.13±0.03	<0.25	<0.04	<0.07
L183	30	0	4.20±0.01	0.56±0.04	1.63±0.02	0.48±0.01
OphD	-20	-50	3.71±0.02	0.39±0.05	1.75±0.02	0.59±0.02
L1689A	0	0	0.15±0.07	<0.13	<0.05	<0.06
L1689B	0	0	1.27±0.05	<0.13	0.09±0.04	0.12±0.06
L158	0	0	0.61±0.05	<0.11	<0.04	<0.05

Table 2.3—Continued

core	RA off ″	DEC off ″	I(N_2H^+(1–0)) K km s^{-1}	I(N_2H^+(3–2)) K km s^{-1}	I(N_2D^+(2–1)) K km s^{-1}	I(N_2D^+(3–2)) K km s^{-1}
L234E-S	0	0	2.06±0.07	0.40±0.26	0.26±0.04	<0.32
B68	0	0	2.37±0.01	0.17±0.02	0.13±0.03	<0.03
L492	20	20	3.95±0.02	<0.10	0.30±0.02	<0.04
L328	0	0	4.46±0.03	0.42±0.09	0.38±0.03	0.19±0.04
L429	-20	20	6.11±0.02	0.57±0.05	2.03±0.02	0.62±0.02
GF5	0	0	0.39±0.05	<0.07	<0.04	<0.10
L694-2	0	0	5.13±0.01	0.36±0.02	1.35±0.02	0.37±0.01
L1197	0	0	2.15±0.04	<0.16	0.18±0.06	<0.05
CB246	-60	-20	2.91±0.03	<0.07	0.11±0.04	0.22±0.06

Note. — Offsets are referred to the positions in Table 2.1. Temperatures are in main beam temperature scale. Calibration errors were not included in the error estimate. Upper limits assume the line-width of N_2H^+(1–0) where available or 0.17 km s^{-1} the smallest line-width observed in our sample.

Table 2.4. Results of the hyperfine structure fitting on the N_2H^+(1–0) and N_2D^+(2–1) spectra at the peak position of each core.

core	N_2H^+(1–0)				N_2D^+(2–1)			
	V_{LSR} km s^{-1}	ΔV km s^{-1}	τ	T_{EX} K	V_{LSR} km s^{-1}	ΔV km s^{-1}	τ	T_{EX} K
L1498	7.822±0.001	0.185±0.001	11.5±0.3	4.5±0.1	7.778±0.010	0.176±0.029	0.1	4.5
L1495	6.807±0.001	0.237±0.003	9.6±0.6	4.8±0.2	6.755±0.025	0.290±0.061	0.1	4.8
L1495B	6.633±0.008	0.390±0.018	0.1	4.8	6.683±0.065	0.500±0.216	0.1	4.8
L1495A-N	7.296±0.003	0.327±0.007	7.6±0.9	4.7±0.3	7.237±0.013	0.244±0.035	0.1	4.7
L1495A-S	7.294±0.007	0.214±0.015	21.3±5.3	4.4±0.4	7.264±0.024	0.284±0.059	0.1	4.4
L1521F	6.472±0.001	0.299±0.001	17.9±0.3	4.9±0.1	6.505±0.004	0.268±0.010	2.2±0.4	4.6±0.3
L1400K	3.196±0.002	0.231±0.005	6.5±0.8	4.4±0.5	···	···	···	···
L1400A	3.355±0.002	0.191±0.006	7.7±1.2	4.4±0.6	3.250±0.036	0.175±0.061	0.1	4.4
TMC2	6.193±0.001	0.210±0.002	8.7±0.4	5.1±0.2	6.157±0.006	0.167±0.015	4.5±1.1	5.0±0.3
TMC1	5.856±0.003	0.269±0.007	11.1±1.2	4.6±0.3	5.870±0.040	0.409±0.113	0.1	4.6
TMC1C	5.196±0.003	0.212±0.006	18.4±2.2	4.4±0.5	5.193±0.009	0.132±0.017	0.1	4.4
L1507A	6.163±0.004	0.220±0.009	12.2±2.1	4.4±0.6	6.159±0.030	0.254±0.071	0.1	4.4
CB23	6.015±0.002	0.166±0.006	14.6±2.2	4.4±0.3	5.985±0.027	0.233±0.075	0.1	4.4
L1517B	5.835±0.001	0.215±0.001	8.8±0.2	4.7±0.1	5.796±0.008	0.218±0.017	0.1	4.7
L1512	7.121±0.001	0.174±0.001	7.3±0.4	5.0±0.2	7.091±0.018	0.274±0.076	0.1	4.8
L1544	7.143±0.002	0.315±0.004	12.6±0.7	5.0±0.2	7.181±0.004	0.289±0.008	5.2±0.4	4.8±0.2
L134A	2.665±0.002	0.215±0.007	4.3±1.0	4.4±0.6	···	···	···	···
L183	2.413±0.001	0.211±0.001	20.3±0.2	4.8±0.1	2.459±0.001	0.214±0.002	4.7±0.2	4.9±0.1
OphD	3.478±0.001	0.223±0.001	4.4±0.1	7.1±0.2	3.515±0.001	0.204±0.003	4.3±0.2	5.3±0.2
L158	3.942±0.007	0.229±0.014	0.1	4.8	···	···	···	···
L1689B	3.481±0.005	0.262±0.011	0.1	4.8	3.642±0.058	0.373±0.148	0.1	4.8

Table 2.4—Continued

core	N_2H^+(1–0) V_{LSR} km s^{-1}	ΔV km s^{-1}	τ	T_{EX} K	N_2D^+(2–1) V_{LSR} km s^{-1}	ΔV km s^{-1}	τ	T_{EX} K
L234E-S	3.164±0.003	0.198±0.008	6.9±1.5	4.7±0.5	3.286±0.015	0.182±0.055	0.1	4.7
B68	3.364±0.001	0.176±0.001	26.2±1.0	4.5±0.5	3.372±0.016	0.124±0.036	0.1	4.5
L492	7.701±0.001	0.263±0.001	11.8±0.2	4.8±0.1	7.726±0.008	0.222±0.022	2.6±0.8	4.4±0.3
L328	6.707±0.002	0.438±0.005	8.1±0.5	4.6±0.2	6.797±0.012	0.419±0.028	0.1	4.6
L429	6.719±0.001	0.394±0.001	12.3±0.1	4.9±0.1	6.705±0.002	0.360±0.005	4.3±0.2	4.4±0.1
L694-2	9.574±0.001	0.266±0.001	13.9±0.1	5.2±0.1	9.567±0.002	0.244±0.004	5.5±0.2	4.1±0.1
L1197	-3.147±0.002	0.249±0.006	6.5±0.9	4.5±0.3	-3.020±0.016	0.180±0.093	0.1	4.5
CB246	-0.830±0.001	0.245±0.003	10.3±0.7	4.5±0.2	-0.730±0.025	0.126±0.039	0.1	4.5

Note. — The hyperfine fitting model assumes constant T_{EX} and homogenous abundance and do not consider velocity gradients effects along the line of sight. L1689A and GF5 spectra were not fitted because of poor S/N.

Table 2.5. Results of the hyperfine structure fitting on the N_2H^+(3–2) and N_2D^+(3–2) spectra at the peak position of each core. Only the fits to high S/N (> 5) spectra are reported.

core	N_2H^+(3–2)			N_2D^+(3–2)		
	V_{LSR} km s^{-1}	ΔV km s^{-1}	τ	V_{LSR} km s^{-1}	ΔV km s^{-1}	τ
L1498	7.786±0.015	0.169±0.040	<0.1	···	···	···
L1495	6.811±0.030	0.288±0.052	<0.1	···	···	···
L1521F	6.391±0.010	0.172±0.021	6.2±1.5	6.507±0.006	0.222±0.025	1.2±0.9
L1517B	5.816±0.030	0.219±0.130	<0.2	···	···	···
L1544	7.138±0.018	0.193±0.080	<0.1	7.208±0.012	0.342±0.026	<0.1
L183	2.412±0.012	0.220±0.036	3.5±1.6	2.445±0.003	0.205±0.012	1.2±0.4
OphD	3.466±0.011	0.131±0.019	6.7±2.2	3.503±0.004	0.196±0.013	2.6±0.6
B68	3.370±0.017	0.231±0.022	0.8±0.4	···	···	···
L429	6.673±0.029	0.373±0.037	2.7±0.4	6.696±0.009	0.262±0.020	5.2±0.9
L694-2	9.532±0.014	0.308±0.060	1.7±1.4	9.560±0.005	0.242±0.016	1.5±0.5

Table 2.6. Integrated intensities and results of the gaussian fitting of the $C^{18}O$(1–0) and (2–1) spectra towards the peak position for the four cores newly observed.

core	$C^{18}O$(1–0)			$C^{18}O$(2–1)		
	I($C^{18}O$(1–0)) K km s^{-1}	V_{LSR} km s^{-1}	ΔV km s^{-1}	I($C^{18}O$(2–1)) K km s^{-1}	V_{LSR} km s^{-1}	ΔV km s^{-1}
L1521F	1.80±0.06	6.458±0.006	0.438±0.014	1.80±0.15	6.427±0.015	0.447±0.034
TMC2	1.05±0.04	6.313±0.007	0.401±0.014	1.09±0.07	6.229±0.010	0.392±0.023
L183	1.89±0.04	2.518±0.006	0.545±0.016	2.14±0.06	2.556±0.008	0.579±0.019
L492	0.76±0.04	7.786±0.017	0.651±0.042	0.58±0.05	7.786±0.022	0.529±0.055
L694-2	1.21±0.04	9.574±0.007	0.433±0.015	1.01±0.04	9.574±0.006	0.415±0.015

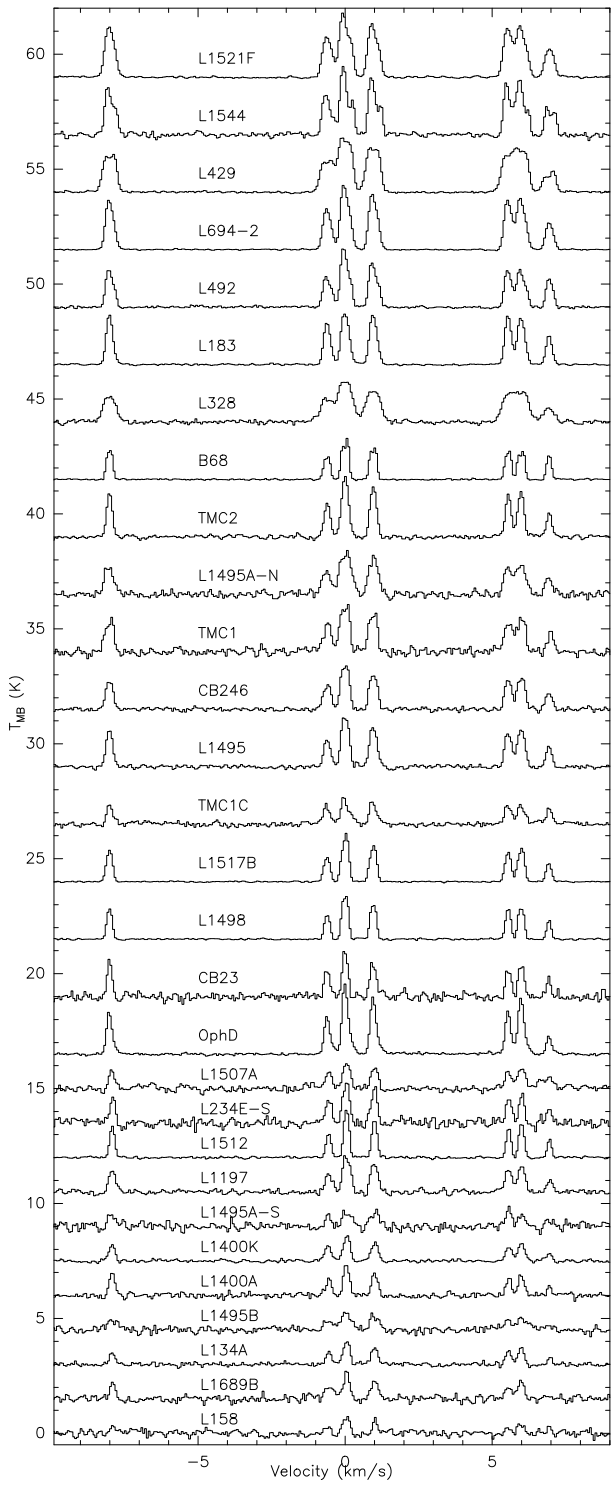

Figure 2.1 N_2H^+(1–0) spectra at peak sorted by decreasing N_2H^+ column density. The two sources with no detection (L1689A and GF5) were omitted.

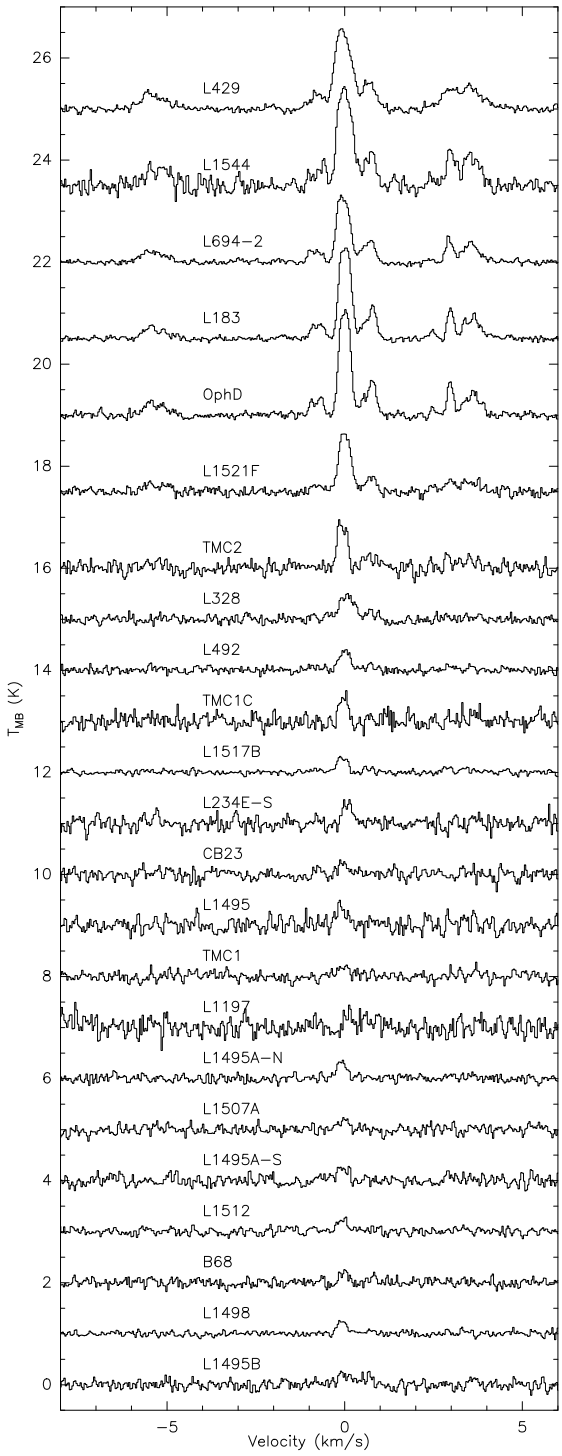

Figure 2.2 N_2D^+(2–1) spectra at peak sorted by decreasing N_2D^+ column density. Eight sources with marginal or no detection were omitted (L1400K, L1400A, L134A, L1689A, L1689B, L158, GF5, CB246).

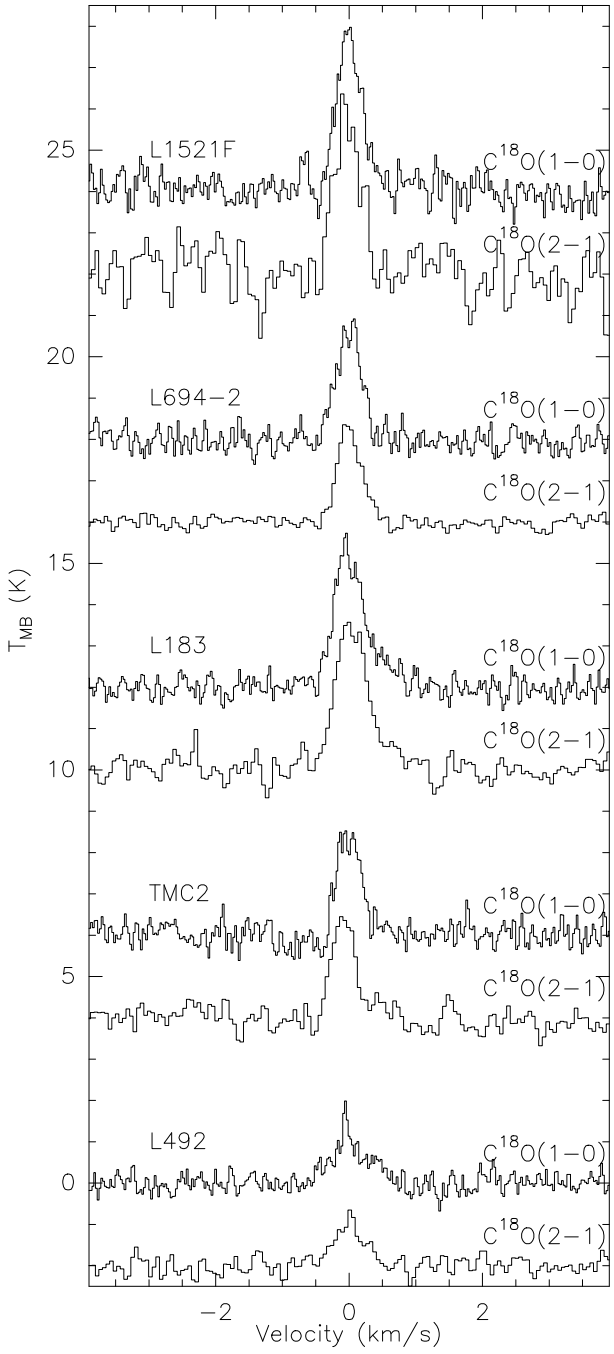

Figure 2.3 $C^{18}O$(1–0) and (2–1) spectra towards L1521F, L694-2, L183, TMC2 and L492. The shown spectra are the arithmetic means of all the observations in the 10″ strip centered around the peak position and going parallel to the Right Ascension direction.

the line of sight and does not consider variations in velocity and line width. To crudely estimate the variations on the more complex spectra, we derived the opacity of the N_2H^+(1–0) spectra in B68 and L1544 by the fit of only a couple of hyperfines and repeating that for all of the different couples. In this way, we found a scatter of a factor of 2 in the resulting opacities around the value derived by the simultaneous fit of all seven components. The results of the hyperfine structure fitting of the high-S/N (> 5) 1mm spectra are reported in Table 2.5. We also show in Figure 2.3 the $C^{18}O$(1–0) and (2–1) spectra towards the peak of L1521F, L694-2, L183, TMC2 and L492. Integrated intensities and results of the Gaussian fits for these observations are reported in Table 2.6.

2.3.2 Maps

Figures 2.4 to 2.9 show maps towards L183, OphD, L429, TMC2, L492 and L694-2, which, together with L1544 and L1521F, stand out from the rest of the sample as having very bright N_2D^+(2–1) lines. Similar maps for L1544 can be found in Caselli et al. (2002a) and Tafalla et al. (2002) and for L1521F in Chapter 3. The N_2H^+ and N_2D^+ data shown in Figures 2.4-2.7 were all convolved with a $26''$ beam in order to reach the same spatial resolution as the N_2H^+(1–0) data and make the comparison easier. The N_2H^+(1–0) map of TMC2 (Figure 2.9) was kept with the original FCRAO resolution ($54''$), while we have not smoothed the N_2D^+(2–1) map of L492 (Figure 2.8) because of the small extension of it. Similarly, all the 1.2-mm maps were smoothed to a $22''$ resolution, the beamsize of the IRAM 30-m at the $C^{18}O$(1–0) frequencies.

The most evident feature of Figures 2.4 to 2.9 is that the $C^{18}O$ does not trace the dust continuum while the N_2H^+ and N_2D^+ emission morphology is similar to that of the dust, as already shown by several authors (e.g. Caselli et al. 1999; Bergin et al. 2001; Tafalla et al. 2002) . While this is true for L1544, L1521F, L429, L694-2 and OphD, there are differences between the 1.2-mm map and the N_2H^+–N_2D^+ maps for L183 and TMC2. For example, the L183 dust emission peaks $30''$ to the south of N_2H^+(1–0) and, especially, N_2D^+(2–1).

TMC2 shows an even more complex situation; in fact, the 1.2-mm maps revealed much more structure than the N_2H^+(1–0) map of Caselli, Benson, Myers & Tafalla (2002) led us to believe. Whereas we found a local 1.2-mm peak next to the N_2H^+(1–0) one, we also found brighter peaks of the dust emission in regions where the N_2H^+(1–0) is fainter. Note that the N_2H^+ map in Figure 2.9 has a lower angular resolution (HPBW = $54''$) than in the other sources; smoothing the dust continuum map to this resolution does not help to

Table 2.7. N_2H^+, N_2D^+ and 1.2-mm maps full width at half maximum.

core	1.2mm	N_2H^+(1–0)	N_2H^+(3–2)	N_2D^+(2–1)	N_2D^+(3–2)
L183	$185'' \times 67''$	$217'' \times 92''$	···	$93'' \times 72''$	···
OphD	$129'' \times 70''$	$170'' \times 70''$	···	$93'' \times 62''$	$67'' \times 65''$
L492	$180'' \times 100''$	$98'' \times 78''$	···	···	···
L429	$102'' \times 53''$	$91'' \times 78''$	$72'' \times 53''$	$60'' \times 56''$	$43'' \times 41''$
L694-2	$77'' \times 55''$	$85'' \times 67''$	···	$68'' \times 60''$	···

reconcile the two emissions, so we present here the 1.2-mm map with the same resolution as in the other cores (i.e. $22''$). We also add in Figure 2.9 the position of a few radio stars and of a couple of *IRAS* point sources; the presence of these objects could explain the discrepancy between the N_2H^+ and the dust maps.

Another common feature clearly seen throughout Figures 2.4 to 2.9 is that the N_2D^+ maps are systematically smaller than the N_2H^+ ones (see Table 2.7). This could indicate that the deuterated species are better tracers of the core nucleus. Similar behaviour is seen when the higher transition maps are compared with those at lower J; this may be caused by the increase in density towards map center.

In OphD (see Figure 2.6), we note the presence of two nuclei embedded in the same envelope; both have a similar brightness in the 1.2-mm continuum although they have a very different intensity in the N_2H^+(1–0), N_2D^+(2–1) and N_2D^+(3–2) (the N_2H^+(3–2) has poor S/N towards the northeast core). The relative intensity of the two nuclei decreases going from the lowest density tracer (N_2H^+(1–0)) to the highest density one (N_2D^+(3–2)), suggesting that the southwest core is more centrally peaked than the northeast one.

2.3.3 Core shapes and kinematics

We underline a marked tendency of the starless cores for having the dust emission peak shifted relative to the centroid of the cores, suggesting that the cores either have been compressed by external agents or have moved relatively to the surrounding environment (but see Walsh, Myers & Burton 2004). In Figure 2.10 we attempt a classification of the shape of the starless cores evaluating a parameter able to quantify the degree of "cometariness" or how much the dust peak is shifted relative to the lower contours of the map. We evaluated the centroid of the map as the mean position of the points within the 50% contour

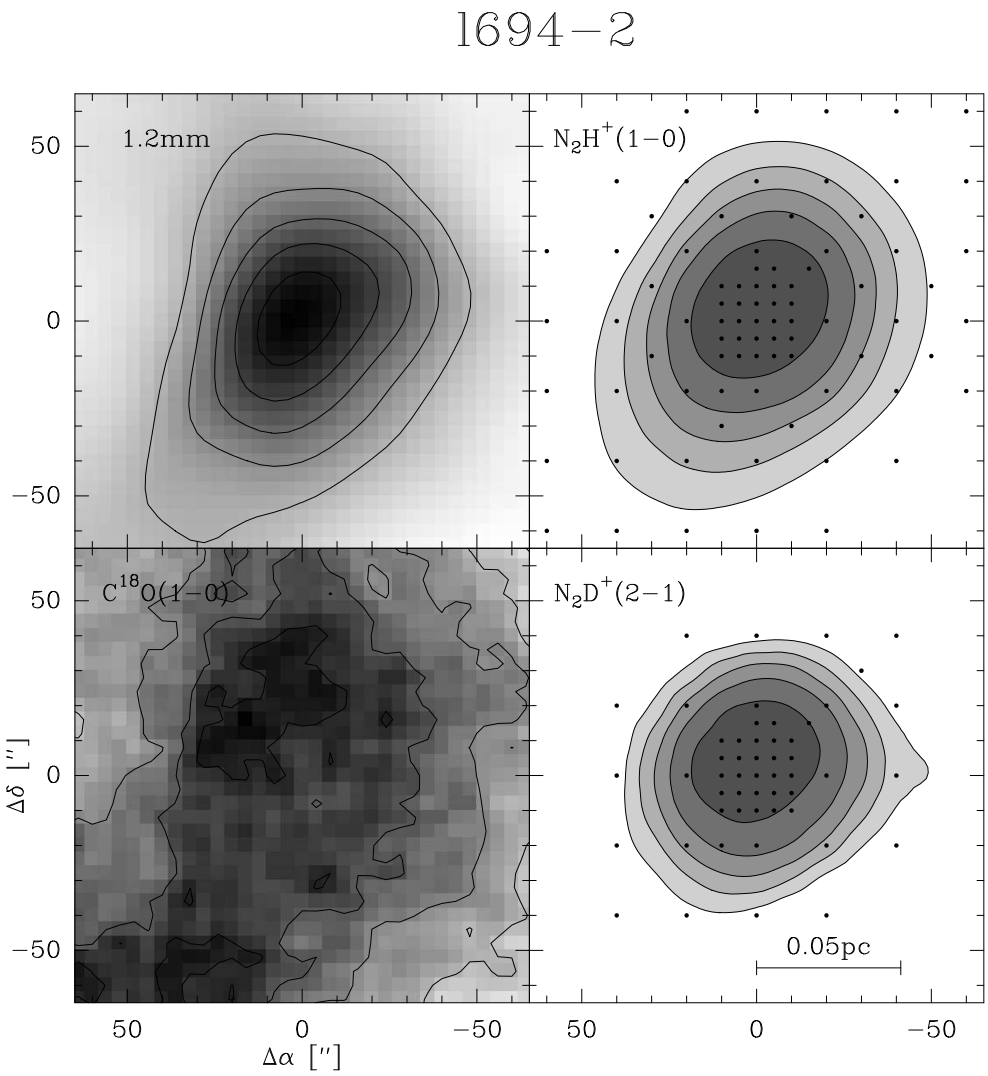

Figure 2.4 L694-2 maps in 1.2-mm continuum, $C^{18}O$(1–0), N_2H^+(1–0) and N_2D^+(2–1) . N_2H^+ and N_2D^+ data were smoothed to a common resolution of 26″ and regridded; the reference position is the one reported in Table 2.1. The 1.2-mm map (M. Tafalla et al. 2005, in preparation) was smoothed to a resolution of 22″. Contour levels are 30% to 90% by 15% of the peak for each map. Peak values are 185 mJy/22″ beam for the 1.2-mm map and 5.16, 1.26 and 1.76 K km s^{-1} for N_2H^+(1–0), N_2D^+(2–1) and $C^{18}O$(1–0) respectively. Available 40″×40″ maps of N_2H^+ and N_2D^+(3–2) are not reported because of poor S/N outside the peak.

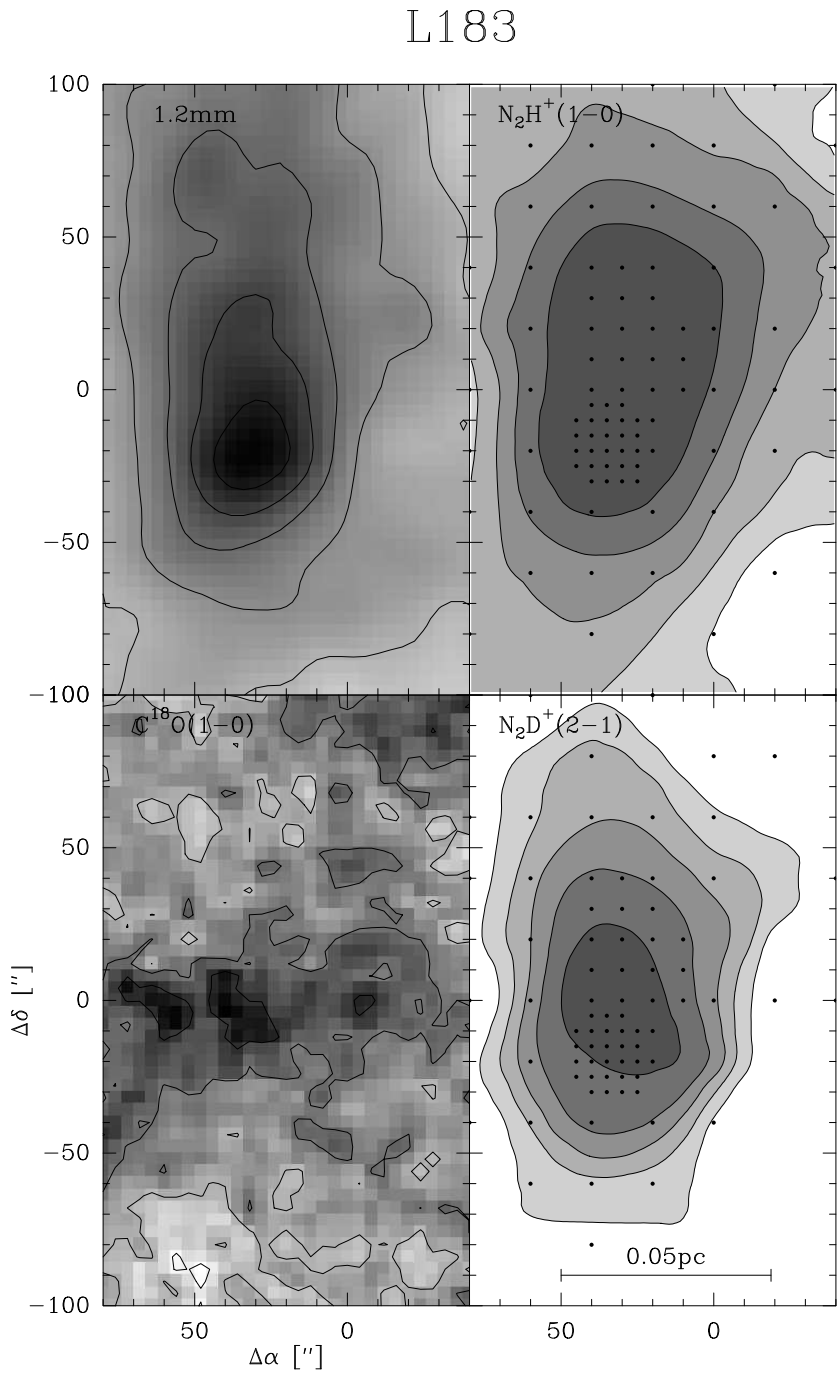

Figure 2.5 L183 maps in 1.2-mm continuum, $C^{18}O$(1–0), N_2H^+(1–0) and N_2D^+(2–1). Same as in Figure 2.4 but for the peak values: here 239 mJy/22″ beam for the 1.2-mm map and 4.31, 1.65, and 2.5 K km s^{-1} for N_2H^+(1–0), N_2D^+(2–1) and $C^{18}O$(1–0) respectively. The 1.2-mm map has been taken from Pagani et al. (2003). Available 30″×60″ maps of $N_2H^+$and N_2D^+(3–2) are not reported because of poor S/N outside the peak.

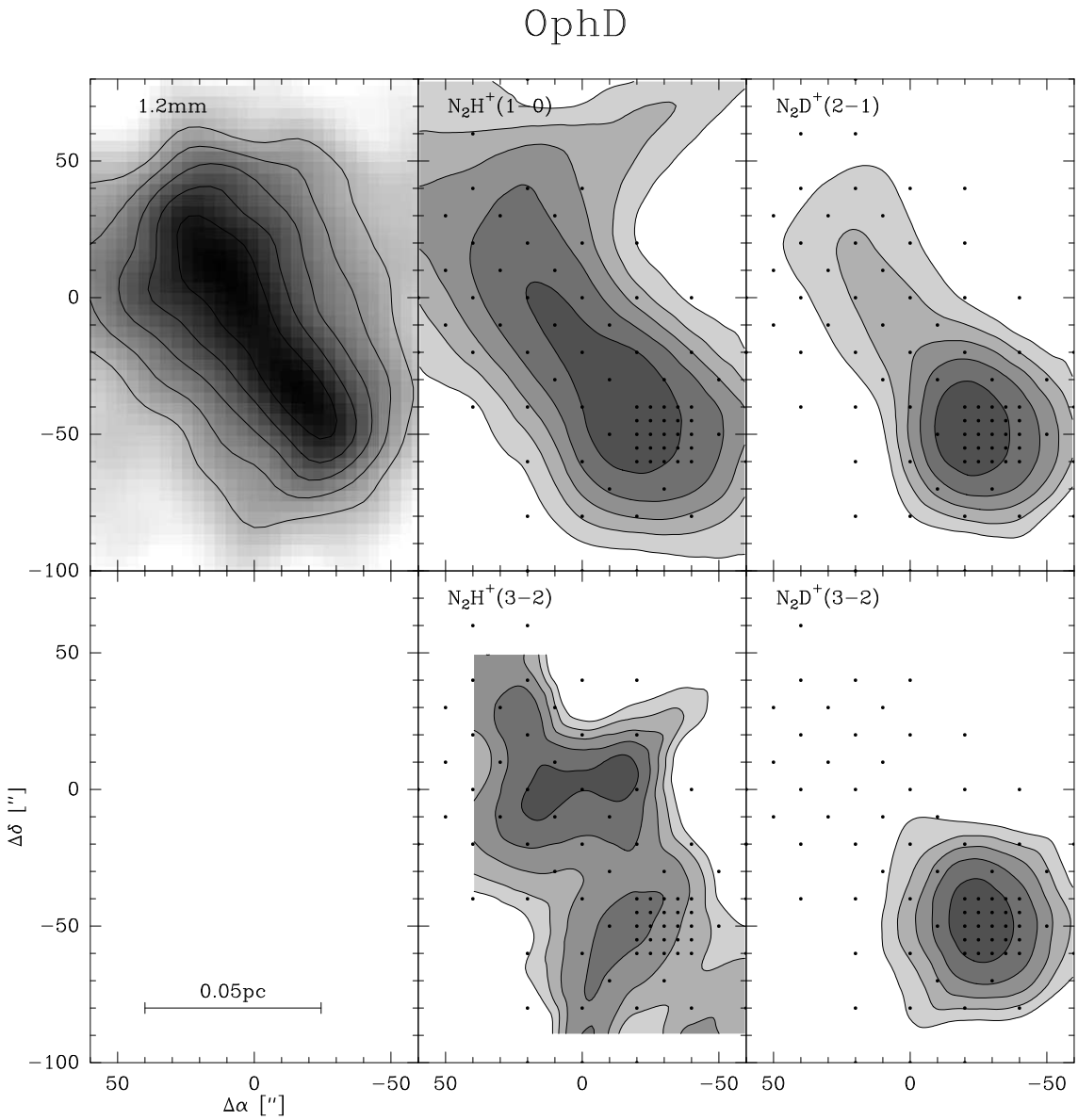

Figure 2.6 OphD maps in 1.2-mm continuum, N_2H^+(1–0) and (3–2) and N_2D^+(2–1) and (3–2). Same as in Figure 2.4 but for the peak values: here 195 mJy/22″ beam for the 1.2-mm map and 3.81, 0.49, 1.75 and 0.60 K km s^{-1} for N_2H^+(1–0) and (3–2), N_2D^+(2–1) and (3–2) respectively. The 1.2-mm map has been taken from Ward-Thompson, Motte & André (1999). The RMS of the N_2H^+(3–2) increases significantly towards north east, thus contours above -20″ have to be taken with caution.

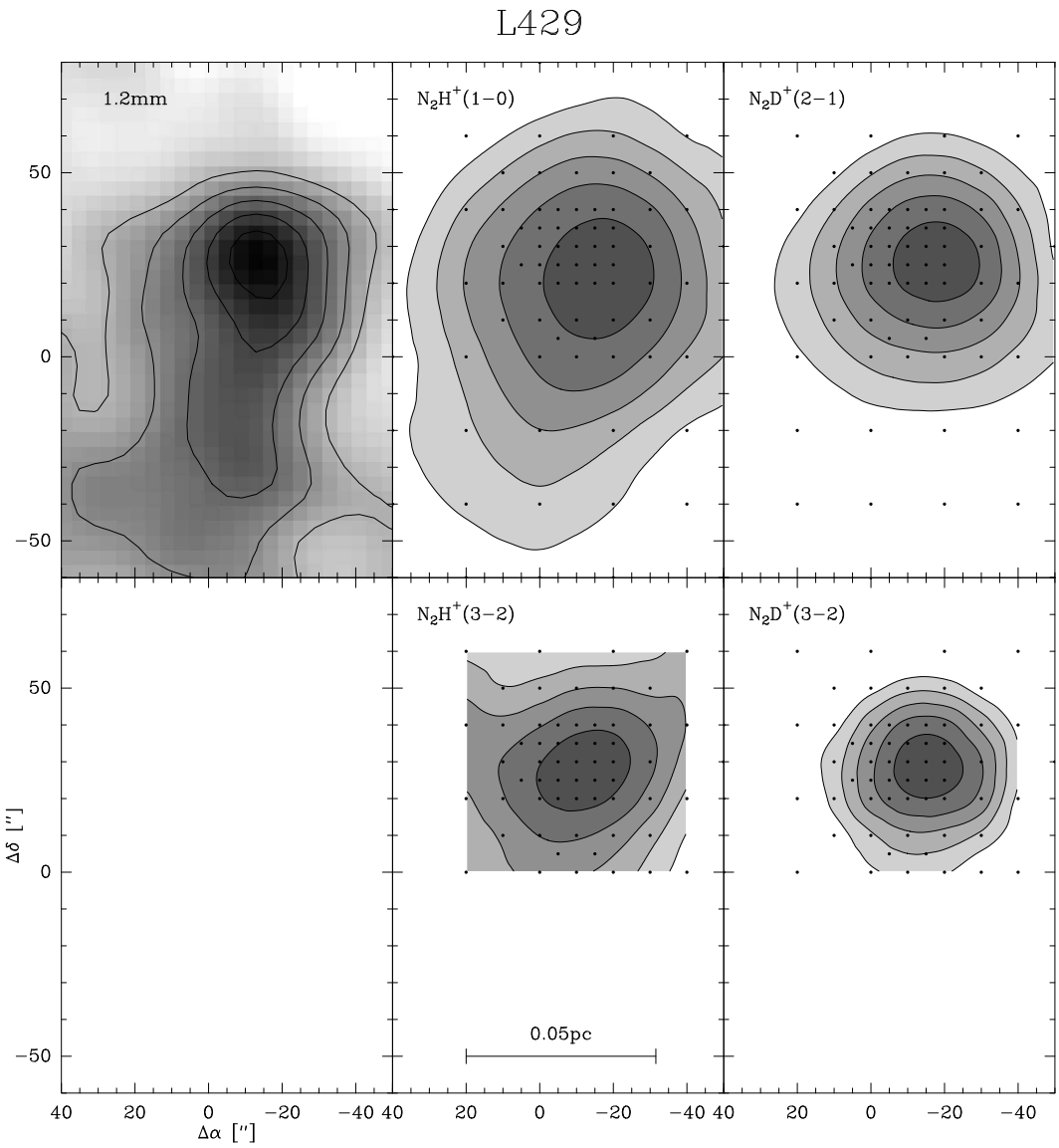

Figure 2.7 L429 maps in 1.2-mm continuum, N_2H^+(1–0) and (3–2) and N_2D^+(2–1) and (3–2). Same as in Figure 2.4 but for the peak values: here 210 mJy/22″ beam for the 1.2-mm map and 6.12, 0.63, 2.07and 0.69 K km s^{-1} for N_2H^+(1–0) and (3–2), N_2D^+(2–1) and (3–2) respectively. The 1.2-mm map has been taken from Bacmann et al. (2000).

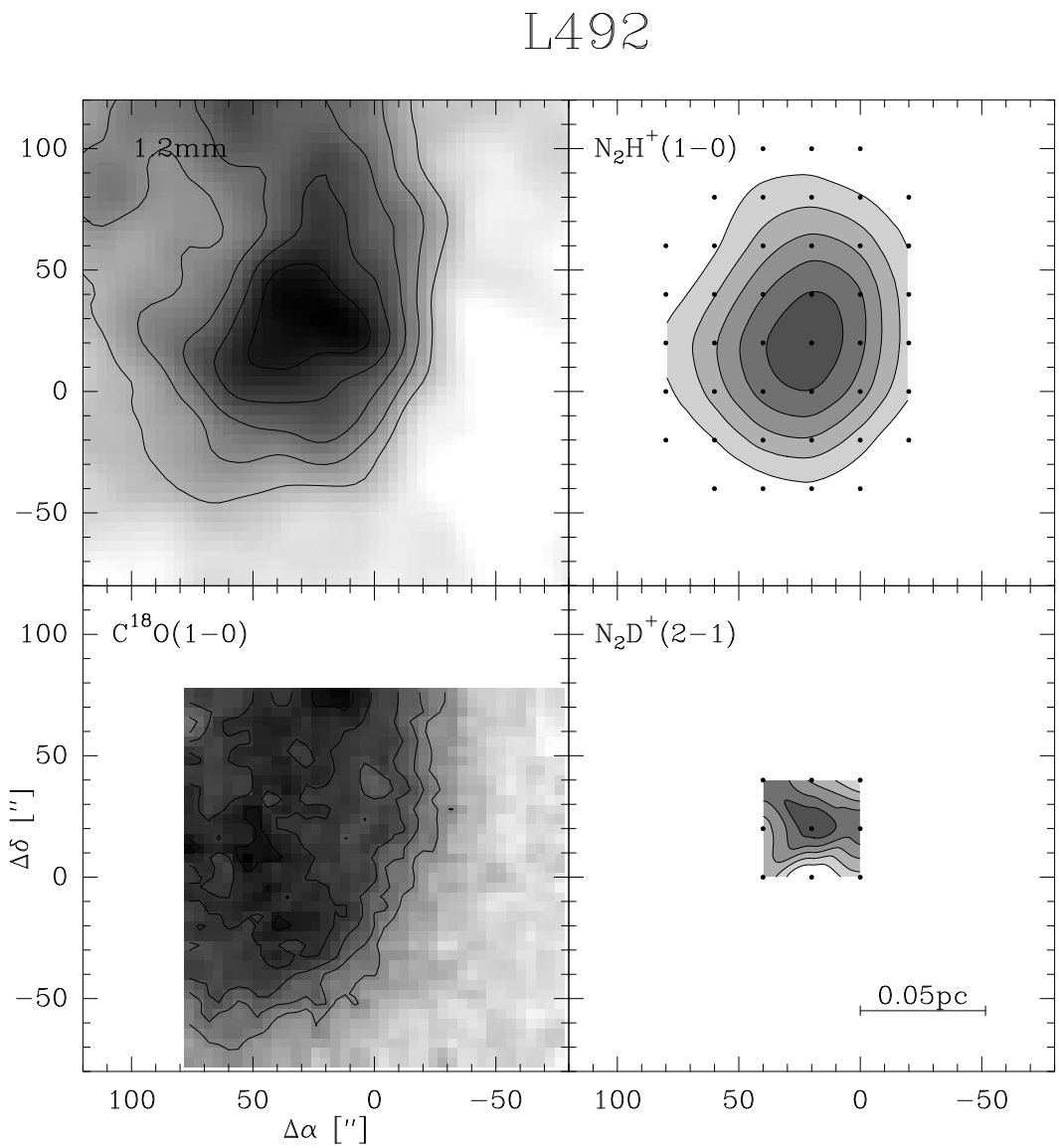

Figure 2.8 L492 maps in 1.2-mm continuum, $C^{18}O$(1–0), N_2H^+(1–0) and N_2D^+(2–1). Same as in Figure 2.4 but for the peak values: here 114 mJy/22″ beam for the 1.2-mm map and 3.96, 0.31 and 1.69 K km s^{-1} for N_2H^+(1–0), N_2D^+(2–1) and $C^{18}O$(1–0) respectively.

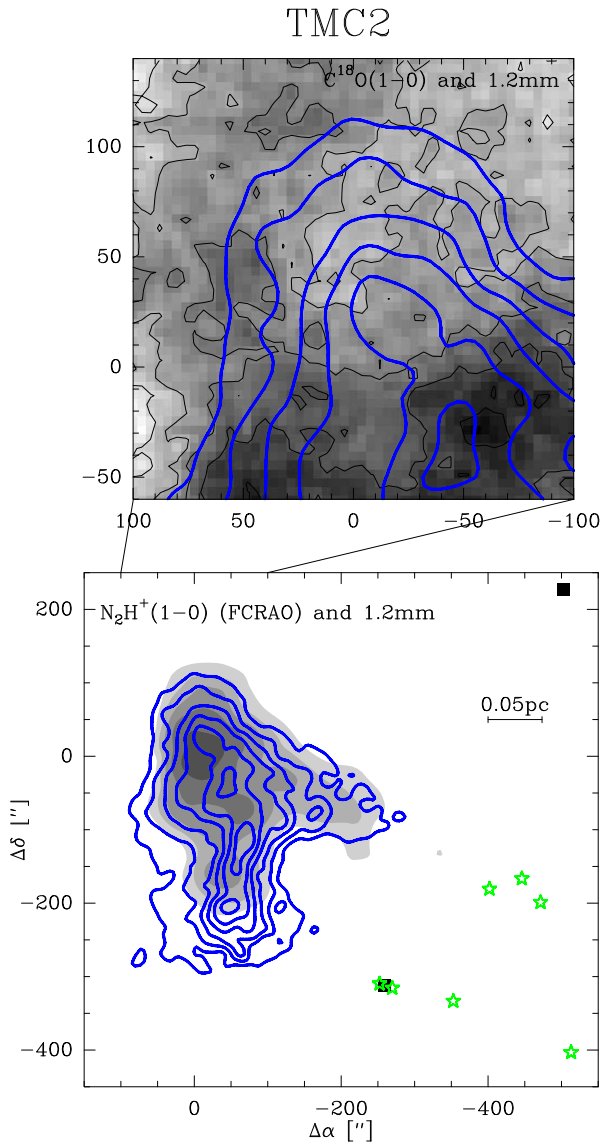

Figure 2.9 TMC2 maps in 1.2-mm emission smoothed to 22″ (contours in both panels) and $C^{18}O$(1–0) (gray scale in the top panel) from new 30m observations and the N_2H^+(1–0) map (gray scale in the bottom panel) taken by Caselli, Benson, Myers & Tafalla (2002) with FCRAO (HPBW 54″; reference position here is the same as in Table 2.1). Contour levels starts from 30% of peak and increase by 15% of it. Peak values are: 138 mJy/22″ beam for the 1.2-mm map, 2.12 K km s^{-1} for the $C^{18}O$ observations. The N_2H^+(1–0) intensity peak is 3.6 K km s^{-1} in T_{MB} temperature. In the bottom panel the positions of seven young stars (in order of ascending RA: JH93, JH90, JH91, JH92, JH94 - Wendker 1995 ; FY Tau, FZ Tau - Nurmanova 1983) are denoted by stars. Two *IRAS* point sources visible in the same field are denoted by a filled square.

Table 2.8. Global and local velocity gradients from N_2H^+(1–0) maps.

core	$\mathcal{G}$ km s^{-1} pc^{-1}	Θ^a $^\circ$	$< \mathcal{G}_l >^b$ km s^{-1} pc^{-1}
L183	1.4±0.1	-49±1	1.5±0.7
OphD	1.6±0.1	-119±1	1.6±1.0
L694-2	0.7±0.1	-18±1	0.8±0.3
L429	0.4±0.1	-33±2	1.9±1.1
L492	0.2±0.1	83±2	1.5±0.8

[a]Direction of increasing velocity, measured East of North.

[b]Mean values of the magnitude of local gradients and corresponding standard error.

and defined the degree of "cometariness" as the distance between this and the dust peak in units of r_{70}, the equivalent radius of the core. OphD and TMC2 were not included in this classification since they harbour multiple peaks within their 50% contour (see Figures 2.6 and 2.9); thus, the "cometariness" parameter is meaningless. From this small subsample we do not notice any clear correspondence between a more marked cometary shape and other kinematical properties of the core (e.g. H_2 density, N_2H^+(1–0) line-width, or r_{70}).

Using the N_2H^+(1–0) velocities from the hyperfine structure fitting, we found strong velocity variations in L183 (0.23 km s^{-1} in a 0.16 pc length) and OphD (0.19 km s^{-1}in a 0.12 pc length), while a smaller variation (0.07 km s^{-1} in a 0.1 pc length) was found in L694-2 and constant velocity fields were seen in the inner 0.08 pc of L429 and L492. We evaluated the total velocity gradients of these cores under the assumption of solid body rotation (see Goodman, Benson, Fuller & Myers 1993). The magnitudes and the direction of the velocity gradients are reported in columns (1) and (2) of Table 2.8. These calculations agree with the velocity variations seen across the cores.
Local velocity gradients, evaluated in 3×3 adjacent points, were also calculated towards these cores (see Caselli et al. 2002a, for details on the procedure). The analysis was performed on regridded data and results are shown in Figure 2.11 and Table 2.8. L183 and OphD present strong motions and a regular velocity field. L429 and L492 show very

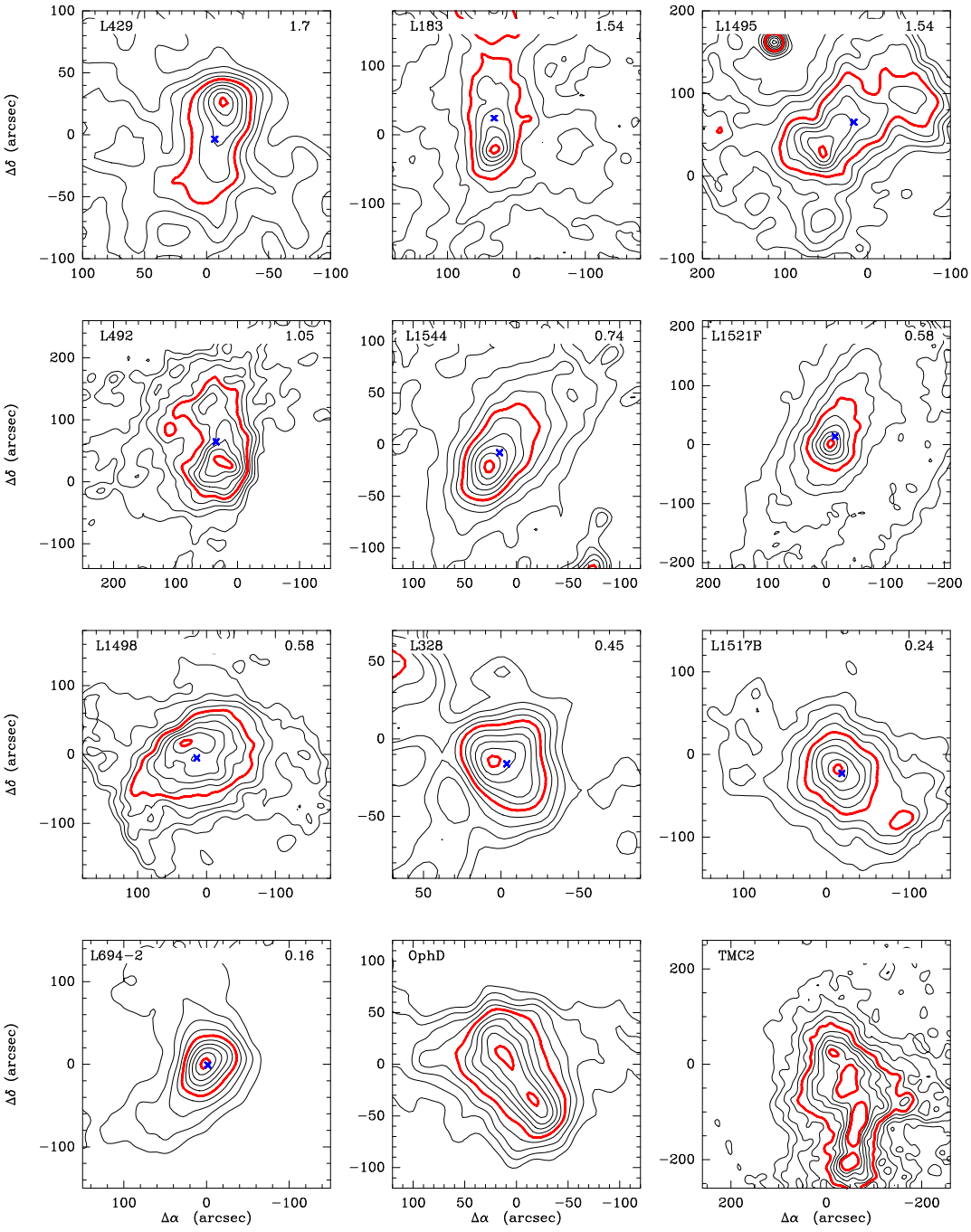

Figure 2.10 The 1.2-mm continuum maps of 12 cores in our sample. Light contours are spaced from 10% to 90% by 10% of the peak, while the 98% and 50% contours are represented by a thick line. The cross marks the mean position of the points within the 50% contour. The cores are ranked for increasing "cometariness". This parameter is reported at the top right corner of each map and is calculated as the distance between the mean point and peak in units of r_{70}. TMC2 and OphD were not included in this classification since they have multiple peaks within their 50% contour, so this technique failed for them.

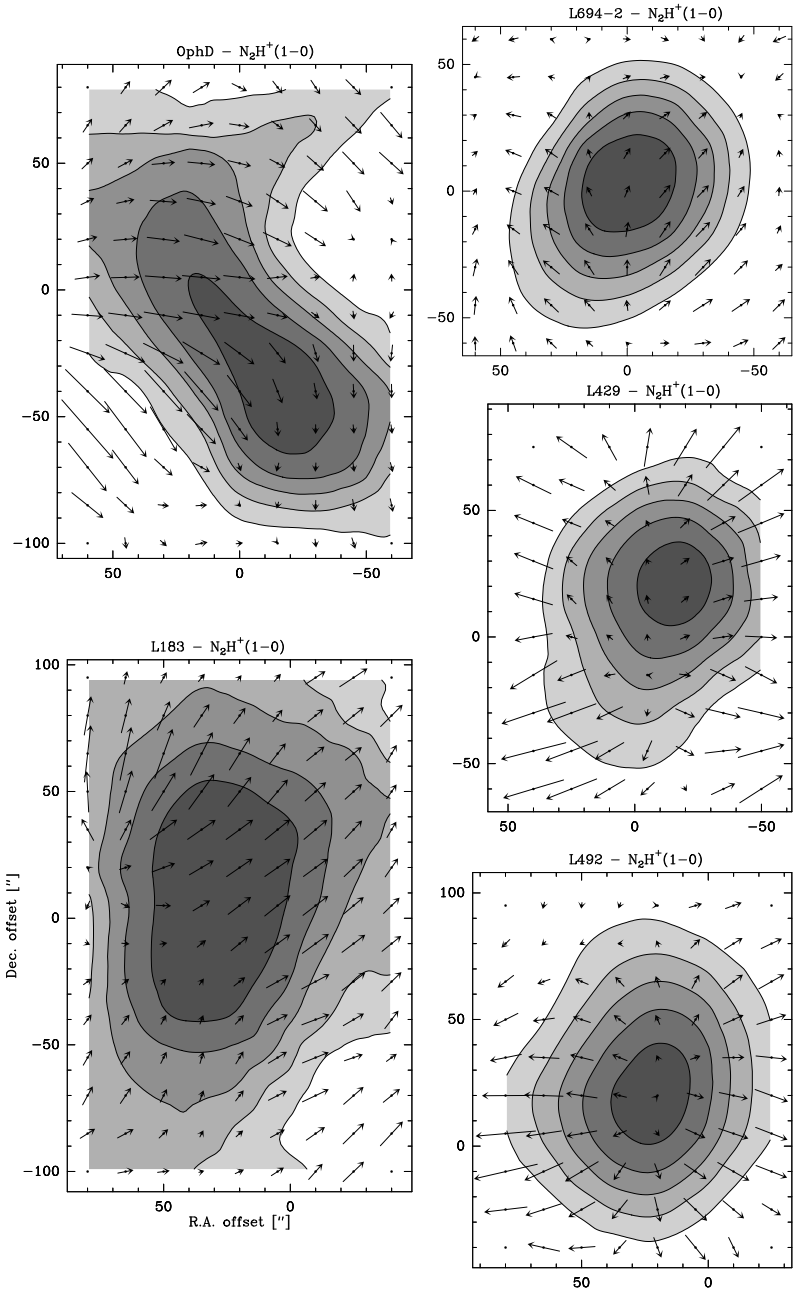

Figure 2.11 N_2H^+(1–0) velocity gradients towards the cores L694-2, OphD, L183, L429 and L492. The N_2H^+(1–0) data were regridded in a regular pattern. The integrated intensity maps are shown in greyscale (see Figures 2.4 - 2.8). Local velocity gradients in the adjacent nine points are represented by an arrow pointing in the direction of increasing velocity and with the length proportional to the magnitude (1 km s^{-1} pc^{-1} corresponds to a $6''$-long arrow). Note that the angular scale of each map is the same.

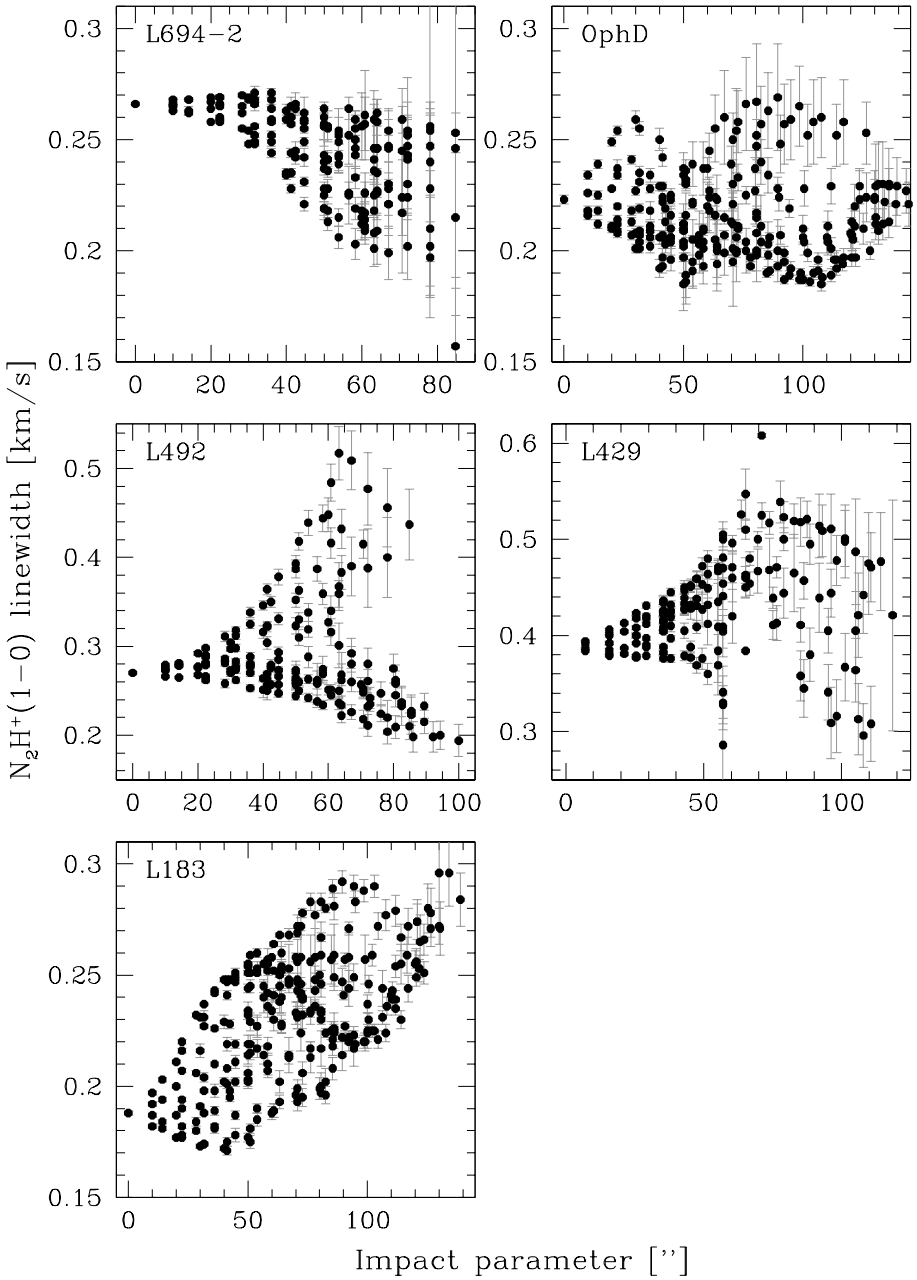

Figure 2.12 N_2H^+(1–0) intrinsic line width gradients within the cores L694-2, OphD, L183, L429 and L492. The angular offset was evaluated from the N_2D^+(2–1) peak position (see Table 2.3).

little motion in the inner parts but larger gradients at the edge of the map with arrows pointing in different directions on different sides of the cores, explaining the absence of velocity variation in the inner part and the small total velocity gradient. Finally, L694-2 shows the smallest local gradients with a regular velocity field only in the inner part.

Using the N_2H^+(1–0) and N_2D^+(2–1) maps, we also checked for the presence of line width gradients in L694-2, OphD, L183, L429 and L492 in the same fashion as for L1544 (Caselli et al. 2002a), B68 (Lada, Bergin, Alves & Huard 2003) and L1521F (Chapter 3). From figure 2.12 we find that only L694-2 shows the line width decrease that was evidenced in L1521F and L1544, while a marginal similarity is found in the first $50''$ around OphD and in the northern part of L492. The opposite behaviour is seen in L429 and L183 (as found in B68). The N_2D^+(2–1) line widths evidenced the same behaviour as in figure 2.12.

In the rest of the chapter we concentrate on the physical and chemical parameters at the relative peak of the whole source sample.

2.4 Analysis

In this section we derive the physical and chemical properties that can best discriminate the evolutionary status of a starless core, either in a chemical sense, as a more pronounced deuterium enrichment and a higher CO depletion factor, or for dynamical reasons, like the presence of a denser and more centrally concentrated H_2 distribution or broader N_2H^+ line widths. We expect to characterize through these parameters the pre–stellar cores, i.e., the subset of starless cores that present enhanced chemical evolution and/or dynamical activity.

2.4.1 Column densities of N_2H^+ and N_2D^+ and the deuterium fractionation

The deuterium fractionation can be evaluated from observations of a hydrogen bearing molecule and one of its deuterated counterparts by calculating the ratio of their column densities. Recent work has made use of HCO^+, H_2CO, HNC, N_2H^+ and NH_3, as well as their single or multiple deuterated isotopologues, to evaluate this parameter in starless cores (Caselli, Walmsley, Terzieva & Herbst 1998; Roueff et al. 2000; Tiné et al. 2000;

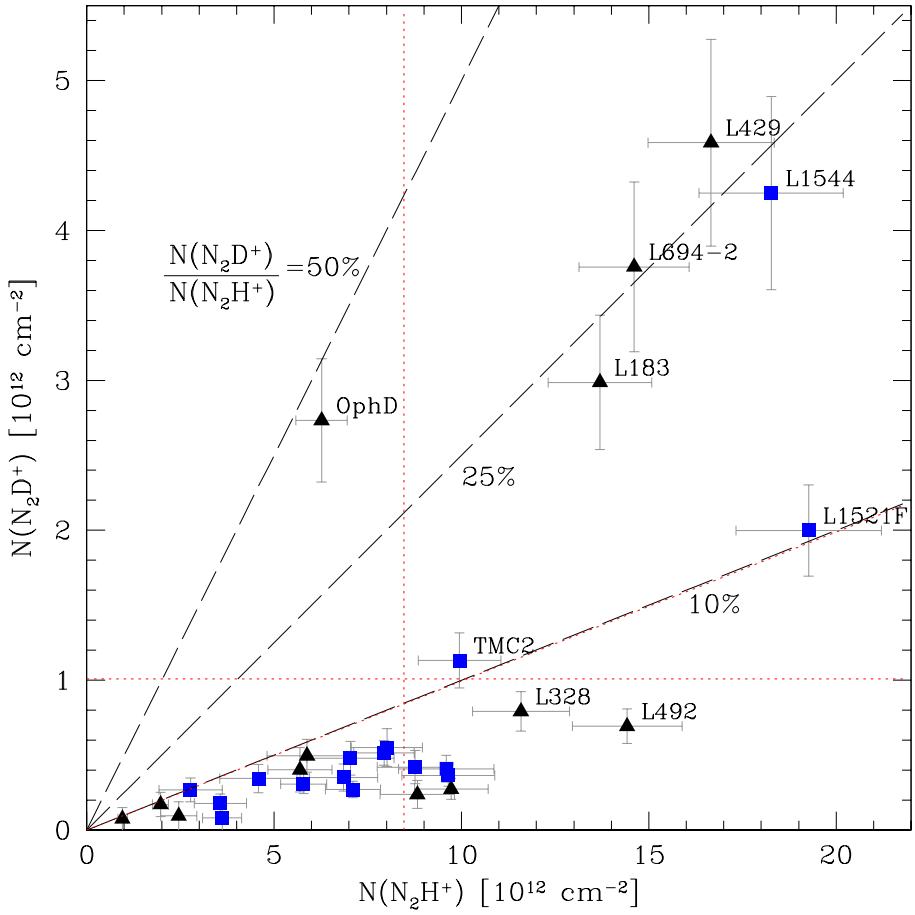

Figure 2.13 N_2H^+ column density vs. N_2D^+ column density at N_2D^+ peak position. Deuterium fractionation can be read from the radial dashed lines (corresponding to $N(N_2D^+)/N(N_2H^+)$ of 0.1, 0.25 and 0.5). Dotted lines are the arithmetic means of the distributions. Cores belonging to the Taurus Molecular Cloud are marked by a square.

Bacmann et al. 2003; Caselli et al. 2002b; Hirota, Ikeda & Yamamoto 2003; Chapter 3). One should note, however, given the depletion of HCO^+ and H_2CO in the core nucleus (Caselli et al. 2002b; Carey et al. 1998), that the deuterium fractionation estimated from this species is relative to an outer shell and not to the high-density nucleus.

In this work we derived N_2H^+ and N_2D^+ column densities assuming a constant excitation temperature (the CTEX method: see the appendix of Caselli et al. 2002b). The excitation temperature of N_2H^+(1–0) was derived from hyperfine fitting of the spectra with well constrained opacities ($\tau/\sigma_\tau > 3$, where the total optical depth τ and its associat-

ed error σ_τ have been derived assuming a constant excitation temperature for the hyperfine components; see also Table 2.4); otherwise the spectrum was assumed optically thin and the excitation temperature was set to 4.8 K (the average excitation temperature in our sample). The excitation temperature of N_2D^+(2–1) was set equal to that of N_2H^+(1–0) in those cases in which the opacity was not well constrained. The effect of underestimating the N_2D^+(2–1) excitation temperature by, e.g., 1 K would be a decrease of $N(N_2D^+)$ by 30%.

As noted above, in the case of N_2H^+, the optically thin assumption is often incorrect and hence we have used the intensity of the ($F_1\,F = 1\,0 \rightarrow 1\,1$) (weak) component normalized appropriately in order to estimate the J=0 column density.

The final result can be seen in Figure 2.13, where the N_2H^+ column density is plotted versus the N_2D^+ column density. The estimated $N(N_2D^+)/N(N_2H^+)$ ratio varies between 0.44 in Oph D and an upper limit of 0.02 in L1400K. It is noticeable that with the exception of OphD, all cores with $N(N_2D^+)/N(N_2H^+)$ ratio above 0.10 have N_2H^+ column densities above 10^{13} cm^{-2}, whereas cores with $N(N_2D^+)/N(N_2H^+)$ lower than 0.10 have $N(N_2H^+)$ lower than 10^{13} cm^{-2} (with a few exceptions). Thus, the impression from Figure 2.13 is that there is a trend in the sense that the $N(N_2D^+)/N(N_2H^+)$ ratio correlates positively with N_2H^+ column density. Table 2.9 summarize the above numbers.

We also determined the N_2H^+ and N_2D^+ column densities in the Large Velocity Gradient (LVG) approximation in those cores with high-S/N N_2H^+ and N_2D^+(3–2) spectra (see Section 2.4.4). Results are shown in Table 2.11. The LVG column density determinations are found to agree with the CTEX values with a dispersion of 30%.

2.4.2 The integrated CO depletion factor

The CO integrated depletion factor is the ratio of the CO canonical abundance ([CO]/[H_2]$\equiv 9.5 \times 10^{-5}$, Frerking, Langer & Wilson 1982) and the CO observed abundance. The CO observed abundance integrated along the line of sight can be calculated from the ratio of the CO column density and the H_2 column density. $C^{18}O$ is measured to be optically thin in some of the cores (L1521F, L183, L694-2, TMC2, L492) where $C^{17}O$ observations are available. Optical depth was derived from the integrated intensity ratio of the two isotopologues assuming equal excitation temperature and the local interstellar medium relative abundance value (3.2, Wilson & Rood 1994). The maximum optical depth was measured to be 0.8 towards L1521F. Thus, for practical purposes, we assumed $C^{18}O$ optically thin in all the cores. To derive N(CO), we used the CTEX approximation on the $C^{18}O$ lines. As

Table 2.9. N_2H^+ and N_2D^+ column densities and relative ratio towards the N_2D^+(2–1) integrated intensity peak.

core	$N(N_2H^+)$ 10^{12} cm^{-2}	$N(N_2D^+)$ 10^{11} cm^{-2}	$N(N_2D^+)/N(N_2H^+)$
L1498	7.1±0.7	2.7±0.6	0.04±0.01
L1495	8.8±1.0	4.2±1.1	0.05±0.01
L1495B	2.8±0.8	2.7±0.8	0.10±0.04
L1495A-N	9.6±1.2	3.6±0.7	0.04±0.01
L1495A-S	4.6±1.0	3.4±1.0	0.08±0.03
L1521F	19.3±1.9	20.0±3.0	0.10±0.02
L1400K	3.6±0.5	<0.8	<0.02
L1400A	3.6±0.7	1.8±0.6	0.05±0.02
TMC2	9.9±1.1	11.3±1.8	0.11±0.02
TMC1	9.6±1.3	4.1±0.9	0.04±0.01
TMC1C	8.0±0.9	5.5±1.3	0.07±0.02
L1507A	6.9±0.9	3.5±0.9	0.05±0.01
CB23	7.0±1.2	4.8±1.1	0.07±0.02
L1517B	7.9±0.8	5.1±0.8	0.06±0.01
L1512	5.8±0.6	3.1±0.6	0.05±0.01
L1544[a]	18.3±1.9	42.5±6.4	0.23±0.04
L134A	2.5±0.5	<0.9	<0.04
L183	13.7±1.4	29.9±4.5	0.22±0.04
OphD	6.3±0.7	27.3±4.1	0.44±0.08
L158	1.0±0.1	<0.7	<0.08
L1689B	2.0±0.2	1.7±0.8	0.09±0.04
L234E-S	5.9±1.1	5.0±1.1	0.08±0.02
B68	9.7±1.0	2.7±0.7	0.03±0.01
L492	14.4±1.5	6.9±1.1	0.05±0.01
L328	11.6±1.3	7.9±1.3	0.07±0.01
L429	16.7±1.7	45.9±6.9	0.28±0.05
L694-2	14.6±1.5	37.6±5.7	0.26±0.05
L1197	5.7±0.9	4.0±1.5	0.07±0.03
CB246	8.8±1.0	2.4±0.9	0.03±0.01

[a]The difference in the L1544 $N(N_2D^+)/N(N_2H^+)$ given by Caselli et al. (2002b) (0.26) and here (0.23) is due to the different approximation used. They evaluated the column density from all the seven hyperfine components correcting for the high optical depth (see their eq. A1) while here we used the optically thin approximation applied on the weakest component only.

already shown in Caselli et al. (2002b) and Chapter 3, this approach reduces the evaluation of the integrated CO depletion factor to the simple formula $f_D = 0.085 \cdot \mathcal{F}_{1.2mm}/W_{C^{18}O}$, where $\mathcal{F}_{1.2mm}$ is the 1.2-mm observed brightness in mJy beam^{-1} and $W_{C^{18}O}$ is the $C^{18}O$ integrated intensity in K km s^{-1}.

The sources of uncertainties in this technique are several, and it is important to keep them in mind in the analysis of the results. First, the "canonical CO abundance" measured by different authors or in different objects varies by a factor of 2 (Lacy, Knacke, Geballe & Tokunaga 1994; Alves, Lada & Lada 1999; Kramer et al. 1999). Second, one has to bear in mind that the integrated CO depletion factor is an average value along the line of sight, thus the local depletion factor in the nucleus of the core is much greater (see, e.g., Caselli et al. 2002b; Chapter 3).

The integrated depletion factors of L1689B, L328, OphD and L429 were already published in Bacmann et al. (2002), that of L1544 in Caselli et al. (2002b) and that of L1521F in Chapter 3. We evaluate the f_D values for L1495, L1498 and L1517B using the data published in Tafalla et al. (2002), for B68 using the $C^{18}O$(1–0) intensities published in Bergin, Alves, Huard & Lada (2002) and the 1.2-mm continuum data published by Bianchi et al. (2003), for L183 using the 1.2-mm map of Pagani et al. (2003) and our $C^{18}O$ observations, for L694-2 using the 1.2-mm map of M. Tafalla et al. (2005, in preparation) and our $C^{18}O$ observations and for TMC2 and L492 using the $C^{18}O$ and the 1.2-mm maps from this work. Results are shown in column (4) of Table 2.10.

2.4.3 H_2 volume density

The H_2 column density can be derived from the millimeter continuum under the approximation of optically thin emission, constant temperature and constant emissivity of the dust at these wavelengths. The equation that relates the H_2 column density to the 1.2-mm flux is:

$$N(H_2) = \frac{S_{1.2mm}}{B_\nu(T)\,\Omega_{beam}\,\kappa_{1.2mm}\,m},$$

where $N(H_2)$ is the H_2 column density, $S_{1.2\ mm}$ is the flux density integrated over the solid angle Ω_{beam}, $B_\nu(T)$ is the Planck function at temperature T, $\kappa_{1.2mm}$ is the dust opacity per unit mass and m is the mean molecular mass. In our calculations, we assume a dust temperature of 10 K and a dust opacity of 0.005 cm^2 g^{-1}. The assumed dust temperature is justified by the estimates obtained from NH_3 (Tafalla et al. 2002) and H_2CO (Bacmann et al. 2002) observations in several cores of our sample. We note that the dust temperature is

Table 2.10. H_2 densities, integrated CO depletion factor, flattened radius, aspect ratios and N_2H^+(1–0) skewness.

core	$N(H_2)$ 10^{22} cm^{-2}	$n(H_2)$ 10^5 cm^{-3}	$f_D(CO)$[a]	r_{70} 10^3 AU	aspect ratio 70% contour	aspect ratio 50% contour	N_2H^+(1–0) skewness [b]
L1498	3.2±1.0	1.0±0.7	7.5±2.5	6.6±0.7	1.6±0.3	1.5±0.3	-0.01±0.05
L1495	3.1±1.0	1.1±0.7	7±2.4	4.7±0.6	2.0±0.4	1.9±0.4	0.10±0.05
L1521F	13.5±2.2	11.0±1.8	15±3.6	3.4±0.5	1.2±0.1	1.6±0.2	0.19±0.06
TMC2	6.0±1.2	3.0±0.8	13±3.3	5.2±0.6	1.2±0.4	1.1±0.3	-0.01±0.05
L1517B	3.7±1.0	2.2±0.8	9.5±2.8	4.0±0.5	1.4±0.1	1.2±0.1	-0.08±0.05
L1544	9.4±1.6	14.0±2.2	14±3.4	3.2±0.4	1.6±0.2	1.9±0.2	0.40±0.09
L183	10.0±1.7	10.0±1.7	12±3.1	4.8±0.6	1.8±0.2	2.5±0.2	0.09±0.05
OphD	8.2±1.5	8.5±1.5	14±3.4	6.1±0.7	2.1±0.4	1.9±0.4	0.54±0.12
B68	1.4±0.3	0.8±0.7	3.4±2.1	3.7±0.9	1.3±0.3	1.3±0.3	-0.09±0.05
L492	4.4±1.1	2.1±0.8	8±2.6	7.8±0.8	1.5±0.2	2.0±0.2	0.25±0.07
L328	5.7±1.2	1.8±0.7	8.5±2.6	3.7±0.5	1.1±0.2	1.2±0.2	-0.02±0.08
L429	8.8±1.6	6.0±1.1	15.5±3.7	3.6±0.5	1.4±0.2	2.1±0.3	-0.20±0.10
L694-2	7.8±1.4	9.0±1.5	11±3.0	5.5±0.6	1.3±0.1	1.4±0.1	0.22±0.07

Note. — For reference to the literature data see text.

[a]The CO depletion factor in L1689B is 4.5±2.2.

[b]N_2H^+(1–0) skewness was measured also in: L1495A-N (-0.04±0.05); L1400K (-0.42±0.10); TMC1 (-0.13±0.06); TMC1C (0.43±0.10); L1512 (0.02±0.05); L234E-S (-0.25±0.07); L1197 (0.08±0.11); CB246 (0.02±0.05).

predicted to drop in the core nucleus (Evans, Rawlings, Shirley & Mundy 2001; Zucconi, Walmsley & Galli 2001); assuming a temperature of 8 K would cause an increase of the column density of a factor of 1.5. We also remark that the dust opacity value, assumed following Andrè, Ward-Thompson & Motte (1996), suffers from an uncertainty of a factor of 2 (Henning, Michel & Stognienko 1995; Bianchi et al. 2003; Kramer et al. 2003).

In this work we both collected 1.2-mm maps from the literature and observed new sources with the bolometers. In Table 2.10 we report the H_2 volume density at the peak of L429 and L328 taken from Bacmann et al. (2000), of L1495, L1498, L1517B and L1544 from Tafalla et al. (2002), of OphD and L1689B from Ward-Thompson, Motte & André (1999), of L694-2 from Harvey et al. (2003) (using their Bonnor-Ebert fit and changing $\kappa_{1.2mm}$ to 0.005 cm^2 g^{-1} for consistency), of L183 from Pagani et al. (2003) and of L1521F from Chapter 3. All the central densities above were determined from 1.2-mm continuum data and using the same basic technique (i.e., a fit of the observed continuum emission starting from a volume density model of the core). We remark that these estimates were obtained assuming spherical symmetry. A strong deviation of the density profile along the line of sight with respect to what is seen in the plane of the sky will cause errors in the volume density determination. For some of these cores other different estimates for the peak density are reported in the literature; these were obtained starting from different data (molecular line or 850 μm continuum) or using different techniques. In the case of multiple estimates all done starting from 1.2-mm continuum data, we adopted the most recent value, e.g., L1544 has three determinations of the density that were done from a 1.2-mm map: 1.5×10^6 cm^{-3} by Ward-Thompson, Motte & André (1999), 4×10^5 cm^{-3} by Bacmann et al. (2000) and 1.4×10^6 cm^{-3} by Tafalla et al. (2002); in this work we adopted the most recent determination from Tafalla et al. (2002).

The H_2 central volume density at the TMC2, L492 and B68 peaks was evaluated with the same technique as for L1521F (Chapter 3). We assumed the analytical model for the volume density given by Tafalla et al. (2002): $n(H_2) = n_0/(1+(r/r_0)^{\alpha})$, where the central density (n_0), the "flattened radius" (r_0) and the steepness of the profile at large radii (α) are free parameters. Then, we searched for the best combination of parameters able to predict the observed continuum measurements. In this way we found at the peak of TMC2 an H_2 density equal to 3×10^5 cm^{-3}, while 2.1×10^5 cm^{-3} is the measured density towards the L492 peak. The B68 central density, derived from lower S/N data (and with the worst angular resolution), was found to be 8×10^4 cm^{-3} with large error bars.

Volume densities were also derived using an LVG program (see Section 2.4.4), whose

results are summarized in Table 2.11. We found systematically lower central densities using the molecular data ($\sim$ 3 times less) than using the dust (as already found in L1544; see Caselli et al. 2002b), suggesting that N_2H^+ and N_2D^+ may be probing a shell exterior to the high-density nucleus (see Figure 2.14 in Section 2.4.4). This indication is consistent with the idea that N_2 could freeze–out for densities higher than 5×10^5 cm^{-3} as suggested by Bergin, Alves, Huard & Lada (2002) and Belloche & André (2004). Keto, Rybicki, Bergin & Plume (2004) found a similar result using N_2H^+ and suggest that a way to reconcile gas density estimates from dust observations with those from molecular line observations is to increase the dust mass opacity to $\kappa = 0.04$ cm^2 g^{-1}, a value typical of fluffy aggregates with ice mantles. We stress that higher resolution observations are strongly needed to confirm this trend.

2.4.4 Density determination in the LVG approximation

The Large Velocity Gradient (LVG) approximation simplifies the radiative transfer treatment assuming that a photon produced in a contracting or expanding cloud is reabsorbed locally and that the local velocity gradient is much larger than the ratio of line width to cloud size. In addition, one normally assumes homogeneous and isothermal conditions. Assuming a temperatutre of 10 K, we have used this approximation, with collisional rates from Green (1975) to compute level populations for N_2H^+ and N_2D^+ and to predict line intensities for these species as a function of density and species column density. We then compared the model predictions with the observed N_2H^+(3–2)/N_2H^+(1–0) intensity ratio and the N_2H^+(1–0) integrated intensity (or the N_2D^+(3–2)/N_2D^+(2–1) and N_2D^+(2–1) intensity) exploiting the fact that the former is mainly sensitive to $n(H_2)$ and the latter to the N_2H^+(N_2D^+) column density. Our results are extremely sensitive to the intensity of the two 3–2 transitions and we hence confine our discussion to the eight cores with S/N$>$ 5 in the 1 mm lines. An extra constraint comes from the total τ of N_2H^+(1–0) (N_2D^+(2–1)). Note that, given the small opacities found in N_2D^+(2–1) (and in many N_2H^+(1–0) spectra), τ has little influence on the $n(H_2)$ determination whereas it is a useful constraint for column density.

In Table 2.11 we summarize the results of the LVG calculations. The ratio of the $N_2H^+$to N_2D^+ column densities inferred from LVG and the relative value found in the CTEX approximation have an arithmetic mean value of 0.9 and a dispersion of 25%. Thus, the LVG results are consistent with the column densities derived assuming a constant rotational temperature. It is interesting to note that the H_2 densities derived from the

Table 2.11. H_2 volume density and N_2H^+–N_2D^+ column densities derived in the LVG approximation.

core	N_2H^+		N_2D^+	
	$n(H_2)$ $10^5 cm^{-3}$	$N(N_2H^+)$ $10^{13} cm^{-2}$	$n(H_2)$ $10^5 cm^{-3}$	$N(N_2D^+)$ $10^{12} cm^{-2}$
L1521F	1.3	3.4	4.5	1.6
TMC2	1.7	1.0	1.5	1.5
L1544	1.5	2.8	2.8	4.6
L183	1.0	2.0	3.5	2.8
OphD	3.2	0.6	4.0	2.6
B68	0.6	1.2	...	...
L429	1.6	3.1	4.3	4.9
L694-2	1.1	2.1	2.2	3.3

Note. — Errors in the LVG determinations are estimated around 30% from comparisons with CTEX determiantions.

molecular data are systematically smaller (a factor of ~ 3) than those derived from the dust observations (see Figure 2.14).

The differences between the two determinations diminish in the low-density cores (a factor of ~ 2). These differences may partially be due to our assumptions concerning the dust millimeter opacity and temperature (see Galli, Walmsley & Gonçalves 2002 for a discussion of the latter and Bianchi et al. 2003 for a discussion of the former). Another possibility is that depletion of N_2 (and hence of N_2H^+ and N_2D^+) may occur in regions with density higher than 5×10^5 cm^{-3} (see also Caselli et al. 1999; Bergin et al. 2001; Caselli et al. 2002b; Chapter 3; Belloche & André 2004). In the latter case, one would expect differences between maps of N_2H^+ and dust continuum (one possible example could be L183, see Section 2.3.2). We note also that there is a hint in our data that densities derived from N_2D^+ are systematically higher than those from N_2H^+ and this again may be consistent with a hole caused by N_2 freeze–out. However, we stress that these trends need confirmation and that measurements with higher sensitivity and angular resolution are needed.

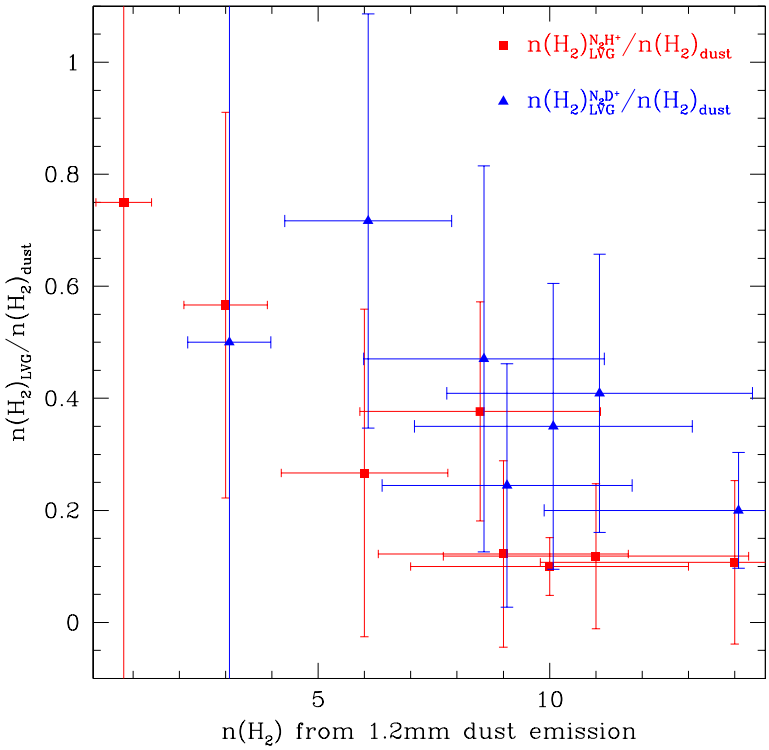

Figure 2.14 H_2 central density derived from dust observation compared with the determination from N_2H^+/N_2D^+ observations. The density inferred from the dust emission is always higher than the one derived from the molecular data, although the difference seems to diminish in the lowest density cores. Moreover, the estimates done starting from N_2D^+ data furnish moderately higher H_2 density, consistently with the idea that N_2D^+ is a better tracer of the dust emission. Data points from N_2D^+ were slightly offset in the *x*-axis in order to show them better.

2.4.5 Dust emission equivalent radius and aspect ratio

In starless cores the H_2 density profile can be approximated by a region of roughly constant density followed by a power-law decrease (Ward-Thompson, Motte & André 1999; Bacmann et al. 2000; Tafalla et al. 2002); this behaviour is reflected in the 1.2-mm continuum emission. Since the "flattened nucleus" is expected to become smaller with the ongoing of infall, its size gives us a measure of the relative contraction stage reached by the cores. Unfortunately each author uses different definitions for the size of the flattened region; thus, we have measured, for the 13 cores with a 1.2-mm map, the area within the

70% contour of the dust peak. We then translated this into a radius (reported as r_{70} in figures and tables) by evaluating the square root of this area divided by π. The resulting values are reported in column (5) of Table 2.10. This approach is useful for a relative comparison of the different cores. The choice of the 70% contour as threshold is justified by the fact that we wanted to limit the influence of the "cometary tail" (see Section 2.3.3) on the r_{70} determination.

We also evaluated the aspect ratio of the dust emission measuring the major and minor axis size of the 50% contour and 70% contour (results are shown in columns (6) and (7) of Table 2.10). We found that the axis ratio increases at lower contours in the more cometary cores, reaching values up to 2.5.

2.4.6 The line asymmetry

The analysis of the line profile gives us clues on the core kinematics. In fact, motions along the line of sight combined with optical depth effects, molecular abundance variations and temperature gradients alter the line profile, causing departures from a Gaussian line shape. In particular, looking at the density peak, we expect a "blue shoulder" in the case of outflow motions and a "red shoulder" in the case of infall motions (see Evans 2002, for a review).

Here, we determine the degree of line asymmetry by calculating the line skewness, or the third moment, of a distribution equivalent to the line profile. This is defined as $\sum_{i=1}^{N}\left((x_i-\bar{x})/\sigma_x\right)^3/N$, where $\bar{x}$ and σ_x are the first and second moments of the same distribution and N is the total number of points (see e.g. Press, Teukolsky, Vetterling & Flannery 1992). By definition, the third moment measures the deviation from a symmetric distribution, as the first moment furnishes its mean and the second yields its dispersion. It is a non-dimensional quantity and assumes positive values for distributions that have a "tail" in the values higher than the mean and negative values in the opposite case. We applied this analysis to the ($F_1\,F = 2\,2 \rightarrow 1\,1$) component of N_2H^+ (the fourth starting from the lower velocities). The "isolated" ($F_1\,F = 0\,1 \rightarrow 1\,2$, the one at lowest velocity) and the "weak" ($F_1\,F = 1\,0 \rightarrow 1\,1$, the one at highest velocity) components show approximately the same behaviour as this one in the very high S/N spectra (RMS < 0.03 K with a 0.063 km s^{-1} channel spacing); thus, in order to enlarge the sample to spectra with slightly lower S/N (RMS < 0.1 K), we used the data from the ($F_1\,F = 2\,2 \rightarrow 1\,1$) component, which also provides a sufficient isolation from the other components even in the spectra with broadest line widths. Moreover, given the role of the optical depth in the produc-

tion of the asymmetric profiles, the ($F_1\,F = 2\,2 \rightarrow 1\,1$) component is supposed to have a more pronounced skewness than the other two components. Results are shown in Table 2.10. Eight cores show red-skewed "contracting" profiles, six cores show blue-skewed "expanding" profiles, and seven cores have symmetric profiles within the error bars. Note that the line peak in the "contracting" profiles falls at lower velocities (or on the blue side) than $\bar{x}$ whereas asymmetric profiles with outflow character are the reverse.

2.5 Discussion

In the following we discuss the relations between the quantities determined in the previous sections and compare them with simple theoretical expectations. We divide this section into two main parts: in the first we concentrate on the connection between deuterium fractionation and the other chemical and dynamical parameters derived in Section 2.4, while in the second we cross-correlate only the parameters linked with the kinematical activity.

2.5.1 Deuterium Fractionation correlations

Deuterium fractionation and CO depletion

An observational proof of the chemical model relating the deuterium fractionation with the CO depletion factor was given in Bacmann et al. (2003) using the ratio of D_2CO over H_2CO in a sample of five cores. Although D_2CO and H_2CO have been shown to deplete in the inner nucleus of the pre–stellar cores (Carey et al. 1998; Maret et al. 2004) and hence do not trace the very inner nucleus, these five cores (included in our sample) showed a good correlation between the CO depletion and the deuterium fractionation in H_2CO with the exception of OphD.

Another possible test is to check for a correlation between the CO depletion factor and the deuterium fractionation within a given core. This test was performed in Chapter 3 showing again an affirmative answer.

Here we searched for a correlation between the integrated CO depletion factor and the deuterium fractionation in a subsample of 14 cores using the high density gas tracers N_2H^+ and N_2D^+ to derive the deuterium fractionation. The result is shown in Figure 2.15, where we denote by enclosed data points our "candidate pre–stellar cores", defined for the purpose of this work as having $N(N_2D^+)/N(N_2H^+) \geq 0.1$.

The correlation is not extremely tight (correlation coefficient 69%; 74% if only Taurus cores are considered), but indeed we can say that the cores that show higher CO depletions do also show higher deuterium fractionation. As in Bacmann et al. (2003), OphD seems to have "too much" deuterium fractionation compared to the CO depletion.

In Figure 2.15 we also show theoretical curves from simple chemical models based on that described by Caselli et al. (2002b). These models all assume that the gas and dust temperatures are constant across the core and equal to 10 K. The chemical network and chemical parameters are also the same in all the models: apart from H_2, the chemical network contains the three neutral species CO, N_2, and O, which can freeze–out onto dust grains and return to the gas phase via thermal desorption or cosmic–ray impulsive heating (following the formulation of Hasegawa & Herbst 1993). On the other hand, the abundances of the molecular ions (N_2H^+, HCO^+, H_3O^+, H_3^+ and their (multiply) deuterated counterparts) are calculated in terms of the instantaneous abundances of the neutral species. This simplification is based on the fact that the "ion chemistry" timescale is much shorter than the depletion timescale (see Caselli et al. 2002b and Chapter 3for details). Here we included the multiply deuterated forms of H_3^+, without any distinction between the ortho and para forms of molecular hydrogen and H_2D^+ and without taking into account the so–called back-reactions between, e.g., ortho–H_2 and ortho–H_2D^+ (Gerlich, Herbst & Roueff 2002), which limit the deuterium fractionation, as discussed in Walmsley, Flower & Pineau des Forêts (2004). However, we adopted the new value of the rate coefficient for the proton–deuteron exchange reaction $H_3^+ + HD \rightarrow H_2D^+ + H_2$ (3.5×10^{-10} cm^3 s^{-1}; Gerlich, Herbst & Roueff 2002). The other parameters used are: the cosmic–ray ionization rate $\zeta = 1.3\times10^{-17}$ s^{-1}; the CO, N_2, and O binding energies: $E(\mathrm{CO}) = 1210$ K, $E(\mathrm{N_2}) = 800$ K, and $E(\mathrm{O}) = 650$ K [3] respectively; and the lower cutoff radius of the MRN (Mathis, Rumpl & Nordsieck 1977) distribution $a_{\mathrm{min}} = 5\times10^{-6}$ cm.

The different model predictions, denoted as n_1, n_2, n_3, n_4 and n_5 in Figure 2.15, refer to model spherical clouds with different density structures, in (rough) analogy with the density structure of the model cloud undergoing infall, described by Ciolek & Basu (2000, hereafter CB00), at successive evolutionary stages (from $t_1 = 2.27$ Myr to $t_5 = 2.684$ Myr: see CB00). We remark that our calculations assume the steady state and thus our model

[3] All the adopted parameters are the same as in Chapter 3, with the exception of $E(\mathrm{O})$, which is now 100 K lower than before. The decrease in this parameter is necessary to keep the deuterium fractionation at a similar level as in Chapter 3, for the particular case of L1521F, after the inclusion of all the multiply deuterated forms of H_3^+. See also Caselli et al. (2002b) for the importance of atomic oxygen in this simple chemical network.

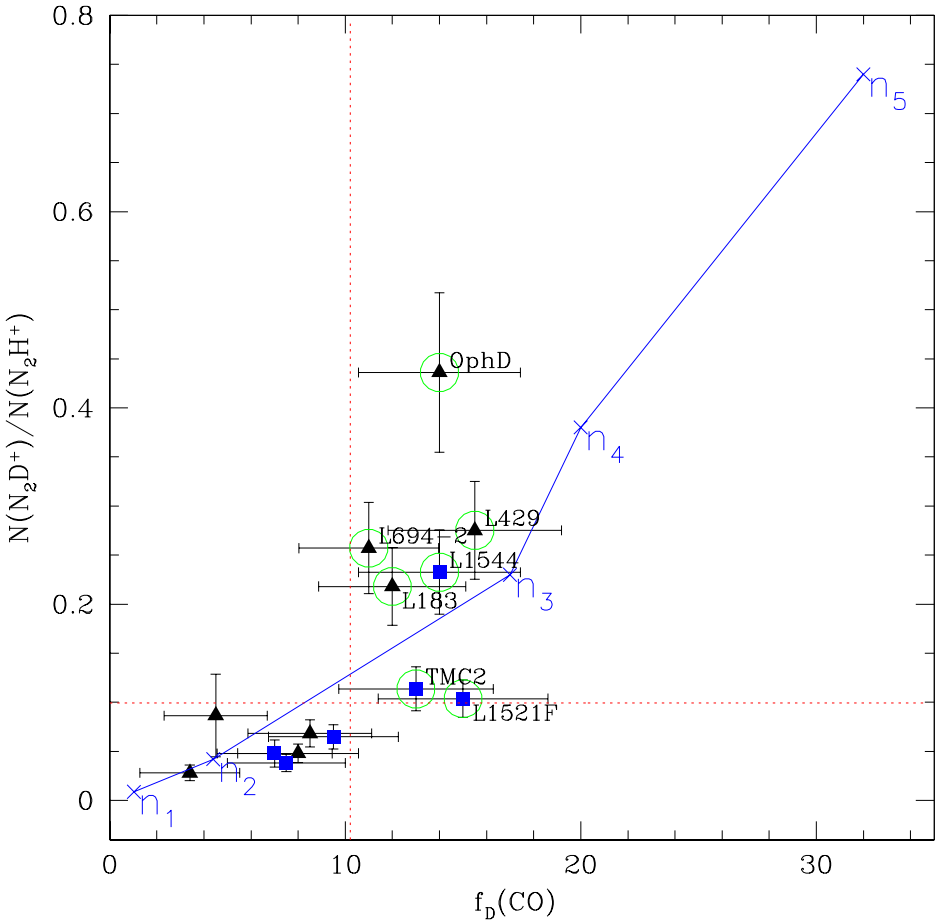

Figure 2.15 Deuterium fractionation vs. integrated CO depletion factor at the N_2D^+ peak position. Depletion factor values were taken from the literature and from present data (see Section 2.4.2 for references). The solid line connects the predictions of chemical models of spherically symmetric dense cores with various degrees of central concentrations (from central densities of 4.4×10^4 cm^{-3} in model n_1 to 4.4×10^8 cm^{-3} in model n_5), roughly simulating (in spherical symmetry) the evolutionary sequence of contracting disk-like clouds in the Ciolek & Basu (2000) model (see text). Dotted lines are the arithmetic means of the distributions. Cores belonging to the Taurus Molecular Cloud are marked by a square; pre–stellar cores candidates are circled.

makes use of the density profile only, and not of the time scale. We also note that the CB00 model has cylindrical (rather than spherical) symmetry and we have neglected this fact assuming the same dependence on spherical radius as that on cylindrical radius in CB00. We assume that the density profiles are given by the analytical formula of Tafalla et al. (2002), with different values of the parameters (namely, the central density, the radius of the inner flat region, and the asymptotic power index) to approximately reproduce the density profiles of Figure 1a of CB00. In particular, the central densities of the cores at each time are given by $10^j \times 4.37 \times 10^3$ cm^{-3} (for j = 1, ..., 5) as in CB00. The abundance profiles obtained in this way have then been converted into column densities via integration along the line of sight and successive convolution with a two-dimensional Gaussian, simulating observations with an HPBW of $22''$. From Figure 2.15 we note that the deuterium fractionation in N_2H^+ and the observed CO depletion factor (f_D) are predicted to increase with core evolution and actually explain the observed trend, although some scatter is expected in the data, given the different environments where they are immersed and their different formation histories. In particular, we expect magnetic field strength, amount of turbulence, external radiation field and external pressure to influence the evolution of a core. Hence two cores with the same mass and same age could have different degrees of evolution depending on the characteristics of the surrounding star-forming region. We note that most of the "pre–stellar" cores are found close to the n_3 result, which, in the CB00 model, is the model of best agreement with the measured density profile of L1544. Therefore, we can conclude that the "pre–stellar core" condition, $N(N_2D^+)/N(N_2H^+) \geq 0.1$, is consistent with values of central densities $n(H_2) \geq 10^6$ cm^{-3}, in agreement with H_2 central densities measured from the dust in Section 2.4.3 for these cores.

We also searched for correlations between the depletion factor and the H_2 column density and found a positive correlation (87% correlation coefficient; 90% for Taurus only), confirming the general chemical scenario about CO depletion (see Dalgarno & Lepp 1984; Roberts & Millar 2000a; Bacmann et al. 2002). Several authors have investigated the chemical structure of pre–stellar cores, coupling together dynamical and chemical evolution with detailed models (Bergin & Langer 1997; Aikawa et al. 2001; Li, Shematovich, Wiebe & Shustov 2002; Shematovich, Wiebe, Shustov & Li 2003). Deuterium and singly deuterated species were, however, only included in Aikawa et al. (2001), who were able to reasonably reproduce the observed molecular D/H ratios toward L1544, although the column density of N_2H^+ was underestimated. Aikawa, Ohashi & Herbst (2003) over-

came this problem by adding surface chemistry to their models. Surface processes significantly enhanced the production of the parent molecule N_2, increasing the N_2H^+ column density to the observed values.

More recently, Roberts, Herbst & Millar (2004) studied the chemistry of pre–stellar cores including multiply deuterated species but neglecting the dynamical evolution. For the particular cases of L1544 and OphD they found $N(N_2D^+)/N(N_2H^+)$ column density ratios significantly (factor of about 5) larger than the observed values, suggesting that the deuterium fractionation process is probably too efficient in their models. Possible causes of this disagreement are: (i) the exclusion of the so–called back reactions of deuterated isotopologues of H_3^+ with ortho-H_2 (Gerlich, Herbst & Roueff 2002) which may lower the molecular D/H ratios (Walmsley, Flower & Pineau des Forêts 2004); (ii) the use of large (radius of 0.1 μm) dust grains in the chemical network, which underestimates the recombination of molecular ions compared to models where a population of smaller grains is present or where an MRN size distribution of dust particles is considered; (iii) the use of UMIST rates, which produce H_3^+ and analogues more efficiently than the "New Standard Model" from Ohio State University (see Roberts, Herbst & Millar 2004, for details).

Deuterium fractionation vs. H_2 central density, dust equivalent radius, N_2H^+ line width and N_2H^+ line skewness

In theoretical simulations, we expect an increase of the central $n(H_2)$ density and a decrease of r_{70}, the equivalent radius of the flat region, with ongoing contraction (e.g., Lizano & Shu 1989; Foster & Chevalier 1993; Ciolek & Mouschovias 1995; Li 1999). Those two parameters can be considered as indicators of "dynamical evolution"; here we cross-correlate them with the deuterium fractionation.

From Figure 2.16 panel a) one can see that there is a positive correlation between $N(N_2D^+)/N(N_2H^+)$ and $n(H_2)$ apart from OphD and L1521F which show opposite behaviours from the rest of the cores. Six of our pre–stellar cores candidates have H_2 volume densities above the average (5.1×10^5 cm^{-3}), and all of these show increases in deuterium fractionation above the average. Our estimate of the volume density depends on the assumed spherical geometry: hence, we also considered the correlation between the deuterium fractionation and the H_2 column density. While the general trend remained the same, the peculiarity of OphD and L1521F becomes more marked.

We check here the relative variation of the flattened region in the 13 cores for which

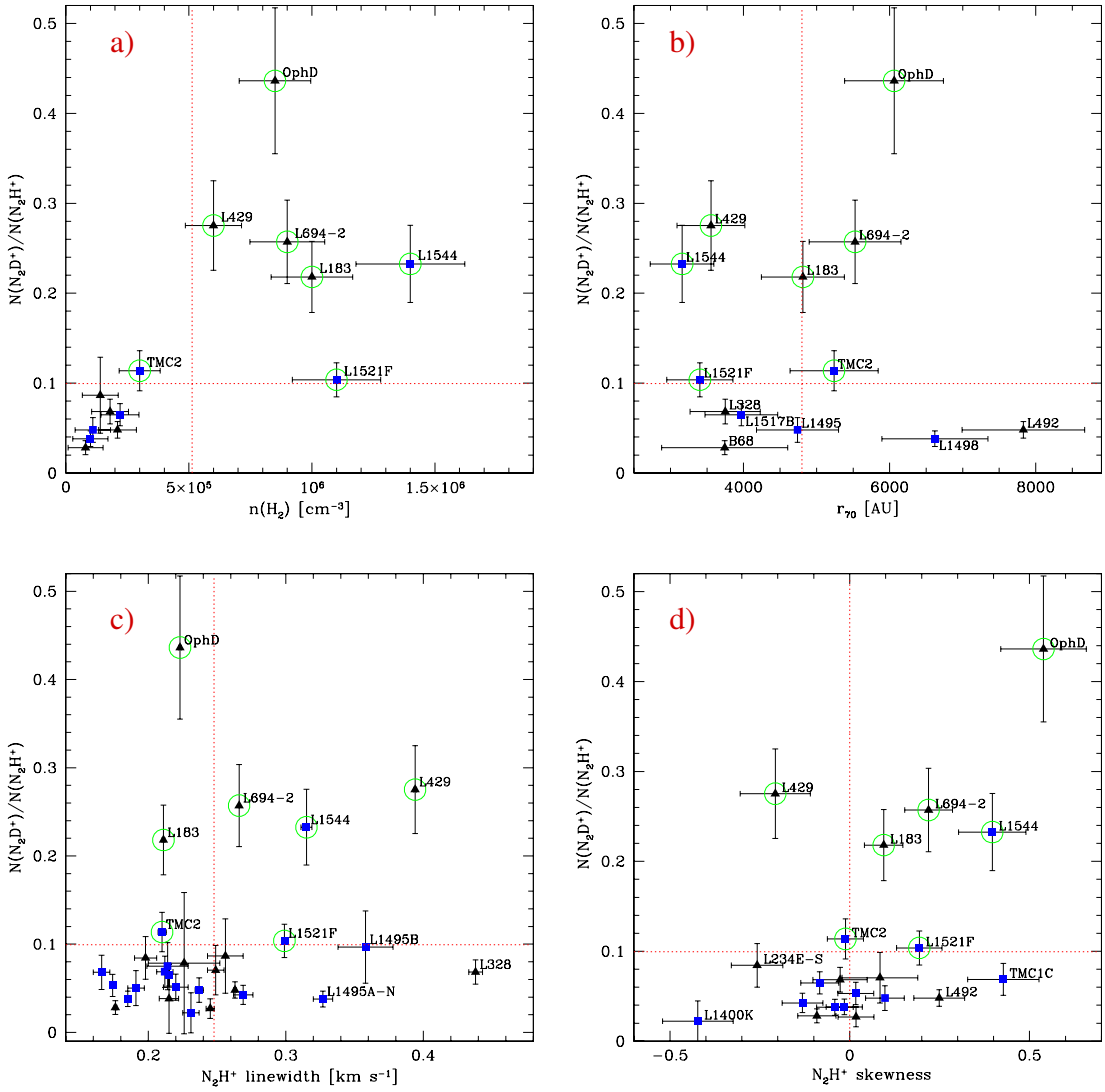

Figure 2.16 Deuterium fractionation correlations. In all panels: dotted lines are the arithmetic means of the distributions (except in panel d)); cores belonging to the Taurus Molecular Cloud are marked by a square; pre–stellar cores candidates are circled; the values were evaluated at N_2D^+ peak position. **Panel a):** Deuterium fractionation vs. H_2 central volume density. The $n(H_2)$ values are taken from the literature (see Section 2.4.3), with the exception of TMC2, L492 and B68, estimated in this work. **Panel b):** Deuterium fractionation vs. equivalent radius of the flattened region r_{70} is defined as $\sqrt{area_{70}/\pi}$, with $area_{70}$ as the area within the 70% contour in the 1.2-mm map. **Panel c):** Deuterium fractionation vs. N_2H^+(1–0) line width evaluated from the simultaneous fit of all the 7 hyperfine components. **Panel d):** Deuterium fractionation vs. N_2H^+(1–0) line asymmetry. The vertical dotted line separates the red-skewed spectra from the blue-skewed ones (the arithmetic mean is 0.07).

we have a 1.2-mm map. Having treated all the cores in a consistent way allows us to consider the differences in r_{70} real and not due to differences in the adopted fitting model. The correlation between deuterium fractionation and r_{70} is shown in Figure 2.16 panel b). A close relationship of the flattened radius with the deuterium fractionation is not found. OphD shows the biggest variation from this picture, but one should notice the presence of a second peak inside its 70% contour. It is thus possible that the OphD equivalent radius is overestimated. A similar argument holds for L183. Limiting the sample to the Taurus cores significantly tightens the correlation, increasing the correlation coefficient from 1% to 64%. Once again, this result suggests that cores embedded in different environments (e.g. external radiation field) hardly represent a homogeneous sample in which to study evolutionary trends.

Caselli et al. (2002a) showed that in L1544 there was a definite trend for the N_2H^+ and N_2D^+ line widths to increase towards the high-density region. This result was interpreted as a sign of increasing infall activity towards the center. The same trend, although less marked, is seen in L1521F (Chapter 3).
In this fashion, we take here the N_2H^+ line width as an indicator of infall activity and thus proximity to the critical state for dynamical collapse and we check if the cores that had larger line widths are the same as those with the largest $N(N_2D^+)/N(N_2H^+)$ ratio, to search for links between physical and chemical evolution. The result is in Figure 2.16 panel c). In our sample we do not see any correlation for larger line width in the nucleus of cores with larger deuterium fractionation. In particular, we note that L328 shows broad lines but low $N(N_2D^+)/N(N_2H^+)$ and that OphD has the opposite behaviour. The two broadest line cores, L328 and L429, have spectra with both flat tops and blue-skewed asymmetry (see Sect. 2.4.6), suggesting that their lines could be broadened for reasons other than infall. We attempted to avoid the environmental differences, as a source of scatter for the correlation, limiting the sample to the Taurus cores only; in this case the correlation coefficient increases from 22% to 40%.
We point out that the above correlation does not make any distinction between cores that do and do not show evidence of central infall (through the N_2H^+(1–0) line width broadening toward the dust peak position, or with the presence of "red shoulders"), so that the different line widths observed in the cores of the present sample may simply arise from different amounts of turbulence in their interiors or other types of motions (e.g., expansion or oscillations) along the line of sight.

We also try to correlate the line skewness with the $N(N_2D^+)/N(N_2H^+)$ ratio in Figure 2.16 panel d). Also in this case there is a general agreement with the proposed idea that cores with higher deuterium fractionation also show signs of kinematical evolution. The main exceptions in this case are given by L429 on the one hand and TMC1C and L492 on the other. It is interesting to note that the correlation between $N(N_2D^+)/N(N_2H^+)$ and the line asymmetry is more tight than that with the line width.

Deuterium fractionation and extended infall

Lee, Myers & Tafalla (1999, 2001) and Lee, Myers & Plume (2004) in a series of papers conducted a search for infall motions towards a sample of 70 starless cores. Infall motions were identified through the presence of velocity shifts between high density tracers (N_2H^+(1–0) probing densities up to a few times 10^6 cm^{-3}) and low density tracers (CS(2–1) tracing the gas up to $\sim 10^4$ cm^{-3}) and through the observation of double-peaked self-absorbed optically thick lines whose blue peak was brighter than the red peak (Lee, Myers & Plume 2004). Given the CS depletion in the inner core, those measurements gauge the infall of the external envelope only.

Twenty-four cores in our sample were observed also in the Lee et al. papers (2001; 2004), including our chemically evolved candidates L1544, L1521F, L694-2, L183, L429, TMC2 and OphD (there known as L1696A). Considering now only this common subsample, Lee, Myers & Plume (2004) found that 12 of these cores show infall signatures in at least three of the seven tests they performed on CS, DCO^+ and N_2H^+ lines, thus they are considered strong infall candidates. All our chemically evolved candidates ($N(N_2D^+)/N(N_2H^+) > 0.1$) (except OphD, which was not studied with all the techniques by Lee, Myers & Plume 2004) were identified as strong infall candidates by the Lee, Myers & Plume (2004) analysis. This seems to show that our chemically evolved candidates, the majority of which show clear signs of central infall, are a subsample of the cores undergoing extended contraction.

We also performed a direct comparison between one of the infall indicators in Lee, Myers & Plume (2004), δV_{DCO^+} ($\equiv (V_{DCO^+} - V_{N_2H^+})/\Delta V_{N_2H^+}$), and our N_2H^+(1–0) skewness on a common subsample of 15 cores. We find a very good agreement between those two parameters with only two cases in which they give a different indication: L429 which has significant outflow signature in the N_2H^+(1–0) skewness but marginal infall indication in δV_{DCO^+}, and L183, which has a very strong outflow behaviour in δV_{DCO^+}

whereas it shows an infall profile in our N_2H^+(1–0) spectrum. For the 13 remaining cores the two indicators correlate with a 70% correlation coefficient.

2.5.2 Dynamical parameters correlations

We cross-correlated our "kinematic activity" indicators, i.e., the N_2H^+(1–0) line width, the radius of the flattened region, the H_2 column density, and the N_2H^+(1–0) line asymmetry, to see whether they give consistent information. The result is encouraging. We can in fact see in panel a) of Figure 2.17 that r_{70} is anti-correlated with N_2H^+(1–0) line width (correlation coefficient 67%; 86% limiting to Taurus cores); note that even cores that in the other plots do not behave like the rest of the sample (OphD and L328) lie here in the common trend.

In panel b) of Figure 2.17 we find that, with the notable exceptions of L328 and L429, the N_2H^+(1–0) line width correlates fairly well with the H_2 central density (correlation coefficient 20% for the total sample; 64% without L328 and L429; 94% for only the Taurus cores).

In the picture given in Section 2.5.1, the cores with strong motions along the line of sight should show stronger asymmetries and broader lines towards the core peak. In Figure 2.17 panel c) we plotted the relation between the width and the skewness of the N_2H^+ line. Although again a tight correlation is not found, we can see that there is a general trend of increased skewness in broader spectra. Remarkable exceptions are constituted by OphD and TMC1-C, having narrow lines strongly skewed towards the red, and by L429 and L328, which have the broadest lines in the sample but do not show any infall asymmetry. Also in this case, limiting the sample to Taurus cores, the correlation coefficient increases from 2% to 21%.

Line width and aspect ratio

The fact that the majority of the cores in our sample (see Figure 2.10 in Section 2.3.3) show large departures from spherical symmetry has considerable significance for our understanding of the dynamics of these objects. Core shape could for example reflect the magnetic field structure and indeed several of the cores in our sample show linear polarization of around 5%-10% (e.g., Crutcher, Nutter, Ward-Thompson & Kirk 2004), suggesting magnetic fields of order 100 μG. However, the observed structures could also be a consequence of dynamical interactions with the core surroundings as is suggested by the

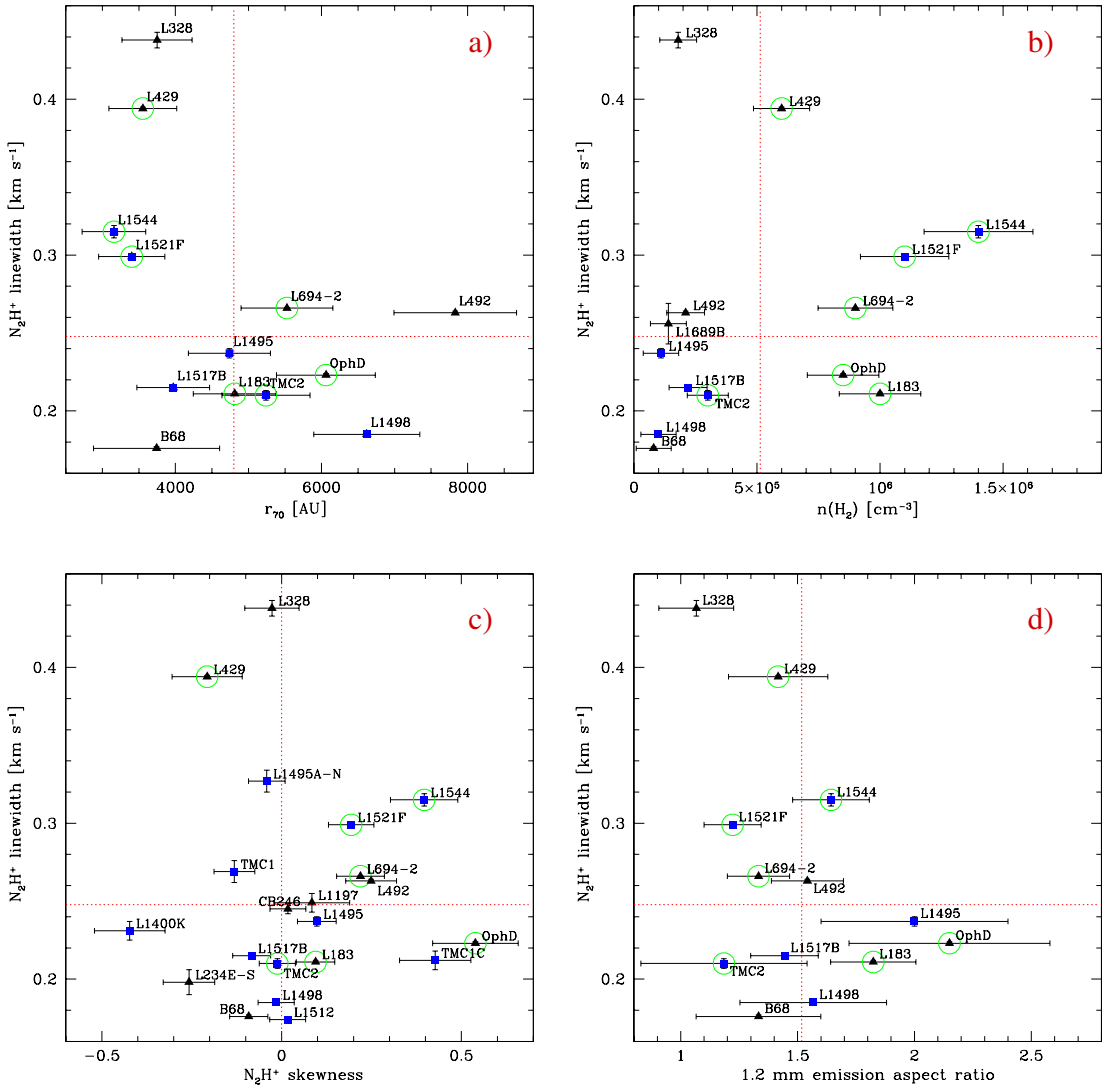

Figure 2.17 Correlations between "dynamical evolution" indicators. In all panels: dotted lines are the arithmetic means of the distributions (but in panel c)); cores belonging to the Taurus Molecular Cloud are marked by a square; pre–stellar cores candidates are circled; the values were evaluated at N_2D^+ peak position. **Panel a):** N_2H^+(1–0) line width vs. equivalent radius of the flattened region r_{70} is defined as $\sqrt{area_{70}/\pi}$, with $area_{70}$ as the area within the 70% contour in the 1.2-mm map. **Panel b):** N_2H^+(1–0) line width vs. H_2 volume density. The $n(H_2)$ values are taken from the literature (see Section 2.4.3), with the exception of TMC2, L492 and B68, estimated in this work. **Panel c):** N_2H^+(1–0) line width vs. N_2H^+(1–0) line asymmetry. The vertical dotted line here separates the red-skewed spectra from the blue-skewed ones (the arithmetic mean is 0.07). **Panel d):** N_2H^+(1–0) line width vs. aspect ratio of the 50% contour of the 1.2-mm emission.

observed "cometary" shapes. It is natural therefore to search for kinematic evidence in our N_2H^+ maps that either excludes or favors one of these scenarios.

There are various possible kinematic probes, including the observed velocity field, but the simplest is to check for a correlation between line width and aspect ratio. Here the interpretation depends considerably on whether the true core shape is "close to oblate" or "close to prolate" (see, e.g., Jones & Basu 2002; Curry 2002, who have attempted to decide this on the basis of the statistics of observed aspect ratios). Present results are inconclusive and we conclude that one must consider both possibilities.

In either case, if cores are magnetically dominated, motion along the field lines will be facilitated. We would expect that in such cases, motions will predominantly be parallel to the axis of symmetry and hence for oblate cores, one might expect the largest line widths for face-on circular sources and for prolate cores for end–on (also circular) objects. On the other hand, ambipolar diffusion necessarily occurs across field lines and this will have the opposite effect. Thus, for example, edge-on oblate cores will have the largest line width. In fact, CB00 have provided predictions for how the velocity field due to the latter process might appear in L1544 and Caselli et al. (2002a) showed that the observations were roughly consistent with the model for this object.

However, this does not seem to be the case in L1521F (Chapter 3) and also not in a more general sample of cores as shown in Figure 2.17 panel d), where we plot the N_2H^+(1–0) line width against aspect ratio from the millimeter continuum maps. There is no clear trend in this plot, and clearly a larger sample is needed. However, our results do not give evidence that in general there are increased line widths towards elongated core nuclei as one might expect on the basis of models such as those of CB00. On the other hand, our results also do not seem to favor the models of Curry & Stahler (2001) which suggest that initially elongated structures should become more spherical as they evolve owing to ambipolar diffusion. We conclude that it would be useful to have more detailed predictions for model pre–stellar cores of the evolution with time of both the line width and the velocity field.

2.5.3 Associated properties

We have shown in this section a series of properties that we think are associated with an evolved stage of starless cores either because of enhanced chemical activity or because of an advanced kinematical process.

Even though we did not find tight one-to-one correlations between the numerical val-

Table 2.12. Chemical and kinematical evolution "probes" in the 13 cores with full data set (N_2H^+, N_2D^+, $C^{18}O$ and 1.2-mm emission).

core	L1544	L1521F	L694-2	L429	L183	OphD	TMC2	L492	L328	L1495	L1517B	B68	L1498
$N(N_2D^+) > 1.0 \times 10^{12}$ cm^{-2}	1	1	1	1	1	1	1	0	0	0	0	0	0
$N(N_2H^+) > 8.5 \times 10^{12}$ cm^{-2}	1	1	1	1	1	0	1	1	1	1	1	1	0
$\frac{[N_2D^+]}{[N_2H^+]} > 0.10$	1	1	1	1	1	1	1	0	0	0	0	0	0
$f_D(CO) > 10.2$	1	1	1	1	1	1	1	0	0	0	0	0	0
$n(H_2) > 5.1 \times 10^5$ cm^{-3}	1	1	1	1	1	1	0	0	0	0	0	0	0
$\Delta V_{N_2H^+} > 0.25$ km s^{-1}	1	1	1	1	0	0	0	1	1	0	0	0	0
infall asym. (*skewness* > 0)	1	1	1	0	1	1	0	1	0	1	0	0	0
$r_{70} < 4800$ AU	1	1	0	1	1	0	0	0	1	1	1	1	0
total	8	8	7	7	7	5	4	3	3	3	2	2	0

Note. — For each value, but the skewness, the thresholds are given by the arithmetic mean value for the sample.

ues it appears that these properties globally isolate a group of cores that look peculiar with respect to the rest of the sample. We summarize these characteristics of the evolved starless cores, or pre–stellar cores, in Table 2.12. L1544 and L1521F were found to be more evolved than the "average" core in each test we performed, while L183, L429 and L694-2 failed just one test and can be considered strong candidates for pre–stellar cores as well. Other cases, such as OphD and TMC2, are more doubtful.

In the presence of an unbiased survey and assuming that all the cores will eventually form a star, one could attempt to estimate the duration for the pre–stellar core phase by dividing the number of pre–stellar core candidates by the total number of objects in the sample. Since our main selection criterion stated that only the sources with stronger N_2H^+(1–0) observations (in the Lee, Myers & Tafalla 2001sample) or stronger dust emission-absorption (in the Bacmann et al. 2000 sample) were observed, we cannot consider our survey unbiased. Nevertheless, taking the number of N_2H^+–detected cores within 250 pc (49) in the Lee, Myers & Tafalla (1999) sample as representative of the total number of the N_2H^+–bright cores and supposing that L1544, L1521F, L183, L429,

L694-2, OphD and TMC2 are the only pre–stellar cores observable in this sample, we can derive a duration of the pre–stellar phase equal to 7/49, or ∼14% of the lifetime of a core since it started to be observable in N_2H^+. Taking the smallest central density observed in our sample (B68: $n(H_2) \sim 8 \times 10^4$ cm^{-3}) as the threshold for N_2H^+ emission, we can derive a lifetime of an N_2H^+–bright core of ∼0.4 Myr (using the CB00 ambipolar diffusion models); hence, the pre–stellar core phase should last around 60,000 yr. An alternative estimate can be made evaluating the free-fall time for the threshold density for a pre–stellar core ($n(H_2) \sim 5.1 \times 10^5$) resulting in a duration of ∼60,000 yr.
The pre–stellar core lifetime can also be estimated from the comparison with the estimated time spent as a Class 0 protostar ($\sim 2 \times 10^4$ yr Visser, Richer & Chandler 2002). From André, Ward-Thompson & Barsony (2000) and Visser, Richer & Chandler (2002), we derive a total number of 11 Class 0 protostars within 250 pc. This, compared to the seven evolved cores found in this work, gives a duration of the pre–stellar phase of ∼10,000 yr, shorter than the estimates above. However, we feel that this discrepancy merely reflects the great uncertainties in both estimates.

2.6 Conclusions

We collected a set of N_2H^+, N_2D^+, $C^{18}O$ and 1.2-mm continuum observations using the IRAM 30-m for a sample of 31 starless cores, completing literature data with new observations. We retrieved from these data chemical and kinematical parameters supposed to discriminate young from more evolved cores such as: deuterium fractionation, integrated CO depletion factor, H_2 density, N_2H^+ line width and line asymmetry. Our conclusions are summarized as follows:

1. We attempted several correlations between the chemical evolution indicators (deuterium fractionation, integrated CO depletion factor and N_2H^+ and N_2D^+ column density) and properties of dynamically evolved cores (such as H_2 volume density, line width and asymmetry and size of the flattened region). Although we did not find very tight dependencies between these quantities, we recognized that all these properties, as a whole more than taken singularly, draw from the total sample those cores with an enhanced state of evolution. As can be seen from Table 2.12, we find that, compared to the total sample, L1544, L1521F, L183, L429, L694-2, OphD and TMC2 globally show:

- higher N_2H^+ column density
- higher N_2D^+ column density

- higher $N(N_2D^+)/N(N_2H^+)$ abundance ratio
- higher H_2 column density
- higher integrated CO depletion factor
- broader N_2H^+ lines
- smaller flattened radius
- stronger infall asymmetries

with some exceptions in each category.

2. Limiting the sample to the cores belonging to the Taurus Molecular Cloud tightens the correlations, probably by diminishing possible effects due to environmental differences such as magnetic field strength, amount of turbulence, external radiation field and external pressure.

3. The picture emerging from the observations is consistent with predictions of chemical models accounting for molecular freezeout, where cores with higher central densities show a lower fraction of CO in the gas phase and a correspondingly larger deuterium enrichment in the core nucleus.

4. N_2D^+ and N_2H^+ emissions, unlike $C^{18}O$, peak very close to the dust continuum maxima in the mapped cores, confirming the fact that those species probe better the conditions of the high density gas. Moreover, the maps of N_2D^+ and N_2H^+(3–2) were found to be systematically smaller than the N_2H^+(1–0) ones in all the mapped cores, consistent with the idea that these trace better the high-density nucleus. We note that central H_2 densities evaluated from the dust emission were found systematically larger than those calculated from LVG modeling of N_2H^+ and N_2D^+ data, suggesting that depletion of N_2 could possibly occur at the highest density peak, although finer resolution data are needed to confirm this effect.

5. The decrease of line-width towards the edge observed in L1544 (Caselli et al. 2002a) and L1521F (Chapter 3) has been found in only one other core (L694-2) with supposedly the same degree of evolution.

Acknowledgements.

We would like to thank the IRAM 30-m staff for help during the observations. We gratefully acknowledge Philippe André, Aurore Bacmann, Simone Bianchi and Laurent Pagani for providing us with electronic versions of their 1.2-mm data. We also thank Luca Dore for communicating new frequency determinations. A. C. was partly supported by NASA "Origins of Solar System Grant" (NAG 5-13050). P. C. and C. M. W. acknowledge support from the MIUR grant "Dust and molecules in astrophysical environments". C. W. L. acknowledges supports from the Basic Research Program (KOSEF R01-2003-000-10513-0) of the Korea Science and Engineering Foundation.

Chapter 3

Observations of L1521F: a highly evolved starless core

Abstract.

We observed the pre–stellar core L1521F in dust emission at 1.2mm and in two transitions each of N_2H^+, N_2D^+, $C^{18}O$ and $C^{17}O$ in order to increase the sample of well studied centrally concentrated and chemically evolved starless cores, likely on the verge of star formation, and to determine the initial conditions for low–mass star formation in the Taurus Molecular Cloud. The dust observation allows us to infer the density structure of the core and together with measurements of CO isotopologues gives us the CO depletion. N_2H^+ and N_2D^+ lines are good tracers of the dust continuum and thus they give kinematic information on the core nucleus. We derived in this object a molecular hydrogen number density n(H_2) $\sim 10^6$ cm^{-3} and a CO depletion factor, integrated along the line of sight, $f_{\rm D} \equiv 9.5\times10^{-5}/x_{\rm obs}({\rm CO}) \sim 15$ in the central 20″, similar to the pre–stellar core L1544. However, the $N(N_2D^+)/N(N_2H^+)$ column density ratio is $\sim$ 0.1, a factor of about 2 lower than that found in L1544. The observed relation between the deuterium fractionation and the integrated CO depletion factor across the core can be reproduced by chemical models if N_2H^+ is slightly (factor of $\sim$2 in fractional abundance) depleted in the central 3000 AU. The N_2H^+ and N_2D^+ line widths in the core center are $\sim$ 0.3 km s^{-1}, significantly larger than in other more quiescent Taurus starless cores but similar to those observed in the center of L1544. The kinematical behaviour of L1521F is more complex than seen in L1544, and a model of contraction due to ambipolar diffusion is only marginally consistent with the present data. Other velocity fields, perhaps produced by accretion of the surrounding material onto the core and/or unresolved substructure, are present. Both chemical and kinematical analyses suggest that L1521F is less evolved than L1544, but, in analogy with L1544, it is approaching the “critical” state.

A. Crapsi, P. Caselli, C.M. Walmsley, M. Tafalla, C.W. Lee, T.L. Bourke and P.C. Myers, 2004, Astronomy & Astrophysics, 420, 957

3.1 Introduction

The pre–stellar core L1544 has recently been the subject of much study because while apparently in hydrostatic equilibrium, there are indications that it is close to the "critical" state at which it will become gravitationally unstable and from which it will dynamically collapse (see discussions by Tafalla et al. 1998; Ciolek & Basu 2000; Caselli et al. 2002a,b). If correct, this is of fundamental importance because it defines the initial conditions for the formation of a protostar, which affects many theoretical studies of low mass star formation.
Clearly trying to extrapolate general trends from a single object is difficult and a larger number of L1544-like cores (preferably with the same external environment) should be studied. Unfortunately there are rather few other objects with similar properties due to the short timescale of this phase. According to the Ciolek & Basu (2000) model, for example, (contraction of a disk driven by ambipolar diffusion) L1544–like properties fit the model structure of a core at times 3-8 $\times 10^4$ years prior to the collapse, after an evolution of 2.6×10^6 years. Thus in that particular model, L1544 finds itself in the last few percent of its evolution prior to becoming a protostar. While this may be a somewhat too literal interpretation of the model results, it shows that "L1544–type cores" should be relatively rare.

Further progress requires the definition of what is a L1544-like core. One answer is to use current estimates of dust emission and absorption selecting cores of dust extinction upwards of 50 mag. Another approach is to say that cores which show signs of infalling gas (as does L1544, see Williams, Myers, Wilner & di Francesco 1999; Tafalla et al. 1998) are "L1544-twins". This latter indicator is complicated by the fact that at the high densities found in the nuclei of cores similar to L1544, many molecular species and in particular CO and CS freeze–out onto dust grain surfaces (see Kramer et al. 1999; Caselli et al. 1999; Bacmann et al. 2002; Bergin, Alves, Huard & Lada 2002; Jørgensen, Schöier & van Dishoeck 2002; Tafalla et al. 2002); observing such tracers implies observing the low density surrounding envelope. However, recent studies indicate that species whose

abundance is linked to that of molecular nitrogen such as N_2H^+ and NH_3 (as well as their deuterated counterparts) do not condense out in the same fashion and hence can be used as tracers of the dense gas (Bergin & Langer 1997). The extent to which this is true is debatable but it is a useful hypothesis and substantiated by the general similarity of the spatial distributions seen for example in dust emission and in maps of N_2H^+(Tafalla et al. 2002; Tafalla, Myers, Caselli & Walmsley 2004).

Caselli et al. (2002a,b) have used N_2H^+ and N_2D^+ to derive the physical, chemical and kinematical properties of L1544. They found that L1544 has a central N_2H^+ column density of 1.5×10^{13} cm^{-2} and a column density ratio $N(N_2D^+)/N(N_2H^+)$ of 0.24. The N_2H^+ line widths towards the nucleus (the dust emission peak) are roughly 0.3 km s^{-1} and decrease as one goes to positions away from the center. The line of sight velocity measured in N_2H^+(1–0) and N_2D^+(2–1) shows a gradient along the minor axis of the elliptical structure seen in 1.3mm dust emission but no clear gradient along the major axis.

In this chapter, we will study another core in the Taurus complex, L1521F (at an assumed distance of 140 parsec) using the same approach as in our study of L1544. Repeating the L1544 study carried out by Caselli et al. (2002a,b) is important because it allows us to check to what extent L1544 is an exceptional case. In order to do this we need another source which has the same general characteristics as L1544. The source selection was made using the results we obtained in a survey carried out at the IRAM-30m telescope (Chapter 2). L1521F stood out as being the only core in Taurus, besides L1544, with strong N_2D^+(2–1) emission compared to N_2H^+(1–0). This suggests enhanced deuterium fractionation implying an advanced evolutionary state (Caselli et al. 2002b). Previous observations of this object have been carried out by Mizuno et al. (1994),Onishi et al. (1996), Codella et al. (1997) and Lee, Ohashi, Moriarty-Schieven & Butner (1999). Onishi, Mizuno & Fukui (1999) also studied L1521F (which they call MC 27), and found a high central density, suggesting that this is the most evolved starless condensation in Taurus. L1521F was also noted by Lee, Myers & Tafalla (1999) as a strong infall candidate, in their survey of CS and N_2H^+ lines in starless cores, although later mapping of the two tracers has shown extended "red" asymmetry in the CS(2–1) profiles (Lee, Myers & Tafalla 2001).

In section 3.2, we describe our observational procedure. In section 3.3 we present the observational results deriving the physical characteristics of the source and analysing its

chemical and kinematical properties. In section 3.4 we discuss the observational results and the summary can be found in Section 3.5.

3.2 Observations

The observations were carried out between April 2002 and January 2003 at the IRAM-30m in three different runs.

In April 2002, we observed the core in N_2H^+(1–0), N_2H^+(3–2), N_2D^+(2–1) and N_2D^+(3–2). In general, we used the symmetric frequency switch mode and the facility autocorrelator; in Table 3.1, we summarize the main observational parameters. The frequencies of the N_2H^+(1–0), N_2D^+(2–1) and N_2D^+(3–2) have been updated following the recent determinations of (Dore et al. 2004); the values in the table refer to the $F_1\,F$ = 2 3 $\rightarrow$ 1 2, 2 3 $\rightarrow$ 1 2, and 4 5 $\rightarrow$ 3 4 hyperfine components of the N_2H^+(1–0), N_2D^+(2–1) and N_2D^+(3–2) transitions, respectively. For N_2H^+(3–2) we used the frequency of the 2 1$\rightarrow$1 0 component as determined by Caselli et al. (2002a). In the case of the April 2002 N_2D^+(3–2) observations, in order to improve the baseline quality, we used also the "Wobbler switching" mode with a 240″ throw. We reached an r.m.s. sensitivity in main-beam brightness units of about 100 mK in all lines except N_2H^+(3–2) ($\sim$ 400 mK). The pointing was checked every 2 hours by means of a 3 or 2 mm continuum scan on nearby quasars and was accurate to within $\sim 4''$.

In order to refine the maps, originally taken with a 20″ spacing, we observed in Nov. 2002 with a 10″ grid (but 5″ spacing in the inner 20 seconds). [htbp]

Between January 2003 and March 2003, we obtained continuum data at 1.2mm together with observations of $C^{18}O$ and $C^{17}O$(1–0) and (2–1). These data were taken in service mode by the IRAM staff.

The continuum data were obtained using MAMBO II, the 117-channels bolometer available at the 30m. We mapped the core within an area of 150″$\times$150″ scanning in azimuth with a 5″/sec speed and an interval between the subscans of 8″. The atmospheric attenuation was measured to be 0.14 based on tipping curves measured after the map. The data were calibrated using the sources HL Tau and L1551 for which we assumed fluxes of 0.9 Jy and 1.4 Jy respectively and the final sensitivity was 5 mJy per 10.5″ beam. The calibration error inherent in this comparison is likely to be at least ten percent due to both atmospheric fluctuations and calibration errors.

The $C^{18}O$ data were taken using the on–the–fly technique. We simultaneously mapped

Table 3.1. Telescope settings and parameters.

line	frequency GHz	HPBW $''$	F_{throw} kHz	T_{SYS} K	Δv_{res} km s^{-1}
N_2H^+(1–0)	93.1737725	26	7.5	150	0.063
N_2H^+(3–2)	279.511385	9	14.3	1900	0.021
N_2D^+(2–1)	154.217137	16	7.5	370	0.038
N_2D^+(3–2)	231.321966	10	14.3	750	0.050
$C^{18}O$(1–0)	109.782160	22	...	170	0.026
$C^{18}O$(2–1)	219.560319	11	...	450	0.033
$C^{17}O$(1–0)	112.358988	21	7.5	230	0.026
$C^{17}O$(2–1)	224.714368	11	14.3	730	0.052

Note. — Col. (2) line rest frequency; Col. (3) Half Power Beam Width; Col. (4) Frequency Throw; Col. (5) Syst. Temperature; Col. (6) Channel Spacing.

the $C^{18}O$(1–0) and $C^{18}O$(2–1) using both polarizations for each line. The area covered was $150'' \times 150''$ and was scanned in the Right Ascension direction; the distance between the subscans was $5''$ as was the angular separation between two successive dumps. We also obtained a 9 points map in $C^{17}O$(1–0) and $C^{17}O$(2–1) centered at the dust peak and spaced by $20''$.

3.3 Results

3.3.1 Integrated intensity maps and continuum emission

We show the observed map of the 1.2mm dust continuum in Figure 3.1, and the map of integrated line intensity, obtained in the observed transitions of N_2H^+, N_2D^+, and $C^{18}O$, in Figure 3.2. The reference position for these maps is (04:28:39.8, 26:51:35) in J2000 coordinates.

The bolometer map was reduced with the IRAM standard reduction program NIC. From Figure 3.1, we see that the observed emission has a "cometary" structure in the sense that the low level contours are well–fitted by an ellipse with the maximum offset

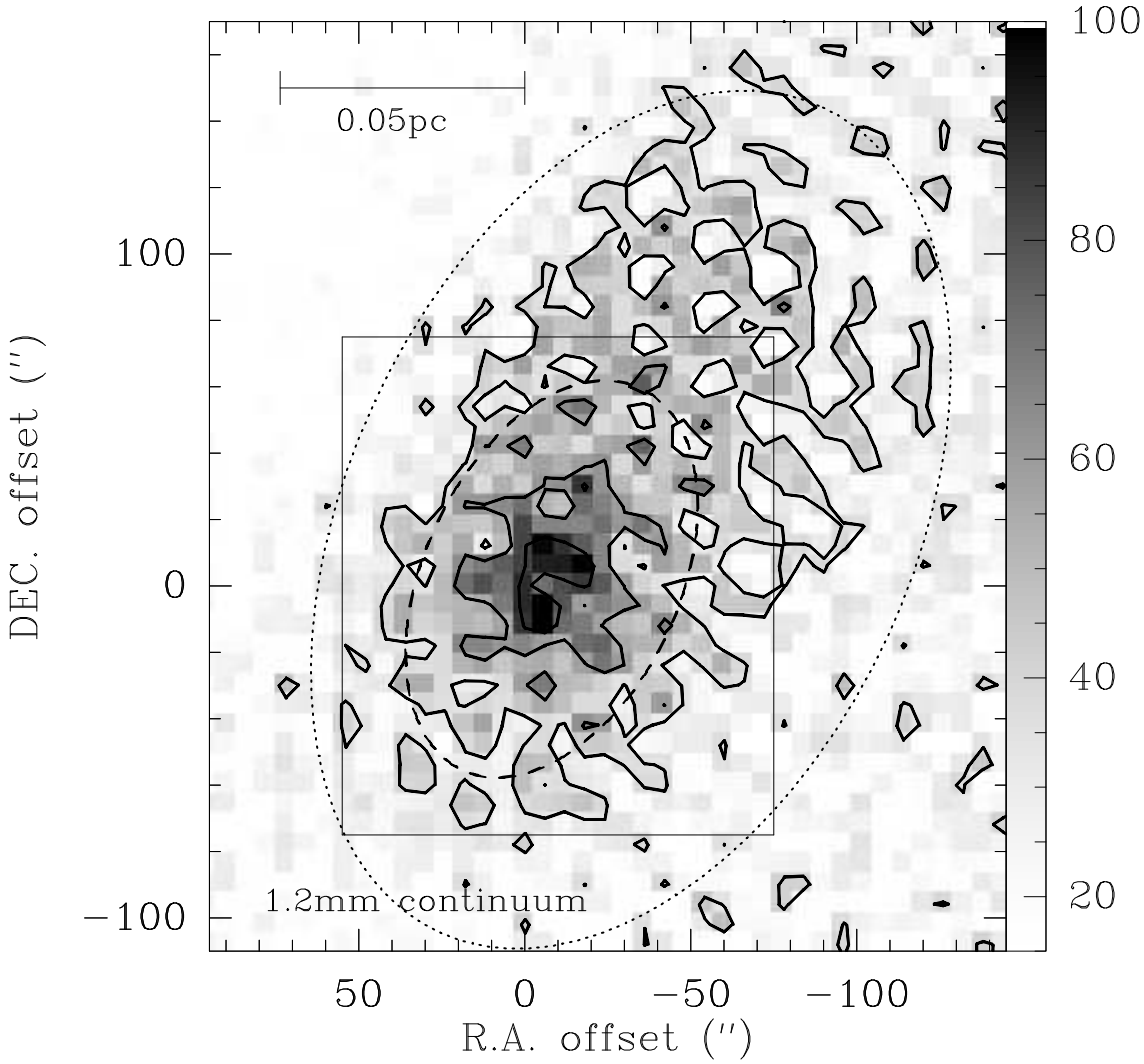

Figure 3.1 Dust emission from L1521F. Levels are 30, 55 and 80 mJy/beam. Reference position is RA: 04:28:39.8 DEC: 26:51:35 (J2000). The dashed ellipse best fits the core structure with a 2D gaussian. The dotted ellipse is the result of a 2D–gaussian fit to the whole map, including the more extended emission. The black rectangle shows the area mapped in line observations (see Figure 3.2).

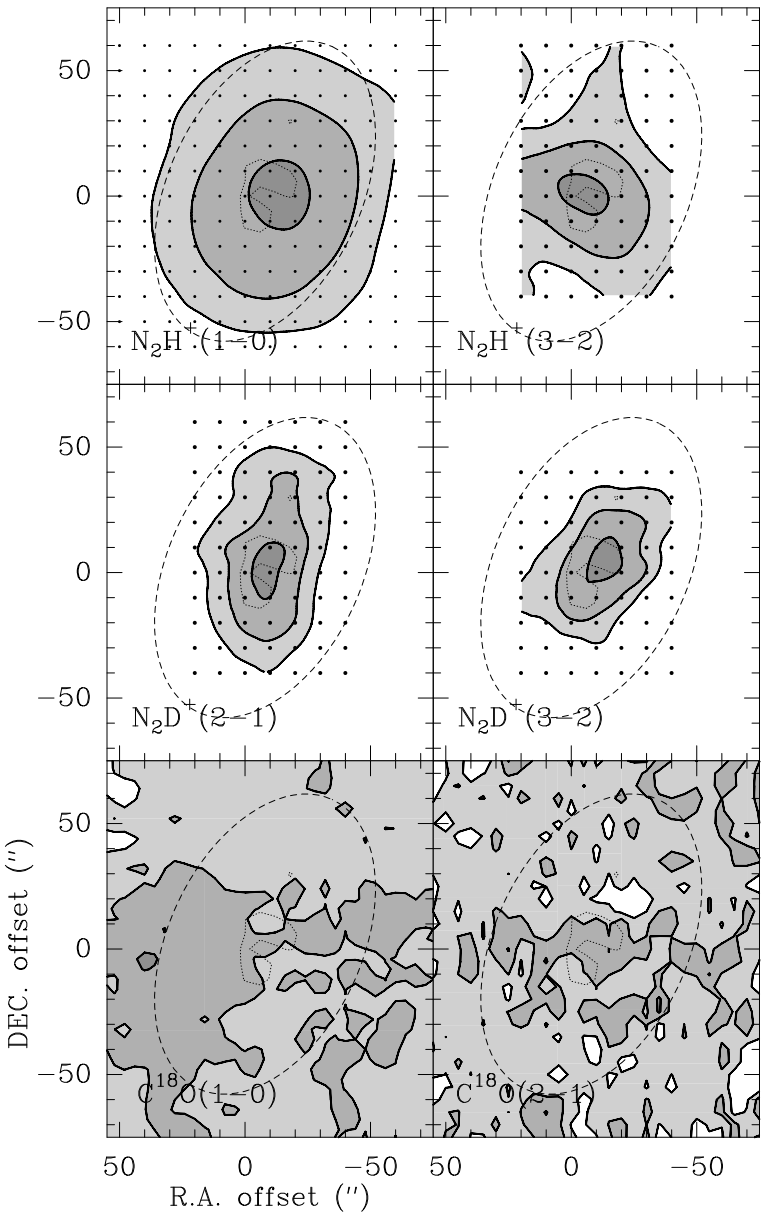

Figure 3.2 L1521F integrated intensity maps in the observed molecular transitions. Contour levels are 45, 70, 95% of the relative peak in each map (whose values are: 5.9, 0.74, 1.1, 0.33, 2.5 and 2.3 K km s^{-1}in N_2H^+(1–0), N_2H^+(3–2),N_2D^+(2–1),N_2D^+(3–2),$C^{18}O$(1–0) and $C^{18}O$(2–1) respectively). The N_2H^+(3–2) data were smoothed to 26″ resolution to increase S/N and help the comparison with N_2H^+(1–0); for the same reasons N_2D^+(3–2) was smoothed to 16″ (the HPBW of the 30m antenna at the frequency of the the N_2D^+(2–1) line). We overlaid on each map the ellipse which best fits the dust emission structure (in dashed line) and the 80 mJy/beam contour (dotted line).

from the center. We can fit the general elliptical structure of the core with a 2D-gaussian centered at offset ($-30''$,$20''$) with full width half–power dimensions of $274'' \times 170''$and position angle 25°. If the more extended emission is not included in the fit, the 2D–gaussian is centered on the dust peak position at ($-10''$,$0''$), has half–power dimensions of $127'' \times 77''$, a position angle of 25° and an aspect ratio equal to 1.6. The peak intensity is 90 mJy/beam.

The spectral line data were reduced using the standard IRAM package CLASS. A summary of line parameters at the dust peak is given in Table 3.2 and the corresponding spectra are shown in Figure 3.3.

The spectra shown in Figure 3.3 (as well as the values in Table 3.2) have been derived from data gaussian–smoothed to a resolution of $26''$ in the cases of N_2H^+ and N_2D^+ , but unsmoothed in the case of $C^{18}O$. These are also the effective resolutions of the N_2H^+ maps shown in Figure 3.2 (the two N_2D^+ maps are smoothed to $16''$, the angular resolution at the (2–1) frequency).

One clear result from Figure 3.3 is that in L1521F there is evidence for an "infall signature" although less marked than in L1544, where it is attributed to extended infall onto the core (Williams, Myers, Wilner & di Francesco 1999) or to central infall in a depleted core nucleus (Caselli et al. 2002a). In fact, we see evidence for asymmetric profiles, with the blue peak brighter than the red peak, in N_2H^+ (1–0) (where we derive an optical depth of order 4 in the main component based on our fit to the hyperfine satellites), but the two peaks are not clearly separated as in the case of L1544.

It is interesting to note that two peaks are present in the spectrum of N_2H^+(3–2) line toward the offset (-10,10), as shown in Figure 3.4. The hyperfine structure (hfs) fit to the N_2H^+(3–2) line, assuming the presence of two velocity components along the line of sight, gives $V_{\rm LSR\,1}$ = 6.35±0.1 km s^{-1} and $V_{\rm LSR\,2}$ = 6.55±0.04 km s^{-1}. The line widths of the two components are Δv_1 = 0.15±0.02 km s^{-1} and Δv_2 = 0.19±0.06 km s^{-1}, marginally (factor $\lesssim$ 1.5) broader than the thermal N_2H^+ line width at 10 K. Although this result should be confirmed with higher sensitivity data, the velocities are consistent with those of the N1 and N2 (N_2H^+) clumps observed by Shinnaga, Ohashi, Lee & Moriarty-Schieven (2004) with interferometric observations. The hfs fit to the N_2H^+(1–0) line, assuming two velocity components and fixing the velocities to the values found with the (3–2) line, is consistent with the observed spectrum (if the two velocities are not fixed, the hfs fitting procedure applied to the N_2H^+(1–0) spectrum does not converge, probably because the two components are not well separated). This suggests that the two clumps observed by

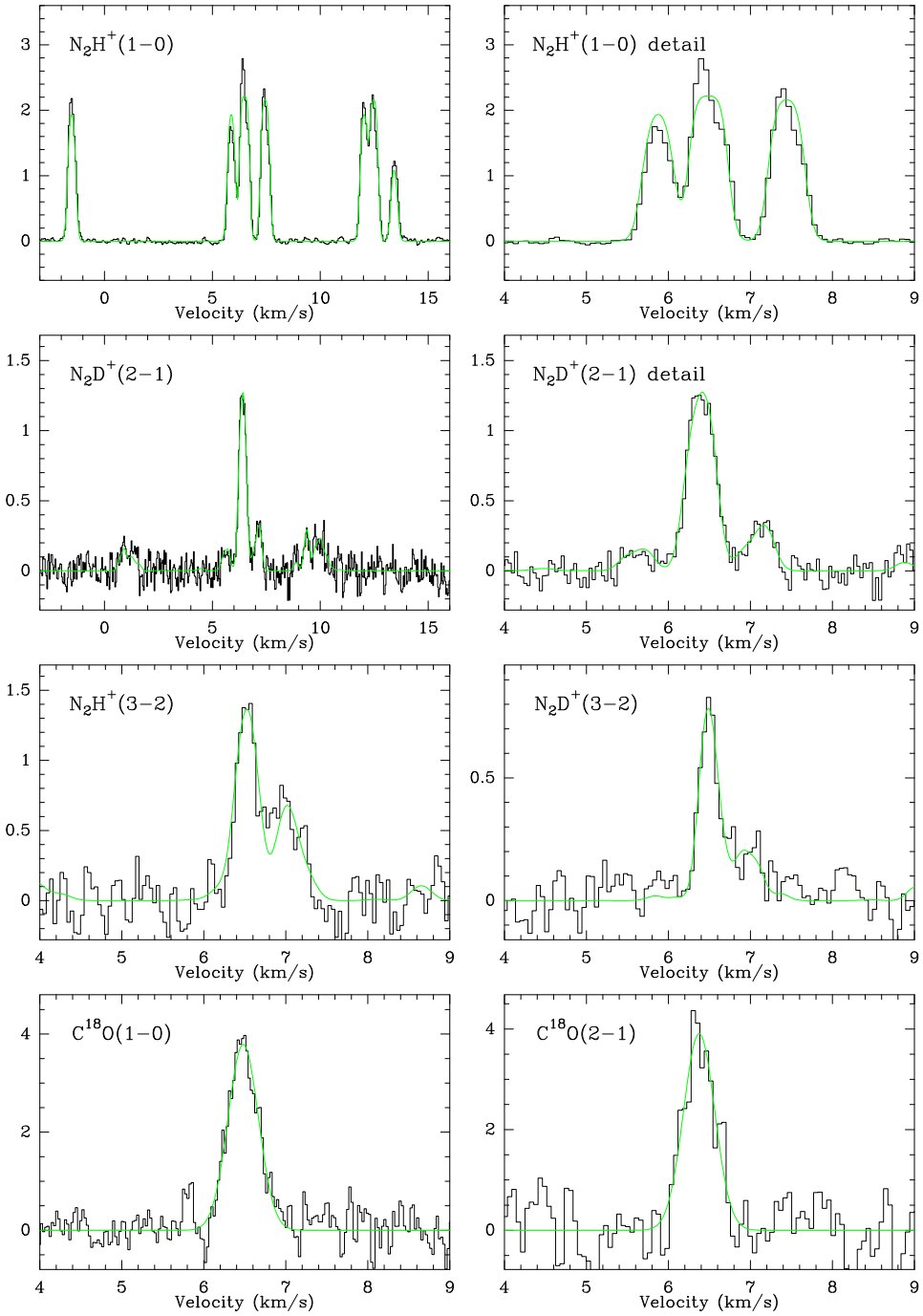

Figure 3.3 Spectra of N_2H^+(1–0), N_2H^+(3–2), N_2D^+(2–1), N_2D^+(3–2), $C^{18}O$(1–0), and $C^{18}O$(2–1) towards the dust emission peak in L1521F. A fit of the hyperfine pattern (or in the case of $C^{18}O$ a gauss fit) of the lines assuming identical excitation temperatures for all satellites is also shown (dashed) for comparison.

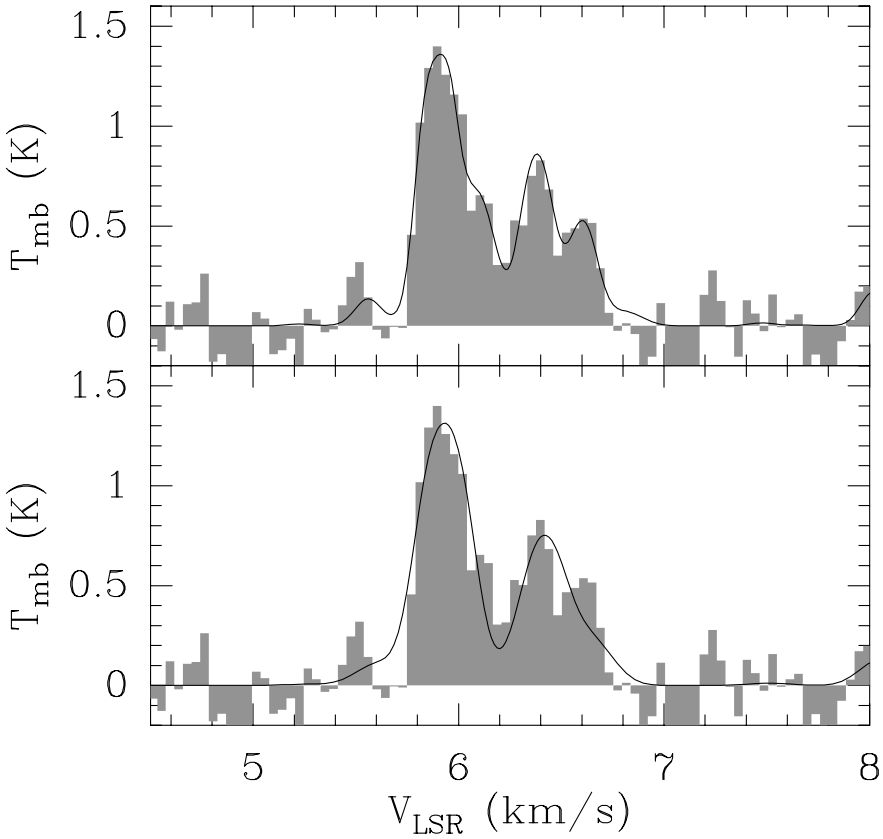

Figure 3.4 Enlargement of the N_2H^+(3–2) spectrum of Figure 3.3 toward offset (−10,10), which shows tentative evidence for a double–peaked feature. The top panel show the line profile (grey histogram) and the hfs fit (black curve) assuming two velocity components; the bottom panel show the hfs fit assuming one velocity component. The velocities of the two components concide with the LSR velocities of clumps N1 and N2 observed by Shinnaga, Ohashi, Lee & Moriarty-Schieven (2004) in their interferometric observations, see Figure 3.11 for reference.

Shinnaga, Ohashi, Lee & Moriarty-Schieven (2004) in N_2H^+(1–0) are also present in our single dish data, although the N_2H^+(1–0) extended emission partially hides the features arising from the central region.

Figure 3.2 shows that L1521F has in common with several other cores (see also Tafalla et al. 2002; Caselli et al. 2002a,b) the property that while the maps of the nitrogen bearing molecules have a similar appearance to those observed in dust emission, maps in rare CO isotopologues such as $C^{18}O$ show no correlation with the dust. In fact, the distribution of $C^{18}O$(1–0) and (2–1) is essentially flat over the area we have mapped, suggesting perhaps

Table 3.2. Line parameters derived from hyperfine structure fitting at position $(-10'',0'')$. The values refer to spatially averaged spectra ($26''$ beam).

line	V_{LSR} km s^{-1}	ΔV km s^{-1}	τ	$\int T_{MB} dV$[b] K km s^{-1}	T_{ex} K
N_2H^+(1–0)	6.472±0.001	0.299±0.001	17.9±0.1	5.859±0.016	4.94±0.03
N_2H^+(3–2)	6.388±0.010[a]	0.290±0.030	1.4±1.0	0.692±0.075	5.1±3.7
N_2D^+(2–1)	6.505±0.004	0.268±0.010	2.2±0.4	0.978±0.026	4.6±0.9
N_2D^+(3–2)	6.507±0.006	0.222±0.024	1.2±0.9	0.332±0.029	4.1±3.2

[a]The N_2H^+(3–2) frequency is as in Caselli et al. (2002a), whereas for the other lines we used the updated values determined by Dore et al. (2004).

[b] The integration includes all hyperfines.

that the layer sampled in $C^{18}O$ is either in the background or foreground relative to that seen in dust emission.

We have been able to make some estimate of the optical depths of the observed $C^{18}O$ lines by comparison with our 9-point $C^{17}O$ map ($20''$ spacing centred on $(-5,-5)$). From the integrated intensity ratio of the $C^{18}O$ and $C^{17}O$(1–0) lines and assuming an intrinsic abundance ratio $[C^{18}O]/[C^{17}O]$ of 3.65 (from $[^{18}O]/[^{17}O]$ = 3.65, Penzias; 1981 see Kramer et al. 1999for a discussion of the validity of these techniques), we can put in general upper limits on the optical depth of $C^{18}O$(1–0) of order unity. At the $(-5,-5)$ and $(-25,-5)$ offsets, there is however evidence that $C^{18}O$(1–0) is optically thick and in fact we derive $C^{18}O$(1–0) optical depths of 1.0 and 1.5 respectively at these two offsets (errors 50%). In these positions we used the $C^{17}O$(1–0) data and, assuming T_{ex} = 10 K (consistent with the observed $C^{17}O$(2–1)/(1–0) line ratio) and $[^{18}O]/[^{17}O]$ = 3.65, we found an average $C^{18}O$ column density of $\sim 2\times10^{15}$ cm^{-2} in the central $25''$.

It is also interesting that we find that N_2H^+(1–0) and dust emission maps have similar sizes, whereas N_2D^+ maps are somewhat smaller. Fitting a 2D gaussian to the N_2H^+ and N_2D^+ maps in the same fashion as for the dust emission, we find the parameters given in Table 3.3 for the angular sizes of N_2H^+ and N_2D^+ in L1521F. We deduce from these data a linear size for L1521F seen in N_2H^+(1–0) of roughly 14000 AU and dimensions in N_2D^+(2–1) of 13000 × 6000 AU. It is interesting to note the smaller sizes derived in the

Table 3.3. Angular Dimensions derived from two dimensional gauss fits to maps in N_2H^+ and N_2D^+

line	Int. K km s^{-1}	$\Delta\alpha$ $''$	$\Delta\delta$ $''$	Maj. Axis $''$	Min. Axis $''$	P.A. $^\circ$
1.2mm		-8	2	127	77	-25
N_2H^+(1–0)	5.82	-12	1	110	90	-18
N_2H^+(3–2)	0.68	-7	1	90	67	+30
N_2D^+(2–1)	1.02	-9	4	90	46	-9
N_2D^+(3–2)	0.34	-11	5	63	38	-33

Note. — Col. (2) Integrated intensity at peak Col. (3) R.A. offset of peak; Col. (4) DEC offset of peak; Col. (5) Major axis size (FWHM); Col. (6) Minor axis size (FWHM); Col. (7) Position angle measured East of North.

higher J transitions of both species, suggesting that they are sampling somewhat higher density gas. The 1.2mm dust continuum on the other hand is more extended suggesting that either an increase in excitation or in abundances is causing the N_2D^+ and N_2H^+(3–2) line emission to increase in relative strength toward the dust peak. Notable also are the large aspect ratios (1.6–1.9) observed in N_2D^+ suggesting an ellipsoidal or triaxial form for the high density core.

3.3.2 Density and mass distribution

We expect the observed continuum emission at mm wavelengths to be optically thin and can relate the 1.2mm flux to the H_2 column density under the approximation of constant dust emissivity and temperature:

$$N(H_2) = \frac{S_{1.2mm}}{\Omega_{\rm beam} B_\nu(T)\, \kappa_{1.2mm}\, m},$$

where $N(H_2)$ is the averaged H_2 column density , $S_{1.2mm}$ is the emitted 1.2mm flux density from the core, $\Omega_{\rm beam}$ is the telescope beam solid angle, $\kappa_{1.2mm}$ is the dust absorption coefficient per gram of gas at 1.2mm, $B_\nu(T)$ is the Planck function at temperature T, and m the mean molecular mass. In our calculations we used a dust temperature $T_{\rm dust}$ = 10 K,

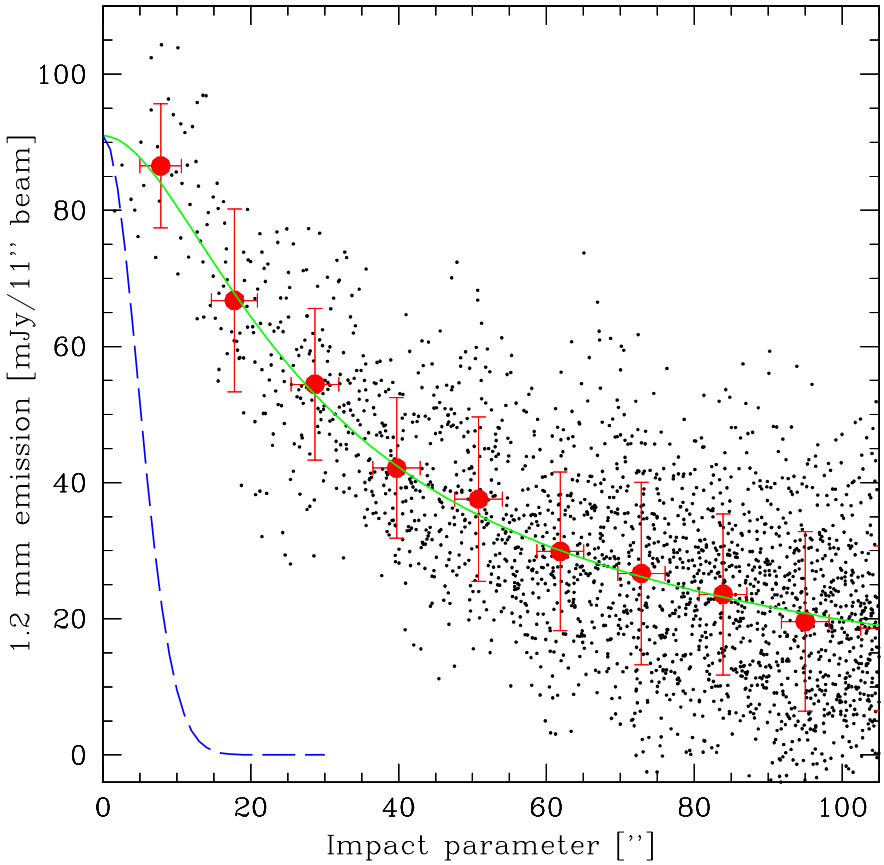

Figure 3.5 Circularly averaged dust emission fitted with the expression $n_0/(1+(r/r_0)^{\alpha})$ convolved with a 10.5″ gaussian. The parameters that best fit the L1521F data are $n_0 = 10^6$ cm^{-3}, $r_0 = 20''$ and $\alpha = 2$. Dots with error bars are binned data and the dashed curve shows the observational beam.

close to the gas temperature found by Codella et al. (1997) using ammonia data (9.1 K), a dust opacity $\kappa_{1.2mm} = 0.005$ cm^2 g^{-1} (Andrè, Ward-Thompson & Motte 1996) and m = 2.33 amu (with uncertainties of typically 50%; see e.g. Bianchi et al. 2003 and Gonçalves, Galli & Walmsley 2004). This expression can be integrated over the 1.2mm map to derive the total gas mass.

In this fashion, we derive a core mass from the continuum measurements, within the large ellipse in Figure 3.1, of 5.5±0.5 $M_{\odot}$ corresponding to an integrated total flux of 3.0 ± 0.3 Jy. (The error is dominated by errors in calibration and baseline removal.)

Within the $26''$ beam, used for our line measurements, the enclosed mass is $0.7M_{\odot}$. It is interesting to note that $5M_{\odot}$ and $0.8M_{\odot}$ are the average total mass and 1 Jeans masss in the Taurus Molcular Cloud complex (Goodwin, Whitworth & Ward-Thompson 2004).

For the purpose of comparison with model calculations, we have used the 1.2 mm continuum data to estimate the density distribution under the assumption of spherical symmetry. This inevitably involves a rough approximation since the L1521F core clearly *is not spherically symmetric* (the aspect ratio in the 1.2mm continuum emission is 1.6, see Tab. 3.3) and would be better approximated with an ellipsoid.

Nevertheless, we have followed the technique adopted by Tafalla et al. (2002) and fit our data with a model of the form:

$$n_{H_2}(r) = \frac{n_0}{1+\left(\frac{r}{r_0}\right)^{\alpha}},$$

We thus circularly averaged the 1.2 mm data around the peak and used a χ^2 routine to fit the dust profile using the above model integrated along the line of sight and convolved with a $10.5''$ gaussian. The result of the fitting procedure can be seen in Figure 3.5 . The parameters that best fit our data are $n_0 = 10^6$ cm^{-3}, $r_0 = 20''$ (corresponding to 0.014 parsec or 2800 AU) and $\alpha = 2.0$.

3.3.3 CO freeze–out

The comparison between the dust continuum emission and the $C^{18}O$ integrated intensity map allows the determination of the amount of CO freeze–out onto dust grain surfaces, integrated along the line of sight. This is possible because the millimeter continuum data furnish $N(H_2)_{1.2mm}$, the column density of molecular hydrogen across the core, assuming optically thin conditions. The same quantity is obtained from $C^{18}O$ lines ($N(H_2)_{CO}$), again under the assumption of optically thin conditions, and adopting the relation between CO and H_2 valid in undepleted conditions ($[CO]/[H_2] \simeq 9.5\times10^{-5} \equiv x(CO)_{can}$, the "canonical" CO abundance value; Frerking, Langer & Wilson 1982). From the $N(H_2)_{1.2mm}/N(H_2)_{CO}$ column density ratio, the integrated CO depletion factor (f_D), or the ratio between the canonical and the observed CO abundance ($x(CO)_{can}/x(CO)_{obs}$), is easily derived.

In practice, this process requires the division of the 1.2mm dust continuum emission ($\mathcal{F}_{1.2mm}$[mJy/beam] = $S_{1.2mm}$[mJy]/Ω_{beam}) map by the $C^{18}O$ integrated intensity ($W_{C^{18}O}$) map. The map–division has been carried out using the IRAM image manipulation soft-

ware GRAPHIC, after degrading the continuum map to the angular resolution of the $C^{18}O$(1–0) observations (22″) so that the integrated depletion factor can be expressed by:

$$\begin{aligned} f_{\rm D} &= x({\rm CO})_{\rm can} \times \frac{N(H_2)_{1.2{\rm mm}}}{N(C^{18}O)} \frac{[^{18}{\rm O}]}{[^{16}{\rm O}]} \\ &= 8.5 \times 10^{-2} \frac{\mathcal{F}_{1.2{\rm mm}}({\rm mJy/22''beam})}{W_{C^{18}O}({\rm K\,km\,s^{-1}})}. \end{aligned} \tag{3.1}$$

To derive eq. (3.1) we have assumed a dust temperature $T_{\rm dust}$ = 10 K, $\kappa_{1.2{\rm mm}}$ = 0.005 cm^2 g^{-1}, and an abundance ratio $[^{16}{\rm O}]/[^{18}{\rm O}]$ = 560 (Wilson & Rood 1994).

There are several *caveats* to the above procedure. One is that the "canonical abundance" appears to vary from cloud to cloud (Lacy, Knacke, Geballe & Tokunaga 1994; Alves, Lada & Lada 1999; Kramer et al. 1999) and is roughly one third of the diffuse cloud carbon gas phase abundance (Sofia, Cardelli, Guerin & Meyer 1997). Given that CO is expected to represent essentially all the gas phase carbon in molecular clouds, this suggests depletion of carbon in some form (not necessarily as solid CO) even on the outskirts of cores (we note that the direct study of CO solid state features in Taurus by (Chiar, Adamson, Kerr & Whittet 1995) shows that solid CO towards 4 field stars in Taurus is less than 40% of the canonical gas phase CO abundance and is observed for extinctions $A_{\rm V}$ greater than 6 magnitudes). Thus we conclude that in particular cases such as L1521F, it is quite possible that we are using a value of $x({\rm CO})_{\rm can}$ which is a factor of order 2 too large or small thus influencing the values of $f_{\rm D}$ which we derive but not the trends over our map.

Another problem is that the values of $f_{\rm D}$ which we derive are integrated along the line of sight in a situation where the observed $C^{18}O$ emission forms in an outer shell whereas the dust emission mainly emanates from the dense core nucleus. As a consequence, we observe $C^{18}O$ mainly from foreground and background gas which (see Figure 3.2) has an essentially flat distribution over the region mapped by us. One concludes that our values of $f_{\rm D}$ are strict lower limits to the CO depletion *in the core nucleus* from which dust emission is observed. It is also the case that in this situation, the form of our map of $f_{\rm D}$ is essentially that of the dust emission (as we indeed find, see eq. 3.2). The *local* distribution of the CO depletion factor (which we call $\mathcal{F}_{\rm D}$, see below) may differ greatly and be much more highly peaked than in our map. Nevertheless, the $f_{\rm D}$ values derived by us are direct observables and we have therefore used them for the purpose of correlating with parameters such as the observed deuterium fractionation. We have also used them for model comparisons (sections 3.4.1 and 3.4.1) bearing in mind the above discussion.

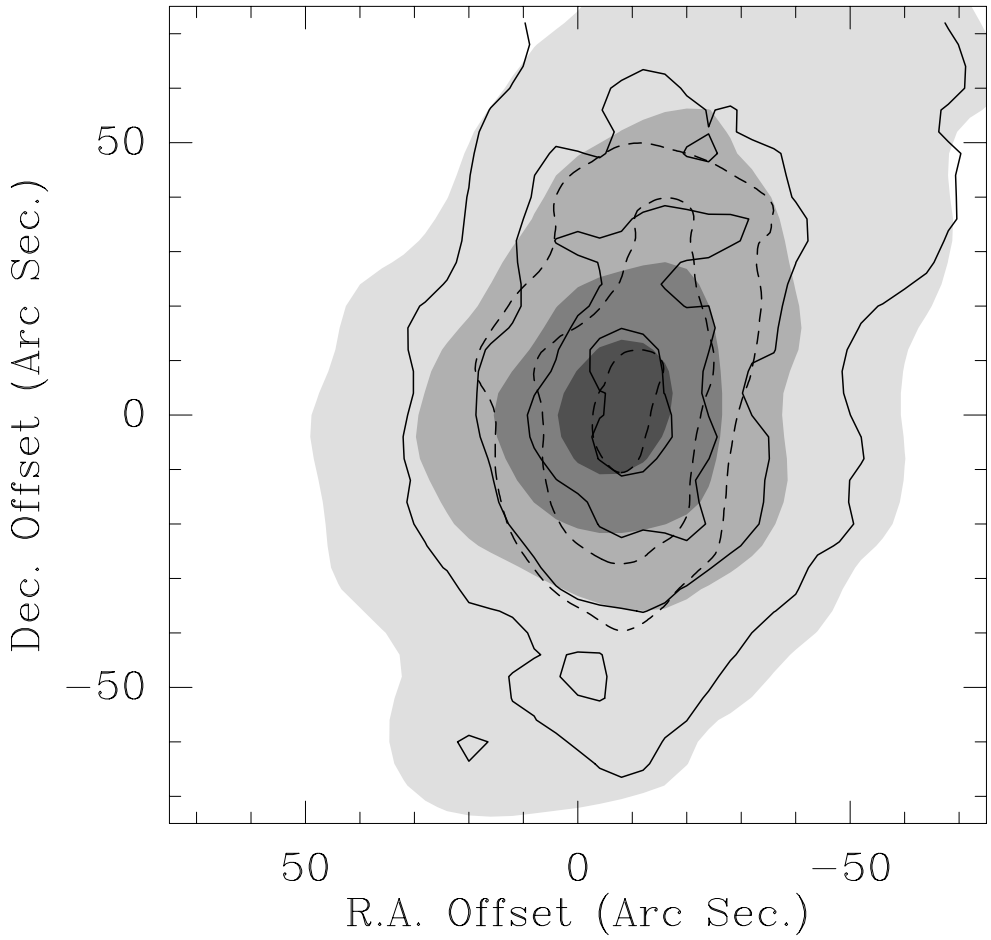

Figure 3.6 CO depletion factor (full contours) against dust emission smoothed to a 22″ beam (grey scale). f_D contours range between 6 and 15, in steps of 3. The maximum value of f_D is 18 and is located at offset (0,9). Note the good correspondence between the distribution of N_2D^+(2–1) (dashed contours) and the CO depletion map.

In Figure 3.6 the f_D map is shown (thick contour) overlapped with the smoothed 1.2mm map (grey scale) and the N_2D^+(2–1) map (dashed contours). The CO depletion factor increases between 6 at the lowest contour of the 1.2mm map ($\mathcal{F}_{1.2mm}$ = 95 mJy/22″ beam) to 18 at the peak position (offset [0,9]), which is 11″ off the millimeter dust emission peak (offset [−8,+2]), where $\mathcal{F}_{1.2mm}$ = 320 mJy/22″ beam). From Figure 3.6 we immediately see that f_D correlates with the N_2D^+ emission (and deuterium fractionation, see Sect. 3.3.4) and the 1.2 mm dust flux. The good correlation between f_D and $\mathcal{F}_{1.2mm}$ is also evident in Figure 3.7, where f_D is plotted as a function of $N(H_2)_{1.2mm}$ ($\equiv 4.25\times10^{20}\mathcal{F}_{1.2mm}$ mJy/(22″ beam), with the assumptions on T_{dust} and $\kappa_{1.2mm}$ as described

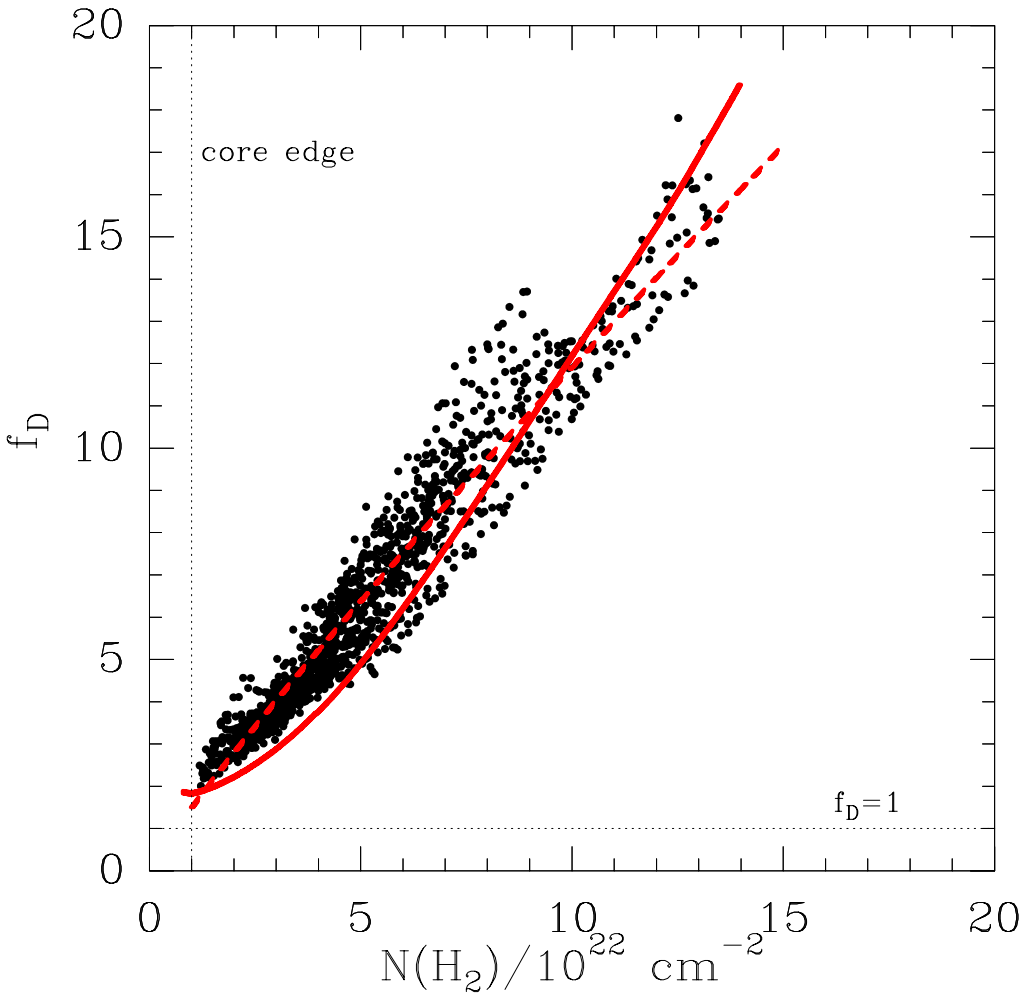

Figure 3.7 Integrated CO depletion factor f_D against H_2 column density as derived from the data in Figure 3.6. The dashed curve is the linear least fit to the data, whereas the solid curve is the f_D vs. $N(H_2)$ relation found in the simple model described in Sect. 3.4.1.

above). Thus, in L1521F, and with the caveats discussed above, f_D is linearly dependent on the H_2 column density ($N(H_2)$); the best fit to the data in Figure 3.7 (dashed curve) gives:

$$f_D = 1.5 \left[\frac{N(H_2)}{10^{22} \mathrm{cm}^{-2}} \right]^{0.9} . \quad (3.2)$$

In retrospect, this is not surprising as $N(C^{18}O)$ does not vary greatly over the map. We note that f_D is always $\gtrsim 2$ in the region traced by the present observations, suggesting

that even at the core edges (where $N(H_2) \sim 10^{22}$ cm^{-2}) CO molecules are partially ($\simeq$ 30%) frozen onto grain mantles. This result is consistent with the average value of CO depletion ($\simeq$ 25%) gauged from observations of solid CO features in the direction of background stars in the Taurus complex (Chiar, Adamson, Kerr & Whittet 1995). The thick curve in Figure 3.7 is the result of a simple chemical model of a centrally concentrated cloud, where CO depletion is taken into account, and where the CO abundance has been integrated along the line of sight to obtain the observed f_D ($f_D = \int F_D(r)\, dl / \int dl$, with $F_D(r)$ being the CO depletion factor *within* the core, thus function of the cloud radius r; see Section 3.4.1). We anticipate here that the f_D value at the cloud center is only a very small fraction ($\sim 1\%$) of F_D in the central few thousand AU of the core.

3.3.4 N_2H^+– N_2D^+ column densities, deuterium fractionation, and volume densities

The N_2H^+ and N_2D^+ column densities have been determined using the "constant–T_{ex}" (CTEX) approximation, which reduces to simple analytic expressions (see Appendix A in Caselli et al. 2002b), and the Large Velocity Gradient (LVG) approximation. Both approaches give reasonable column density estimates as long as optical depths are small. When, as for example for N_2H^+(1–0), the optical depths in the main hyperfine satellites are large, one is best (independent of method) to use the weakest of the satellites or alternatively the optical depth inferred from the intensity ratio of the weakest satellite to the strong main components. The errors in any case stem from the difficulties in estimating the optical depth of thick lines compounded with possible non-LTE effects for the hyperfine satellites (Caselli, Myers & Thaddeus 1995). Errors due to the estimate of the partition function (i.e. the fraction of the species in unobserved levels) appear to be less. We in general report column densities for N_2H^+ using the CTEX approach based on the integrated intensity of the weakest satellite of N_2H^+(1–0) and for N_2D^+ assuming optically thin conditions. From comparison between the different approaches employed by us, we estimate the column density errors to be 30 percent.

We have also used LVG estimates to infer the density towards the peak and edges of our N_2H^+ map. Here, we assume a temperature of 10 K and have used rates from Green (1975) for collisions of He with N_2H^+. Based on the values in Tab. 3.2 (data smoothed to 26″ spatial resolution) for the integrated intensities of N_2H^+, we find $n(H_2) = 4 \times 10^5$ cm^{-3} towards the dust peak of L1521F and 2.5×10^5 cm^{-3} 30″ North (offset [−10, 30]). For N_2D^+(2–1) and (3–2), the corresponding numbers are 6×10^5 cm^{-3} and 3.5×10^5 cm^{-3},

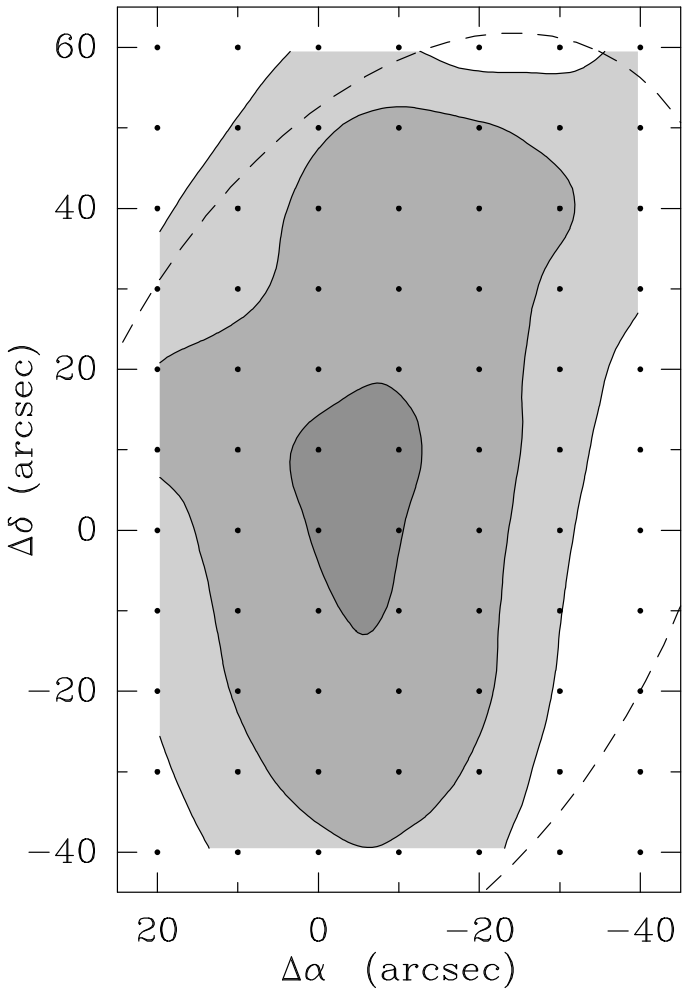

Figure 3.8 $[N_2D^+]/[N_2H^+]$ in the central region as estimated from CTEX calculations (see Sect. 3.3.4). Levels are 0.066, 0.078, and 0.091. The dashed contour is the small ellipse of Figure 3.2.

at the peak and $(-10, 30)$ offset positions, respectively. These values are similar to the corresponding values for L 1544 consistent with the idea that they have similar density distributions. The density estimates are somewhat smaller than estimates based on the dust emission, probably due to the different (factor of 2.4 lower) spatial resolution[1], and consistent perhaps with the idea that N_2H^+ is abundant in a shell outside but close to the dust peak. However, given that the LVG method assumes homogeneous conditions, the

[1]The central density obtained with the continuum data reduces to $\sim 6\times10^5$ cm^{-3} when averaged within $26''$.

LVG–derived densities are averages along the line of sight, thus lower values are expected when compared to the continuum data analysis, which takes into account the core density structure.

The deuterium fractionation is directly estimated from the $N(N_2D^+)/N(N_2H^+)$ column density ratio ($\equiv R_{\rm deut}$), and the $R_{\rm deut}$ map in L1521F, assuming CTEX conditions, is shown in Figure 3.8. $R_{\rm deut}$ ranges between ~ 0.02 at the core edge to 0.1 in a region about $20''$ in size and centered on the dust peak position. The peak value of $R_{\rm deut}$ is about a factor of 2 smaller than that found in L1544 (Caselli et al. 2002b). We note that the column density of N_2H^+ is similar in the two cores, and that the factor of 2 of difference in deuterium fractionation is due to the (factor of 2) larger N_2D^+ column density in L1544. This suggests that, although the two cores are similar in structure, L1521F is probably slightly less evolved than L1544 (see Sect. 3.4).

3.3.5 Line width vs. impact parameter

Quiescent starless cores mapped in NH_3(1,1) and N_2H^+(1–0) lines typically show a "velocity coherent" zone of nearly constant line width (Δv) within the half-maximum contour map, followed by a Δv rise at larger distances from core center (e.g. Goodman, Barranco, Wilner & Heyer 1998). There are however exceptions to this general trend, as pointed out by Caselli, Benson, Myers & Tafalla (2002). In particular, L1544 shows a significant increase of N_2H^+ and N_2D^+ (but not $H^{13}CO^+$ and DCO^+) line widths toward the center (factor of 1.5 within $\sim 50''$; Caselli et al. 2002a). This increase has been interpreted as evidence of infall in the central few thousands AU, where CO and related species (such as $H^{13}CO^+$ and DCO^+) are heavily depleted. Indeed, the line–width increase is consistent with models of ambipolar diffusion (see Sect. 3.4.2).

The same trend has been observed in L1521F using N_2H^+ and N_2D^+ lines, and in Figure 3.9 we show the results obtained in N_2H^+(1–0) lines (the line width corrected for optical depth, or the intrinsic line width, is plotted). The figure also shows two theoretical predictions which will be discussed in Sect. 3.4.2. The decrease of the intrinsic line width with impact parameter in L1521F, although not as steep as in L1544, is clear in Figure 3.9, where the average value of Δv within bins of $15''$ (see big dots) ranges between 0.3 km s^{-1} at the dust peak to 0.25 km s^{-1} at a projected distance of $80''$.

One might interpret this line width gradient as being due to increased optical depth towards the dust peak. This however seems unlikely as illustrated in Figure 3.10, where the profiles of the isolated hyperfine component of the N_2H^+(1–0) line along the 45° and

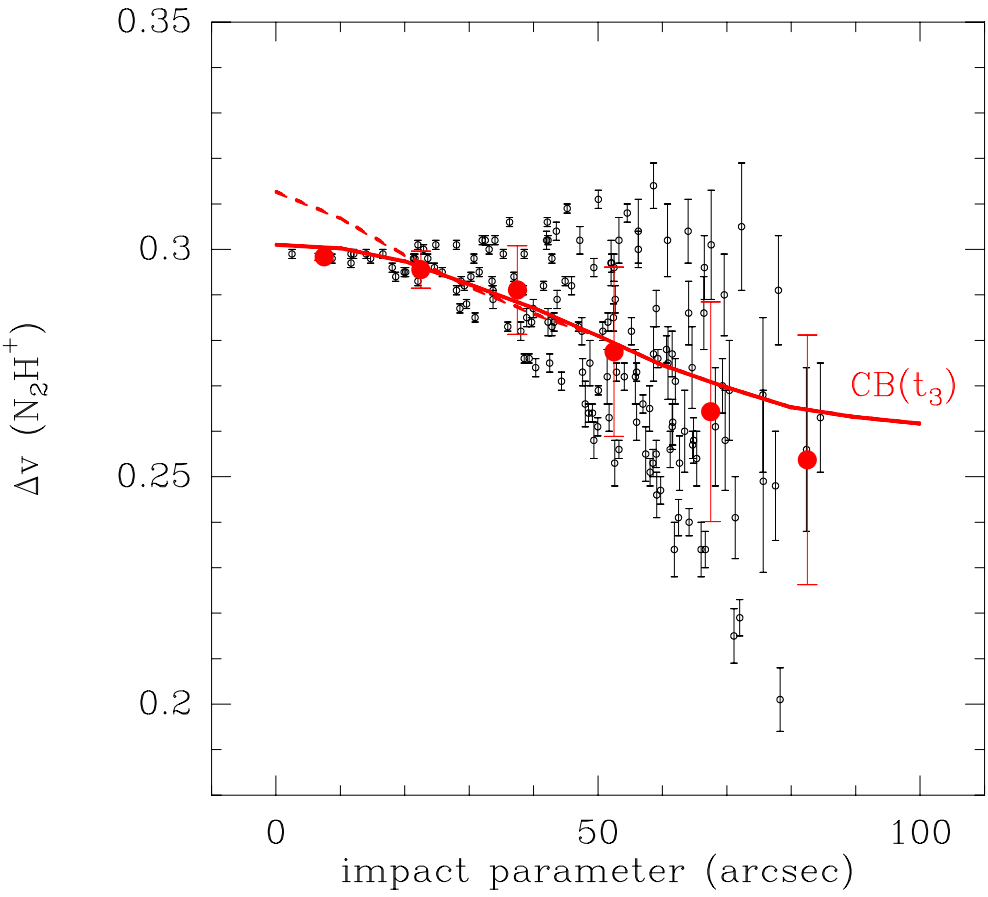

Figure 3.9 N_2H^+(1–0) intrinsic line–width vs. impact parameter. The big dots are averages of the data points within 15″ bins. The solid curve is the $\Delta v - b$ relation derived from the velocity field predicted by the t_3 model of Ciolek & Basu (2000) (see Caselli et al. 2002a), where a constant turbulent field across the cloud has been included, and the dashed curve is from the same model but accounting for the presence of a central molecular "hole" of 2000 AU in size (see text).

-45° axes, passing through the dust peak position, are shown. If the line is self–absorbed toward the core center, the hyperfine components with the largest statistical weight will be broadened compared to the weakest ones, affecting the hfs fit. However, we performed gaussian fits to all the hyperfines components, finding the same Δv values within the uncertainties. In fact, a similar trend is also observed if one plots the line width of the $F_1\,F$ = 1 0 → 1 1 (or weakest) component of the N_2H^+(1–0) line versus the impact parameter. This line, being thin and symmetric across the core, is not affected by self–absorption.

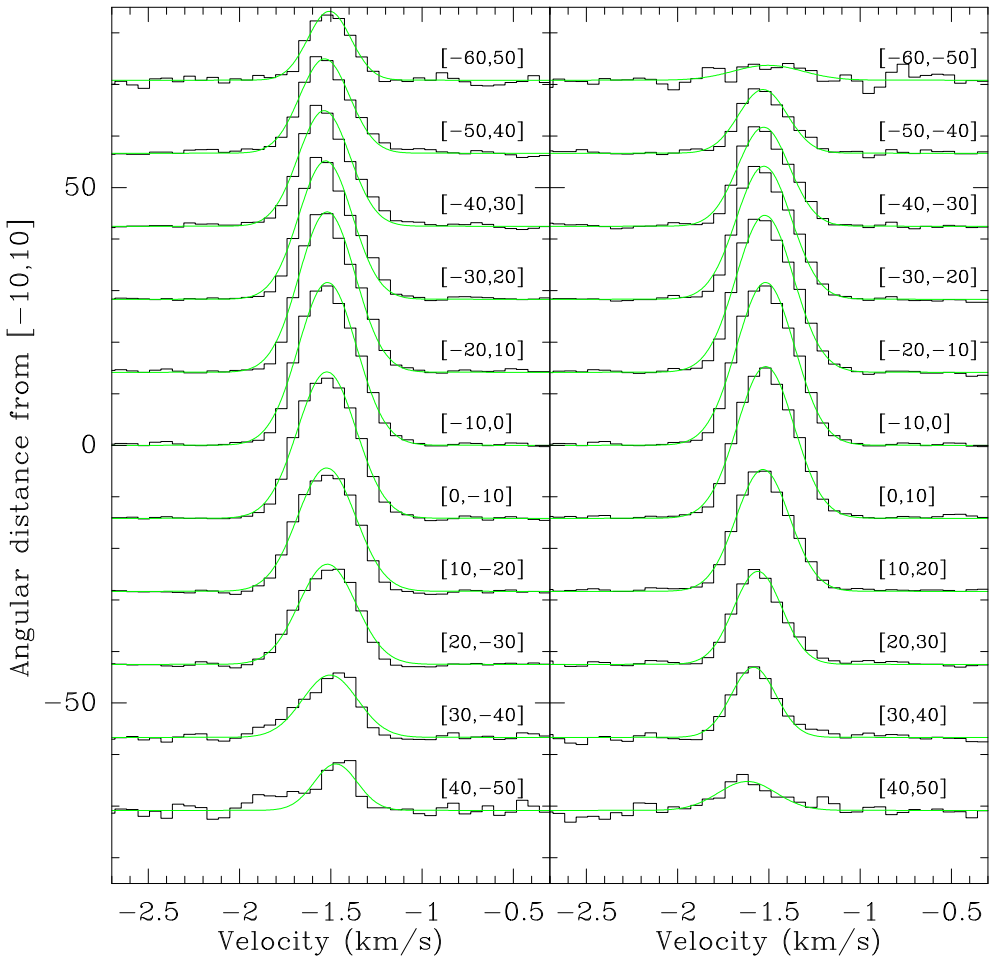

Figure 3.10 Isolated component profile along the P.A. = 45°axis passing through (−10,0) (left panel) and -45°axis passing through (−10,0) (right panel). This figure shows how the line width increases going from the edge of the core to the center. Fits are gaussian fits to this component.

We believe that this is a characteristic of unstable or supercritical (e.g. Mouschovias & Spitzer 1976) cores on the verge of star formation, more briefly called *pre–stellar cores*, a term which we use to characterize the *subset of starless cores undergoing central infall* (see also Ward-Thompson, Kirk, & André 2003).

Table 3.4. Results of velocity gradient fits.

line	$\mathcal{G}$ (km/s/pc)	Θ[a] (deg)	$<\mathcal{G}_l>$[b] (km/s/pc)
N_2H^+(1–0)	0.366±0.005	−133.6±0.7	1.9±0.1
N_2H^+(3–2)	1.1±0.1	−168±9	2.7±0.3
N_2D^+(2–1)	0.95±0.06	+145±5	3.5±0.2
N_2D^+(3–2)	0.4±0.2	−128±27	4.7±0.4

[a] Direction of increasing velocity, measured East of North.

[b] Mean values of the magnitude of local velocity gradients and corresponding standard error.

3.3.6 Velocity field

Assuming that L1521F is in solid body rotation, we determined the magnitude $\mathcal{G}$ and the direction Θ of the corresponding velocity gradient following the procedure described in Goodman, Benson, Fuller & Myers (1993). The magnitude $\mathcal{G}$ ranges between 0.4 and 1 km s^{-1} pc^{-1} depending on the tracer used, and large variations are also obtained for the gradient direction Θ (see Tab. 3.4, columns 2 and 3). There is no tendency for $\mathcal{G}$ to increase for higher density tracers, as observed in L1544 (Caselli et al. 2002a).

To investigate in more detail the internal motions of L1521F, we determined "local" velocity gradients (see Caselli et al. 2002a), where $\mathcal{G}_l$ and Θ_l have been calculated in adjacent 3×3–point grids of the maps. The results are shown in Figs. 3.11 and 3.12 for N_2H^+ and N_2D^+ maps, respectively. The arrows across the map indicate the magnitude and the direction of local gradients, and they are centered on the 9–point grid used to estimate the corresponding $\mathcal{G}_l$ and Θ_l values. From the figures it is clear that L1521F is *not* undergoing solid body rotation. The velocity structure is quite complex, showing portions of the core where the gradient direction changes rapidly. For example, if we concentrate on the N_2H^+(1–0) map (see Figure 3.11 [left panel]), which has the highest sensitivity, three converging velocity gradient patterns are clearly visible: (i) toward South–West in the Northern half, (ii) toward North–East in the SE quadrant, and (iii) toward North–West in the SW quadrant of the core. A similar structure is also present in the other maps (see

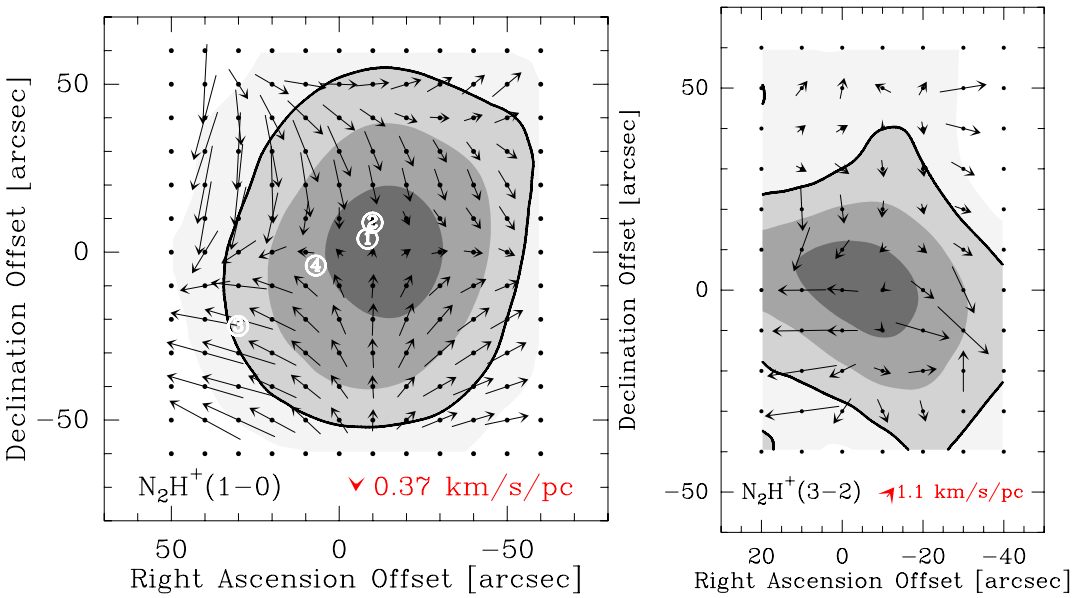

Figure 3.11 Velocity gradient vectors in L1521F derived from the two N_2H^+ maps. The integrated intensity of N_2H^+(1–0) (left) and N_2H^+(3–2) (right) is shown as grey scale. The thick contour marks the integrated intensity half–maximum contour. The arrows across the map are "local" velocity gradients obtained in a 3×3–point grid of positions centered on the corresponding grid, indicating the magnitude and the direction. The arrow in the bottom right of the figure is the "total" velocity gradient derived from the whole set of available positions with $A/\sigma_A > 10$ (A being the integrated intensity). Note the large variation in magnitude and direction of the local gradients. The white circles in the left figure locate the positions of the four N_2H^+ clumps detected by Shinnaga, Ohashi, Lee & Moriarty-Schieven (2004).

Figs. 3.11 [right panel] and 3.12).

Interestingly, the mean of the local–gradient magnitudes ($< \mathcal{G}_l >$) increases going from N_2H^+(1–0) to N_2D^+(3–2) (see column 4 of Tab. 3.4), suggesting that internal motions, although complex (Θ_l widely varies across the cloud), tend to become more prominent toward the core center. Moreover, N_2D^+ gradients appear larger than those derived from N_2H^+. If the observed velocity structure is at least partially due to inward motions in the core center, the larger local–gradient magnitudes detected in N_2D^+ can be explained by N_2D^+ being a better tracer of the core central regions, as found in L1544 (see also Sect. 3.4.1, Caselli et al. 2002a,b). However, the magnitude of the local gradients is generally within a few km s^{-1} pc^{-1} (see Tab. 3.4), thus they are produced by small velocity variations ($\delta v \simeq 0.02$–0.05 km s^{-1}) within $\simeq 0.01$ pc, the size of the grid where local

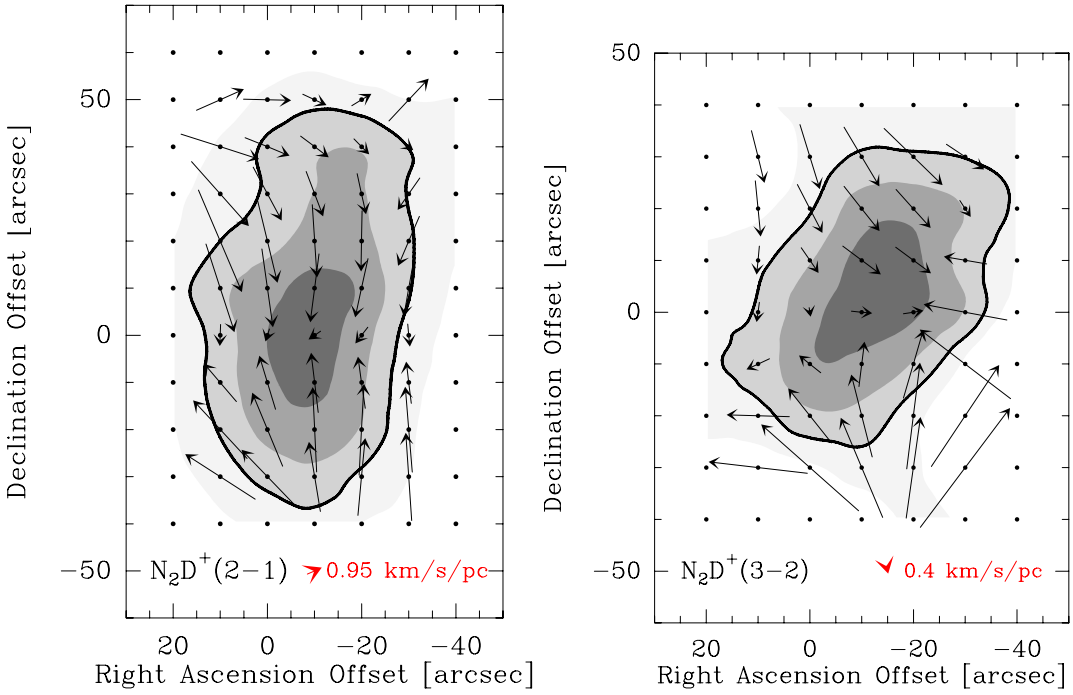

Figure 3.12 Same as Figure 3.11 for N_2D^+ data. A similar pattern is present.

gradients have been estimated (see also Sect. 3.4.2 for discussion).

We note that the velocity gradient found with the present N_2H^+(1–0) observations is significantly smaller than that deduced by Shinnaga, Ohashi, Lee & Moriarty-Schieven (2004) using interferometric observations, probably because they resolve out the more extended emission, with smaller or almost opposite (see Shinnaga, Ohashi, Lee & Moriarty-Schieven 2004) velocity gradients, compared to the central regions.

3.4 Discussion

The previous sections described the results found in our analysis of L1521F. The density profile, the CO depletion factor, the deuterium fractionation and the velocity field in the core have been presented. We found several similarities between L1521F and L1544, including the density structure (with $n(H_2) \simeq 10^6$ cm^{-3} at the center), the amount of integrated CO depletion ($f_D \simeq 15$) toward the dust peak, and the decrease of line width with increasing distance from the cloud center. Differences are however present in the amount of deuterium fractionation (factor of ~ 2 less than in L1544) and in the velocity

structure. In this section we will discuss these findings in view of our knowledge of the chemical and physical processes in dense cloud cores. The discussion is thus split in two subsections, one focussing on the chemistry and the other on the kinematics of L1521F.

3.4.1 Chemistry

In cold clouds, the exothermicity of the proton–deuteron exchange reaction

$$H_3^+ + HD \quad \rightarrow \quad H_2D^+ + H_2 + \Delta E, \tag{3.3}$$

where $\Delta E/k$ = 230 K (e.g. Millar, Bennett & Herbst 1989), is responsible for the enhancement of the H_2D^+/H_3^+ abundance ratio well above the local elemental abundance of deuterium (1.5×10^{-5}; Oliveira et al. 2003). As a consequence, given that H_2D^+ transfers its deuterium to neutral species such as CO and N_2, producing DCO^+ and N_2D^+, the $N(DCO^+)/N(HCO^+)$ and $N(N_2D^+)/N(N_2H^+)$ column density ratios reach the values observed towards dense cloud cores ($\simeq$ 0.02–0.2; e.g. Butner, Lada & Loren 1995; Williams et al. 1998; Caselli et al. 2002b; Sect. 3.3.4).

However, the freeze–out of neutral species, such as CO, O, and N_2, boosts the deuterium fractionation (e.g. Dalgarno & Lepp 1984). In fact, a decrease in the fractional abundance of gas phase CO leads to a decrease of the H_3^+ and H_2D^+ destruction rates and to an increase (caused by the higher H_3^+ abundance) of the H_2D^+ formation rate (e.g. Roberts & Millar 2000a, see reaction 3.3). An empirical relation between CO depletion and deuterium fractionation in prestellar cores has been determined by Bacmann et al. (2003) using doubly deuterated formaldehyde, whose abundance is also predicted to largely increase with CO freeze–out (Roberts & Millar 2000b; see also Roberts, Herbst & Millar 2003).

In the previous sections, we found that in L1521F, CO is depleted (with percentages ranging from 30% at the core edge to 93% at the center, deduced from the integrated CO depletion factor) and, similarly to L1544, the deuterium fractionation is large. The present estimates of $R_{deut} \equiv N(N_2D^+)/N(N_2H^+)$ as a function of distance from the dust peak allow us to study the relation between deuterium fractionation and CO freeze–out across a dense core for the first time and test chemical models. In Figure 3.13, R_{deut} is plotted as a function of f_D for all the positions present in Figure 3.8. We note a clear tendency for the deuterium fractionation to increase with integrated CO depletion factor.

In the following, we will analyse the observational results with simple chemical models, to better understand the observed f_D–$N(H_2)$ and R_{deut}–f_D trends shown in Figs. 3.7

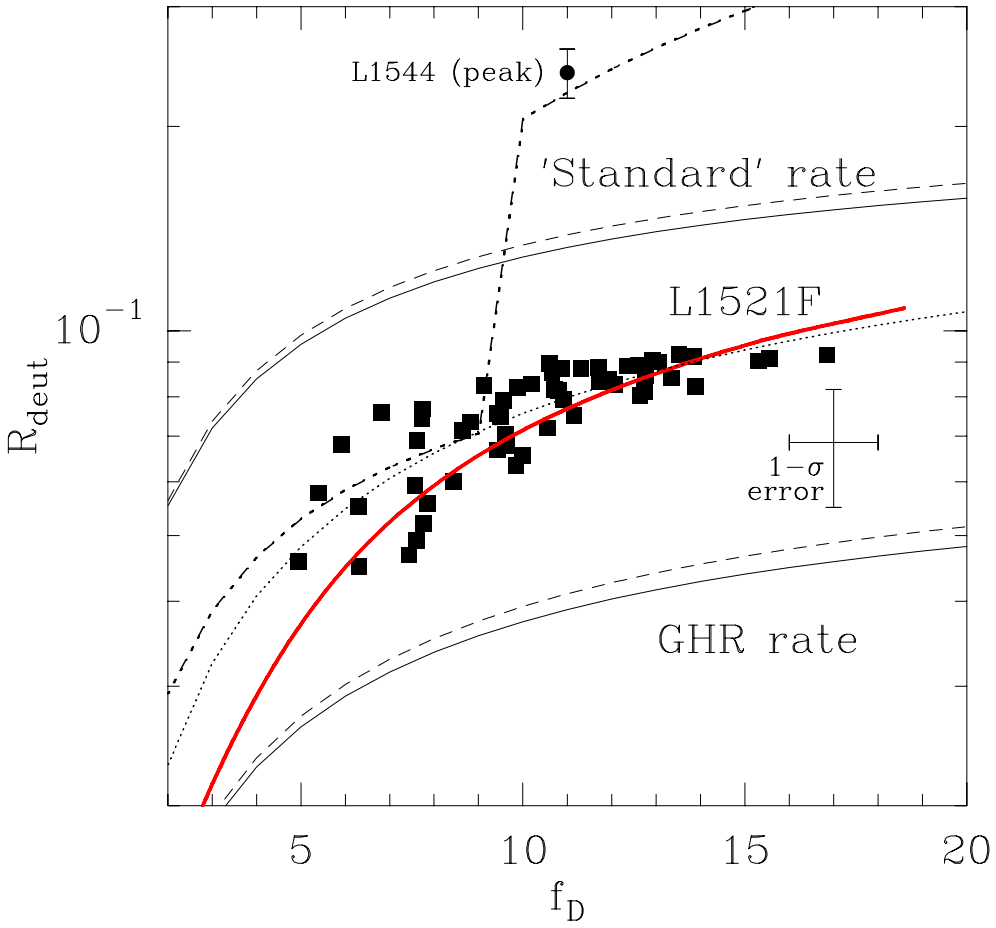

Figure 3.13 Deuterium fractionation ($R_{\rm deut} \equiv N(N_2D^+)/N(N_2D^+)$) as a function of integrated CO depletion factor. Filled squares are data from this work and the filled circle with error bar is our result for the dust peak of L1544 (Caselli et al. 2002b). Thin full curves are predictions from a simple chemical model using different rate coefficients for the proton–deuteron exchange reaction (3.3): the "standard" rate of 1.5×10^{-9} cm^3 s^{-1} and the "GHR" rate of 3.5×10^{-10} cm^3 s^{-1}, recently determined by Gerlich, Herbst & Roueff (2002). Dashed curves refer to the same models but with larger value of $a_{\rm min}$, the minimum radius of dust grains in the adopted MRN grain–size distribution (see Sect. 3.4.1). The dotted curve is the best fit to the data, found if $k_{\rm HD} = 7.5\times10^{-10}$ cm^3 s^{-1}. The thick curve is the result of a more comprehensive chemical model which takes into account the density structure of the core (see Sect. 3.4.1). Typical 1–σ error bars are shown. To reproduce the $R_{\rm deut}$ value observed in L1544, N_2 freeze–out and multiply deuterated forms of H_3^+ have to be included in the model (dash–dotted curve).

and 3.13, and the differences between L1521F and L1544. It will be interesting to see whether in L1521F there is evidence of the so–called "molecular hole", or the region where all species heavier than helium are heavily ($\gtrsim 98\%$) depleted from the gas phase, as deduced in the case of L1544. In fact, the recent detection of H_2D^+ toward the L1544 dust peak is consistent with the presence of a molecular hole in the central $\sim$ 2800 AU (Caselli, van der Tak, Ceccarelli & Bacmann 2003; Walmsley, Flower & Pineau des Forêts 2004)). Then, the N_2H^+ and N_2D^+ emission maps should show a central hole or emission plateau of similar size, but this has not been observed perhaps because of the poor spatial coverage of the central region and the limited spatial resolution ($\sim$ 2000 AU; Caselli et al. 2002a). Such a "molecular hole" was predicted by Caselli et al. (1999) and Caselli et al. (2002a) in an attempt to interpret the origin of double peaked optically thin lines for the case of L1544, including the thinnest N_2H^+(1–0) hyperfine component. In the case of L1521F, molecular lines, although asymmetric, do not clearly show two separated peaks. Thus, if the line asymmetry is due to the presence of a molecular hole in a contracting core, the hole should have a smaller size than in the case of L1544. Evidence for N_2H^+ depletion toward core centers has also been claimed in B68 (Bergin, Alves, Huard & Lada 2002) and L1512 (Lee, Evans, Shirley & Tatematsu 2003), two starless cores with central densities $\sim 10^5$ cm^{-3} and close to hydrostatic equilibrium, thus in a different chemical and dynamical phase compared to L1544 and L1521F.

A simple analytical model

The four thin curves in Figure 3.13 refer to the outputs of a simple steady state analytical chemical model including H_3^+, H_2D^+, H_2, HD, CO, N_2, HCO^+, DCO^+, N_2H^+, N_2D^+, electrons and negatively charged grains. The recombination on grain surfaces uses the rates from Draine & Sutin (1987), assuming that the grains are bare and that their abundance by number is given by the MRN (Mathis, Rumpl & Nordsieck 1977) distribution with upper cutoff radius of 0.25 μm and lower cutoff radius $a_{\rm min}$ = 50 Å(standard case, solid curves), and that all grains are negatively charged (a more realistic value for the fraction of negatively charged grains may be $\sim$ 0.5; see Flower & Pineau des Forêts 2003). We also considered a larger $a_{\rm min}$ (= 500 Å, dashed curves) to roughly take into account the process of grain coagulation in dense cores (e.g. Ossenkopf & Henning 1994). As expected, *larger grains cause a (slightly) higher deuterium fractionation*, given that the number density of dust grains decreases and does also the recombination rate on grains of H_2D^+ molecular ions (further increasing the grain size does not significantly change

the result, given that dissociative recombination becomes more important). This simple model also assumes that the electron fractional abundance $x(e)$ varies with density as $1.3\times10^{-5}\,n(H_2)^{-0.5}$ (McKee 1989)[2], and that $n(\mathrm{H_2}) = 9.9\times10^3\,f_\mathrm{D}^{1.4}$ (in the density range between 3×10^4 cm^{-3} and 10^6 cm^{-3}), as found from a linear least square fit to the observed f_D data in Figure 3.6 and the $n(\mathrm{H_2})$ data derived in Sect. 3.3.2 from the 1.2 mm continuum observations. This allows us to find a simple relation for the deuterium fractionation as a function of f_D in "L1544–like" cores, if one neglects multiply deuterated forms of H_3^+ (see below):

$$R_\mathrm{deut} \equiv \frac{[N_2D^+]}{[N_2H^+]} \simeq \frac{1/3[H_2D^+]/[H_3^+]}{1+2/3[H_2D^+]/[H_3^+]}, \tag{3.4}$$

and

$$\frac{[\mathrm{H_2D^+}]}{[[\mathrm{H_3^+}]} = \frac{k_\mathrm{HD}[\mathrm{HD}]}{k_\mathrm{CO}[\mathrm{CO}]+k_{\mathrm{N_2}}[\mathrm{N_2}]+k_e[e]+k_{gr}[gr]}, \tag{3.5}$$

where k_HD is the rate coefficient of reaction 3.3 (see below), [HD]/[H_2] $\equiv 2\times$[D]/[H] = 3×10^{-5} (Oliveira et al. 2003), $k_\mathrm{CO} = 3.3\times10^{-9}\,(T/10\mathrm{K})^{-0.5}$ cm^3 s^{-1} is the rate coefficient of the reaction H_2D^+ + CO $\rightarrow$ *products* , $k_{\mathrm{N_2}} = 1.7\times10^{-9}$ cm^3 s^{-1} is the rate coefficient for the reaction H_2D^+ + $N_2\rightarrow$ *products*, [N_2]/[H_2] = 2×10^{-5} (Lee, Bettens & Herbst 1996), $k_e = 5.5\times10^{-7}\,(T/10\mathrm{K})^{-0.65}$ cm^3 s^{-1} is the dissociative recombination rate of H_2D^+ (see Caselli, Walmsley, Terzieva & Herbst 1998), and k_{gr} is the rate of recombination of H_2D^+ on negatively charged dust grains, which, following Draine & Sutin (1987), is given by:

$$\begin{aligned} k_{gr}(\mathrm{cm^3 s^{-1}}) &= 1.6\times10^{-7}\frac{a_\mathrm{min}}{10^{-8}\mathrm{cm}}\left(\frac{T}{10\,\mathrm{K}}\right)^{-0.5} \\ &\quad\times\left(1+3.6\,10^{-4}\frac{T}{10\,\mathrm{K}}\frac{a_\mathrm{min}}{10^{-8}\mathrm{cm}}\right). \end{aligned} \tag{3.6}$$

Note that $k_{gr}\times[gr]$ is equivalent to α_{gr} in Draine & Sutin (1987), where $[gr] = n_\mathrm{gr}/n(\mathrm{H_2})$ is the fractional abundance of dust grains and $n_\mathrm{gr} = \int n_\mathrm{gr}(a)da$. Introducing numerical values into eq. 3.5, we obtain an expression for [H_2D^+]/[H_3^+] which only depends on f_D and a_min:

$$\frac{[\mathrm{H_2D^+}]}{[\mathrm{H_3^+}]} = \frac{(k_\mathrm{HD}/1.5\times10^{-9}\mathrm{cm^3 s^{-1}})}{7/f_\mathrm{D}+2.8+1.6/f_\mathrm{D}^{0.7}+37.8\,f(a_\mathrm{min})}, \tag{3.7}$$

[2]The use of the relation found in L1544 by Caselli et al. (2002b) shifts the theoretical curves up by a factor of $\sim$ 1.3 in deuterium fractionation.

where

$$f(a_{\rm min}) \;=\; \left(\frac{k_{gr}}{1.6\times10^{-7}{\rm cm^3 s^{-1}}}\right)\left(\frac{a_{\rm min}}{10^{-8}{\rm cm}}\right)^{-2.5}. \qquad (3.8)$$

The last term in the denominator of eqn. 3.7 can be neglected as soon as $a_{\rm min} = 0.05$ μm or larger, so that, for molecular ions, dissociative recombination becomes more important than recombination on grains. Hence, it can be neglected in dense clouds, where small grains are likely to be depleted on the surface of large grains or coagulated in larger fluffy structures (Ossenkopf 1993). Depletion itself causes $a_{\rm min} \approx 0.01$ μm (Walmsley, Flower & Pineau des Forêts 2004).

The value of $k_{\rm HD}$ typically used in chemical codes is 1.5×10^{-9} cm^{3}s^{-1}, which we call the "standard rate" (see e.g. Roberts, Herbst & Millar 2003). However, Gerlich, Herbst & Roueff (2002) have recently measured a lower value for this rate (3.5×10^{-10} cm^{3}s^{-1}, the "GHR rate") and in Figure 3.13 results obtained with the "standard" and "GHR" rate are shown. The observed data points lie between the two curves, and the best fit (dotted curve in bottom figure) is obtained with $k_{\rm HD} = 7.5\times10^{-10}$ cm^3 s^{-1}, which may suggest that a rate slightly (factor or ~ 2) larger than the one recently measured is probably needed to explain observations. However, one should note that in the case of L1544 ($R_{\rm deut} \sim 0.24$ at $f_{\rm D} \sim 10$), even the "standard rate" fails to reproduce the large deuterium fractionation observed toward the dust peak. The only way to reach $R_{\rm deut} \sim 0.24$ with this analytical model (dash–dotted curve in Figure 3.13) is to allow a drop in the abundance of N_2 in the central regions where $f_{\rm D} \geq 10$ and include in the chemical scheme D_2H^+([3]), which becomes abundant in heavily (CO, N_2, and O) depleted regions (Roberts, Herbst & Millar 2003; Walmsley, Flower & Pineau des Forêts 2004). Therefore, the difference in deuterium fractionation between L1521F and L1544 is likely to be due to a different evolutionary stage, with L1521F being less evolved than L1544 (see also Aikawa, Ohashi & Herbst 2003). The inclusion of the reaction H_2D^+ + HD $\rightarrow$ D_2H^+ + H_2 (Gerlich, Herbst & Roueff 2002) in this model leads to an increase of the deuterium fractionation by a factor of 2–3. However, in this simple chemical scheme we did not include the so–called "back" reactions due to ortho–H_2 (Gerlich, Herbst & Roueff 2002, see), which have the effect of reducing the deuteration degree (Walmsley, Flower & Pineau des Forêts 2004, see); this analysis is beyond the scope of the present work.

[3] When D_2H^+ is included in the model, equation 3.4 becomes:

$$R_{\rm deut} \;\simeq \frac{1/3[H_2D^+]/[H_3^+]+2/3([H_2D^+]/[H_3^+])^2}{1+2/3[H_2D^+]/[H_3^+]+1/3([H_2D^+]/[H_3^+])^2}.$$

A simple chemical model in a centrally concentrated core

The analytic calculation outlined in the previous section has at least two major defects. One is the assumption of no abundance variations within the dense core, which should be computed first in order to estimate molecular abundances as a function of radius and then determine the column densities via integration along the line of sight. The second is our neglect of reactions with species such as O which also act to limit deuterium fractionation. Here, we present a small toy model aimed at overcoming these problems, and already described in Caselli et al. (2002b). This model follows the (steady–state) chemistry of a spherically symmetric cloud with a density profile deduced from the 1.2mm dust continuum emission (see Sect. 3.3.2), and constant temperature T = 10 K. Neutral species in the model are H_2, CO, N_2, and atomic oxygen. We follow depletion of these species onto dust grains and their desorption due to the cosmic ray impulsive heating of the dust, following the procedure by Hasegawa & Herbst (1993). The abundance of molecular ions such as HCO^+, N_2H^+ and corresponding deuterated isotopologues are given by the steady state chemical equations using the istantaneous abundances of neutral species. Analogously, the electron fraction $x(e)$ can be computed in terms of global estimates for the molecular and metallic ions and using the same istantaneous abundances of CO, N_2, and O in the gas phase. The approach we have adopted is a simplified version of the reaction scheme of Umebayashi & Nakano (1990), which includes molecular ion recombination on grain surfaces using rates from Draine & Sutin (1987) (see Caselli et al. 2002b, for details).

This model furnishes the abundances of gaseous species as a function of radius, and the corresponding column densities as a function of impact parameter are calculated taking into account the appropriate beam convolution to simulate the observations. We used the new value of the dissociative recombination rate for H_3^+ (4×10^{-7} cm^3 s^{-1} at 10 K) determined by McCall et al. (2003), assumed $k_{\rm HD} = 3.5\times10^{-10}$ cm^3 s^{-1} (see previous section) and varied other parameters (essentially the binding energies on grain surfaces of N_2 and O). The model has been forced to reproduce within 10% the observed $C^{17}O$, N_2H^+, and N_2D^+ column densities toward the dust peak position (5.5×10^{14}, 1.6×10^{13}, and 1.5×10^{12} cm^{-2}, respectively), and to reproduce within a factor of 2 the observed column density profiles in the above molecules. The best fit binding energies for N_2 and O (800 K and 750 K, respectively) are quite close to the values deduced from theoretical calculations and laboratory measurements (800 K and 750 K, for N_2 and O, respectively; see discussion in Hasegawa, Herbst & Leung 1992 and Bergin & Langer 1997).

As illustrated in Figure 3.14, the fractional abundance of N_2H^+ decreases from about

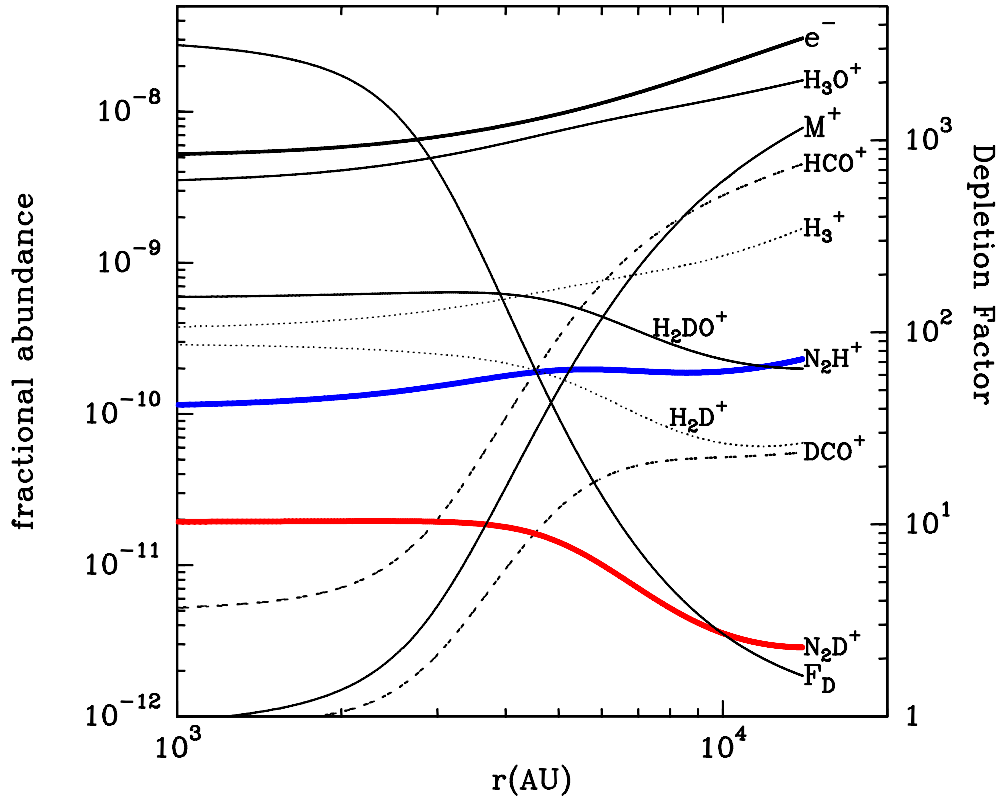

Figure 3.14 Fractional abundances, $n(i)/n(\mathrm{H_2})$, as a function of radius in L1521F. The symbol $\mathrm{M^+}$ refers to metals (see text). The adopted density profile is the one described in Sect. 3.3.2. This model reproduces the observed column densities of CO, $\mathrm{N_2H^+}$, and $\mathrm{N_2D^+}$. The $\mathrm{N_2H^+}$ abundance decreases towards the center by a factor of about 2, whereas $\mathrm{N_2D^+}$ increases by a factor of $\sim$7 from core edge to core center. Note that the $\mathrm{H_2D^+}$ abundance is predicted to be $\sim 3\times10^{-10}$ at the core center, a factor of 3 smaller than observed in L1544. In analogy with L1544, the $\mathrm{HCO^+}$ and $\mathrm{DCO^+}$ abundance profiles present a steep drop within about 5000 AU. The right axis refers to the CO depletion factor (see the curve labelled "F_D"). The set of parameters used to obtain this model are: $E_\mathrm{D}(\mathrm{CO}) = 1210$ K, $E_\mathrm{D}(\mathrm{N_2}) = 800$ K, $E_\mathrm{D}(\mathrm{O}) = 750$ K, $\zeta = 1.3\times10^{-17}$ s^{-1}, $a_\mathrm{min} = 5\times10^{-6}$ cm, and $x(\mathrm{N_2}) = 2\times10^{-5}$, where $E_\mathrm{D}(i)$ is the binding energy of species i and ζ is the cosmic–ray ionization rate (see Caselli et al. 2002b for details of the model).

2×10^{-10} at the edge of the cloud to about 1×10^{-10} at the center. The increase of the $\mathrm{H_2D^+/H_3^+}$ abundance ratio toward the center boosts the formation of $\mathrm{N_2D^+}$, which presents an abundance increase of about one order of magnitude from the edge (where $x(\mathrm{N_2D^+}) = 3\times10^{-12}$) to the central 4000 AU ($x(\mathrm{N_2D^+}) = 2\times10^{-11}$) of the core. Therefore,

in the case of L1521F, we do not need to invoke any "molecular hole" as in the case of L1544 (see Caselli, van der Tak, Ceccarelli & Bacmann 2003), although the present data do not allow us to distinguish between the models with different amounts of N_2 freeze out (and consequent N_2H^+ depletion) within few thousands AU. On the other hand, recent observations of *ortho*-H_2D^+ toward this object (Caselli, van der Tak, Ceccarelli et al., in preparation) strongly suggest that the molecular hole in L1521F must be smaller than in L1544, given that the line is about two times less intense than in L1544. Indeed, we predict here an H_2D^+ abundance of 3×10^{-10} at radii less than 3000 AU, a factor of about 3 lower than in L1544 (see Caselli, van der Tak, Ceccarelli & Bacmann 2003). This is another indication that L1544 is likely to be more evolved, and more centrally concentrated, than L1521F. This seems to contradict the observational evidence that the central densities in the two cores are quite similar. However, one should keep in mind that the central density values (and the density structure) in the two cores have been obtained assuming isothermal conditions. Allowing the temperature to decrease toward the center, as predicted by models of dense clouds heated by the external radiation field (e.g. Galli, Walmsley & Gonçalves 2002) one finds that lower values of the central temperature implies larger central densities (e.g. Evans, Rawlings, Shirley & Mundy 2001; Zucconi, Walmsley & Galli 2001). One possible solution to the L1521F/L1544 puzzle is that L1544 is colder and more centrally concentrated than L1521F and hence is more depleted in the nucleus. This is consistent with L1544 being more evolved and closer to the "critical" state than L1521F.

We note that the chemical composition shown in Figure 3.14 reproduces the observed $R_{\rm deut}$–$f_{\rm D}$ (see the thick curve in Figure 3.13) and $f_{\rm D}$–$N(H_2)$ (see the thick curve in Figure 3.7) relations, without any need to change the value of $k_{\rm HD}$ (see previous section). This demonstrates the importance of taking into account core structure and differential molecular freeze–out in chemical models. Moreover, note that the depletion factor *within* the cloud, $F_{\rm D}$, is significantly larger (more than two orders of magnitude) than the integrated CO depletion factor $f_{\rm D}$, which is "diluted" along the line of sight (compare $F_{\rm D}$ in Figure 3.14 with $f_{\rm D}$ in Figure 3.7). Finally, the central value of the electron fraction is $\sim5\times10^{-9}$, implying an ambipolar diffusion time scale (see e.g. Shu, Adams & Lizano 1987) of $\sim2.5\times10^{13}x(e) = 1.2\times10^{5}$ yr, only slightly (factor of $\sim$3) larger than the free–fall time scale, once again suggesting that the core is close to dynamical collapse (although not as close as L1544). As in L1544, the major ion in the core is H_3O^+, which is due to the presence of a significant fraction of gaseous atomic oxygen in the model (see

also Aikawa et al. 2001 for similar results). We should however point out that the more recent models of Aikawa, Ohashi & Herbst (2003), where surface chemistry is included, predict a much lower abundance of O in the gas phase, given that in this model, an O–atom sticking to a grain is converted to water, which remains on the surface (assuming desorption due to the cosmic–ray impulsive heating of dust grains; see Hasegawa & Herbst 1993). Low ionization potential elements, essentially S^+, Mg^+, Fe^+, Si^+, Na^+, generically called "metals" (M^+ in Figure 3.14), are assumed to freeze out onto dust grains at the same rate as CO molecules. For this reason, they are negligible carriers of positive charges within the core, in our model.

3.4.2 Kinematics

In order to facilitate the comparison between L1521F and L1544, we analyzed the kinematical properties of L1521F using the same models as in Caselli et al. (2002a). In particular, starting from the velocity field predicted by the ambipolar diffusion models of Ciolek & Basu (2000, hereafter CB), we have derived the line width gradient and the line profile in a disk–like geometry and compare the results with our observations.

From the analysis of N_2H^+(1–0) data, we found that the line width, similarly to L1544, decreases with distance from the dust peak (see Figure 3.9). As seen in Caselli et al. (2002a), this observational evidence is consistent with the predictions of the CB model. Here, we applied the kinematic analysis of L1544 (Caselli et al. 2002a) to the case of L1521F, assuming that the cloud has a disk–like shape and is centrally concentrated, with the center coincident with the 1.2mm dust continuum map peak. From the core axial ratio, and following equation (1) of CB, the angle between the vertical axis of the model and the plane of the sky is found to be 18°. The disk is contracting via ambipolar diffusion and the resultant velocity field is used as input in a model which computes synthetic profiles of optically thin lines for all lines of sight across the model disk (for details, see Caselli et al. 2002a). As in the case of L1544, we also assumed that the density profile and the radial velocity field is given by the CB model at time t = 2.66 Myr ($\equiv t_3$ in CB), which best reproduces the continuum observations of both cores. Line broadening is both due to thermal motions (σ_{th} = 0.05 km s^{-1} at 10 K) and microturbulence described by a turbulent velocity σ_{tu} independent of position.

Figure 3.15 shows the comparison between observed (hystogram) and synthetic (curves) profiles of the N_2H^+(1–0) isolated hyperfine component (F_1F = 01→12) along the minor and major axes of the L1521F core. The (optically thin) weakest component (F_1F =

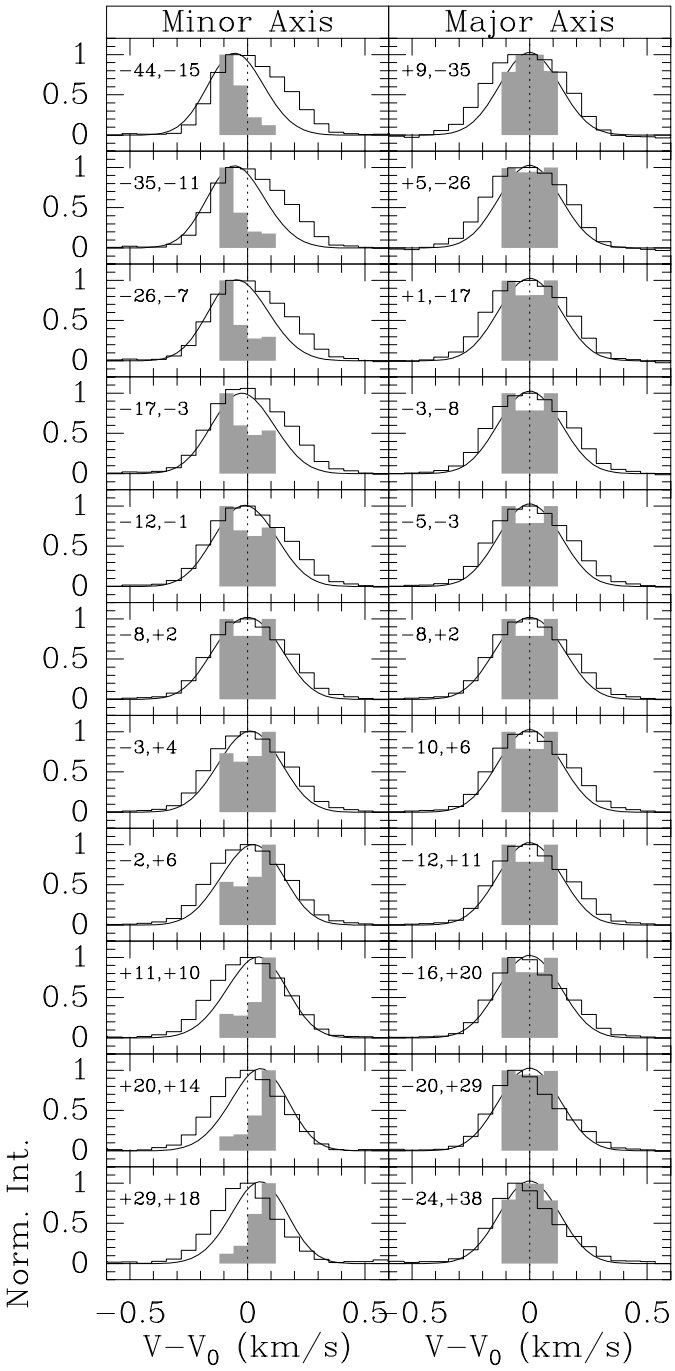

Figure 3.15 Observed line profiles of the F_1F = 0 1→1 2 hyperfine component of N_2H^+(1–0) (empty histograms) along the minor (left panels) and major (right panels) axis of L1521F compared with predictions based on the Ciolek & Basu (2000) velocity field at time $t = t_3$ (full curves), convolved with a σ = 0.11 km s^{-1} gaussian to reproduce the observed intrinsic line width of the central spectrum (see Figure 3.9). The filled histograms are model line profiles computed assuming no turbulent or thermal broadening. The core center is defined by the dust peak, located at offset (−8,+2).

10→11) shows very similar profiles; so that we decided to present the higher sensitivity observations of the isolated component. We also considered two different conditions in the model: (1) the N_2H^+ abundance is constant throughout the core, so that the N_2H^+ column density simply follows the dust, and (2) there is a "hole" (2000 AU in size) in the N_2H^+ distribution. The difference between the two synthetic profiles is not significant (only a 4% increase of the line width toward the center, in the presence of the molecular hole, see Figure 3.9), after the convolution with a gaussian with $\sigma = \sqrt{\sigma_{th} + \sigma_{tu}} = 0.11$ km s^{-1}, needed to match the intrinsic line width toward the center[4], and thus only one profile is shown in Figure 3.15. Also shown in the Figure 3.15 are model profiles for the limiting case of no turbulent or thermal broadening (filled histograms). The thing to note is that the agreement with the data is mixed, in the sense that the predicted velocity gradient along the minor axis is observed but it is restricted to the south–west half of the axis. Along the major axis there is no clear gradient in the north–west half of the axis, as expected in absence of disk rotation, but a (0.06 km s^{-1}) blue shift of the line is present toward south–east.

The synthetic profiles become narrower as we move away from the central 40″ of the disk–like cloud, given that the inward velocity in the adopted t_3 model reaches its maximum (0.12 km s^{-1}) at radius 0.025 pc (or 37″) before rapidly dropping to 0 at the cloud edge (see Figure2 of CB). We have analysed this line width variation to check its consistency with the observed trend shown in Figure 3.9. The solid curve in Figure 3.9 is the CB prediction in the case of no central "hole", whereas the dashed curve illustrates the effects on the line width of a molecular "hole" in the central 2000 AU (i.e. a region where all heavy elements have condensed onto dust grains). The line width of model lines has been calculated as the second moment of the velocity profile and it has been "normalized" to the value of the line width observed in the central position by convolving the purely–kinematic profiles with a Gaussian with $\sigma = 0.11$ km s^{-1}, which can be interpreted as the combination of thermal broadening plus a constant turbulent field across the cloud. The comparison between the curves and the big dots (the binned data, see Sect.3.3.5) suggests that our data are consistent with the CB model. In particular, the correspondence between the solid curve and the data indicates that the molecular hole is not present in L1521F,

[4]The line width toward the center and the observed Δv–b trend can also be matched assuming a central infall speed 1.5 times larger than the one calculated by CB in their model t_3 and no extra broadening (e.g. turbulence) needs to be invoked. However, this is not consistent with the CB model at time t_3 and we do not further discuss this possibility. On the other hand, recent H_2D^+ observations toward L1544 (Caselli, van der Tak, Ceccarelli & Bacmann 2003) also imply larger central infall speed than predicted by CB–t_3 (van der Tak et al. 2004).

in agreement with the chemical analysis (see previous section). On the other hand, the steeper Δv–b relation found in L1544 (see Figure 5 of Caselli et al. 2002a) suggests that the molecular hole is likely to be present in that source, again in agreement with the chemical analysis (see e.g. Caselli, van der Tak, Ceccarelli & Bacmann 2003).

As shown in Sect. 3.3.6, the kinematics of L1521F is also characterized by complex motions which may be the result of turbulence (see e.g. Burkert & Bodenheimer 2000) or accretion of material onto the core or a combination of both. Local gradients have been determined in order to quantify these motions, and we found that the magnitude of local gradient vectors tends to increase toward the core center. This suggests that turbulence (expected to dissipate more rapidly in denser environments), is probably not the driving source of the observed velocity field. Moreover, unresolved substructure may further complicate the velocity field, as suggested by the N_2H^+ clumps observed by Shinnaga, Ohashi, Lee & Moriarty-Schieven (2004) (see Figure 3.11): with the exception of their clump "N4", the kinematics of the other clumps (N1–N3) is consistent with the velocity field inferred from our local gradient maps (see also Sect. 3.3.1) and the (marginal, see Figure 3.4) evidence for two velocity components in N_2H^+(3–2), resembling clumps N1 and N2).

It is interesting to compare our data with predictions from the non–magnetic turbulent models of Ballesteros-Paredes, Klessen & Vázquez-Semadeni (2003), who derived velocity profiles for dense cloud cores. As an example, Figure 3.16 shows the velocity cuts observed across L1521F. Within the half maximum contour of N_2H^+(1–0), the *largest* velocity variation observed is $\lesssim 0.04$ km s^{-1} on a scale of 0.027 pc, corresponding to a velocity gradient of $\lesssim 1.5$ km/s/pc. On the other hand, Ballesteros-Paredes, Klessen & Vázquez-Semadeni (2003) found that the *smallest* velocity variation for their clump 13 at time $t1$ (see their Figure 9) is $\gtrsim 0.3$ km s^{-1} within 0.15 pc or $\gtrsim 2$ km/s/pc. Thus, current supersonic turbulent models predict velocity gradients which are somewhat too large. We also note that the reversal in the velocity gradient direction observed in L1521F (see bottom panel of Figure 3.16) is not present in the model examples shown in Ballesteros-Paredes, Klessen & Vázquez-Semadeni (2003), but it is predicted by the turbulent models of Burkert & Bodenheimer (2000)).

In the two starless cores L1498 and L1517B, Tafalla, Myers, Caselli & Walmsley (2004) found a good correlation between the distribution of CS and the distribution of the high velocity N_2H^+(1–0). The authors argue that the high velocity wing of the N_2H^+(1–0) lines comes from a gas shell that is being accreted by the starless core; therefore it has not

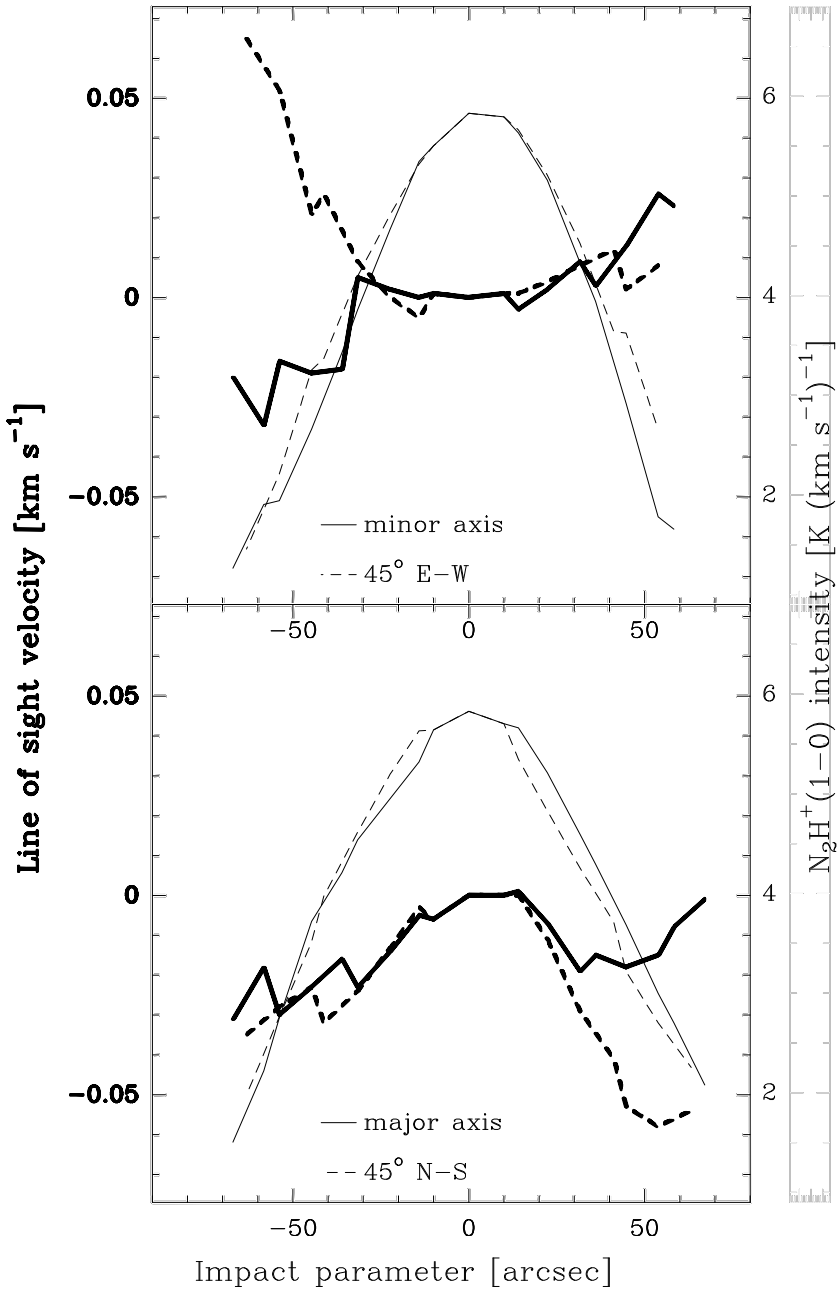

Figure 3.16 Intensity (thin lines) and velocity (thick lines) of N_2H^+(1–0) along four different cuts; in the top panel continuous lines refer to the minor axis (PA 115°) while the dashed line refers to a cut at PA 70°; in the bottom panel, the continuous lines show the behaviour along the major axis (PA 25°) and the dashed lines represent the other bisector (PA 160°).

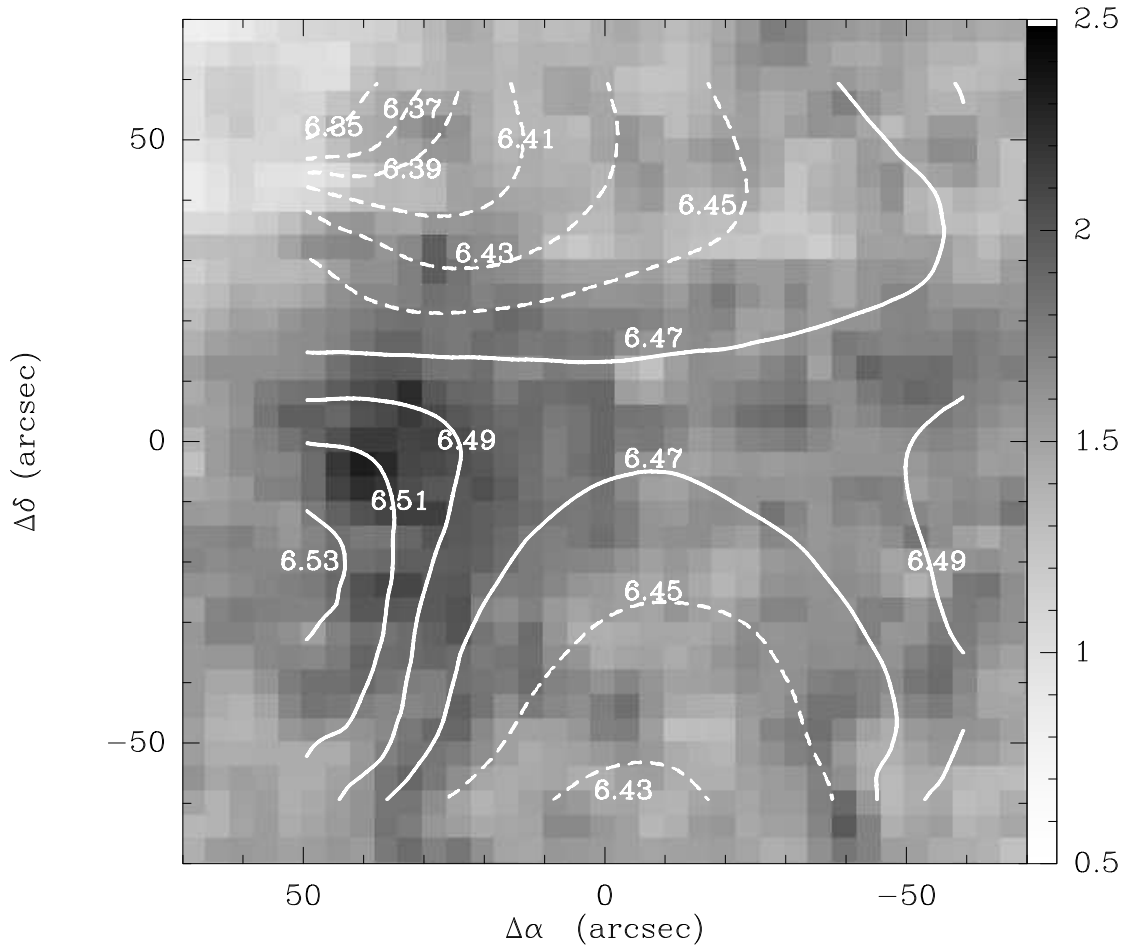

Figure 3.17 $C^{18}O$(1–0) integrated intensity map (greyscale; wedge units are K km s^{-1}) overlaid by the N_2H^+(1–0) velocity map (contours). N_2H^+ velocity levels are from 6.37 km s^{-1} to 6.55km s^{-1}spaced by 0.02 km s^{-1}; higher velocity contours are represented as solid lines.

experienced the high density in the core nucleus and hence its depletion factor is low. We repeated the same experiment in L1521F producing channel maps of the core in N_2H^+(1–0) but we did not find any strong deviation from the total intensity distribution. However, we did find that the N_2H^+(1–0) velocity pattern across the core is similar to the $C^{18}O$ distribution. In fact, as shown in Figure 3.17, N_2H^+(1–0) presents red–shifted velocities where CO is bright. The difference in magnitude of this effect here and in L1517B and L1498 could be due to a brighter core that saturates the emission from the high velocity wing.

A final thing to note is that Figure 3.17, together with Figure 3.11 (left panel), suggests

the presence of a coherent velocity field resembling low-frequency spatial oscillations of the outer cloud layers around some equilibrium dynamical state as recently proposed by Lada, Bergin, Alves & Huard (2003) in the case of the starless core B68. However, L1521F is more massive than B68 and is approaching the critical state for the onset of collapse, so that a situation of near–equilibrium for L1521F may be due to a balance between gravity and a combination of magnetic and thermal forces. If this is the case, the normal modes for L1521F would be more complicated than in the purely thermal case of B68, since the spherical symmetry that is a fair approximation for a thermal–pressure supported cloud such as B68 will no longer be valid for a magnetically supported object (G. E. Ciolek, *priv. comm.*). In fact, we observe L1521F not to be spherically symmetric (see Tab. 3.3).

3.4.3 Other possible interpretation

Finally, in this section we discuss some more speculative interpretations of the evolutionary state of L1521F. Firstly, it seems that L1521F is likely to be in an earlier stage of evolution than L1544, which is probably colder ($\sim$ 7 K in the central $\sim$ 2000 AU, see e.g. Zucconi, Walmsley & Galli 2001) and more centrally concentrated (central densities $\sim$ 10^7 cm^{-3}; e.g. Evans, Rawlings, Shirley & Mundy 2001) than L1521F, and hence more depleted in the nucleus. For example, in the CB model, this implies that whereas the density profile of L1521F is consistent with the cloud model at time t_3=2.66 Myr, L1544 is closer to t_4=2.68 Myr, and thus the estimated age difference is roughly 20,000 yr. However, these age estimates should be taken with caution given that the two cores may have had a different formation and contraction history and that, in general, cores, like stars, can differ in properties such as size, mass, and temperature regardless of their relative age.

An alternative view can be based on the clumpy structure observed in L1521F (Shinnaga, Ohashi, Lee & Moriarty-Schieven 2004), but not in L1544 (e.g. Williams, Myers, Wilner & di Francesco 1999), using BIMA. If the more complex kinematics in L1521F is due to the unresolved clumpy substructure, one may speculate that L1521F is close to the formation of a group of low mass protostars, whereas L1544 is likely to form one or two stellar objects. Thus, the two cores may show chemical and physical properties characteristic of the initial conditions of different modes of star formation in low mass cores. One should also note that L1521F resides in the middle of the main filament of the Taurus Cloud, whereas L1544 is at the edges of the complex and hence the different environments of the two cores may be responsible for the different kinematics and chemical

properties of apparently similar (in the dust continuum and $C^{18}O$ emission) dense cores.

3.5 Conclusions

We have analysed physical and chemical properties of L1521F, a starless core in the Taurus Molecular Cloud, with characteristics similar to the pre–stellar core L1544. The main similarities and differences between the two cores are listed below:

1. the dust emission distributions are similar, implying a fairly closely matched density structure, with central densities of $n_0 \sim 10^6$ cm^{-3}, the radius of the "flat" region r_0 = 20″, and similar asymptotic power index α (see Sect. 3.3.2 and Tafalla et al. 2002). In particular, the aspect ratio is quite similar: 1.6 and 1.8 in L1521F and L1544, respectively.

2. The line width decreases with distance from the cloud center ($\sim$ 0.3 km s^{-1}) to 80″ away ($\sim$ 0.25 km s^{-1}; see Figure 3.9), in analogy with L1544, and consistent with the predictions of ambipolar diffusion models, although any gravity–driven contraction in 2-3D is expected to get localized line broadening. The particular model which best fits the data will be investigated in the future.

3. The amount of CO freeze–out (integrated CO depletion factor f_D = 15) is also comparable to L1544, as is the column density of N_2H^+ toward the dust peak ($\simeq 1.5\times10^{12}$ cm^{-2}).

4. The deuterium fractionation toward the L1521F dust peak ($R_{deut} \sim 0.1$) is however a factor $\sim$ 2 smaller than in L1544, due to the (factor of 2) smaller column density of N_2D^+ toward L1521F. This can be understood if L1521F is less chemically evolved than L1544, with a smaller ($r < 2000$ AU) central molecular hole.

5. Unlike in L1544, the velocity field in L1521F maintains a complex structure even at the small scales traced by N_2D^+ and N_2H^+(3–2) (see Figs. 3.11,3.12). This may be due to the presence of clumps in the central few thousand AU (as deduced by the interferometric observations of Shinnaga, Ohashi, Lee & Moriarty-Schieven 2004), but could also be caused by normal mode pulsations, as in the case of B68 studied by Lada, Bergin, Alves & Huard (2003). The ambipolar diffusion model with infall of Ciolek & Basu (2000) has problems in reproducing the whole velocity field observed across the core. This may be due to the fact that part of the observed bulk motions result from residual core contraction, as suggested by (Tafalla, Myers, Caselli & Walmsley 2004) in their study of L1517B and L1498, thus preventing a clear determination of the velocity field within the core nucleus.

6. The line profiles in L1521F show asymmetric structure, although the two peaks

are not well separated as in L1544. This is consistent with smaller (factor of 1.5) infall velocities in the central few thousand AU of L1521F.

In any case, the large central density ($\sim 10^6$ cm^{-3}) and the evidence of central infall (broader line widths toward the center and central infall asymmetry in N_2H^+(1–0)) indicate that L1521F is another starless core on the verge of star formation, or a pre–stellar core. Although a study of a more complete sample is needed, assuming that L1544 and L1521F are the only two cores in Taurus close to dynamical collapse, and given that the total number of starless cores in Taurus is 44 (Onishi et al. 2002), we can argue that this process of contraction towards the "critical" stage, or the "L1544–phase", may last about five percent of the core lifetime.

A more detailed analysis of N_2H^+ line profiles will be presented in a future work, where the observed chemical abundances will be introduced in a non spherically symmetric Monte Carlo radiative transfer code. This is needed to understand the nature of the N_2H^+(1–0) line asymmetry, which may be caused by self–absorption plus infall, or to infall plus a molecular hole, or to the relative motion of different clumps, or to a mixture of the above possibilities.

Acknowledgements. *The authors are grateful to the staff of the IRAM 30m antenna, for their support during observations, and to Richard Crutcher and Daniele Galli for discussion. We also thank the referee, Glenn Ciolek, for clarifying several statements in this work and Floris van der Tak for a critical reading of the submitted manuscript. PC and CMW aknowledge support from the MIUR project "Dust and Molecules in Astrophysical Environments". CWL acknowledges support from the Basic Research Program (grant KOSEF R01-2003-000-10513-0) of the Korea Science and Engineering Foundation.*

Chapter 4

Dynamical and chemical properties of the "former starless" core L1014

Abstract.

Spitzer Space Telescope observations of a point-like source, L1014-IRS, close to the dust peak of the low-mass dense core L1014 have questioned its starless nature. The presence of an object with colors expected for an embedded protostar makes L1014-IRS the lowest luminosity isolated protostar known, and an ideal target with which to test star formation theories at the low mass end.

In order to study its molecular content and to search for the presence of a molecular outflow, we mapped L1014 in at least one transition of ^{12}CO, N_2H^+, HCO^+, CS and of their isotopomers ^{13}CO, C^{18}O, C^{17}O, $N_2D^+$and H^{13}CO$^+$, using the Five College Radio Astronomy Observatory (FCRAO), the IRAM 30 meter antenna and the Caltech Submillimeter Observatory (CSO).

The data show physical and chemical properties in L1014 typical of the less evolved starless cores: i.e. H_2 central density of a few 10^5 molecules cm^{-3}, estimated mass of $\sim$2 M$_\odot$, CO integrated depletion factor less than 10, $N(N_2H^+) \simeq 6 \times 10^{12}$ cm^{-2}, $N(N_2D^+)/N(N_2H^+)$ equal to 10% and relatively broad N_2H^+(1–0) lines (0.35 km s^{-1}). Infall signatures and significant velocity shifts between optically thick and optically thin tracers are not observed in the line profiles.

No classical signatures of molecular outflow are found in the ^{12}CO and ^{13}CO observations. In particular, no high velocity wings are found, and no well-defined blue-red lobes of ^{12}CO emission are seen in the channel maps. If sensitive, higher resolution observations confirm the absence of an outflow on a smaller scale than probed by our observations, L1014-IRS would be the only protostellar object known to be formed without driving an outflow.

A. Crapsi, et al., 2005, Astronomy & Astrophysics, accepted

4.1 Introduction

Starless cores are cold ($\sim$ 10-20 K) and dense ($> 10^4$ cm^{-3}) condensations of gas and dust in which no sign of the presence of a central protostellar object has been found. Previously, the easiest way to determine if dust emission was associated with a protostellar object was to search for a source emitting at mid-infrared wavelengths in the *IRAS* catalogue. This technique was obviously limited by the *IRAS* sensitivity.

A clear example is represented by IRAM 04191: although André, Motte & Bacmann (1999) found a clear sign of the presence of a Class 0 object represented by a clear collimated bipolar outflow departing from the core peak, *IRAS* does not show a point source towards the dust emission peak. Moreover, the CS line they observed towards the nucleus confirmed the presence of star formation activity showing a clear double peaked profile with the blue peak brighter than the red one. This spectral asymmetry has been recognized as an indicator of systematic inward motion (Snell & Loren 1977; Zhou 1992; Tafalla et al. 1998; Lee, Myers & Tafalla 1999).

In the same fashion, we present here the case of L1014. This core, listed as an opacity class 6 object in the Lynds (1962) catalogue, lies $-0\overset{\circ}{.}25$ below the galactic plane, has a line of sight velocity of $\sim$4 km s^{-1} with respect to the local standard of rest and is projected just $10'$ south of another dark globule B362 [1]. These cores can be seen in the Digital Sky Survey optical image presented in Figure 4.1, where we have overlaid visual extinction contours derived from near-infrared color excesses of background stars listed in the 2MASS catalog using the *NICE* technique (e.g. Lada, Lada, Clemens & Bally 1994; Alves et al. 1998).

L1014 was included in a survey for infall asymmetry in starless cores performed observing CS(2–1) and N_2H^+(1–0) (Lee, Myers & Tafalla 1999); given the weak detection in CS, no N_2H^+ observations were attempted. The dust continuum from L1014 was first detected at 260 μm using the NASA Kuiper Airborne Observatory (KAO) Keene (1981). Subsequently a 850 μm emission map (Visser, Richer & Chandler 2001) taken with SCUBA showed a dust emission peak at ($21^h24^m07\overset{''}{.}6$, $49^\circ59'02''$, J2000) coincident with the visual extinction peak. These authors then performed an unsuccessful search for high velocity gas, observing ^{12}CO(2–1) at five points around the dust peak with a sensitivity of 0.3 K km s^{-1} in a 0.2 km s^{-1}channel.

The Spitzer Space Telescope (hereafter Spitzer) observed L1014 in December 2003

[1] We note that B362 and L1014 were renamed "L1014-1" in Lee & Myers (1999) In this paper we keep the original names as in Lynds (1962) and Barnard (1927).

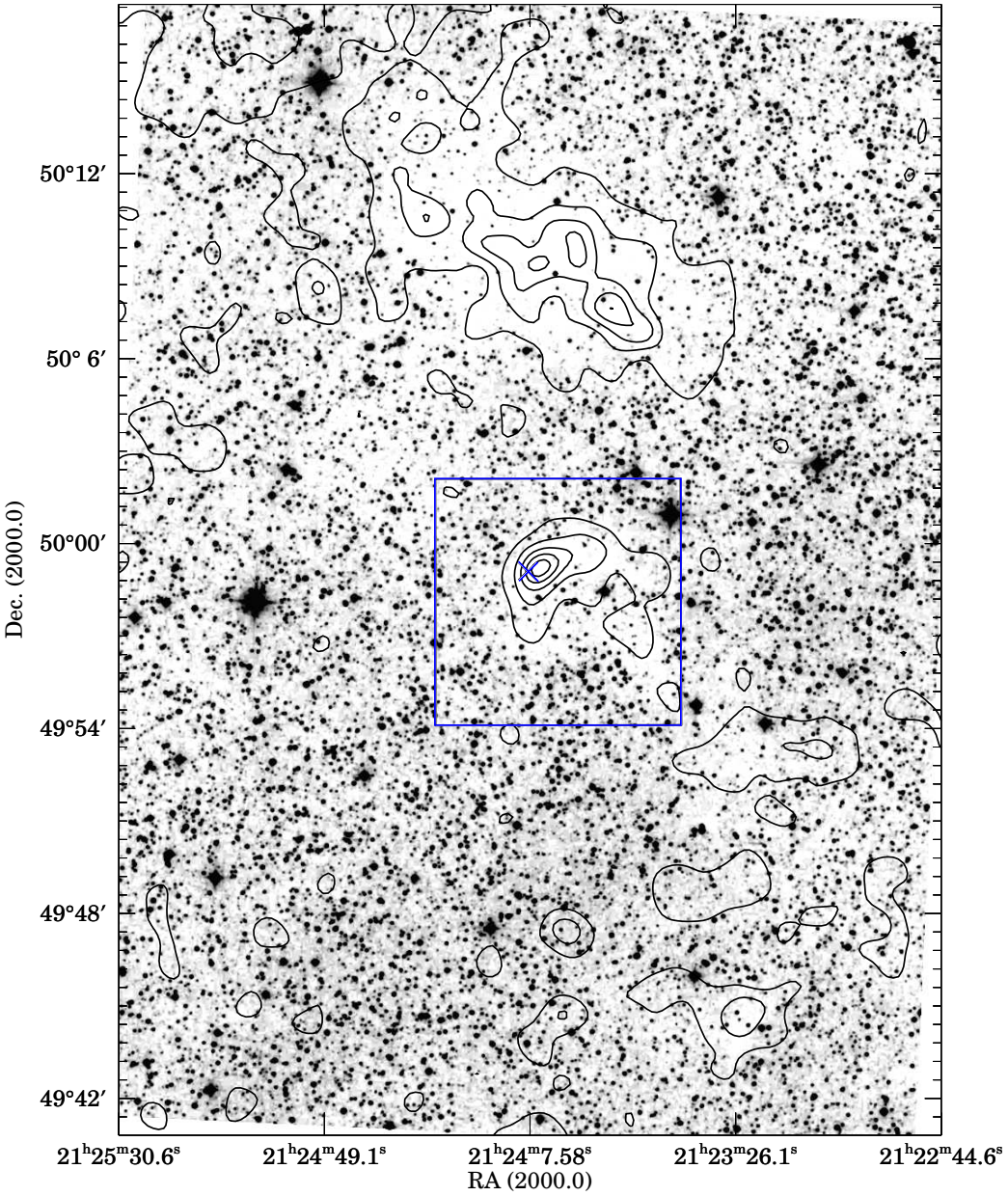

Figure 4.1 Optical image of the $27' \times 37'$ field around L1014 from the Digital Sky Survey. Overlaid onto the image are contours of beam-averaged visual extinction, following the *NICE* technique (e.g., Lada, Lada, Clemens & Bally 1994; Alves et al. 1998) of convolving line-of-sight measurements of the H−K color excesses of 2MASS sources with a $30''$ Gaussian beam. The contours are drawn at A_V=[3, 5, 7, 9, 11] magnitudes. Our FCRAO observations mapped much of this region in CO(1–0) and ^{13}CO(1–0), while the N_2H^+(1–0), CS(2–1) and $C^{18}O$(1–0) observations covered the area represented by the rectangle in the figure. L1014 is seen in the center of the field, while B362 can be seen $10'$ north of L1014. The cross indicates the position of L1014-IRS, the point source observed with the Spitzer Space Telescope consistent with being an embedded protostar.

as part of the Legacy program "From Molecular Cores to Planet Forming Disks" (Evans et al. 2003). Surprisingly, a strong (81.8±16 mJy) point source was detected at 24 μm towards the center of L1014 (Young et al. 2004), being coincident with both the 850 μm peak (Visser, Richer & Chandler 2001) and 1.2 mm peak (Young et al. 2004; Kauffmann et al., in preparation). This object, referred to as L1014-IRS, is also clearly detected in each of the 4 IRAC bands (3.6, 4.5, 5.8 and 8.0 μm) and at 70 μm with MIPS and, most importantly, shows a Spectral Energy Distribution (SED) compatible with an embedded protostar having an effective temperature of 700 K. Using the bolometric temperature (T_{bol}= 50 K) and the ratio between bolometric and sub-millimeter luminosity (L_{bol}/L_{smm}= 20), Young et al. (2004) classified L1014-IRS as a Class 0 protostar (see André 1994, for a review on Class 0 properties). Since the chance alignment of a starless core nucleus with an uncommonly bright infrared point source is unlikely, the authors proposed that L1014-IRS is associated with the L1014 core. Subsequently, deep near-infrared observations of L1014 have demonstrated conclusively that L1014-IRS is indeed embedded within this core (Huard et al. 2005, in prep.). Assuming a distance to the core of 200 pc, Young et al. (2004) determine a luminosity of 0.09 $L_\odot$ for L1014-IRS.

Outflows are an ubiquitous tracer of protostellar activity (André 1994; Richer et al. 2000), and so, in an attempt to support the classification of L1014-IRS as a Class 0 protostar, we deepened the search for high velocity ^{12}CO with a better combination of resolution and sensitivity than in past searches. We report here on observations of ^{12}CO, ^{13}CO, C^{18}O, C^{17}O, CS, N_2H^+, N_2D^+, HCO^+ and $H^{13}CO^+$ aimed at surveying the molecular content of L1014 and at studying its kinematical properties.

4.2 Observations

Observations were performed during March and April 2004, using the 32-pixel SEQUOIA focal plane array mounted on the Five College Radio Astronomy Observatory (FCRAO) 14 meter telescope.

We mapped L1014 in CO(1–0), ^{13}CO(1–0), C^{18}O(1–0), N_2H^+(1–0) and CS(2–1) using the on-the-fly position switching mode. Adopted frequencies, telescope half power beam widths, system temperatures, channel spacings and size of the mapped area are in Table 2.2. Temperatures were converted in the main beam brightness scale according to the efficiencies tabulated in the FCRAO web page[2]. Data were reduced and convolved onto

[2]http://www-astro.phast.umass.edu/∼fcrao/observer/status14m.html#ANTENNA

Table 4.1. FCRAO settings and parameters.

line (1)	frequency (2)	HPBW (3)	T_{SYS} (4)	Δv_{res} (5)	vel. cov. (6)	Mapped region (7)
N_2H^+(1–0)	93.1737725	54	280	0.157	$-94 \rightarrow 57$	$5' \times 5'$
CS(2–1)	97.980953	52	280	0.149	$-90 \rightarrow 55$	$5' \times 5'$
$C^{18}O$(1–0)	109.782173	46	280	0.133	$-60 \rightarrow 70$	$5' \times 5'$
^{13}CO(1–0)	110.201370	46	440	0.133	$-81 \rightarrow 45$	$20' \times 32'$
^{12}CO(1–0)	115.271203	44	920	0.127	$-78 \rightarrow 43$	$20' \times 32'$

Note. — Col. (2) line rest frequency (GHz); Col. (3) Half Power Beam Width ($''$); Col. (4) System Temperature (K, main beam scale); Col. (5) Channel Spacing (km s^{-1}); Col. (6) Usable velocity coverage (km s^{-1}); Col. (7) R.A. and Dec. extension of the mapped region.

a $20''$ spaced grid (circa Nyquist sampling) using the otftool software (Heyer, Narayanan & Brewer 2001)[3] available at FCRAO and then analysed using CLASS, the spectral line analysis software of IRAM and Observatoire de Grenoble (see Buisson et al. 2002, for a manual).
Angular offsets throughout this paper are relative to the 1.2-mm continuum peak position ($21^h24^m07.''5$, $49°59'05''$, J2000), which is $4''$ south of L1014-IRS position.

Complementary higher-resolution observations of N_2H^+(1–0), (3–2), N_2D^+(1–0), (2–1), (3–2) and $C^{17}O$(1–0) were obtained in August 2004 using the IRAM-30m telescope. The observations consisted in a 5-pointings cross spaced by $20''$ around the 1.2-mm peak position for N_2H^+(1–0), N_2D^+(1–0) and N_2D^+(3–2), while N_2H^+(3–2) and N_2D^+(2–1) were observed only at the (0,0), (20,0) and (−20,0) and $C^{17}O$(1–0) only at the peak position. These data were taken in frequency switching mode using the facility autocorrelator as the backend. Information about the telescope parameters (channel spacing, HPBW, system temperatures) are reported in Table 4.2. Intensities were converted in the main beam brightness scale using the efficiencies reported in the IRAM web site[4].

Finally, we used the Caltech Submillimeter Observatory in August 2004 to obtain

[3] http://www-astro.phast.umass.edu/∼fcrao/library/manuals/otfmanual.html
[4] http://www.iram.fr/IRAMES/telescope/telescopeSummary/telescope_summary.html

Table 4.2. IRAM-30m and CSO telescope settings and parameters.

line (1)	frequency (2)	HPBW (3)	T_{SYS} (4)	Δv_{res} (5)	vel. cov. (6)	N_{obs} (7)
IRAM-30m observations						
N_2H^+(1–0)	93.1737725	26	165	0.021	$-10 \rightarrow 16$	5
N_2H^+(3–2)	279.511385	9	1500	0.042	$-16 \rightarrow 12$	3
N_2D^+(1–0)	77.109626	32	155	0.025	$-14 \rightarrow 20$	5
N_2D^+(2–1)	154.217137	16	300	0.026	$-10 \rightarrow 11$	3
N_2D^+(3–2)	231.321966	11	440	0.050	$-16 \rightarrow 16$	5
$C^{17}O$(1–0)	112.358990	22	240	0.034	$-10 \rightarrow 16$	1
CSO observations						
$C^{18}O$(2–1)	219.560352	34	390	0.130	$-29 \rightarrow 37$	13
$C^{17}O$(2–1)	224.714214	33	330	0.128	$-29 \rightarrow 37$	5
HCO^+(3–2)	267.557620	28	320	0.107	$-21 \rightarrow 28$	1
$H^{13}CO^+$(3–2)	260.255478	29	300	0.110	$-24 \rightarrow 32$	1
HCN (3–2)	265.886434	28	500	0.054	$-24 \rightarrow 31$	1

Note. — Col. (2) line rest frequency (GHz); Col. (3) Half Power Beam Width ($''$) Col. (4) System Temperature (K, main beam scale); Col. (5) Channel Spacing (km s^{-1}); Col. (6) Usable velocity coverage (km s^{-1}); Col. (7) Number of observed positions.

HCO^+(3–2), $H^{13}CO^+$(3–2) and HCN(3–2) spectra towards the central position and a small map in $C^{18}O$(2–1) and $C^{17}O$(2–1). Spectra were obtained in position switching mode. Although the single pointing observations were performed $6''$ south of L1014-IRS, the $\sim 30''$ beam allow us to consider them as relative to the infrared source position. Conversion factor to the main beam temperature ($\eta_{230GHz} = 0.64$) was evaluated from observations of planets. Other informations for the telescope set-up are reported in Table 4.2.

The pointing accuracy for all our observations was measured to be $\approx 4 - 6''$.

4.3 Results

4.3.1 Maps

In Figure 4.2, we present integrated intensity emission maps of L1014 ($V_{LSR} \simeq 4.2$ km s^{-1}) in N_2H^+(1–0), CS(2–1) and $C^{18}O$(1–0) taken with FCRAO together with the 1.2-mm continuum from Young et al. (2004), the 5-points map of N_2H^+(1–0) taken with the IRAM-30m and the 13-points map of $C^{18}O$(2–1) from CSO. The half maximum contour of each map is rendered in white. The white cross shows the position of L1014-IRS, the candidate protostellar object embedded in L1014 according to Young et al. (2004). The area observed with the FCRAO is $10' \times 10'$ in size, but only the inner $8' \times 8'$ region where emission was detected is shown in Figure 4.2.

N_2H^+(1–0) emission, which comes from the high density nucleus of the core, is very concentrated (FWHM $\sim 70''$, in the FCRAO observations) and peaks $\sim 10''$ west of the dust emission (within the uncertainties due to the $54''$ FCRAO beam width and the Nyquist sampling of the observations). Since the emitting region is comparable in size with the telescope beam some dilution is very likely. In fact, IRAM-30m observations of N_2H^+(1–0) with a $26''$ beam showed spectra 3 times brighter than those observed by FCRAO towards the dust continuum peak, although still the emission does not seem to be fully resolved. In these higher resolution observations, the integrated intensity peak falls $5''$ south of L1014-IRS. We note that the equivalent radius of the N_2H^+(1–0) emission from FCRAO (=0.034 pc, evaluated as the square root of the area within the 50% contour divided by π) is among the smallest radii found in Lee, Myers & Tafalla (2001) and Caselli, Benson, Myers & Tafalla (2002), which observed 63 starless cores altogether using FCRAO and evaluated the equivalent radius with the same technique. The integrated intensity of N_2H^+(1–0) at peak observed with FCRAO is also lower (a factor of 2) than any other core reported in Lee, Myers & Tafalla (2001) and Caselli, Benson, Myers & Tafalla (2002), although the beam dilution should be kept in mind. Following Caselli, Benson, Myers & Tafalla (2002), we calculated the virial mass of L1014 from $M_{vir}(M_\odot) = 210\, r\,(\mathrm{pc})\, \Delta v_m^2\,(\mathrm{km^2 s^{-2}})$, where r is the typical radius of the N_2H^+ emission from FCRAO and Δv_m^2 is the velocity dispersion of the mean mass molecule (see Caselli, Benson, Myers & Tafalla 2002, for the definition). In this way we obtained a virial mass of 2.1 $M_\odot$, again, among the smallest in the Caselli, Benson, Myers & Tafalla (2002) sample. This estimate is in agreement with the mass evaluated from the extinction map in Figure 4.1. In fact, using a conversion factor of 1×10^{21} molecules $\mathrm{cm^{-2}}$ per magnitude

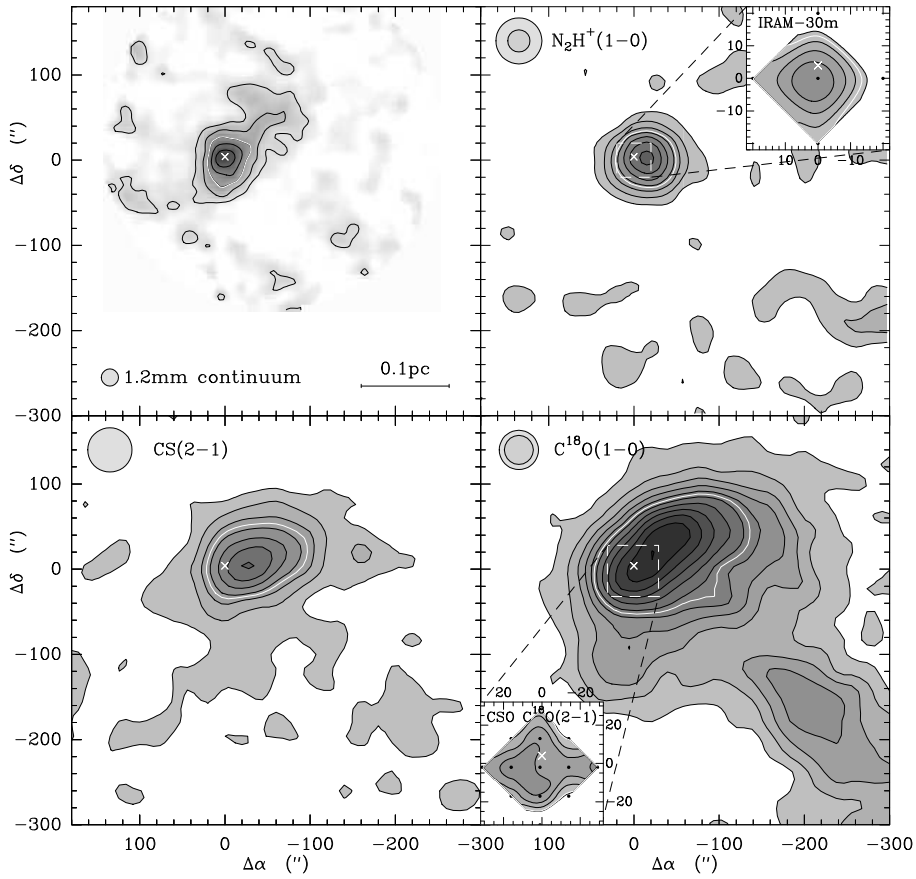

Figure 4.2 1.2-mm continuum, N_2H^+(1–0), CS(2–1) and $C^{18}O$(1–0) emission towards L1014. Molecular line maps were taken at FCRAO with the exception of the N_2H^+(1–0) map in the inset (from IRAM-30m) and the $C^{18}O$(2–1) map in the inset (from CSO) The 1.2-mm continuum was taken from Young et al. (2004) and it was observed with IRAM-30m. Contour levels start at and increase by 0.08 K km s^{-1} for the FCRAO molecular data and 4 mJy/(11″ beam)$^{-1}$ for the dust continuum . The white contour represents the half peak intensity in all the maps. Beam sizes are displayed at the top-left of each map but the 1.2-mm map. The white cross places the position of a point like source detected by the Spitzer Space Telescope with colors compatible with an embedded protostar. Angular offsets are relative to the 1.2-mm continuum peak ($21^h24^m07.''5$, $49°59'05''$, J2000). The inset on the N_2H^+(1–0) FCRAO map shows the 5 points observations of N_2H^+(1–0) at IRAM-30m. Levels start at 0.8 K km s^{-1}and increase by 0.3 K km s^{-1}. The IRAM-30m beam size is shown inside that of the FCRAO. Similarly, the inset in the $C^{18}O$(1–0) FCRAO map shows the 13 points map of $C^{18}O$(2–1) taken at CSO. Levels start at 0.35 K km s^{-1}and increase by 0.1 K km s^{-1}. The CSO beam size is shown inside that of the FCRAO.

of visual extinction (Bohlin, Savage & Drake 1978), we obtained a mass of 1.5 $M_\odot$ above the $A_V = 5$ magnitudes contour.

The CS(2–1) emission is much more extended than the 1.2-mm continuum and N_2H^+(1–0), as expected due to its lower critical density and possible depletion effects (Tafalla et al. 2002). The integrated intensity peak lies $\sim 30''$ west of the dust emission, although the same caveats about the limited resolution and sampling apply here as in the N_2H^+ map.

$C^{18}O$(1–0) observations reveal more structure than previous observations, showing a secondary peak at $(-200'', -200'')$ from the reference position. Note that the 1.2-mm map did not cover that area. Also the $C^{18}O$(1–0) integrated intensity peaks west of the continuum, although the peak is less constrained than the other tracers. The flatness of the $C^{18}O$ map and the offset of its peak with respect to the dust are typical features of starless cores (Tafalla et al. 2002), where CO (and its isotopomers) freeze-out onto dust grains in the high density nucleus. To test if this is the situation in L1014, we follow Caselli et al. (2002b) evaluating the degree of CO depletion as the ratio of the canonical CO abundance ([CO]/[H_2]$\equiv 9.5 \times 10^{-5}$, Frerking, Langer & Wilson 1982) and the observed abundance derived from the ratio of $C^{18}O$ and H_2 column densities (for details see Caselli et al. 2002b). Following Chapter 3, the CO column density was derived under the constant excitation temperature approximation (CTEX, see Appendix of Caselli et al. 2002b) starting from the $C^{18}O$ observations while the H_2 column density was inferred from the 1.2-mm emission assuming constant dust temperature and emissivity. In this way, we found a depletion factor equal to 9 at the dust peak, whereas it drops to 5 at the $C^{18}O$ peak $(-20'', 20'')$. These values are typical of starless cores with moderate chemical evolution (e.g. L1495, L1498, L492) with densities of about a few 10^5 cm^{-3}(Chapter 3). The $30''$ map of $C^{18}O$(2–1) obtained at CSO is shown in an inset of Figure 4.2. Note that the error on the integrated intensity for the points outside the peak is 2.5 times the value reported in Table 4.3. As for the N_2H^+ high–resolution observations, the $C^{18}O$(2–1) from CSO seems to peak south of L1014-IRS.

While the 1.2-mm emission peak in L1014 (23 mJy $(11''$ beam$)^{-1}$) is comparable in intensity with the majority of N_2H^+ emitting starless cores (see e.g Chapter 3), it is relatively weak if compared with *high-density, evolved* pre–stellar cores such as L1544 (> 60 mJy $(11''$ beam$)^{-1}$, Ward-Thompson, Motte & André 1999). Consequently, the H_2 central volume density inferred from it is 6 times less (2.5×10^5 cm^{-3} in L1014 vs. 1.4×10^6 cm^{-3} in L1544) when evaluated with the same technique and physical parameters (dust temperature of 10 K, dust opacity of 0.005 cm^2 g^{-1} and mean molecular mass

Table 4.3. Line parameters at the 1.2-mm continuum peak position from line profile fitting.

line (1)	intensity (2)	V_{LSR} (3)	ΔV (4)	τ (5)
FCRAO spectra				
N_2H^+(1–0)	0.52±0.03	4.239±0.014	0.354±0.033	4.6±3.2
CS(2–1)	0.41±0.02	4.279±0.014	0.677±0.031	···
$C^{18}O$(1–0)	0.84±0.02	4.224±0.005	0.484±0.012	4.4[a]
^{13}CO(1–0)	3.18±0.07	4.258±0.008	0.864±0.019	8.6[a]
^{12}CO(1–0)	9.30±0.17	4.211±0.022	2.261±0.049	225[a]
IRAM-30m spectra				
N_2H^+(1–0)	1.850±0.032	4.242±0.004	0.354±0.009	6.1±0.8
N_2H^+(3–2)	0.263±0.036	4.258±0.039	0.443±0.058	<0.100
N_2D^+(1–0)	0.203±0.010	4.248±0.007	0.284±0.020	2.1±1.6
N_2D^+(2–1)	0.182±0.015	4.273±0.010	0.307±0.029	<0.100
N_2D^+(3–2)	0.066±0.014	4.303±0.044	0.315±0.128	<0.100
$C^{17}O$(1–0)	0.476±0.022	4.229±0.009	0.310±0.027	2.4±1.5
CSO spectra				
$C^{18}O$(2–1)	0.641±0.036	4.270±0.017	0.575±0.044	1.4[b]
$C^{17}O$(2–1)	0.344±0.035	4.092±0.023	0.489±0.051	< 0.100
HCO^+(3–2)	0.316±0.015	4.410±0.019	0.819±0.041	···
$H^{13}CO^+$(3–2)	0.025±0.019	···	···	···
HCN (3–2)[c]	<0.03	···	···	···

Note. — Col. (2) $\int T_{MB} dV$ (K km s^{-1}) (in presence of hyperfine structure we integrated over all the components; ^{12}CO and ^{13}CO lines were integrated between 1 and 7 km s^{-1} and 3 and 5.5 km s^{-1} respectively); Col. (3) Rest velocity (km s^{-1}) Col. (4) Full width half maximum (km s^{-1}); Col. (5) Sum of the opacity of all the hyperfine components.

[a]Opacity was evaluated from the ratio with the $C^{17}O$(1–0) integrated intensity and assuming the relative abundance as in Wilson & Rood (1994).

[b]Opacity was evaluated from the opacity of $C^{17}O$ (2–1) and assuming the relative abundance as in Wilson & Rood (1994).

[c]Upper limit on integrated intensity was evaluated for a line-width equal to $H^{13}CO^+$(3–2).

equal to 2.33 a.m.u.) as in Tafalla et al. (2002). Note that the central H_2 density value given in Young et al. (2004) (1.5×10^5 cm^{-3}) was evaluated using a dust opacity equal to 0.0104 cm^2 g^{-1}.

4.3.2 Spectra towards dust peak

The spectra observed towards the dust emission peak with FCRAO are shown in Figure 4.3 while those observed with IRAM-30m are shown in Figure 4.4 and those taken at CSO in Figure 4.5. Gaussian fits were performed using the CLASS fitting procedure and results are presented in Table 4.3. In the case of lines with hyperfine structure, all the hyperfine components were simultaneously fit. This kind of fit also furnishes the opacity of the line in the presence of high S/N spectra. The N_2H^+(1–0) line widths (0.35 km s^{-1}) are slightly broader than the prototype of evolved starless core L1544 (0.31 km s^{-1}, Caselli et al. 2002a), suggesting a combination of nonthermal and systematic motions in the inner nucleus of L1014. Using the CTEX approximation on the higher resolution (IRAM-30m) data, we found a column density at the integrated intensity peak position of $N(N_2H^+) = 6 \pm 2 \times 10^{12}$ cm^{-2}, comparable to other starless cores moderately evolved in a chemical sense like e.g. L1512, L1498, L1495, L1517B (Chapter 3), and a factor of 2-3 less than in IRAM 04191, the other very low-luminosity Class 0 object known (Belloche & André 2004). Similarly, the N_2D^+ column density derived from the N_2D^+(1–0) and (2–1) IRAM-30m spectra yielded a value of $= 6 \pm 1 \times 10^{11}$ cm^{-2} from both lines. The deuterium fractionation at the peak of L1014 was, thus, found to be 10%, a value higher than the average starless core (Chapter 3). N_2H^+ and N_2D^+ column densities were calculated also in the Large Velocity Gradient approximation (see e.g. Chapter 3, for details) yielding values of 5.3×10^{12} cm^{-2} and 5.2×10^{11} cm^{-2} respectively. This approach furnishes also an estimate of the H_2 volume density from observations of multiple rotational transitions; in this way we obtained $n(H_2) \simeq 1.9 \times 10^5$ cm^{-3} from N_2H^+ and $n(H_2) \simeq 4.0 \times 10^5$ cm^{-3} from N_2D^+, both estimates are consistent within their errors with the central density evaluated from the dust continuum.

The ^{12}CO(1–0) profile is much more asymmetric than the other lines and its observed line width ($\sim$2 km s^{-1}) is much larger than the rest ($\sim$0.5 km s^{-1}). This occurrence could be explained considering the very high optical depth of ^{12}CO. In fact, the integrated intensity ratio of ^{12}CO/C^{17}O, ^{12}CO/C^{18}O and ^{12}CO/^{13}CO ($\sim$20, $\sim$11 and $\sim$3 respectively) are much lower than the local interstellar medium relative abundance values (1792, 560 and 77, Wilson & Rood 1994). C^{17}O(1–0) opacity was found to be 2.4 ± 1.5 from hy-

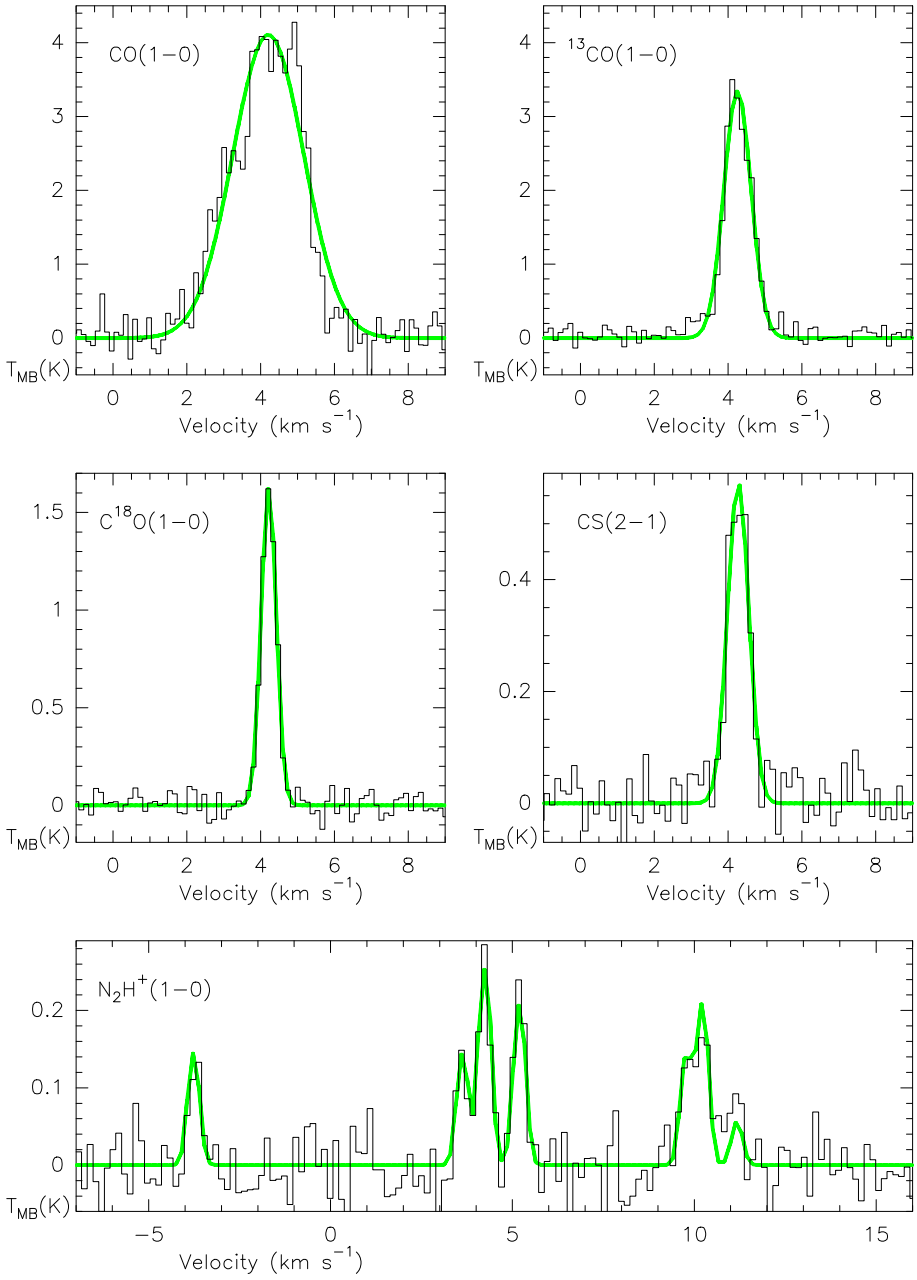

Figure 4.3 CO(1–0), ^{13}CO(1–0), C^{18}O(1–0), CS(2–1) and N_2H^+(1–0) spectra observed with FCRAO towards the 1.2-mm peak of L1014. Gaussian (or hyperfine in the case of N_2H^+(1–0)) fits are plotted.

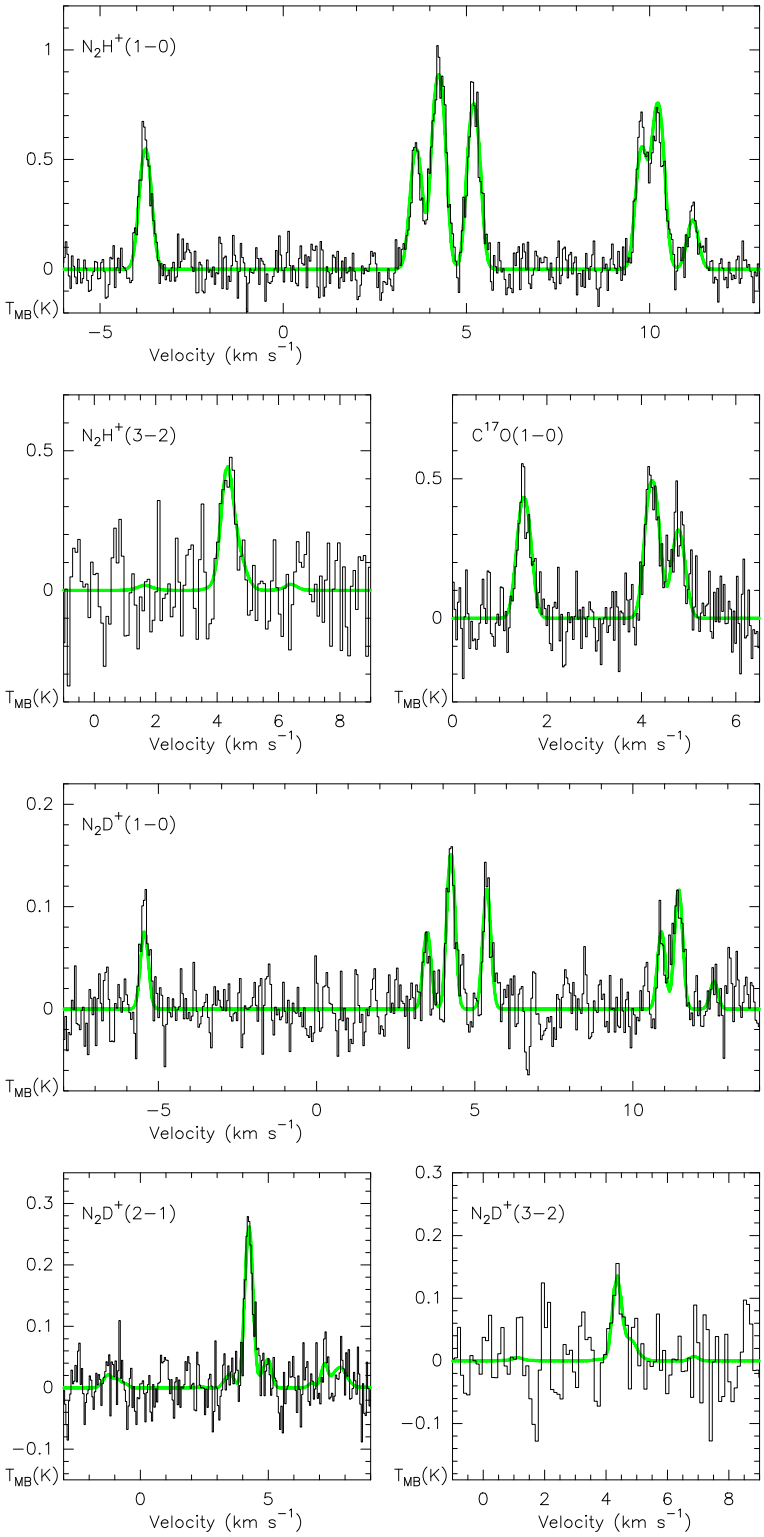

Figure 4.4 N_2H^+(1–0), N_2H^+(3–2), $C^{17}O$(1–0), N_2D^+(1–0), N_2D^+(2–1) and N_2D^+(3–2) spectra observed with the IRAM-30m towards the 1.2-mm peak of L1014. Hyperfine fits are plotted.

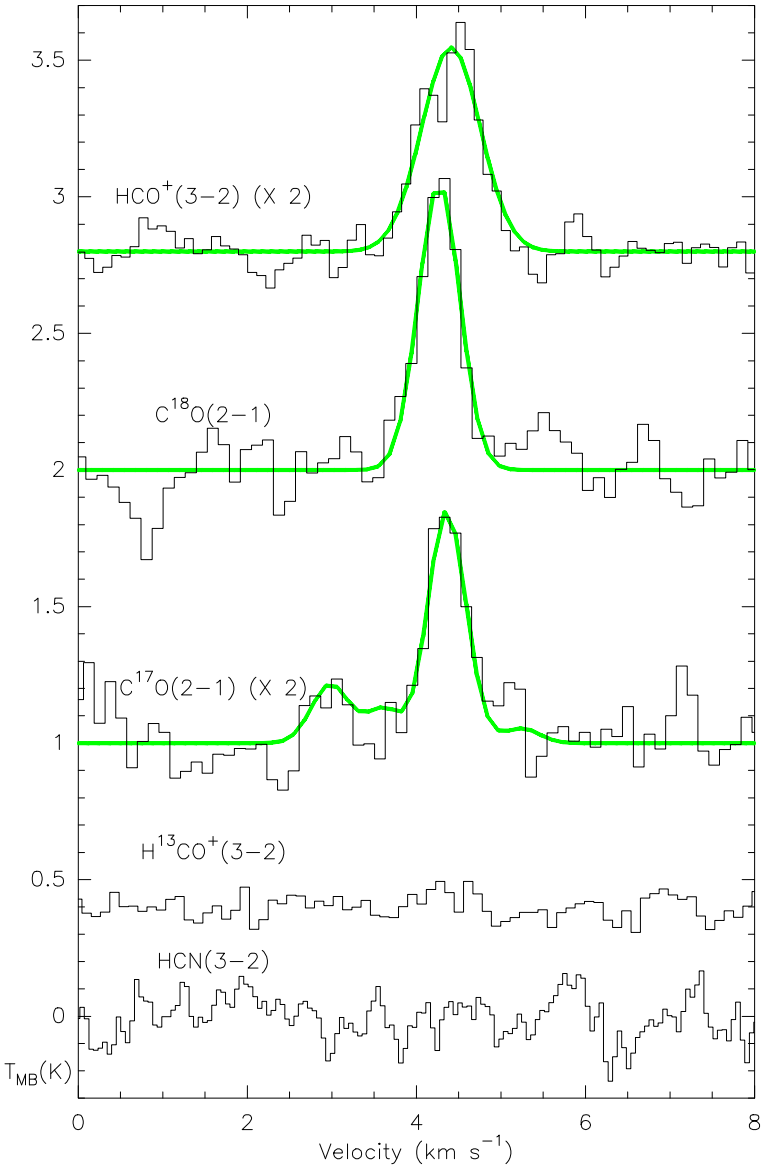

Figure 4.5 $C^{18}O(2–1)$, $C^{17}O(2–1)$, $HCO^+(3–2)$, $H^{13}CO^+(3–2)$ and HCN(3–2) spectra observed with the CSO towards the 1.2-mm peak of L1014. Gaussian or hyperfine fits are plotted. The asymmetric shape of $HCO^+(3–2)$ is consistent with outward motions of the gas.

perfine structure fitting. Using this value and assuming equal excitation temperature for all CO isotopomers, we can derive an optical depth value of 225 for the ^{12}CO line, 8.6 for the ^{13}CO and 4.4 for $C^{18}O$ from the observed integrated intensity ratios. If we broaden a gaussian line having the $C^{17}O$ intrinsic line width (0.31 km s^{-1}), accounting for the effect

of optical depth of 225, 8.6 and 4.4, we end up with flat-topped lines with FWHM of 0.9, 0.6 and 0.5 km s^{-1}for ^{12}CO, ^{13}CO and C^{18}O respectively. We deduce that optical depth broadening of a Gaussian line cannot account entirely for the very broad ^{12}CO and ^{13}CO lines observed, while they are consistent with the observed C^{18}O line width.

Interestingly, our CS(2–1) spectra do not show the asymmetric double peaked structure, with the blue peak stronger than the red one, typical of the cores undergoing infall (Zhou 1992; Mardones et al. 1997; Lee, Myers & Tafalla 1999). This feature was clearly seen in IRAM 04191 (André, Motte & Bacmann 1999). Moreover, the difference in line velocity between CS and N_2H^+ in units of the N_2H^+(1–0) line width ($\delta V_{CS} = (V_{CS} - V_{N_2H^+})/\Delta V_{N_2H^+}$), that is supposed to gauge the extended infall motions of the core (Mardones et al. 1997; Lee, Myers & Tafalla 1999), is very small in L1014 (0.04).

On contrary, HCO$^+$(3–2) observations show the opposite asymmetry revealing a red peak brighter than the blue peak (see Figure 4.5). This line profile can be produced by a rotating, expanding, or pulsating core (Lada, Bergin, Alves & Huard 2003). We note that the velocity of the self absorbed feature corresponds to the velocity of the optically thin C^{18}O(2–1) line as predicted by the models. Given the moderate signal to noise ratio of the present data, it is necessary to confirm these indications with higher sensitivity and higher resolution observations and to retrieve a map of HCO$^+$ in order to search for spatial patterns for the expansion asymmetry.

We failed to detect H^{13}CO$^+$(3–2) and HCN(3–2) towards L1014-IRS up to a 0.02 and 0.03 K km s^{-1} level respectively.

4.3.3 The search for the outflow in L1014

In Figure 4.6, we present channel maps of CO(1–0) (top) and ^{13}CO(1–0) (bottom) in a range of velocities, -9 km s^{-1} to 15 km s^{-1}, centered around the L1014 typical velocity ($\sim$4.2 km s^{-1}). Emission was integrated in 2 km s^{-1} intervals. No CO emission was found anywhere in the mapped area between -35 km s^{-1} and -9 km s^{-1} and between 15 km s^{-1} and 25 km s^{-1}, i.e at velocities departing more than 10 km s^{-1} from the L1014 rest velocity. The 1σ errors for the ^{12}CO and ^{13}CO channel maps are 0.06 K km s^{-1} and 0.03 K km s^{-1} respectively, less than the lowest contours adopted in Figures 4.6 and 4.8

Using IRAM 04191 (André, Motte & Bacmann 1999) as a guide, we searched for ^{12}CO(1–0) wing emission at velocities 3 km s^{-1} $< |V - V_0| <$ 9 km s^{-1}. No wing-like emission was found in this range (see maps labeled -5, -3, -1 and 7, 9, 11 in Figure 4.6).

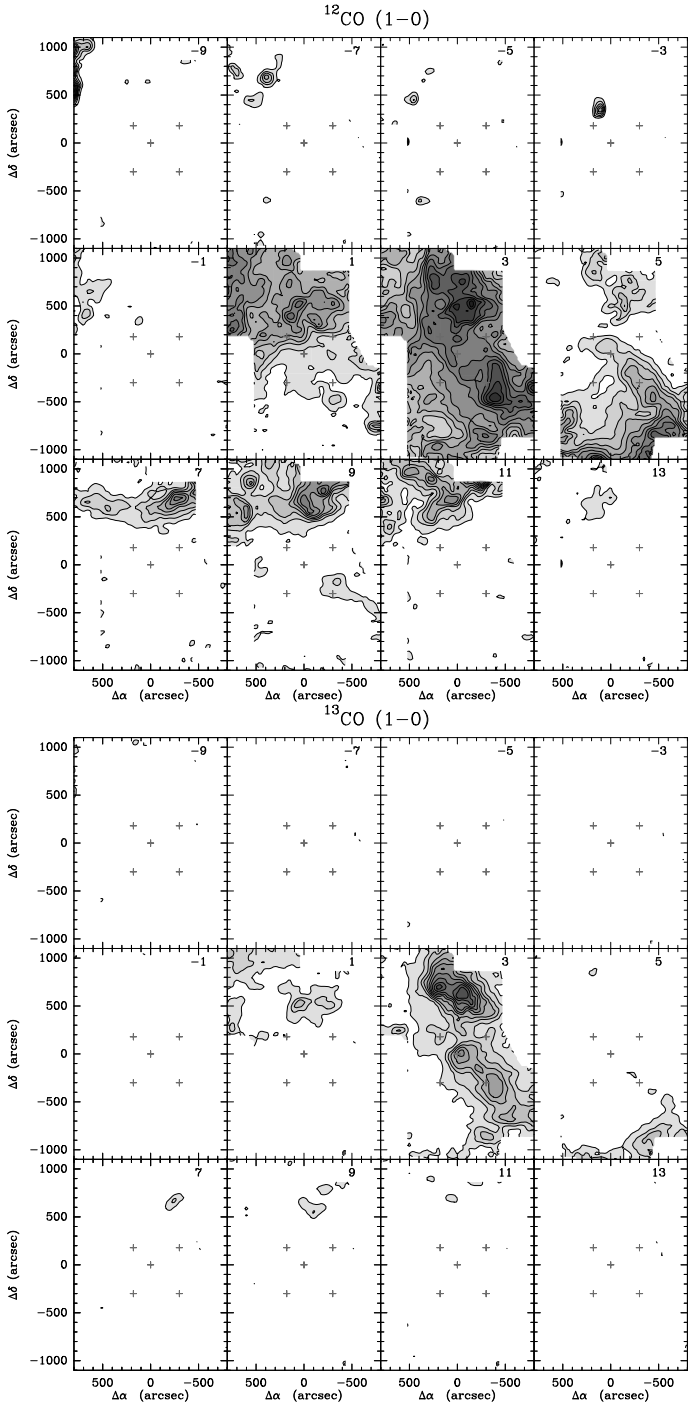

Figure 4.6 Channel maps of the CO(1–0) (top panel) and ^{13}CO(1–0)(bottom panel) lines around the rest velocity of L1014. Contours levels start and increase by 0.8 K km s^{-1} for the CO data and by 0.05 K km s^{-1} for the ^{13}CO ones. Velocity bins are spaced by 2 km s^{-1}and the starting velocity of the bin is reported in the top right of each map. The central cross in each map indicates the dust peak while the other four delineates the area shown in Figure 4.2. The solid line shows the direction of the cut studied in Figure 4.7.

Nevertheless, given the very low luminosity of L1014-IRS we examined also the possibility of less energetic wings. The most likely outflow feature present in L1014 is along position angle 45° (measured East of North) where we can see red emission in the SW lobe between 5 and 7 km s^{-1} and blue emission in the NE part in the bin 1 to 3 km s^{-1}. This axis was identified mainly from the jet-like appearance of the "red lobe", but the fact that this feature is also seen in the ^{13}CO(1–0) and C^{18}O(1–0) emission, which typically are not sensitive to outflows, poses serious questions as to whether this is indeed due to a classical outflow lobe. Moreover, as can be seen in the sequence of spectra along this axis (Figure 4.7), we do not see the typical outflow features in the line profiles. For example:

^{12}CO

i) (1–0) line at the cloud rest velocity is not present throughout all the cut and is not the dominant component in all the positions,

ii) the "low velocity wings", seen for example in the positions (−500, −500) in the red lobe or (100,100) in the blue lobe, look less like wings in the following positions (−200, −200) and (400, 400).

From the spectra in Figure 4.7, we deduce that the red lobe and the blue extended emission seen in the ^{12}CO map arise from different parts of the cloud with different velocities along the line of sight. This view is reinforced also by the observations of ^{13}CO and C^{18}O emission in the same region and with consistent velocities. The presence of gas with different velocities along the same line of sight would also explain the relatively large ^{12}CO and ^{13}CO line widths found towards the entire map (see Section 4.3.2).

A peculiar feature of the ^{12}CO channel maps is the presence of several small spots of emission in the NW part of the map at velocities smaller than 1 km s^{-1} and one spot at 9 km s^{-1} in the SE. Although these may be interpreted as molecular bullets coming from the L1014 nucleus, their asymmetric positioning, low velocity and large distance from the nucleus (0.05 pc) make them very different from the prototypical cases (Bachiller 1996).

We conclude that no classical outflow signature is present at the large scales investigated with the FCRAO. Further sensitive observations must be performed with smaller beams to probe the CO emission within the inner 45″ (the FCRAO beam size).

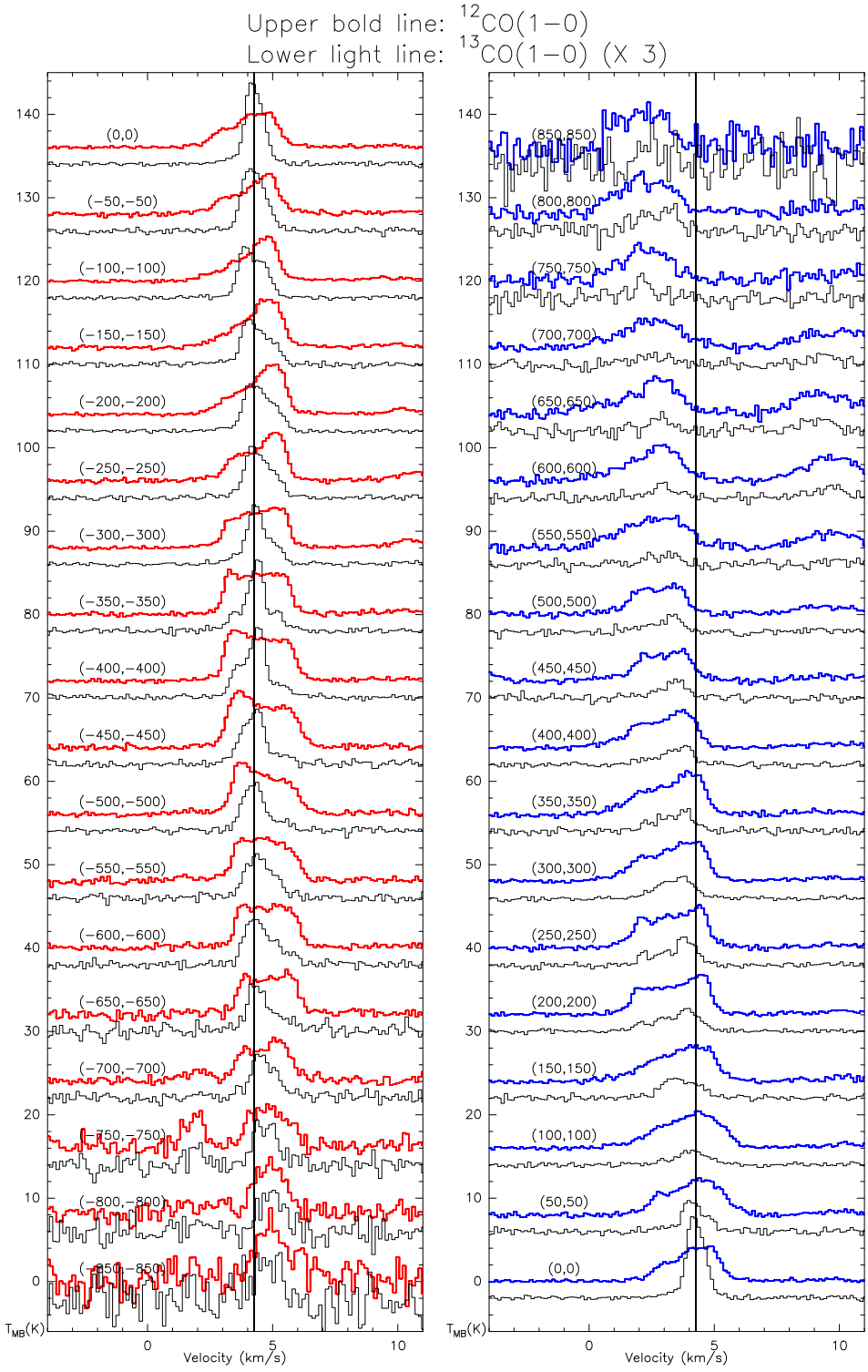

Figure 4.7 CO(1–0) (upper bold line) and ^{13}CO(1–0) (lower light line) spectra along the direction of the best-candidate outflow. South-West (red) branch is in the left panel and North-East (blue) branch is in the right panel. ^{13}CO(1–0) spectra were multiplied by 3.

4.3.4 The background component

The Spitzer observations presented by Young et al. (2004) left open the possibility of L1014-IRS being a more massive but less embedded distant protostar aligned by chance with the L1014 nucleus. Although the relative rarity of embedded protostar and starless cores do not favour this chance, the fact that we are looking close to the galactic plane and towards the Perseus spiral arm did not allow us to disregard it just on a statistical basis. Now, recent deep near-infrared observations confirm that L1014-IRS is associated with the nearby L1014 core (Huard et al. 2005, in prep.), our FCRAO observations are consistent with this finding.

We searched for signatures of infall-outflow activity towards L1014-IRS also at the Perseus arm velocity (near -40 km s^{-1}). No N_2H^+(1–0), CS(2–1) and $C^{18}O$(1–0) emission was detected at these velocities, most likely because of beam dilution given the small scales traced by those species and the large Perseus arm distance (2.6 kpc, Brand & Blitz 1993). Young et al. (2004) calculated that, assuming a distance of 2.6 kpc for L1014-IRS, the protostar whose emission would fit best the observed SED would have a luminosity of 16 $L_\odot$. Class I and Class 0 protostars with comparable bolometric luminosity like L1165 (Visser, Richer & Chandler 2002), L1448 and L1157 (Bachiller 1996) drive outflows of $\approx$0.3 pc in size, corresponding to $\approx 20''$ at the Perseus arm distance. Although this size is smaller than the FCRAO beam, we performed a search for high velocity wings in the -40 km s^{-1} component. CO and ^{13}CO channel maps at these velocities are shown in Figure 4.8, with the same intensity scale as in Figure 4.6. No emission was detected below -58 km s^{-1} and above -36 km s^{-1}. As for the component around 4 km s^{-1}, no clear-cut outflow features are seen in the channel map.

4.4 Discussion

The contradiction between the relatively young evolutionary status of L1014 derived from chemical indicators and the presence of a protostellar object embedded in its nucleus is puzzling. L1014 shows continuum and line intensities much lower than well-studied starless cores; in particular, the H_2 volume density, N_2H^+ column density and the degree of CO depletion are smaller than the average starless core, from which we did not expect L1014 to be close to the star formation. Moreover, the CS observation does not indicate the presence of inward motions, and the HCO^+ line profile show hints of outward motions. On the other hand, we report also relatively high deuterium fractionation and broad (if

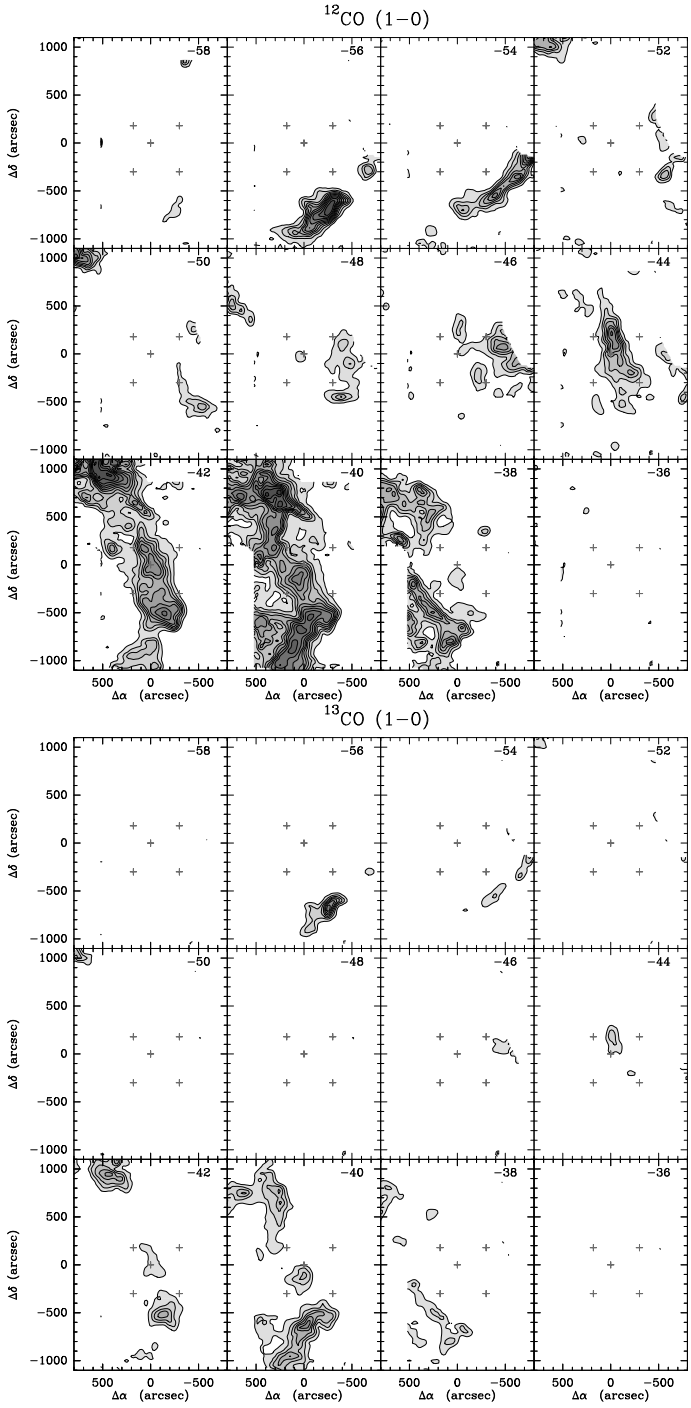

Figure 4.8 Channel maps of the CO(1–0) (top panel) and ^{13}CO(1–0)(bottom panel) lines for a second feature visible at ~ -40km s^{-1} and probably associated with the Perseus Arm. Contours levels start and increase by 0.8 K km s^{-1} for the CO data and by 0.05 K km s^{-1} for the ^{13}CO ones. Velocity bins are spaced by 2 km s^{-1}and the starting velocity of the bin is reported in the top right of each map. The central cross in each map indicates the dust peak while the other four delineates the area shown in Figure 4.2.

compared to other low-mass starless cores) N_2H^+ and N_2D^+ lines which are typical of more evolved objects.

We speculate that either i) the very low-luminosity nature of the central source (0.09 $L_\odot$, Young et al. 2004) makes its chemical and dynamical evolution different to any other observed core or ii) that a low-mass, low-luminosity "seed" is present long before the protostellar phase in every "starless" core. Boss & Yorke (1995) and Masunaga, Miyama & Inutsuka (1998) modeled the early phase of protostar formation introducing the "first hydrostatic core" or "Class –I" protostar as a short lived precursor of the Class 0. During this phase, the central temperature should reach a value of 200 K (3 times lower than the temperature derived by Young et al. 2004) and no outflow emission is expected. According to the duration of this phase, we could expect the detection of similar sources in the nuclei of some other starless cores in future Spitzer observations.

Considering that L1014-IRS was classified as a Class 0 protostar (Young et al. 2004) having met the requirements of $T_{bol} < 70$ K and $L_{bol}/L_{smm} < 200$ (André, Ward-Thompson & Barsony 1993), our observations indicate that L1014-IRS might be the first Class 0 protostar not associated with an observed molecular outflow. Even IRAM 04191, which has a bolometric luminosity comparable to L1014-IRS ($\sim$0.15 $L_\odot$), has an easily detected, very extended outflow (André, Motte & Bacmann 1999); thus, it seems unlikely that the weakness of the central source is responsible for the lack of the outflow detection. In any case, one should bear in mind that differences in the inclination angle, collimation factor, in the age, as well as in the external environment could make the detection of the outflow more difficult even in presence of two jets with comparable momenta. We can speculate that either the accretion rate of L1014-IRS is currently too little to power the outflow or that the magnetic field that threads the disk is too weak (Bachiller 1996). Alternatively, we may have caught L1014 in the epoch between the protostar formation and the outflow ignition (see e.g. Boss & Yorke 1995; Masunaga, Miyama & Inutsuka 1998), although this hypothesis seems less likely given the short lifetime associated to this phase.

We remark that our observations do not probe small scale outflows that would be diluted in the 45″ FCRAO beam, in particular if the outflow is very young and therefore compact. Strong molecular outflows are a hallmark of Class 0 protostar (André 1994) , thus it is of fundamental importance to extend the search for the outflow to a smaller scale.

4.5 Conclusions

We observed the starless core L1014 with the FCRAO antenna in N_2H^+(1–0), CS(2–1), $C^{18}O$(1–0), ^{13}CO(1–0) and ^{12}CO(1–0), combined with literature 1.2-mm continuum data and new N_2H^+(1–0), N_2H^+(3–2), N_2D^+(1–0), N_2D^+(2–1), N_2D^+(3–2) and $C^{17}O$(1–0) observations from the IRAM-30m and $C^{18}O$(2–1), $C^{17}O$(2–1), HCO^+(3–2), $H^{13}CO^+$(3–2) and HCN(3–2) spectra from CSO to study its chemical status and to search for the presence of a molecular outflow.

1. The chemical and physical properties of L1014 derived from the present observations are not typical of *highly evolved* low-mass starless cores. In particular, we found: molecular hydrogen volume density of $n(H_2) \simeq 2.5 \times 10^5$ cm^{-3}, N_2H^+ column density of $N(N_2H^+) \simeq 6 \times 10^{12}$ cm^{-2}, $M_{vir} = 2.1$ $M_\odot$, CO integrated depletion factor equal to 9, absence of CS double peaked profile with infall signature, absence of velocity shifts between self-absorbed optically thick (CS) and optically thin (N_2H^+) tracers and a profile asymmetry in HCO^+(3–2) consistent with outward motions. On the other hand, we found an enhanced degree of deuterium fractionation equal to 10% which is higher than the average starless core, and broad N_2H^+ and N_2D^+ lines suggestive of unresolved kinematical activity in the inner nucleus.

These diverging indications could be reconciled considering that we are observing either a very young stage of star formation or an extremely low-luminosity object exhibiting characteristics that differ significantly from previously known cases.

2. No classical signatures of a molecular outflow were found towards L1014. In particular, we note the absence of high velocity wing and of symmetric well-defined red-blue lobes in the CO channel maps. Bearing in mind that the scale probed by the present observations might be too large to detect the outflow in L1014, we suggest that the formation of a protostar might occur prior to or in absence of the molecular outflow.

The presence of a protostar in L1014 seems to challenge the idea that there is a unique path to forming a protostar that all cores must follow.

Acknowledgements. *We gratefully thank Paola Caselli and Arnaud Belloche for taking care of the observations at the IRAM-30m. A.C. was partly supported by NASA "Origins of Solar System Grant" (NAG 5-13050). C.W.L. acknowledges supports from*

the Basic Research Program (KOSEF R01-2003-000-10513-0) of the Korea Science and Engineering Foundation.

Bibliography

Aikawa, Y., Ohashi, N., Inutsuka, S., Herbst, E., & Takakuwa, S. 2001, *the Astrophysical Journal*, 552, 639

Aikawa, Y., Ohashi, N., & Herbst, E. 2003, *the Astrophysical Journal*, 593, 906

Alves, J., Lada, C. J., Lada, E. A., Kenyon, S. J., & Phelps, R. 1998, *the Astrophysical Journal*, 506, 292

Alves, J., Lada, C. J., & Lada, E. A. 1999, *the Astrophysical Journal*, 515, 265

Alves, J. F., Lada, C. J., & Lada, E. A. 2001, *Nature*, 409, 159

André, P., Ward-Thompson, D., & Barsony, M. 1993, *the Astrophysical Journal*, 406, 122

André, P. 1994, *The Cold Universe*, 179

Andrè, P., Ward-Thompson, D., & Motte, F. 1996, *Astronomy & Astrophysics*, 314, 625

André, P., Motte, F., & Bacmann, A. 1999, *the Astrophysical Journal*, 513, L57

André, P., Ward-Thompson, D., & Barsony, M. 2000, *Protostars and Planets IV*, 59

Arons, J. & Max, C. E. 1975, *the Astrophysical Journal*, 196, L77

Bachiller, R. 1996, *Annual Review of Astronomy & Astrophysics*, 34, 111

Bacmann, A., André, P., Puget, J.-L., Abergel, A., Bontemps, S., & Ward-Thompson, D. 2000, *Astronomy & Astrophysics*, 361, 555

Bacmann, A., Lefloch, B., Ceccarelli, C., Castets, A., Steinacker, J., & Loinard, L. 2002, *Astronomy & Astrophysics*, 389, L6

Bacmann, A., Lefloch, B., Ceccarelli, C., Steinacker, J., Castets, A., Loinard, L. 2003, *the Astrophysical Journal*, 585, L55

Ballesteros-Paredes, J., Klessen, R. S., & Vázquez-Semadeni, E. 2003, *the Astrophysical Journal*, 592, 188

Barnard, E. E. 1927, *Catalogue of 349 dark objects in the sky*, University of Chicago Press

Bash, F. N. & Peters, W. L. 1976, *the Astrophysical Journal*, 205, 786

Belloche, A., André, P., Despois, D., & Blinder, S. 2002, *Astronomy & Astrophysics*, 393, 927

Belloche, A. & André, P. 2004, *Astronomy & Astrophysics*, 419, L35

Benson, P. J. & Myers, P. C. 1989, *the Astrophysical Journal Supplement Series*, 71, 89

Bergin, E. A. & Langer, W. D. 1997, *the Astrophysical Journal*, 486, 316

Bergin, E. A., Ciardi, D. R., Lada, C. J., Alves, J., & Lada, E. A. 2001, *the Astrophysical Journal*, 557, 209

Bergin, E. A., Alves, J., Huard, T., & Lada, C. J. 2002, *the Astrophysical Journal*, 570, L101

Bianchi, S., Gonçalves, J., Albrecht, M., Caselli, P., Chini, R., Galli, D., & Walmsley, M. 2003, *Astronomy & Astrophysics*, 399, L43

Blitz, L. 1993, *Protostars and Planets III*, 125

Bloemen, J. B. G. M., et al. 1986, *Astronomy & Astrophysics*, 154, 25

Bohlin, R. C., Savage, B. D., & Drake, J. F. 1978, *the Astrophysical Journal*, 224, 132

Bok, B. J. 1937, *The distribution of the stars in space*, University of Chicago Press

Bok, B. J. & Reilly, E. F. 1947, *the Astrophysical Journal*, 105, 255

Boss, A. P. & Yorke, H. W. 1995, *the Astrophysical Journal*, 439, L55

Bourke, T. L., Myers, P. C., Robinson, G., & Hyland, A. R. 2001, *the Astrophysical Journal*, 554, 916

Brand, J. & Blitz, L. 1993, *Astronomy & Astrophysics*, 275, 67

Broguière, D., Neri, R., Sievers, A., & Wiesemeyer, H. 2003, *NIC Bolometer Users Guide*, IRAM

Buisson G., Desbats L., Duvert G., Forveille T., Gras R., Guilloteau S., Lucas R., & Valiron P. 2002, *CLASS manual*, IRAM

Burkert, A. & Bodenheimer, P. 2000, *the Astrophysical Journal*, 543, 822

Butner, H. M., Lada, E. A., & Loren, R. B. 1995, *the Astrophysical Journal*, 448, 207

Carey, S. J., Clark, F. O., Egan, M. P., Price, S. D., Shipman, R. F., & Kuchar, T. A. 1998, *the Astrophysical Journal*, 508, 721

Caselli, P., Myers, P. C., & Thaddeus, P. 1995, *the Astrophysical Journal*, 455, L77

Caselli, P., Walmsley, C. M., Terzieva, R., & Herbst, E. 1998, *the Astrophysical Journal*, 499, 234

Caselli, P., Walmsley, C. M., Tafalla, M., Dore, L., & Myers, P. C. 1999, *the Astrophysical Journal*, 523, L165

Caselli, P., Walmsley, C. M., Zucconi, A., Tafalla, M., Dore, L., & Myers, P. C. 2002, *the Astrophysical Journal*, 565, 331

Caselli, P., Walmsley, C. M., Zucconi, A., Tafalla, M., Dore, L., & Myers, P. C. 2002, *the Astrophysical Journal*, 565, 344

Caselli, P., Benson, P. J., Myers, P. C., & Tafalla, M. 2002, *the Astrophysical Journal*, 572, 238

Caselli, P. 2002, *Planetary and Space Science*, 50, 1133

Caselli, P., van der Tak, F. F. S., Ceccarelli, C., & Bacmann, A. 2003, *Astronomy & Astrophysics*, 403, L37

Chandrasekhar, S., & Fermi, E. 1953, *the Astrophysical Journal*, 118, 113

Chiar, J. E., Adamson, A. J., Kerr, T. H., & Whittet, D. C. B. 1995, *the Astrophysical Journal*, 455, 234

Choi, M., Evans, N. J., Gregersen, E. M., & Wang, Y. 1995, *the Astrophysical Journal*, 448, 742

Ciolek, G. E. & Basu, S. 2000, *the Astrophysical Journal*, 529, 925 (CB00)

Ciolek, G. E. & Mouschovias, T. C. 1995, *the Astrophysical Journal*, 454, 194

Clemens, D. P. & Barvainis, R. 1988, *the Astrophysical Journal Supplement Series*, 68, 257

Codella, C., Welser, R., Henkel, C., Benson, P. J., & Myers, P. C. 1997, *Astronomy & Astrophysics*, 324, 203

Crapsi, A., Caselli, P., Walmsley, C. M., Tafalla, M., Lee, C. W., Bourke, T. L., & Myers, P. C. 2004, *Astronomy & Astrophysics*, 420, 957 **(Chapter 3)**

Crapsi, A., Caselli, P., Walmsley, C. M., Myers, P. C., Tafalla, M., Lee, C. W., & Bourke, T. L. 2005, *the Astrophysical Journal*, 619, in press **(Chapter 2)**

Crapsi, A., et al. 2005, *Astronomy & Astrophysics*, accepted **(Chapter 4)**

Crutcher, R. M. 1999, *the Astrophysical Journal*, 520, 706

Crutcher, R. M., Nutter, D. J., Ward-Thompson, D., & Kirk, J. M. 2004, *the Astrophysical Journal*, 600, 279

Curry, C. L. & Stahler, S. W. 2001, *the Astrophysical Journal*, 555, 160

Curry, C. L. 2002, *the Astrophysical Journal*, 576, 849

Dalgarno, A. & Lepp, S. 1984, *the Astrophysical Journal*, 287, L47

de Boisanger, C., Helmich, F. P., & van Dishoeck, E. F. 1996, *Astronomy & Astrophysics*, 310, 315

Dore, L., Caselli, P., Beninati, S., Bourke, T., Myers, P. C., & Cazzoli, G. 2004, *Astronomy & Astrophysics*, 413, 1177

Draine, B. T. 1980, *the Astrophysical Journal*, 241, 1021

Draine, B. T. & Sutin, B. 1987, *the Astrophysical Journal*, 320, 803

Draine, B. T. 2003, *Annual Review of Astronomy & Astrophysics*, 41, 241

Elmegreen, B. G. & Lada, C. J. 1977, *the Astrophysical Journal*, 214, 725

Evans, N. J. 1978, IAU Colloq. 52: *Protostars and Planets*, 153

Evans, N. J. 1999, *Annual Review of Astronomy & Astrophysics*, 37, 311

Evans, N. J., Rawlings, J. M. C., Shirley, Y. L., & Mundy, L. G. 2001, *the Astrophysical Journal*, 557, 193

Evans, N. 2002, *Chemistry as a Diagnostic of Star Formation*, p. 27

Evans, N. J., et al. 2003, *Publications of the Astonomical Society of the Pacific*, 115, 965

Flower, D. R. & Pineau des Forêts, G. 2003, *Monthly Notices of the Royal Astronomical Society*, 343, 390

Foster, P. N. & Chevalier, R. A. 1993, *the Astrophysical Journal*, 416, 303

Frerking, M. A., Langer, W. D., & Wilson, R. W. 1982, *the Astrophysical Journal*, 262, 590

Galli, D., Walmsley, M., & Gonçalves, J. 2002, *Astronomy & Astrophysics*, 394, 275

Gammie, C. F. & Ostriker, E. C. 1996, *the Astrophysical Journal*, 466, 814

Gerlich, D., Herbst, E., & Roueff, E. 2002, *Planetary and Space Science*, 50, 1275

Glassgold, A. E. 1985, *Protostars and Planets II*, 641

Goldreich, P. & Kwan, J. 1974, *the Astrophysical Journal*, 189, 441

Gonçalves, J., Galli, D., & Walmsley, M. 2004, *Astronomy & Astrophysics*, 415, 617

Goodman, A. A., Benson, P. J., Fuller, G. A., & Myers, P. C. 1993, *the Astrophysical Journal*, 406, 528

Goodman, A. A., Barranco, J. A., Wilner, D. J., & Heyer, M. H. 1998, *the Astrophysical Journal*, 504, 223

Goodwin, S. P., Whitworth, A. P., & Ward-Thompson, D. 2004, *Astronomy & Astrophysics*, 419, 543

Green, S. 1975, *the Astrophysical Journal*, 201, 366

Gregersen, E. M., Evans, N. J., Zhou, S., & Choi, M. 1997, *the Astrophysical Journal*, 484, 256

Guelin, M., Langer, W. D., & Wilson, R. W. 1982, *Astronomy & Astrophysics*, 107, 107

Harvey, D. W. A., Wilner, D. J., Lada, C. J., Myers, P. C., & Alves, J. F. 2003, *the Astrophysical Journal*, 598, 1112

Hasegawa, T. I., Herbst, E., & Leung, C. M. 1992, *the Astrophysical Journal Supplement Series*, 82, 167

Hasegawa, T. I. & Herbst, E. 1993, *Monthly Notices of the Royal Astronomical Society*, 263, 589

Henning, T., Michel, B., & Stognienko, R. 1995, *Planetary and Space Science*, 43, 1333

Heyer, M. H., et al. 1996, *the Astrophysical Journal*, 464, L175

Heyer, M. H., Narayanan, G., & Brewer, M. K. 2001, *On the Fly Mapping at the FCRAO 14m Telescope*, FCRAO

Hirota, T., Ikeda, M., & Yamamoto, S. 2003, *the Astrophysical Journal*, 594, 859

Jijina, J., Myers, P. C., & Adams, F. C. 1999, *the Astrophysical Journal Supplement Series*, 125, 161

Jones, C. E. & Basu, S. 2002, *the Astrophysical Journal*, 569, 280

Jørgensen, J. K., Schöier, F. L., & van Dishoeck, E. F. 2002, *Astronomy & Astrophysics*, 389, 908

Keene, J. 1981, *the Astrophysical Journal*, 245, 115

Keto, E., Rybicki, G. B., Bergin, E. A., & Plume, R. 2004, *the Astrophysical Journal*, 613, 355

Kramer, C., Alves, J., Lada, C., Lada, E., Sievers, A., Ungerechts, H., & Walmsley, M. 1998, *Astronomy & Astrophysics*, 329, L33

Kramer, C., Alves, J., Lada, C. J., Lada, E. A., Sievers, A., Ungerechts, H., & Walmsley, C. M. 1999, *Astronomy & Astrophysics*, 342, 257

Kramer, C., Richer, J., Mookerjea, B., Alves, J., & Lada, C. 2003, *Astronomy & Astrophysics*, 399, 1073

Kuiper, T. B. H., Langer, W. D., & Velusamy, T. 1996, *the Astrophysical Journal*, 468, 761

Lacy, J. H., Knacke, R., Geballe, T. R., & Tokunaga, A. T. 1994, *the Astrophysical Journal*, 428, L69

Lada, C. J. & Wilking, B. A. 1984, *the Astrophysical Journal*, 287, 610

Lada, C. J., Lada, E. A., Clemens, D. P., & Bally, J. 1994, *the Astrophysical Journal*, 429, 694

Lada, C. J., Bergin, E. A., Alves, J. F., & Huard, T. L. 2003, *the Astrophysical Journal*, 586, 286

Lazarian, A., Goodman, A. A., & Myers, P. C. 1997, *the Astrophysical Journal*, 490, 273

Lee, C. W. & Myers, P. C. 1999, *the Astrophysical Journal Supplement Series*, 123, 233

Lee, C. W., Myers, P. C., & Tafalla, M. 1999, *the Astrophysical Journal*, 526, 788

Lee, C. W., Myers, P. C., & Tafalla, M. 2001, *the Astrophysical Journal Supplement Series*, 136, 703

Lee, C. W., Myers, P. C., & Plume, R. 2004, *the Astrophysical Journal Supplement Series*, 153, 523

Lee, J., Evans, N. J., Shirley, Y. L., & Tatematsu, K. 2003, *the Astrophysical Journal*, 583, 789

Lee, H.-H., Bettens, R. P. A., & Herbst, E. 1996, *Astronomy & Astrophysics Supplement Series*, 119, 111

Lee, S.-W., Ohashi, N., Moriarty–Schieven, G., & Butner, H. M. 1999, *Proceedings of Star Formation 1999*, Editor: T. Nakamoto, Nobeyama Radio Observatory, 179

Leger, A. 1983, *Astronomy & Astrophysics*, 123, 271

Li, Z. & Shu, F. H. 1996, *the Astrophysical Journal*, 472, 211

Li, Z. 1999, *the Astrophysical Journal*, 526, 806

Li, Z., Shematovich, V. I., Wiebe, D. S., & Shustov, B. M. 2002, *the Astrophysical Journal*, 569, 792

Lintott, C. J., Viti, S., Rawlings, J. M. C., Williams, D. A., Hartquist, T. W., Caselli, P., Zinchenko, I., & Myers, P. 2005, *ArXiv Astrophysics e-prints*, [astro-ph/0410653]

Lizano, S. & Shu, F. H. 1989, *the Astrophysical Journal*, 342, 834

Loren, R. B. 1976, *the Astrophysical Journal*, 209, 466

Luhman, M. L. & Jaffe, D. T. 1996, *the Astrophysical Journal*, 463, 191

Lynds, B. T. 1962, *the Astrophysical Journal Supplement Series*, 7, 1

Nurmanova, U. A. 1983, *Peremennye Zvezdy*, 21, 777

Mac Low, M., Klessen, R. S., Burkert, A., & Smith, M. D. 1998, *Physical Review Letters*, 80, 2754

Mardones, D., Myers, P. C., Tafalla, M., Wilner, D. J., Bachiller, R., & Garay, G. 1997, *the Astrophysical Journal*, 489, 719

Maret, S., et al. 2004, *Astronomy & Astrophysics*, 416, 577

Masunaga, H., Miyama, S. M., & Inutsuka, S. 1998, *the Astrophysical Journal*, 495, 346

Mathis, J. S., Rumpl, W., & Nordsieck, K. H. 1977, *the Astrophysical Journal*, 217, 425

McCall, B. J., et al. 2003, *Nature*, 422, 500

McKee, C. F. 1989, *the Astrophysical Journal*, 345, 782

McKee, C. F., Zweibel, E. G., Goodman, A. A., & Heiles, C. 1993, *Protostars and Planets III*, 327

Mestel, L. & Spitzer, L. 1956, *Monthly Notices of the Royal Astronomical Society*, 116, 503

Millar, T. J., Bennett, A., & Herbst, E. 1989, *the Astrophysical Journal*, 340, 906

Mizuno, A., Onishi, T., Hayashi, M., Ohashi, N., Sunada, K., Hasegawa, T., & Fukui, Y. 1994, *Nature*, 368, 719

Mouschovias, T. C. & Spitzer, L. 1976, *the Astrophysical Journal*, 210, 326

Moriarty-Schieven, G. H., Wannier, P. G., Mangum, J. G., Tamura, M., & Olmsted, V. K. 1995, *the Astrophysical Journal*, 455, 190

Myers, P. C. 1983, *the Astrophysical Journal*, 270, 105

Myers, P. C. & Goodman, A. A. 1988, *the Astrophysical Journal*, 326, L27

Myers, P. C. & Ladd, E. F. 1993, *the Astrophysical Journal*, 413, L47

Myers, P. C., Bachiller, R., Caselli, P., Fuller, G. A., Mardones, D., Tafalla, M., & Wilner, D. J. 1995, *the Astrophysical Journal*, 449, L65

Myers, P. C., Evans, N. J., & Ohashi, N. 2000, *Protostars and Planets IV*, 217

Norman, C. & Silk, J. 1980, *the Astrophysical Journal*, 238, 158

Oliveira, C. M., Hébrard, G., Howk, J. C., Kruk, J. W., Chayer, P., & Moos, H. W. 2003, *the Astrophysical Journal*, 587, 235

Onishi, T., Mizuno, A., Kawamura, A., Ogawa, H., & Fukui, Y. 1996, *the Astrophysical Journal*, 465, 815

Onishi, T., Mizuno, A., & Fukui, Y. 1999, *Publications of the Astonomical Society of Japan*, 51, 257

Onishi, T., Mizuno, A., Kawamura, A., Tachihara, K., & Fukui, Y. 2002, *the Astrophysical Journal*, 575, 950

Ossenkopf, V. 1993, *Astronomy & Astrophysics*, 280, 617

Ossenkopf, V. & Henning, T. 1994, *Astronomy & Astrophysics*, 291, 943

Padoan, P. & Nordlund, Å. 1999, *the Astrophysical Journal*, 526, 279

Pagani, L. et al. 2003, *Astronomy & Astrophysics*, 406, L59

Palla, F. & Stahler, S. W. 1993, *the Astrophysical Journal*, 418, 414

Palla, F. & Stahler, S. W. 2002, *the Astrophysical Journal*, 581, 1194

Patel, N. A., Goldsmith, P. F., Heyer, M. H., Snell, R. L., & Pratap, P. 1998, *the Astrophysical Journal*, 507, 241

Penzias, A. A. 1981, *the Astrophysical Journal*, 249, 518

Pratap, P., Dickens, J. E., Snell, R. L., Miralles, M. P., Bergin, E. A., Irvine, W. M., & Schloerb, F. P. 1997, *the Astrophysical Journal*, 486, 862

Preibisch, T., Ossenkopf, V., Yorke, H. W., & Henning, T. 1993, *Astronomy & Astrophysics*, 279, 577

Press, W. H., Teukolsky, S. A., Vetterling, W. T., & Flannery, B. P. 1992, *Numerical Recipes in C. The art of scientific computing*, (2nd ed.; Cambridge: Cambridge University Press)

Rachford, B. L., et al. 2002, *the Astrophysical Journal*, 577, 221

Richer, J. S., Shepherd, D. S., Cabrit, S., Bachiller, R., & Churchwell, E. 2000, *Protostars and Planets IV*, 867

Ridge, N. A. & Moore, T. J. T. 2001, *Astronomy & Astrophysics*, 378, 495

Roberts, H. & Millar, T. J. 2000a, *Astronomy & Astrophysics*, 361, 388

Roberts, H. & Millar, T. J. 2000b, *Astronomy & Astrophysics*, 364, 780

Roberts, H., Herbst, E., & Millar, T. J. 2003, *the Astrophysical Journal*, 591, L41

Roberts, H., Herbst, E., & Millar, T. J. 2004, *Astronomy & Astrophysics*, 424, 905

Roueff, E., Tiné, S., Coudert, L. H., Pineau des Forêts, G., Falgarone, E., & Gerin, M. 2000, *Astronomy & Astrophysics*, 354, L63

Sadlej, J., Rowland, B., Devlin, J. P., & Buch, V. 1995, *Journal of Chemical Physics*, 102, 4804

Savage, B. D., Drake, J. F., Budich, W., & Bohlin, R. C. 1977, *the Astrophysical Journal*, 216, 291

Scalo, J. M. 1986, *Fundamentals of Cosmic Physics*, 11, 1

Shematovich, V. I., Wiebe, D. S., Shustov, B. M., & Li, Z. 2003, *the Astrophysical Journal*, 588, 894

Shirley, Y. L., Evans, N. J., Rawlings, J. M. C., & Gregersen, E. M. 2000, *the Astrophysical Journal Supplement Series*, 131, 249

Shinnaga, H., Ohashi, N., Lee, S., & Moriarty-Schieven, G. H. 2004, *the Astrophysical Journal*, 601, 962

Shu, F. H. 1977, *the Astrophysical Journal*, 214, 488

Shu, F. H., Adams, F. C., & Lizano, S. 1987, *Annual Review of Astronomy & Astrophysics*, 25, 23

Snell, R. L. & Loren, R. B. 1977, *the Astrophysical Journal*, 211, 122

Sofia, U. J., Cardelli, J. A., Guerin, K. P., & Meyer, D. M. 1997, *the Astrophysical Journal*, 482, L105

Spitzer, L. 1978, *Physical Processes in the Interstellar Medium* New York, Wiley-Interscience

Stone, J. M., Ostriker, E. C., & Gammie, C. F. 1998, *the Astrophysical Journal*, 508, L99

Sugitani, K., Fukui, Y., & Ogura, K. 1991, *the Astrophysical Journal Supplement Series*, 77, 59

Tafalla, M., Mardones, D., Myers, P. C., Caselli, P., Bachiller, R., & Benson, P. J. 1998, *the Astrophysical Journal*, 504, 900

Tafalla, M., Myers, P. C., Caselli, P., Walmsley, C. M., & Comito, C. 2002, *the Astrophysical Journal*, 569, 815

Tafalla, M., Myers, P. C., Caselli, P., & Walmsley, C. M. 2004, *Astronomy & Astrophysics*, 416, 191

Tiné, S., Roueff, E., Falgarone, E., Gerin, M., & Pineau des Forêts, G. 2000, *Astronomy & Astrophysics*, 356, 1039

Umebayashi, T. & Nakano, T. 1990, *Monthly Notices of the Royal Astronomical Society*, 243, 103

Vazquez-Semadeni, E., Ostriker, E. C., Passot, T., Gammie, C. F., & Stone, J. M. 2000, *Protostars and Planets IV*, 3

van der Tak, F., Caselli, P., Walmsley, C. M., Ceccarelli, C., Bacmann, A., & Crapsi, A. 2004, *The Dense Interstellar Medium in Galaxies*, 549

van Dishoeck, E. F. & Blake, G. A. 1998, *Annual Review of Astronomy & Astrophysics*, 36, 317

Verhoeve, P., Zwart, E., Versluis, M., Drabbels, M., Ter Meulen, J. J., Meerts, W. L., Dymanus, A., & McLay, D. B. 1990, *Review of Scientific Instruments*, 61, 1612

Visser, A. E., Richer, J. S., & Chandler, C. J. 2001, *Monthly Notices of the Royal Astronomical Society*, 323, 257

Visser, A. E., Richer, J. S., & Chandler, C. J. 2002, *the Astronomical Journal*, 124, 2756

Walmsley, C. M., Flower, D. R., & Pineau des Forêts, G. 2004, *Astronomy & Astrophysics*, 418, 1035

Walsh, A. J., Myers, P. C., & Burton, M. G. 2004, *the Astrophysical Journal*, 614, 194

Ward-Thompson, D., Buckley, H. D., Greaves, J. S., Holland, W. S., & André, P. 1996, *Monthly Notices of the Royal Astronomical Society*, 281, L53

Ward-Thompson, D., Motte, F., & André, P. 1999, *Monthly Notices of the Royal Astronomical Society*, 305, 143

Ward-Thompson, D., Kirk, J., & André, P. 2003, *IAU Symposium*, 221

Wendker, H. J. 1995, *Astronomy & Astrophysics Supplement Series*, 109, 177

Weintraub, D. A., Goodman, A. A., & Akeson, R. L. 2000, *Protostars and Planets IV*, 247

White, G. J., Lefloch, B., Fridlund, C. V. M., Aspin, C. A., Dahmen, G., Minchin, N. R., & Huldtgren, M. 1997, *Astronomy & Astrophysics*, 323, 931

Williams, J. P., Bergin, E. A., Caselli, P., Myers, P. C., & Plume, R. 1998, *the Astrophysical Journal*, 503, 689

Williams, J. P., Myers, P. C., Wilner, D. J., & di Francesco, J. 1999, *the Astrophysical Journal*, 513, L61

Wilson, T. L. & Rood, R. 1994, *Annual Review of Astronomy & Astrophysics*, 32, 191

Young, J. S. & Scoville, N. Z. 1991, *Annual Review of Astronomy & Astrophysics*, 29, 581

Young, C. H. et al. 2004, *the Astrophysical Journal Supplement Series*, 154, 396

Zhou, S. 1992, *the Astrophysical Journal*, 394, 204

Zhou, S., Evans, N. J., Kömpe, C., & Walmsley, C. M. 1993, *the Astrophysical Journal*, 404, 232

Zucconi, A., Walmsley, C. M., & Galli, D. 2001, *Astronomy & Astrophysics*, 376, 650

Zweibel, E. G. 1998, *the Astrophysical Journal*, 499, 746

Curriculum Vitæ and publication list

Personal data

Name:	Crapsi Antonio
Born:	29-12-1977
in:	Campobasso (CB), Italy
Personal address:	Via Nuova di Pozzolatico, 1, Firenze (FI), I-50125
	tel. +39 340 7762635 (mobile)
Arcetri address:	Largo Enrico Fermi, 5, Firenze (FI), I-50125
	tel. +39 055 2752238
	e-mail: crapsi@arcetri.astro.it

Education

From October 2003 to September 2004, Pre-Doctoral Fellow at Harvard–Smithsonian Center for Astrophysics (advisor: Dr. Philip C. Myers).

From January 1^{st} 2002, Ph.D. student in Astronomy at University of Florence (advisors: Dr. Paola Caselli and Dr. Malcolm Walmsley).

"Laurea" degree in Astronomy (equivalent of M.Sc.) approved with 110/110 "cum laude" (July 20^{th} 2001), discussing a thesis on "Molecular clouds and radio continuum in star-forming galaxies" (advisors: Prof. Loretta Gregorini and Dr. Matteo Murgia).

From September 1996 to September 2000 undergraduate student in Astronomy at the University of Bologna.

Scientific High School degree achieved in 1996 at Liceo Scientifico "A.Romita" (Campobasso), approved with 53/60.

Languages

Good knowledge of English both spoken and written.

Computing skills

General knowledge of OS: UNIX-LINUX, MS-DOS, VAX-VMS.
General knowledge of programming languages and development environments as Fortran, C++ and IDL.
Basic knowledge of programming languages: html, Java.
Experienced with the whole GILDAS package for data reduction.
Confident with Smongo, LaTeX and the general programs used in scientific work.
Good knowledge of MIR, MIRIAD and other interferometric data reduction packages.

Publications on refereed papers

• *Dynamical and chemical properties of the "former starless" core L1014*
Crapsi, A., DeVries, C. H., Huard, T. L., Lee, J.-E., Myers, P. C., Ridge, N. A., Bourke, T. L., Evans, et al. 2005, A&A, accepted

• *Probing the evolutionary status of starless cores through N_2H^+ and N_2D^+ observations*
Crapsi, A., Caselli, P., Walmsley, C. M., Tafalla, M., Lee, C. W., Bourke, T. L., & Myers, P. C. 2005, ApJ, 619, in press

• *A "Starless" Core that Isn't: Detection of a Source in the L1014 Dense Core with the Spitzer Space Telescope*
Young, C. H., Jørgensen, J. K., Shirley, Y. L., Kauffmann, J., Huard, T., Lai, S.-P., Lee, C. W., **Crapsi, A.**, et al. 2004, ApJS, 154, 396

• *Observations of L1521F: A highly evolved starless core*
Crapsi, A., Caselli, P., Walmsley, C. M., Tafalla, M., Lee, C. W., Bourke, T. L., & Myers, P. C. 2004, A&A, 420, 957

• *Radio continuum and CO emission in star-forming galaxies*
Murgia, M., **Crapsi, A.**, Moscadelli, L., & Gregorini, L. 2002, A&A, 385, 412

Non-refereed publications

• *Chemistry and kinematics of the pre-stellar core L1544: constraints from H_2D^+*
van der Tak, F., Caselli, P., Walmsley, C. M., Ceccarelli, C., Bacmann, A., & **Crapsi, A.** 2004, The Dense Interstellar Medium in Galaxies, p. 549.

• *Radio continuum and CO emission in star-forming galaxies*
Gregorini, L., Murgia, M., **Crapsi, A.**, & Moscadelli, L. 2003, Revista Mexicana de Astronomia y Astrofisica Conference Series, 17, 90

Observational Experience and Data Reduction

I took part in five observing runs at IRAM-30m in Pico Veleta learning how to use the 30m telescope in the different modes (continuum and lines) and the different techniques (frequency switching, wobbler switching, on-the-fly).

I observed with the Swedish-ESO Submillimeter Telescope (now dismantled) in La Silla getting confident with the whole process of line observation at this telescope.

I also observed remotely with the Five College Radio Astronomy Observatory 14m antenna using the on-the-fly technique.

In Mauna Kea, I both used the CSO 10.4m telescope with the SIS receiver and I had experiences at the Sub Millimeter Array, the 8-elements interferometer.

The data reduction I performed on all these data sets has been done using the GILDAS package. This includes the extensive use of CLASS, NIC, CLIC, GRAPHIC, MAPPING. Moreover, I used the MIR and MIRIAD packages to reduce the SMA data and the OTFTOOL software to handle the FCRAO observations.

Attended Schools

• 32^{nd} "Saas-Fee Advanced Lectures": The Cold Universe.
Grimentz (CH), March 18-23, 2002.

• "Scuola nazionale di Astrofisica" VI cycle (2001-2002) 3^{rd} course: Turbulence in space plasmas - Galaxies and galaxy systems
Cetraro (CS), June 3-7, 2002

• "Scuola Nazionale di Astrofisica" VI cycle (2001-2002) 4^{th} course: Cosmology - Relativistic astrophysics

Asiago (VI), September 8-14, 2002

• Third IRAM Millimeter Interferometry School
Grenoble (F), September 30-October 5, 2002

• Introduzione al C++
Bologna, March 31-April 4, 2003

• "Scuola Nazionale di Astrofisica" VII cycle (2003-2004) 1^{st} course: Local group galaxies - The telescopes of the next generation
Marciana (LI), May 12-16, 2003

• "Scuola Nazionale di Astrofisica" VII cycle (2003-2004) 2^{nd} course: ISM astrophysics - Compact objects and pulsars
Cagliari, September 27-October 3, 2003

Conferences Contributions

• XLV S.A.It meeting: "Prospettive scientifiche ed organizzative dell'astronomia italiana alla luce delle nuove strumentazioni",
Bologna, May 2-5, 2001.

• Star Formation Workshop 2002: Magnetohydrodynamics, Radiation diagnostics and Chemistry of Star Formation
Taroko Gorge (Taiwan), June 12-17, 2002
– *poster contribution:* A. Crapsi, P. Caselli, C.M. Walmsley, M. Tafalla, C.W. Lee, P. Myers, *"N_2H^+ and N_2D^+ in prestellar cores"*

• 4th Cologne-Bonn-Zermatt-Symposium - The Dense Interstellar Medium in Galaxies
– *poster contribution:* A. Crapsi, P. Caselli, C.M. Walmsley, M. Tafalla, C.W. Lee, P. Myers, T. Bourke *"L1521F vs. L1544: a comparison of evolved starless cores in Taurus"*
– *poster contribution:* T. Bourke, P. Myers, M. Tafalla, D. Wilner, C.W. Lee, A. Crapsi, P. Caselli *"Inward motions in the starless cores L1544 and L694-2"*

• 1^{st} Spanish Meeting on Molecular Astrophysics
– *poster contribution:* M. Tafalla, P.C. Myers, P. Caselli, C.M. Walmsley, A. Crapsi, J. Santiago *"The chemical structure of starless cores"*

Acknowledgments

I would like to take this opportunity to thank all the persons who helped me to reach this final page of my Ph.D. thesis.
First of all, it is a pleasure to thank Dr. Paola Caselli and Prof. Malcolm Walmsley who enthusiastically introduced me three years ago to the study of star formation and stimulated my curiosity in understanding its mechanisms. The wide range of knowledges that I gained under their patient guidance and wise advices is invaluable to me. I greatly appreciated the trust they granted me committing tasks of high responsibility and their support in accomplishing them.

A special thanks goes to Prof. Phil Myers, my advisor at Center for Astrophysics. I consider my experience at CfA a privilege and working with Prof. Myers was really inspiring. The combination of his perceptive advices, the exciting projects he shared with me and the autonomy he left me enriched enormously my staying at CfA.

I would like to express my gratitude to my main collaborators Dr. Mario Tafalla, Dr. Tyler Bourke, Dr. Chang Won Lee and the huge *L1014 group*, including Prof. Neal J. Evans, Dr. Chadwick Young, Dr. Christopher De Vries, Dr. Tracy Huard and Dr. Naomi Ridge.

I would also like to thank the whole Star Formation group in Arcetri and the Radio and Geoastronomy group in Cambridge which represented a huge reservoir of knowledges to draw on. In particular, I would like to thank Dr. Riccardo Cesaroni, Dr. Daniele Galli and Dr. Henrik Beuther who always gave me a helping hand whenever I needed.

Many thanks go to my office mates Carmelo, Gianni, Tracy, Luis, Niccolò and Guia and more generally to all the friends at the observatory Stefano, Francesco, Tommaso, Marco, Matteo, Jacopo, Enrico, Pasquale, Roberto,

Paola, Luca, Antonella, Giovanni, Filippo, Andrea and Claudio and the coffee club Paula, Alessandro (I, II, III), Peter, Amy, Rui, Jesus, Vallia, Francesca, Francesco, Betty and Salvio for the good laughs and for making *certain* days much more enjoyable.

This work may not have been done without the sponsoring of my family who may still confuse telescopes with binoculars or astronomy with astrology but was (and will) always be there for me.
Speaking of which, a really special thanks goes to Lara, the most talented person I ever met, for sharing all my emotions since a long time and for always supporting me, regardless.

A final thanks to David Ortiz and the Boston Red Sox for showing everyone that it is never finished before the last out.